

## University of Southampton Research Repository ePrints Soton

Copyright © and Moral Rights for this thesis are retained by the author and/or other copyright owners. A copy can be downloaded for personal non-commercial research or study, without prior permission or charge. This thesis cannot be reproduced or quoted extensively from without first obtaining permission in writing from the copyright holder/s. The content must not be changed in any way or sold commercially in any format or medium without the formal permission of the copyright holders.

When referring to this work, full bibliographic details including the author, title, awarding institution and date of the thesis must be given e.g.

AUTHOR (year of submission) "Full thesis title", University of Southampton, name of the University School or Department, PhD Thesis, pagination

**UNIVERSITY OF SOUTHAMPTON**

**FACULTY OF ENGINEERING AND THE ENVIRONMENT**

Civil, Maritime and Environmental Engineering and Science

**Mathematical Model of High Speed Planing Dynamics and  
Application to Aircraft Ditching**

by

**Prin KANYOO**

Thesis for the degree of Doctor of Philosophy

September 22, 2016



UNIVERSITY OF SOUTHAMPTON

ABSTRACT

FACULTY OF ENGINEERING AND THE ENVIRONMENT

Civil, Maritime and Environmental Engineering and Science

Doctor of Philosophy

MATHEMATICAL MODEL OF HIGH SPEED PLANING DYNAMICS AND  
APPLICATION TO AIRCRAFT DITCHING

by **Prin KANYOO**

A nonlinear mathematical model capable of predicting loads and motions of high speed planing craft in the longitudinal plane has been developed. The development of the model is based on the mathematical model presented by [Zarnick \(1978\)](#). Following the principle of 2D strip theory and wedge water entry problem, a high speed planing hull is divided into a number of transverse sections. Sectional forces and motions are evaluated, and then, by integrating along the ship length, total force and moment are obtained which leads to corresponding instantaneous acceleration. By integration using a time marching scheme, velocity and displacement are obtained. The influence of the controlling parameters, such as number of sections and time step, on the accuracy and stability of the simulation in calm water, regular and irregular waves is investigated. The accuracy of the underlying mathematical model is investigated and the deficiencies identified. The optimum model is finally validated against the original model of [Zarnick \(1978\)](#) and the experiments of [Fridsma \(1969\)](#).

An extension of the model to be capable of simulating roll motion is proposed and implemented. This extension may be useful when the prediction of high speed planing motions in oblique seas is proposed. The initial validation process has been carried out but subjected to the full validity of application.

Moreover, as the original approach of the mathematical model was used in prediction of seaplane landing ([Wagner, 1931](#)), an additional aim and objective to the present PhD project is to find a novel technique to predict the loads on fuselage of an aircraft emergently landing (ditching) into the water. Experimental tests related to these simulations are planned and carried out in order to use their results as validation references to the modified mathematical model. The deliverable of the project is an analysis of optimization of the mathematical model capable of predicting loads and motions of high speed planing craft. As well as the implementation of capability of predicting impact loads and initial post-impact motions of aircraft ditching into the water.





# Contents

<b>Declaration of Authorship</b>	<b>xvii</b>
<b>Acknowledgements</b>	<b>xix</b>
<b>Nomenclature</b>	<b>xxi</b>
<b>1 Introduction</b>	<b>1</b>
1.1 Background . . . . .	3
1.2 Aims and Objectives . . . . .	4
1.3 Application to Transverse Motions . . . . .	6
1.4 Application to Aircraft Ditching . . . . .	6
1.5 Novel Contributions . . . . .	7
1.6 Thesis Structure . . . . .	8
<b>2 Literature Review and Relevant Theories</b>	<b>11</b>
2.1 General . . . . .	11
2.2 Model Experiments and Empirical Formulations . . . . .	12
2.3 2D Strip Theory Approach . . . . .	18
2.4 3D CFD Solvers . . . . .	29
2.5 Aircraft Ditching . . . . .	31
<b>3 Verification and Validation of Mathematical Model of Calm Water and Regular Wave Simulations</b>	<b>37</b>
3.1 Coordinate Systems . . . . .	38
3.2 System of Equations of Motions . . . . .	39
3.3 Verification of the Mathematical Model . . . . .	45
3.3.1 Hypothesis of Accuracy of Time Histories . . . . .	45
3.3.2 Pressure Distribution Evaluation . . . . .	46
3.3.3 Methodologies of Convergence Analysis and Optimization Consideration . . . . .	49
3.3.4 Time Integration Numerical Solvers Verification . . . . .	49
3.3.4.1 Fixed Step Solver and Variable-Step Solver . . . . .	50
3.3.4.2 Comparison and Verification of Time Integration Methods . . . . .	51
3.3.4.3 Influence of Time Step Size: $\Delta t$ . . . . .	52
3.3.5 Limitations and Optimization of Mathematical Model in Time History Evaluations . . . . .	54
3.3.5.1 Influence of Number of Sections: $N_s$ on Sectional Added Mass and Its Associated Terms . . . . .	55

3.3.5.2	Influence of Number of Sections: $N_s$ and Time Step Size: $\Delta t$ in Full Time History Evaluations . . . . .	55
3.3.5.3	Optimal Parameters for Time History Simulations . . . . .	59
3.3.5.4	Effects on Variable Deadrise Angles Hull . . . . .	60
3.3.5.5	Scale Effects . . . . .	63
3.4	Validation . . . . .	65
3.4.1	Calm Water Simulations . . . . .	65
3.4.2	Regular Waves Simulations . . . . .	67
<b>4</b>	<b>Verification and Validation of Simulations in Irregular Waves</b>	<b>73</b>
4.1	Irregular Waves Generations . . . . .	73
4.1.1	Fourier Series . . . . .	73
4.1.2	Wave Energy Spectrum . . . . .	73
4.1.3	Choices of Wave Spectra . . . . .	74
	Pierson-Moskowitz Spectrum: . . . . .	75
	Bretschneider Spectrum: . . . . .	75
	Ochi 6-Parameters Spectrum: . . . . .	75
	JONSWAP: . . . . .	76
	ITTC Spectrum: . . . . .	76
4.1.4	Representation of the Seaway . . . . .	76
4.2	Model Simulations . . . . .	78
4.2.1	Generated Irregular Waves Analysis . . . . .	78
4.2.2	Response Data Analysis . . . . .	79
4.3	Verification of the Mathematical Model . . . . .	81
4.3.1	Influence of Number of Section $N_s$ and Time Step Size $\Delta t$ in Different Deadrise Angle and Sea Conditions . . . . .	81
4.3.2	Validation of Irregular Waves Simulations . . . . .	83
<b>5</b>	<b>Extension to Transverse Asymmetric Motions</b>	<b>89</b>
5.1	Definition of Coordinate Systems . . . . .	92
5.2	Definition of Wave Characteristics . . . . .	93
5.3	Equations of Motions of Coupled Heave, Roll and Pitch Motions . . . . .	94
5.3.1	Hydrodynamic Lift Force . . . . .	96
5.3.2	Cross-Flow Drag: . . . . .	99
5.3.3	Buoyancy: . . . . .	100
5.3.4	Total Forces and Moments . . . . .	101
5.4	Simulations and Validations . . . . .	104
5.4.1	Fixed Heel Angle Simulations . . . . .	104
5.4.2	Coupled Heave, Roll and Pitch Motions Simulations . . . . .	105
<b>6</b>	<b>Application to Aircraft Ditching: Development and Verification of Mathematical Model</b>	<b>113</b>
6.1	Application to Aircraft Fuselage Form . . . . .	115
6.1.1	Sectional Added Mass Coefficient . . . . .	115
	Sectional Added Mass Coefficient Suggested by Payne (1994):	115
	Sectional Added Mass Coefficient Suggested by Vorus (1996):	116
	Sectional Added Mass Suggested by Faltinsen (2000): . . . . .	116

	Sectional Added Mass Evaluated using Lewis Conformal Mapping: . . . . .	116
6.1.2	Sectional Added Mass of Semi-Circular Shape . . . . .	116
6.1.2.1	Hypothesis . . . . .	118
6.1.2.2	Verification of Sectional Added Mass Coefficient . . . . .	118
6.1.2.3	Expression of Sectional Added Mass of Semi-Circular Shape . . . . .	121
6.1.2.4	Validation of the Expression . . . . .	125
6.1.3	Other Force Components . . . . .	125
6.1.3.1	Expression of Sectional Cross-Flow Drag . . . . .	125
6.1.3.2	Expression of Sectional Buoyancy . . . . .	126
6.1.3.3	Global Equations of Motions . . . . .	127
6.2	Numerical Experiments . . . . .	127
6.2.1	Test Configurations . . . . .	128
6.2.2	Results, Discussion and Cross Validation . . . . .	129
6.2.2.1	Cylinder Drop Simulations . . . . .	129
6.2.2.2	Constant Horizontal Speed Towed Conditions . . . . .	129
6.2.2.3	Constant Vertical Speed Drop Simulations . . . . .	130
6.2.2.4	Accelerated Vertical Speed with Zero Forward Speed Simulations . . . . .	130
6.2.2.5	Constant Horizontal Speed with Vertical Acceleration Simulations . . . . .	130
<b>7</b>	<b>Application to Aircraft Ditching: Ditching Experiments</b>	<b>141</b>
7.1	Background . . . . .	141
7.2	Experimental Planning and Procedure . . . . .	142
7.2.1	Facility . . . . .	142
7.2.2	Preliminary Simulations . . . . .	142
7.2.3	Fuselage Model . . . . .	147
7.2.4	Equipment . . . . .	147
7.2.5	Instrumentation . . . . .	147
7.2.6	Launching Technique . . . . .	149
7.2.7	Uncertainty Analysis of the Instruments . . . . .	149
7.2.8	Experimental Run Log . . . . .	151
7.3	Signal Processing . . . . .	153
7.3.1	Vertical Displacement . . . . .	153
7.3.2	Vertical Acceleration . . . . .	156
7.3.3	Vertical Impact Force . . . . .	158
7.4	Validation . . . . .	160
7.4.1	Hydrodynamic Impact Force Extraction . . . . .	160
7.4.2	Simulations for Experimental Tests . . . . .	163
7.4.3	Comparison . . . . .	163
<b>8</b>	<b>Conclusion and Further Work</b>	<b>167</b>
8.1	Conclusion . . . . .	167
8.2	Future Work . . . . .	174
<b>A</b>	<b>Detailed Development of Equations of Motions</b>	<b>175</b>

A.1	System of Equations of Motions . . . . .	175
A.2	Sectional Forces . . . . .	177
A.2.1	Sectional Hydrodynamic Lift Forces . . . . .	177
A.2.2	Sectional Cross Flow Drag Force and Moment . . . . .	180
A.2.3	Sectional Buoyancy Force . . . . .	180
A.3	Total Forces and Moments . . . . .	181
A.3.1	Total Hydrodynamic Forces and Moments . . . . .	181
A.3.2	Drag Force and Moment . . . . .	182
A.4	The Global System and Matrix Form . . . . .	183
Heave Equation:	. . . . .	184
Pitch Equation:	. . . . .	185
A.5	Modification to Application in Asymmetric Conditions . . . . .	187
A.5.1	Hydrodynamic Lift Force: . . . . .	187
A.5.2	Cross-Flow Drag: . . . . .	191
A.5.3	Buoyancy: . . . . .	191
A.5.4	Total Forces and Moments: . . . . .	192
Heave Equation:	. . . . .	194
Roll Equation:	. . . . .	195
Pitch Equation:	. . . . .	196
<b>B</b>	<b>Detailed Evaluation of Terms in Equations of Motions and Choices of Numerical Methods</b>	<b>199</b>
B.1	Evaluation of Wave Functions . . . . .	199
B.1.1	Wave Elevation and Its Time Derivative: $r$ and $\dot{r}$ . . . . .	200
B.1.2	Wave Vertical Orbital Velocity and Its Time Derivative: $w_w$ and $\dot{w}_w$ . . . . .	201
B.1.3	Space Partial Derivative of Wave Vertical Orbital Velocity: $\frac{\partial w_w}{\partial x^j}$ . . . . .	201
B.2	Evaluation of Section Submergence and Its time Derivative: $h$ and $\dot{h}$ . . . . .	202
B.3	Evaluation of Sectional Added Mass and Its Time Derivative . . . . .	204
B.3.1	Availability of Sectional Added Mass Coefficients $C_m$ . . . . .	206
Added mass coefficient suggested by Faltinsen (2000):	. . . . .	206
Added mass coefficient used by Zarnick (1978):	. . . . .	206
Added mass coefficient suggested by Payne (1994):	. . . . .	206
Added mass coefficient suggested by Vorus (1996):	. . . . .	207
B.4	Evaluation of Space Partial Derivative of Sectional Added Mass: $\frac{\partial m_a}{\partial x^j}$ . . . . .	207
B.5	Evaluation of Sectional Cross-Flow Drag . . . . .	209
B.5.1	Evaluation of Sectional Buoyancy . . . . .	209
B.6	Evaluation of Drag . . . . .	210
B.7	Evaluation of Coefficients $C_A$ to $C_R$ and Total Forces and Moments . . . . .	211
B.8	Time Marching Integration Methods . . . . .	212
B.8.1	Basic Algorithms of Equations of Motions . . . . .	212
B.8.2	Euler Algorithm . . . . .	214
B.8.3	Modified Euler Method or Simple Predictor-Corrector Method . . . . .	214
B.8.4	Runge-Kutta Method . . . . .	215
B.8.5	Runge-Kutta-Merson Method . . . . .	215
B.8.6	Runge-Kutta-Fehlberg . . . . .	216

<b>C Aircraft Ditching Load Prediction Tools Provided by Stirling Dynamics Ltd.</b>	<b>219</b>
C.1 SDL Ditching Loads Calculation Methodology . . . . .	219
C.1.1 Added Mass Loads . . . . .	220
C.1.2 Steady Hydrodynamic Loads (Doublet Lattice Method) . . . . .	221
C.1.3 Hydrostatic Loads . . . . .	222
C.1.4 SD-GLOSS Simulation Tool . . . . .	222
C.2 CFD Model . . . . .	224
C.2.1 Aircraft Fuselage Geometry . . . . .	224
C.2.2 CFD Physical Model . . . . .	224
C.2.3 Computational Mesh . . . . .	225
<b>D Ditching Experimental Equipment and Instrumentation</b>	<b>227</b>
Main Rig: Component A: . . . . .	227
Sliding Post: Component B: . . . . .	228
Loadcell Case: Component C: . . . . .	228
Trim Fitting: Component D: . . . . .	228
D.0.1 Sensors and Instruments . . . . .	228
NOVATECH F332 2 Axis Loadcell: . . . . .	228
PCB PIEZOTRONICS 353B31 Single Axis Accelerometer: . . . . .	228
Linear String Potentiometer PT5A: . . . . .	228
National Instruments CompactDAQ Controllers cDAQ-913x: . . . . .	229
<b>Bibliography</b>	<b>235</b>



# List of Figures

1.1	Comparison of different ship motions evaluations. . . . .	4
1.2	Implementation of relevant works and novel contributions. . . . .	8
1.3	Novel contributions to Zarnick (1978). . . . .	9
2.1	Korvin-Kroukovski definition. . . . .	19
2.2	Wedge penetrating into water and equivalent flat plate. . . . .	22
2.3	Power boat model jumping in oblique waves at 9 m/s (Azcueta et al., 2003). . . . .	30
2.4	Numerical mesh around hull (Azcueta et al., 2003). . . . .	31
2.5	Pressure hull for $C_\Delta = 0.608$ $L/B = 4$ and $\beta = 20^\circ$ speed ratio = 2, 3, 4, 5, 6 (from left to right) (Fu et al., 2013). . . . .	32
2.6	Three-quarter bottom view of the model of fineness ratio 6 in basic configuration (McBride and Fisher, 1953). . . . .	33
2.7	Guided ditching experimental test facility at INSEAN (Siemann et al., 2012). . . . .	34
2.8	CFD (VOF) model used to simulate airframe loads for steady conditions (Bonanni et al., 2015). . . . .	35
3.1	Coordinate systems. . . . .	39
3.2	Free body diagram of forces, velocities and accelerations. . . . .	40
3.3	Dynamic process in the present mathematical model. . . . .	46
3.4	Pressure distribution along the ship length. . . . .	47
3.5	Flow - hull characteristic zones (longitudinal). . . . .	47
3.6	Flow-hull characteristic (transverse). . . . .	48
3.7	Time histories of accelerations and motions using different solvers with $\Delta t = 0.01$ s. . . . .	53
3.8	Time histories of accelerations and motions using PCA solvers with different $\Delta t$ . . . . .	53
3.9	Error metrics representation of normalized heave motion comparing different integration methods. . . . .	54
3.10	Statistical representation of normalized heave motion comparing different integration methods. . . . .	54
3.11	Variation of sectional added mass and its associated terms with different $N_s$ along the ship length. . . . .	56
3.12	Error metrics of time histories and Pareto front line of heave motion of planing hull model $\beta = 20^\circ$ , $\lambda/L = 4.0$ , $H/B = 0.1$ . . . . .	57
3.13	Comparison of $RMSE_{z_G}$ of different $\beta$ and $H/B$ at $\lambda/L = 4.0$ with $N_s = 200$ . . . . .	57



3.14	Error metrics of time histories and Pareto front line of heave motion of planing hull model with variable $\beta$ .	62
3.15	Comparison of $RMSE_{z_G}$ of variable $\beta$ hull at $\lambda/L = 4.0$ .	62
3.16	Error metrics of time histories and Pareto front line of heave motion of planing hull model $\beta = 20^\circ$ , $\lambda/L = 4.0$ and $H/B = 0.1$ with 10 times scaled-up.	63
3.17	Comparison of $RMSE_{z_G}$ of $\beta = 20^\circ$ planing hull at $\lambda/L = 4.0$ varying $H/B$ and scales.	64
3.18	Comparison of CG's accelerations at $\lambda/L = 4.0$ with different $\beta$ and scales.	64
3.19	Comparison of running attitude in calm water showing sinkage, trim and resistance.	66
3.20	Response motions and accelerations of planing hull model $\beta = 20^\circ$ , $V/\sqrt{L} = 4.0$ , $H/B = 0.1$ .	68
3.21	Response motions and accelerations of planing hull model $\beta = 20^\circ$ , $V/\sqrt{L} = 6.0$ , $H/B = 0.1$ .	69
3.22	Response motions and accelerations of planing hull model $\beta = 10^\circ$ , $V/\sqrt{L} = 6.0$ , $H/B = 0.1$ .	70
3.23	Response motions and accelerations of planing hull model $\beta = 30^\circ$ , $V/\sqrt{L} = 6.0$ , $H/B = 0.1$ .	71
4.1	Error metric of time histories and Pareto front line of heave motion of planing hull model $\beta = 20^\circ$ , $V/\sqrt{L} = 6.0$ , $H_{1/3}/B = 0.2$ .	81
4.2	Comparison of $RMSE_{z_G}$ of different $\beta$ and $H_{1/3}/B$ at $\lambda/L = 4.0$ .	82
4.3	Statistic of response motions of different $\beta$ hulls with $H_{1/3}/B = 0.4$ , $V/\sqrt{L} = 6.0$ .	86
4.4	Statistic of response motions of $\beta = 20^\circ$ hulls varying $H_{1/3}/B$ .	87
5.1	Transversal plane coordinate systems.	92
5.2	Oblique wave definition.	94
5.3	Asymmetric geometrical equivalent I.	97
5.4	Asymmetric geometrical equivalent II.	97
5.5	Asymmetric geometrical of buoyancy.	101
5.6	Sample of time histories of response motions in $\lambda/L = 2.0$ .	105
5.7	Comparison of response motions of fixed heel simulations.	106
5.8	Comparison of response heave motions.	109
5.9	Comparison of response pitch motions.	110
5.10	Comparison of response roll motions.	111
5.11	Comparison of bow accelerations.	112
6.1	Hypothesis of transformation of semi-circular shape.	118
6.2	Comparison of variation sectional added mass coefficients between wedge shape and semi - circular shape in term of deadrise angle.	119
6.3	Comparison of sectional added mass evaluated by Lewis and Payne's methodologies.	119
6.4	Geometry definition of 2D semi-circular shape.	120
6.5	Geometry definition of 2D semi-circular shape after flow separation.	120
6.6	Equivalent deadrise angle in term of submergence to half beam ratio.	121

6.7	Normalized sectional forces of different geometries in term of submergence to half beam ratio. . . . .	124
6.8	Comparison of sectional added mass coefficient of different methodologies in term of submergence to half beam ratio. . . . .	126
6.9	Time histories of sectional force of 2D cylinder drop tests. . . . .	132
6.10	9 sectional forces of constant horizontal speed $\dot{x}_G = 10 \text{ m/s}$ . . . . .	133
6.11	9 sectional forces of constant horizontal speed $\dot{x}_G = 50 \text{ m/s}$ . . . . .	134
6.12	9 sectional forces of constant drop test of vertical speed $\dot{z}_G = 2 \text{ m/s}$ . . . . .	135
6.13	9 sectional forces of constant drop test of vertical speed $\dot{z}_G = 4 \text{ m/s}$ . . . . .	136
6.14	9 sectional forces of accelerated drop test with vertical acceleration $\ddot{z}_G = 2 \text{ m/s}^2$ . . . . .	137
6.15	9 sectional forces of accelerated drop test with vertical acceleration $\ddot{z}_G = 4 \text{ m/s}^2$ . . . . .	138
6.16	9 sectional forces of constant horizontal speed with vertical acceleration $\ddot{z}_G = 2 \text{ m/s}^2$ . . . . .	139
6.17	9 sectional forces of constant horizontal speed with vertical acceleration $\ddot{z}_G = 2 \text{ m/s}^2$ varying flow separation locations. . . . .	139
6.18	Simplified assumption of different locations of flow separation. . . . .	140
7.1	Impact force in term of model length. . . . .	144
7.2	Impact force in term of landing speed. . . . .	145
7.3	Impact force in term of low landing speed in different masses. . . . .	145
7.4	Impact force in term of model's mass. . . . .	146
7.5	Impact force in term of low landing speed extrapolating to $10 \text{ m/s}$ . . . . .	146
7.6	Full launching equipment. . . . .	147
7.7	Schematic of instruments installation. . . . .	148
7.8	Samples of time series of repeating free falling runs. . . . .	150
7.9	Sample of a displacement data with envelope curve zooming into the interval of impact. . . . .	154
7.10	Definition of first impact location. . . . .	154
7.11	Sample of smooth displacement and velocity and acceleration derivation. . . . .	155
7.12	Sample of FFT analysis and smooth acceleration signals. . . . .	157
7.13	Sample of FFT analysis and smooth impact force signals. . . . .	159
7.14	Free body diagram of the experimental rig system. . . . .	160
7.15	Sample of time histories of ditching event with variation of landing speed. . . . .	161
7.16	Sample of time histories of impact force resulting from simulations with ideal gravitational acceleration. . . . .	162
7.17	Variation of impact forces in term of landing speed from simulations with ideal gravitational acceleration. . . . .	162
7.18	Sample of experiment's simulations. . . . .	163
7.19	Sample of time histories resulting from both methodologies of a fixed trim varying landing speed . . . . .	164
7.20	Impact forces in term of landing speed of experiments vs simulations. . . . .	164
A.1	Asymmetric Geometrical Equivalent I . . . . .	189
A.2	Asymmetric Geometrical Equivalent II . . . . .	189
A.3	Asymmetric Geometrical of Buoyancy . . . . .	192

B.1	Wave elevation and its time derivative. . . . .	200
B.2	Wave orbital vertical velocity and its time derivative. . . . .	201
B.3	Partial derivative of wave vertical orbital velocity along the ship length. . . . .	203
B.4	Section submergence and its time derivative. . . . .	203
B.5	Flow-hull characteristic zones (longitudinal). . . . .	204
B.6	Flow-hull characteristic zones (transverse). . . . .	205
B.7	Sectional added mass and its time Derivative. . . . .	207
B.8	Partial derivative of sectional added mass along the ship length. . . . .	209
B.9	Sectional cross-flow drag. . . . .	210
B.10	Sectional buoyancy . . . . .	211
C.1	Added mass term evaluated by formulation of Korobkin (2004). . . . .	220
C.2	Hydrodynamic loads are calculated from the pressure distribution of the Doublet Lattice Method (Bonanni et al., 2015). . . . .	222
C.3	SD - GLOSS methodology summary. . . . .	223
C.4	A fuselage shape has been used for validation of the loads calculation methodologies. . . . .	225
C.5	Example of the Unstructured Cartesian CFD mesh employed for loads cal- culation. . . . .	226
D.1	Full launching equipment. . . . .	227
D.2	Main rig. . . . .	229
D.3	Sliding post. . . . .	230
D.4	Loadcell case. . . . .	230
D.5	Pitch fitting. . . . .	231
D.6	NOVATECH F332 2 Axis Loadcell. . . . .	231
D.7	Accelerometer. . . . .	232
D.8	Linear String Potentiometer PT5A. . . . .	232
D.9	National Instruments CompactDAQ Controllers cDAQ-913x. . . . .	233
D.10	Overview of the rig installed on the carriage (1). . . . .	233
D.11	Overview of the rig installed on the carriage (2). . . . .	234
D.12	Overview of the rig installed on the carriage (3). . . . .	234

# List of Tables

2.1	Fridsma's model configurations. . . . .	13
2.2	Range of applicability of Savitsky and Brown (1976)'s Formulae. . . . .	15
2.3	Range of applicability of Brown and Klosinski's formulae. . . . .	18
3.1	Convergence criteria of variable steps solver. . . . .	51
3.2	Computational times of Runge-Kutta integration methods varying $N_s$ and $\Delta t$ . . . . .	53
3.3	RMSE VS $T_{c_s}$ of planing hull model $\beta = 20^\circ$ , $\lambda/L = 4.0$ , $H/B = 0.1$ . . . .	60
3.4	RMSE VS $T_{c_s}$ of planing hull model $\beta = 20^\circ$ , $\lambda/L = 4.0$ , $H/B = 0.3$ . . . .	60
3.5	RMSE VS $T_{c_s}$ of planing hull model $\beta = 30^\circ$ , $\lambda/L = 4.0$ , $H/B = 0.1$ . . . .	60
3.6	RMSE VS $T_{c_s}$ of planing hull model $\beta = 30^\circ$ , $\lambda/L = 4.0$ , $H/B = 0.3$ . . . .	60
3.7	RMSE VS $T_{c_s}$ of planing hull model $\beta = 10^\circ$ , $\lambda/L = 4.0$ , $H/B = 0.1$ . . . .	60
3.8	RMSE VS $T_{c_s}$ of planing hull model $\beta = 10^\circ$ , $\lambda/L = 4.0$ , $H/B = 0.3$ . . . .	60
3.9	Model configuration of variable $\beta$ hull (Rosén and Garne, 2006). . . . .	61
3.10	Model Configurations for Regular Seas Validation. . . . .	65
4.1	Wave representing discrete spectrum. . . . .	78
4.2	Planing hull model configurations for irregular waves simulations. . . . .	78
4.3	RMSE VS $T_{c_s}$ of planing hull model $\beta = 20^\circ$ , $H_{1/3}/B = 0.2$ , $V/\sqrt{L} = 4.0$ . . .	83
4.4	RMSE VS $T_{c_s}$ of planing hull model $\beta = 20^\circ$ , $H_{1/3}/B = 0.6$ , $V/\sqrt{L} = 4.0$ . . .	83
4.5	RMSE VS $T_{c_s}$ of planing hull model $\beta = 20^\circ$ , $H_{1/3}/B = 0.2$ , $V/\sqrt{L} = 6.0$ . . .	83
4.6	RMSE VS $T_{c_s}$ of planing hull model $\beta = 20^\circ$ , $H_{1/3}/B = 0.6$ , $V/\sqrt{L} = 6.0$ . . .	83
4.7	RMSE VS $T_{c_s}$ of planing hull model $\beta = 30^\circ$ , $H_{1/3}/B = 0.2$ , $V/\sqrt{L} = 6.0$ . . .	83
4.8	RMSE VS $T_{c_s}$ of planing hull model $\beta = 30^\circ$ , $H_{1/3}/B = 0.6$ , $V/\sqrt{L} = 6.0$ . . .	84
4.9	RMSE VS $T_{c_s}$ of planing hull model $\beta = 10^\circ$ , $H_{1/3}/B = 0.2$ , $V/\sqrt{L} = 6.0$ . . .	84
4.10	RMSE VS $T_{c_s}$ of planing hull model $\beta = 10^\circ$ , $H_{1/3}/B = 0.6$ , $V/\sqrt{L} = 6.0$ . . .	84
4.11	Statistic Comparison of Irregular Waves Simulations. . . . .	85
5.1	Model configuration used by Rosén and Garne (2006). . . . .	107
6.1	Steady cases. . . . .	128
6.2	Constant speed drop test cases. . . . .	128
6.3	Accelerated drop test cases. . . . .	128
6.4	Accelerated drop test + forward speed cases. . . . .	129
7.1	Froude scaling of controlling parameters of free falling technique (1). . . .	143
7.2	Froude scaling of controlling parameters of free falling technique (2). . . .	143
7.3	Standard deviations and mean absolute errors of the instruments. . . . .	151

7.4	Experimental test run log. . . . .	152
7.5	Time shift between instant of initial impact and maximum impact. . . .	156
7.6	Maximum impact accelerations and time shift between reading and deriva- tive data. . . . .	158
7.7	Data comparison of simulations vs experiments. . . . .	165
B.1	Comparison of integration methods along the ship length. . . . .	213

## Declaration of Authorship

I, **Prin KANYOO** , declare that the thesis entitled *Mathematical Model of High Speed Planing Dynamics and Application to Aircraft Ditching* and the work presented in the thesis are both my own, and have been generated by me as the result of my own original research. I confirm that:

- this work was done wholly or mainly while in candidature for a research degree at this University;
- where any part of this thesis has previously been submitted for a degree or any other qualification at this University or any other institution, this has been clearly stated;
- where I have consulted the published work of others, this is always clearly attributed;
- where I have quoted from the work of others, the source is always given. With the exception of such quotations, this thesis is entirely my own work;
- I have acknowledged all main sources of help;
- where the thesis is based on work done by myself jointly with others, I have made clear exactly what was done by others and what I have contributed myself;
- parts of this work have been published as: ([Bonanni et al., 2015](#)), ([Kanyoo et al., 2015](#)) and ([Vandewaeter et al., 2015](#))

Signed:.....

Date:.....



## Acknowledgements

First of all, the actual career and activities could not be done without the great reliability and opportunity from Professor Wilson. Without him, I hadn't had the chance to pursue my dream completing the PhD career.

Then, the following enormous gratitudes I have to give is to Dominic and James. Thanks to their supports, advices, guides and the patience they gave me during the whole career. Without them both, I wouldn't be able to find the way I should follow and wouldn't be able improve the skill I should have, to be a good researcher.

Also to my friends who have been also supporting me, Sarawuth, Phaisan , Ponprot, Trewut, Supakarn and Kantapon for their support in the Towing Tank, and Orasa for her Grammary Account.

Thanks to Stirling Dynamics Ltd. for the sponsorship and the ideas to form a part of the project.

Thanks to Mom and Dad who have been always implanting me into the good paths, since I was born until I am what currently I am.

Finally, the whole thing in this career and my whole life could not be completed without the supports, encourages and above all, love from my wife, Ears. Thanks for your endless supply of encourage, patience, smiles and love.





# Nomenclature

$a_{bf}$ :	Buoyancy correction coefficient $[-]$
$B$ :	Beam $[m]$
$b$ :	Half beam $[m]$
$\ddot{b}$ :	Bow acceleration $[m/s^2]$
$C_{D,C}$ :	Cross-flow drag coefficient $[-]$
$C_{pu}$ :	Pile-up correction factor $[-]$
$C_{tr}$ :	Near transom correction factor $[-]$
$C_m$ :	Sectional added mass coefficient $[-]$
$D$ :	Drag force $[N]$
$F_b$ :	Total buoyancy $[N]$
$F_{cfd}$ :	Total cross-flow drag $[N]$
$F_h$ :	Total hydrodynamic force $[N]$
$F_{nB}$ :	Breadth Froude number $[-]$
$f_b$ :	Sectional buoyancy $[N/m]$
$f_{cfd}$ :	Sectional cross flow drag $[N/m]$
$f_h$ :	Sectional hydrodynamic force $[N/m]$
$H$ :	Wave height $[m]$
$H_{1/3}$ :	Significant wave height $[m]$
$h$ :	Section submergence $[m]$
$I_{xx}$ :	Roll moment of inertia matrix $[kg \cdot m^2]$
$I_{yy}$ :	Pitch moment of inertia matrix $[kg \cdot m^2]$
$LCG$ :	Longitudinal centre of gravity from aft $[m]$
$M$ :	Mass matrix $[kg]$
$M_b$ :	Buoyancy moment $[N \cdot m]$
$M_{cfd}$ :	Cross-flow drag moment $[N \cdot m]$
$M_h$ :	Hydrodynamic moment $[N \cdot m]$
$m_a$ :	Sectional added mass $[kg/m]$
$N_s$ :	Number of strip sections $[-]$
$R$ :	Radius of aircraft fuselage $[m]$
$RMSE$ :	Root mean square error $[-]$
$r$ :	Wave elevation $[m]$
$T_c$ :	Computational time $[s]$

---

$T_{c_{min}}$ :	Minimum computational time [s]
$T_{c_s}$ :	Computational time ratio $T_c/T_{c_{min}}$ [—]
$U$ :	Velocity parallel to keel [m/s] / Horizontal landing speed (Chapter 7)
$V$ :	Velocity perpendicular to keel [m/s] / Vertical landing speed (Chapter 7)
$VCG$ :	Vertical centre of gravity from keel [m]
$W$ :	Ship's weight [ $N \cdot m/s^2$ ]
$w_w$ :	Wave vertical orbital velocity [m/s]
$x_D$ :	Drag force lever arm [m]
$x_G$ :	Displacement of CG in $x$ direction (surge) [m]
$\dot{x}_G$ :	Velocity of CG in $x$ direction [m/s]
$\ddot{x}_G$ :	Acceleration CG in $x$ direction [m/s <sup>2</sup> ]
$x'$ :	Ship coordinate in longitudinal direction [m]
$y_G$ :	Displacement of CG in $y$ direction (sway) [m]
$\dot{y}_G$ :	Velocity of CG in $y$ direction [m/s]
$\ddot{y}_G$ :	Acceleration CG in $y$ direction [m/s <sup>2</sup> ]
$y'$ :	Ship coordinate in transverse direction [m]
$z_G$ :	Displacement of CG in $z$ direction (heave) [m]
$\dot{z}_G$ :	Velocity of CG in $z$ direction [m/s]
$\ddot{z}_G$ :	Acceleration CG in $z$ direction [m/s <sup>2</sup> ]
$\beta$ :	Deadrise angle [°] / [rad]
$\Delta t$ :	Time step size [s]
$\lambda$ :	Wavelength [m]
$\phi$ :	Rotation about $x$ direction (roll) [rad]
$\dot{\phi}_G$ :	Rotation velocity about $x$ direction [rad/s]
$\ddot{\phi}_G$ :	Rotation acceleration about $x$ direction [rad/s <sup>2</sup> ]
$\theta$ :	Rotation about $y$ direction (pitch) [rad]
$\dot{\theta}_G$ :	Rotation velocity about $y$ direction [rad/s]
$\ddot{\theta}_G$ :	Rotation acceleration about $y$ direction [rad/s <sup>2</sup> ]
$\psi$ :	Rotation about $z$ direction (yaw) [rad]
$\dot{\psi}_G$ :	Rotation velocity about $z$ direction [rad/s]
$\ddot{\psi}_G$ :	Rotation acceleration about $z$ direction [rad/s <sup>2</sup> ]

# Chapter 1

## Introduction

Since the Industrial Revolution, certain means of transportation have been developed over the time. The oldest of these are those associated with marine transport, which has been serving over the historical time. That could be because of its abundant source of applicable energy, for instance, wind energy that of course, appears to be complicated to apply in land and air transportation. Then, when modern and high potential source of energy such as fossil fuel had been discovered, land and air transportations have gained their significant influence in the contemporary world. This because they are capable of fulfilling the notable disadvantage of sea transportation, which is time duration. Until recently, land and air transport have been developing dramatically their speed, while the majority of sea transport remains with the identical speed as it did a century ago.

The primary cause of this occurrence is that the land and air vehicles are moving in a single phase fluid domain. Moreover, air can be considered as inviscid fluid, although the required energy to move the vehicles is nonlinearly and directly proportional to speed, but it is in a very low order that sometimes, it could be considered as quasi-linear. The difference from the others, marine vehicle is moving in two phase fluid domains involving with a free surface and its boundary issue. Here, the main problem is caused by apart from the interface of both domains, the viscous characteristics together with the density of water do not allow the vehicle to develop the speed that easily. In this case, the required energy is again nonlinearly and directly proportional to the speed but in extremely high order. In other words, it is out of interest for industries to develop a vehicle to run a very high speed against the cost of applied energy. Nevertheless, although the time in transportation can be saved by using land or air transportation, sea transportation keeps occupying the majority part of the world transportation due to its lower cost compared with the others.

However, the problems of high-speed phenomenon in marine vehicles can be avoided by making them moving in only one domain. This means the intersection plane surface area between both domains should be eliminated or at least reduced as much as possible.

There have been two different ways to achieve this idea. The first one is moving the vehicles underwater. That is quite complicated comparing to the second way that is moving them out of the water or reducing the wetted surface area. As moving the vehicles under the water needs to account for a notable increment of fluid friction due to the increase in wetted surface area. Lifting the vehicle out of the water appears to be the most appropriate choice. The earliest solutions of this choice have been presented in the following ways:

- **Air cushion vehicle or hovercraft:** It uses blowers to produce a large volume of air below the hull that is slightly above atmospheric pressure. The pressure difference between the higher pressure air below the hull and lower pressure ambient air above it produces lift, which causes the hull to float above the running surface. Significant advantage of this craft is that it can travel easily over any reasonably smooth surface. Disadvantages are that its mechanism is noisy and consume a lot of fuel, implying inefficient carried weight to power ratio. Moreover, when considering manoeuvrability issue, it could slide sideways as easily as it slides forward, which is not effective for precision manoeuvring.
- **Hydrofoil:** This craft is supported by underwater foils, not unlike the wings of an aircraft. At high speeds these underwater surfaces develop lift and raise the hull out of the water. It experiences much lower vertical accelerations in moderate sea states making them more comfortable to ride. Moreover, comparing to the others, it has the highest forward speed in practice. Nevertheless, it becomes uncomfortable or even dangerous in heavy sea states due to the foils breaking clear of the water and the hull impacting the waves. On the other hand, the need for the hydrofoils to produce enough upward force to lift the ship out of the water places practical constraints on the vessel's size.
- **Planing craft:** This craft can act in different modes due to its forward speed. At repose or low speed, it is in displacement mode being supported by the buoyancy. While at high speed, due to the disturbed and altered direction of flow around the hull, hydrodynamic lift takes place and takes over the hull support role. This can be considered as the definition of planing mode following its characteristic of skimming itself over the water. Although it presents some disadvantages over the others such as lower maximum speed and manoeuvrability, simpler lifting mechanism lower building cost still attract the attention in many fields of applications.

Applications of hovercraft and hydrofoil are limited in specialised fields, while the planing craft shows a wider possibility of application.

## 1.1 Background

High-Speed Planing Craft plays a very important role nowadays in many fields of application, due to their high performance and flexible manoeuvrability and operability. The typical applications of this kind of vessel can be found in; rescue vessels, pilot boats, crew boats, leisure boats and some small coastal naval vessels. The main difference from conventional vessels is that the predominant force supporting the hull is hydrodynamic lift force rather than hydrostatic or buoyancy force.

The pressure acting on the hull of a planing craft travelling at high forward speed in calm water is characterized by a small hydrostatic force and large hydrodynamic force respectively. There is a relative velocity between the hull and water as a consequence of its trim angle and high forward speed that generates hydrodynamic pressure proportional to the square of this speed. Moreover, at a very high forward speed, most of the hull is supported by the hydrodynamic pressure. In waves, the relative velocity gets an additional contribution from the relative motions between the hull and waves. Consequently, the resulting motions and accelerations in most wave conditions result in high impact loads. Generally, a planing craft is proved to be very effective in calm water, due to its outstanding high speed and small resistance. However, when it is navigating in extreme sea conditions, violent motions and large vertical accelerations take place and the hull is subjected to high impact loads. These occurrences can cause some structural failures leading to catastrophic situations during the navigation. On the other hand, as its main application involves fundamentally with Special Operations and human transportation, it is stated in [Ensign et al. \(2000\)](#)'s report that such extreme behaviours in waves could also lead to discomfort, injury and performance degradation of the crew, that affects directly to the operability of these vessels.

Therefore, it is necessary to get an appropriate understanding of planing craft behaviours in waves, in order to be capable of developing novel designs with the expected operability and performance in rough seas. Moreover, this understanding will also be useful for the operators to help with decision making.

Historically, several researchers carried out investigations related to planing craft. Originally, [von Karman \(1929\)](#) and [Wagner \(1931\)](#) developed a mathematical tool based on potential flow theory to predict water-structure landing load of a seaplane. Their investigation deduced that the impact load can be presented by the form of rate of change of fluid momentum and that the predominant parameter on the impact load is the fluid added mass. The simple wedge water entry geometry can be replaced by an expanding flat plate at the same rate of change of geometrical width. [Martin \(1976b\)](#) and [Zarnick \(1978\)](#) used this principal to develop a mathematical model approaching the load, acceleration and motion prediction of high-speed planing craft due to their behaviour similarity. The planing hull geometry used in simulations carried out by Martin and Zarnick are based upon [Fridsma \(1969\)](#)'s series of experiments. Later, [Keuning \(1994\)](#),

## METHODS OF CALCULATING SHIP MOTIONS

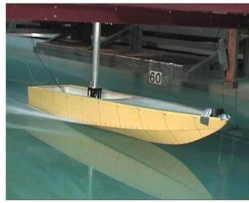
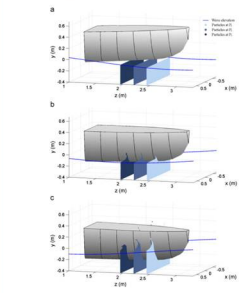
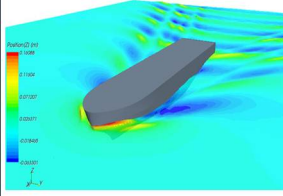
Model Experiment	2D Strip Theory	3D CFD
<ul style="list-style-type: none"> <li>Most classical and essential.</li> </ul>  <p>Source: D.J. Taunton, Characteristic of a series of high speed hard chine planing hulls – Part I</p>	<ul style="list-style-type: none"> <li>Most suitable for high Froude Number ships.</li> </ul>  <p>Source: D. Veen and Tim Courlay, A Combined Strip Theory and Smoothed Particle Hydrodynamics Approach for Estimating Slamming Loads on a Ship in Head Sea.</p>	<ul style="list-style-type: none"> <li>Most realistic results but requires advanced tools.</li> </ul>  <p>Source: www.stxmarine.net</p>

Figure 1.1: Comparison of different ship motions evaluations.

Akers (1999), Garne (2004b) and Deyzen (2008) implemented the model adding correction factors and additional components to make the model more efficient. Nevertheless, none of those works explain in detail about the verification of the model approaching the selection of numerical methodologies, including the appropriate use of the methodology in term of controlling parameters.

## 1.2 Aims and Objectives

Traditionally, there are three different methods widely used in evaluation of planing craft motions; experimental tests including both model and full scales, 2D strip method and less common but on the increase is 3D CFD simulations. The comparison of advantages and disadvantages of the three methodologies for evaluating load and motions are shown in Figure 1.1. Model experiments appear to be capable of giving the most realistic physical phenomenon, but due to the high cost of resource and time in setting up, it is preferable to avoid except when essential. 3D CFD is also computationally very expensive. The 2D strip theory although it appears to be the least accurate comparing to the other two, but when considering time consumption in calculation, it is the most useful for performing preliminary design simulations.

The principle aim of this present research is to develop and optimize a tool capable evaluating planing craft behaviours, which include loads, motions and accelerations, in calm water, regular and irregular waves. It aims to develop a numerical tool capable of simulating the coupled heave and pitch motions, which are the most significant motions for a planing craft. As well as the possibility to extend to more degrees of freedom, such

as roll motions which is also another significant motion and influence operability. Above all, it is of interest to find the most efficient methodology to use with conventional tools such as personal computer. To fulfil the aim of the research, the modified 2D strip method appears to be the most preferable for the early stage of design, due to its simplicity and low computational overhead.

A mathematical model capable of predicting loads, motions and accelerations of a high-speed planing craft has been developed and implemented following the pioneering work of Zarnick (1978, 1979). This mathematical model was capable of predicting dynamic behaviours of planing craft in head seas. It was limited to the simulations in only coupled heave and pitch motions, however, these are the fundamental motions of a planing craft. Some notable contributions to Zarnick's original works were followed, extended and implemented by Keuning (1994) and Akers (1999). The results of response motions and accelerations were validated against the series of experimental test carried out by Fridsma (1969, 1971) and showed a good overall agreement. Nevertheless, the detailed verification and validation process of the resulting time histories and their convergence behaviours has not been published, including the influence of relevant controlling parameters on convergence when using these existing mathematical models.

Therefore, "Hypothesis of Accuracy of Time Histories" is introduced in order to verify the accuracy and convergence of the resulting time histories evaluated by the present mathematical model. Basically, the hypothesis consists of analysis of the fact that, in a dynamical process, the accuracy of simulated time history (closest to the reality) of an object is dependent of the accuracy of evaluation process in the corresponding equation of motions. The most fundamental source of error in the process is related to the force acting on the object. Then, the direct effect of the force is acceleration and the corresponding velocity and displacement. Following the principle of 2D strip method, the vessel's hull is divided into a number of 2D transverse strips. At each instant (time step), the force acting on each individual section is evaluated and by integrating along the hull length, total force and moment and accelerations are obtained. Then, by letting the time flows and integrating the acceleration over time, velocity and displacement are obtained for each time step. Consequently, the relevant controlling parameters of the convergence of time histories of motions and accelerations are the number of sections defining the hull geometry,  $N_s$  and the time step size,  $\Delta t$ .

The consideration for optimal simulation is that the accuracy of time histories (convergence behaviour) should be presented whilst minimizing computational time and effort. Analysis of the optimal pair of those parameters is carried out and leads back to the selection of the optimal parameters. Moreover, apart from the analysis approaching the original Fridsma (1969, 1971)'s constant deadrise planing hull models, an investigation of the effect of those controlling parameters on simulations of variable deadrise hull and scaled up model is also carried out. Then, the simulations in calm water regular and



irregular head seas are performed and validated against the data of [Fridsma \(1969\)](#) and [Zarnick \(1978\)](#).

### 1.3 Application to Transverse Motions

As a part of the research, transverse plane motion prediction capability is also developed, verified and validated as the first extension to simulating more degrees of freedom. Due to its complication in flow characteristic, modification corresponding to this extension is mainly simplified based on the works of [Sebastiani et al. \(2008\)](#) and [Ruscelli \(2009\)](#). The planing hull is supposed to fulfil also the assumption of slenderness, unlike the longitudinal strips, in transverse point of view, it will be split in only port and starboard side equivalent to the full symmetrical wedges. This simplification provides a possibility of simulating several asymmetrical motions in transverse plane such as, fixed heel navigation due to transverse instability and roll motion in lateral or oblique waves, etc. The resulting data from this implementation is also validated against some existing experimental data ([Rosén and Garne, 2006](#)).

### 1.4 Application to Aircraft Ditching

By considering the definition of planing event mentioned previously, seaplane landing, planing boat travelling and aircraft ditching behave identically as they are skimming over the water rather moving underneath. Due to their similar behaviour, a possible application of the present mathematical model is to simulate and analyse the aircraft ditching. As the survivability of an aircraft when landing on the water in an emergency situation is a regulatory requirement and consideration for the aircraft manufacturers. Another aim and objective of the present research is to find a robust reliable technique to predict the loads on the fuselage of an air plane when ditching into the water.

Therefore, the present mathematical model is modified to fulfil this approach. In literature, there is a similar “Seaplane Landing Simulation” presented by [Wagner \(1931\)](#) which also forms a core principle in the work related to planing craft dynamics. His research led to a number of applications and implementations by many researchers when referring to the simulations of loads and motions of high-speed planing craft, as due to his principle, the impact load on the cross section of the craft can be evaluated by applying potential theory based boundary value problems. This led to the evaluation of the expression of sectional force on the geometry that later appears in the form of rate of change of fluid momentum.

The principal implementation to the original mathematical model of high-speed planing is the development of the sectional added mass expression for semi-circular shape. Verification and cross-validation of the model are carried out using data provided by Stirling Dynamics Ltd. (Bonanni et al., 2015; Vandewaeter et al., 2015). Once the mathematical model is developed, verified and preliminarily cross-validated, a series of experimental tests is carried out using the available facility (Southampton Solent University's Towing Tank). The results from the tests are finally used as the confirmation of validity of the tool of simulation validity.

## 1.5 Novel Contributions

Regarding the aims and objectives mentioned in Section 1.2, the novel contributions presented in this thesis are firstly, the detailed verification of the mathematical model. The accuracy of the resulting motions and acceleration time histories is analysed and discussed in terms of the relevant controlling parameters of number of sections,  $N_s$  and time step size,  $\Delta t$ , including the optimal usage in order to minimize computation time and effort. As it can be seen in previous research, although limitations of their models were mentioned in term of different parameters, there was no detailed recommendation available for the optimal application. Furthermore, the data represented in previous research was already treated in form of response amplitude operator or probability of exceedance, the accuracy and fitting of time histories comparing to the physical reality could not be guaranteed. This is important when considering that significantly different time histories can give similar statistics.

Secondly, the extension of application to asymmetric forms and roll motion is evaluated. There were available in literature the investigations of mathematical model of planing roll motion, however, most of them applied linear conventional strip theory. Thus, the present research aims to evaluate a fully nonlinear mathematical model based on modified 2D strip theory using only heave coefficient (following the wedge water entry analogy) to predict also the roll motion. This model would transform the sectional roll motion into equivalent vertical motion and give a reasonable accuracy of results. The contributions approaching the verification, controlling parameter analysis and optimization of the mathematical model are presented in Figures 1.2 - 1.3.

Finally, in connection to the aircraft ditching load prediction, as the original sectional force evaluation planned to use in the research was applied to seaplane landing load prediction, the actual mathematical model is also modified and implemented to fulfil that capability using the simple expanding flat plate replacement approach to evaluate the added mass contribution. It allows the ditching load prediction to be easily evaluated with a conventional desktop PC, without the necessity of conducting full-scale destructive tests, as they were carried out previously during the war periods. The final

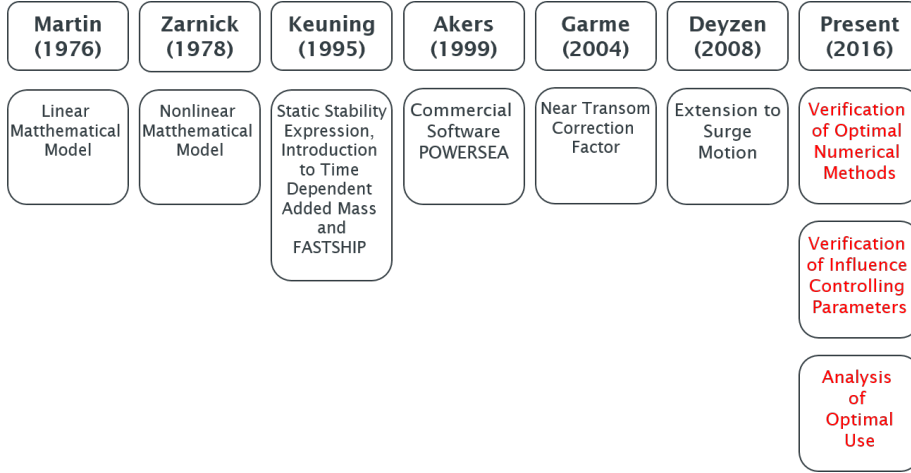


Figure 1.2: Implementation of relevant works and novel contributions.

approach of this application is useful for aircraft structural design and analysis, including some emergency landing simulations. Moreover, other possible applications when this load prediction tool is validated are, i.e., impact load prediction of torpedo launching from the air to the water, impact load of small UAV landing on the water, etc. As the limitation of geometrical applicability is overcome by using the simple technique of the original expanding flat plate.

Another point of view of a considerable novel contribution is the application of added mass contribution. The whole work proved that the simple geometry approach presented by [Wagner \(1931\)](#) can be applied to various geometries. The expanding flat plate replacement is not only valid for the original symmetrical wedge shape, but also for the assumption of asymmetrical transverse plane motions approach, including the semi-circular shape of aircraft.

## 1.6 Thesis Structure

The works done in the present research are development and optimization of a mathematical model capable of predicting planing craft loads, motions, and accelerations in waves, as well as the application to aircraft ditching. Chapter 2 gives a general overview of previous research about the performance of high-speed planing craft and aircraft ditching, Chapter 3 explains briefly the development and evaluation of the mathematical model commencing from the 2<sup>nd</sup> Law of Newton, and the simplification to two degrees of freedom (coupled heave and pitch) for the purpose of verification and optimization analysis. Also, simulations and validations in calm water and regular head waves are presented in this chapter. Chapter 4 follows the same work-flow of Chapter 3 but in irregular waves simulations. Chapter 5 gives a fundamental overview of the assumption to extend the present mathematical model to be capable of including the prediction of transverse plane motions with appropriate existing validation references.

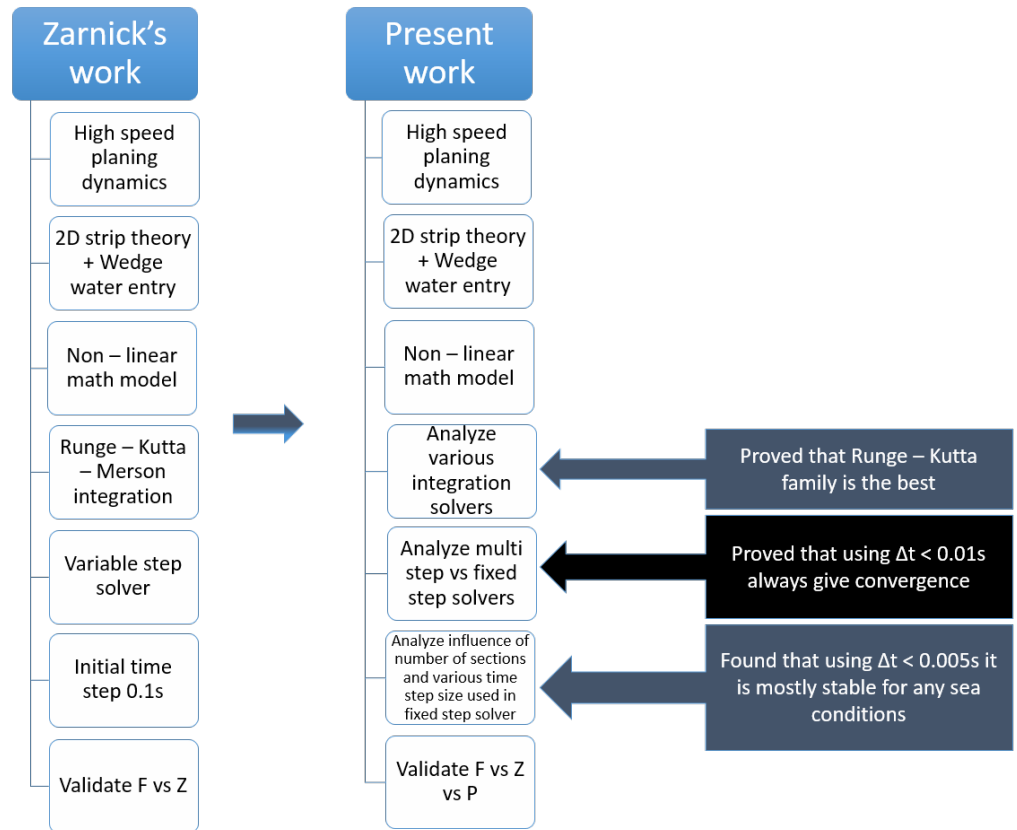


Figure 1.3: Novel contributions to [Zarnick \(1978\)](#).

Then, connecting with aircraft ditching, the modification of present mathematical model to be capable of applying in ditching load prediction, the series of experimental tests and the overall validation are presented in Chapter 6 and Chapter 7 respectively. Finally, in Chapter 8, the conclusion of the research is discussed and further works are suggested.



## Chapter 2

# Literature Review and Relevant Theories

The summary of relevant works is presented in this chapter, together with the theories associated with high-speed planing dynamics and aircraft ditching.

### 2.1 General

Previously, there has been a number of research related to the performance of high-speed planing craft. These can be classified into two groups; running attitude in calm water and seakeeping behaviour in waves. The aim of the present research is to develop, implement and verify a mathematical model capable of predicting high-speed planing motions in six degrees of freedom. However, the steady characteristic in calm water is still of importance as it is fundamental data for detailed investigation of this kind of vessels. Due to the complexity of the flow around a planing hull, the analytical investigation was complicated when deducing the efficiency, the earliest relevant investigations were based on a series of model tests. Similar to the investigation of other vessels, experimental methods have been considered the most reliable and widely used as the superior reference data for the preliminary design purpose. An inconvenience of model experiments is the high costs, thus, many researchers had commenced finding alternative techniques of investigations. By implementing the development of potential flow theory together with the high-performance computation, the flow characteristics of the planing craft have then been simulated.

The primary difference between planing craft and conventional vessels is that the predominant force supporting the conventional or displacement vessels is hydrostatic force or buoyancy. While in the case of planing craft, the buoyancy is replaced by hydrodynamic lift force due to the flow and pressure generated when the vessel is running

at a high forward speed. However, the hydrostatic force still has significant influence and cannot be totally neglected. Due to the high forward speed and trim angle, the flow around and under the planing hull changes its momentum, and causes a lift force according to the 2<sup>nd</sup> Law of Newton. In other words, there is a relative velocity between the hull and water that causes a hydrodynamic pressure which translates to the hydrodynamic lift force acting on the hull surface. Then, for the case of behaviour in waves, an additional contribution of ship motions is necessary to be accounted for in the water-hull relative velocity, resulting in nonlinear characteristics.

Generally, there are three principal methods of evaluating ship motions; model experiments, 2D Strip Method, and 3D CFD tool. The model experiments appear to give the most realistic answers but at the highest cost. The implementation of strip theory gave an excellent alternative technique for investigation of ship dynamics. Strip theory is widely used in the evaluation of seakeeping characteristics of conventional vessels based on the linearised boundary condition of the flow around the hull. In an identical way for high-speed planing craft, strip method has been modified to the form of 2.5D method accounting for the different flow phenomena. The most significant difference is the assumption of linear characteristics, ship motions of planing craft appear to be strongly nonlinear, and consequently, the same assumption of linearity is valid only under the limitation of small disturbance motions. Thus, the equations of motions had been modified but still on the basis of the 2<sup>nd</sup> Law of Newton. 2.5D method is a form of slender body theory providing a simplification of 3D ship geometry into a number of 2D cross sections. The pioneering work used as the primary basis for this project is that of [Zarnick \(1978\)](#). Nevertheless, due to a certain simplifications of 2.5D method, it lacks the capability of modelling the exact flow behaviour around the planing hull. 3D CFD based on Navier-Stokes equations has been developed over the last few decades. Providing the complexity of its fundamental principle, it is supposed to be the most complete tool compared with the other two methods but still presents an inconvenience in time consumption in calculation and the advanced computational requirement. The last method allows the more complex flow characteristics, such as jet flow, spray root, to be modelled with more accuracy.

## 2.2 Model Experiments and Empirical Formulations

Regarding the model experiments, [Fridsma \(1969, 1971\)](#) carried out an extensive series of model tests with a series of constant deadrise angle models varying other dimensions. The model configurations used during his experiments are shown in Table 2.1:

In his experiments, [Fridsma \(1969\)](#) systematically varied the deadrise angle: ( $\beta$ ) of the model, the length to beam ratio: ( $L/B$ ), the speed to length ratio: ( $V/\sqrt{L}$ ), the running trim: ( $\tau_0$ ), the load coefficient: ( $C_\Delta$ ) and the longitudinal position of the centre

Table 2.1: Fridsma's model configurations.

Model	$L$ (m)	$L/B$	$B$ (m)	$\beta$ (deg)	$C_\Delta$	$LCG$ (%L)	$k_{yy}$ (%L)	$V/\sqrt{L}$ (knot/ft <sup>2</sup> )	$V$ (m/s)
A	1.15	5	0.23	20	0.608	59.0	25.1	4	3.99
B	1.15	5	0.23	20	0.608	62.0	25.5	6	5.99
C	1.15	5	0.23	20	0.608	61.5	25.3	2	1.99
D	1.15	5	0.23	20	0.608	67.5	26.5	2	1.99
E	1.15	5	0.23	20	0.608	65.5	26.2	4	3.99
F	1.15	5	0.23	20	0.912	58.0	20.4	4	3.99
G	1.15	5	0.23	20	0.912	58.0	20.4	6	5.99
H	1.15	5	0.23	10	0.608	62.0	25.6	2	1.99
I	1.15	5	0.23	10	0.608	59.5	25.0	4	3.99
J	1.15	5	0.23	10	0.608	68.0	26.2	6	5.99
K	1.15	5	0.23	30	0.608	61.0	24.7	4	3.99
L	1.15	5	0.23	30	0.608	62.5	24.9	2	1.99
M	1.15	5	0.23	30	0.608	60.5	24.8	6	5.99
N	1.15	5	0.23	20	0.608	64.5	24.8	4	3.99
O	1.15	5	0.23	20	0.912	60.0	20.0	4	3.99
P	1.15	5	0.23	20	0.631	52.5	23.7	4	3.99

of gravity: (LCG) in the regular head wave tests. The resulting information of influences of those parameters were obtained and systematically analysed and finally presented in the form of “design charts” in order to be a useful tool for designers. Above all, he found in that planing craft possess a significant nonlinear behaviour when travelling in head waves. However, linearity is found to be in general, a function of speed and wavelength at low speed to length ratio. The results from Fridsma's experiments, apart from the “design charts” for designers, have been widely used by many researchers as validation references in seakeeping characteristic of planing monohull investigations. Among them were [Martin \(1976a,b\)](#) and [Zarnick \(1978, 1979\)](#). Many researchers, although mainly using Fridsma's results as the reference, also performed their own experiments in order to match their particular studies.

[Savitsky \(1964\)](#) performed an extensive series of experiments and presented a series of formulations based on the resulting data. Actually, the formulae are widely used as preliminary calculation of running attitude in calm water for a planing craft design. Then, in 1968, [Savitsky \(1968\)](#) performed an analysis of available data on the seakeeping behaviours to define and classify hydrodynamic characteristics associated with various speeds. He found that the different behaviours of planing hull at low speed ( $F_{n\Delta} < 2$ ) or in semi-displacement regime are similar to the seakeeping of displacement hull at high speed regime ( $F_{n\Delta} > 2$ ), in which, hydrodynamic force dominates.

Savitsky's Formulae are expressed as follows:



$$F_{L\beta} = \frac{1}{2}\rho U^2 B^2 C_{L\beta} \quad (2.1)$$

$$C_{L\beta} = C_{L0} - 0.0065\beta C_{L0}^{0.6} \quad (2.2)$$

$$C_{L0} = \tau_{deg}^{1.1} \left( 0.012\lambda_w^{0.5} + 0.0055 \frac{\lambda_w^{2.5}}{F_{nB}^2} \right) \quad (2.3)$$

$$\frac{l_p}{\lambda_w B} = 0.75 - \frac{1}{5.21 \frac{F_{nB}^2}{\lambda_w^2} + 2.39} \quad (2.4)$$

Where:

- $C_{L0}$  is lift coefficient for zero deadrise angle ( $\beta = 0$ ).
- $C_{L\beta}$  is lift coefficient.
- $F_{L0}$  is lift force for zero deadrise angle ( $\beta = 0$ ).
- $F_{L\beta}$  is lift force.
- $\lambda_w = (L_k + L_c)/(2B)$  is mean wetted length to beam ratio.
- $L_k$  is keel wetted length.
- $L_c$  is chine wetted length.
- $\tau_{deg}$  trim angle is degrees.
- $\tau$  is trim angle in radians.
- $\beta$  is angle of deadrise in degrees.
- $B$  is beam.
- $F_{nB} = U/\sqrt{gB}$  is Beam Froude number.

The reason of using beam as the reference dimension in Froude number is that the wetted beam of a planing craft is mostly constant whereas the wetted length, such as the keel wetted length is unknown before the resolution of equations of equilibrium for vertical force and trim moment associated with a given forward speed is found. Besides, the lift force obtained by Savitsky's Formulae already includes the buoyancy component, thus, for the further use in the system of equations of motions (used in [Keuning \(1994\)](#)'s work), it should be noted that an inclusion of the other buoyancy component will lead to the inaccurate results.

Then, [Savitsky and Brown \(1976\)](#) performed hydrodynamic studies of motions in waves of several planing hulls and presented the results of several studies in conjunction with

Table 2.2: Range of applicability of [Savitsky and Brown \(1976\)](#)'s Formulae.

Parameter	Range
$\Delta / (0.01 \cdot L)^3$	100 – 250
$L/b$	3 – 5
$\tau^o$	3 – 7
$\beta^o$	10 – 30
$H_{1/3}/b$	0.2 – 0.7
$V/\sqrt{L}$	2 – 6

the work done by [Fridsma \(1971\)](#). This firstly summarized the earlier work done by [Savitsky \(1964\)](#), then moved on to the consideration of effect of trim tabs, the effect of warp, re-entrant free hull and pre-planing resistance. The final set of experiments which [Savitsky and Brown \(1976\)](#) have detailed are the behaviours of a planing craft in a seaway. The results of the investigation were used to develop a series of design charts for prediction of the added resistance in waves. In other words, the power requirement of the planing craft, impact load on hull structure at the bow and CG of the craft and the amplitudes of heave and pitch motions. It is noticeable that for cases of calm water and rough water, in determining the performance of different hull forms, it is necessary to evaluate them at the identical dynamic trim (running trim), as well as the same load and speed.

The results deduced that deadrise has a favourable effect on performance in waves, for example, increasing the deadrise from 20 to 30 degrees reduced the added resistance by 20%. Motions are also attenuated by higher deadrise angle at high speed. It is on the impact accelerations that the deadrise has a most significant effect, increasing deadrise from 10 to 30 degrees halves the impact accelerations. Reducing the trim also has a favourable effect on loads and motions, i.e., reducing dynamic trim from 6 to 4 degrees causes 33% reduction of impact accelerations although resistance could significantly increase. Increasing the load decreases the impact accelerations, the amplitude of motions at high speed and normally reduces the added resistance. Increasing the length to beam ratio raises the acceleration levels at all speeds and increases the motions at high speed. At low speed, increasing the length to beam ratio increases the added resistance, and at high speed, the added resistance is reduced.

The data was implemented into equations for predicting the added resistance in waves and the impact CG and bow accelerations. These facilitate the performance prediction, and are comparable in accuracy with the charts they originated from. As the equations are the basis of empirical data, it is necessary to account for the range of applicability and not to make extrapolation beyond the range. These empirical formulae are suitable for computational use and are given in Table 2.2.

[Savitsky and Brown \(1976\)](#)'s formulae can be summarized in the following paragraph:

**Added Resistance at  $V/\sqrt{L} = 2$** 

$$\frac{R_{AW}}{wB^3} = 66 \cdot 10^{-6} \cdot \left( \frac{H_{1/3}}{B} + 0.5 \right) \cdot \frac{(L/B)^3}{C_{\Delta}} + 0.0034 \cdot (\tau - 4) \quad (2.5)$$

Note: No effect of deadrise: Precision  $\pm 20\%$

**Added Resistance at  $V/\sqrt{L} = 4$** 

$$\frac{R_{AW}}{\Delta} = \frac{0.3 \cdot H_{1/3}/B}{1 + 2 \cdot H_{1/3}/B} \cdot \left( 1.76 - \frac{\tau}{6} - 2 \cdot \tan^3 \beta \right) \quad (2.6)$$

Note: No effect of length to beam ratio: Precision  $\pm 20\%$

**Added Resistance at  $V/\sqrt{L} = 6$** 

$$\frac{R_{AW}}{wB^3} = \frac{0.158 \cdot H_{1/3}/B}{1 + (H_{1/3}/B) \cdot (-0.12 \cdot \beta - 21 \cdot C_{\Delta} \cdot (5.6 - L/B) + 7.5 \cdot (6 - L/B))} \quad (2.7)$$

Note: No effect of trim: Precision  $\pm 10\%$

**Average Impact Acceleration at CG (g)**

$$\eta_{CG} = 0.0104 \cdot \left( \frac{H_{1/3}}{B} - 0.084 \right) \cdot \frac{\tau}{4} \cdot \left( \frac{5}{3} - \frac{\beta}{30} \right) \cdot \left( \frac{V}{\sqrt{L}} \right)^2 \cdot \left( \frac{L/B}{C_{\Delta}} \right) \quad (2.8)$$

Note: Precision  $\pm 20\%$

**Average Impact Acceleration at Bow (g)**

$$\eta_{bow} = \eta_{CG} \left( 1 + \frac{3.8 \cdot (L/B - 2.25)}{V/\sqrt{L}} \right) \quad (2.9)$$

Note: Precision  $\pm 20\%$

Where:

- $R_{AW}$  is added resistance in waves.

- $w$  is Weight density of water.
- $H_{1/3}$  is significant wave height.
- $\Delta$  is displacement mass.

Savitsky and Brown (1976) presented their results in conjunction with Fridsma (1969)'s experiments, Fridsma's work was divided into two volumes, a systematic study of rough water performance of planing boat in regular waves and irregular waves (Fridsma, 1971). The main conclusion of his earlier work was that added resistance, motion responses and accelerations are generally a nonlinear function of wave height. Linear behaviours occur at the extremes of wave height, i.e., contouring of waves at low speeds and planing at very high speed. Furthermore, it was seen that the wavelength of the maximum resistance was constantly shorter than the wavelength of the maximum response motions. The results of model tests were collapsed into a simpler form by using a wavelength coefficient:

$$C_\lambda = \frac{L}{\lambda} \cdot \left( \frac{C_\Delta}{(L/B)^2} \right)^{\frac{1}{3}} \quad (2.10)$$

Fridsma (1971)'s report has been summarized by the work of Savitsky and Brown (1976), with design charts and preliminary equations for designer's use.

Taunton et al. (2011a,b) carried out tests of a series of high-speed hard chine planing hulls with variable deadrise angles in calm water and irregular seas. Their work provided a new series of hard chine planing hull design data. Their tests were conducted in support of design for performance of crew on board small high-speed craft.

Regarding the transverse stability of planing boat, Brown and Klosinski (1995) performed experiments in order to determine the added inertia and damping of planing boat in roll motion. Their study was carried out to support the U.S. Coast Guard's pursuit of R & D projects that would enable it to evaluate advanced marine vehicle and advance technologies. The objective of this research was to obtain basic hydrodynamic information about planing hulls by using captive model tests. The tests gave results of time histories of free decay roll motions in calm water, obtained by varying speeds, deadrise, trim and yaw angles. The results were used to determine added roll moment of inertia and roll damping assuming the evaluation of linear roll equation of motion. They deduced empirical formulae to predict the hydrodynamic roll moment of inertia and roll damping as follows:

$$I_{yy} = 0.010237 \cdot \rho \cdot B^5 \cdot (L/B) \cdot (1 - \sin \beta) \quad (2.11)$$

$$B_\phi = w \cdot B^4 \sqrt{B/g} \cdot (1 - \sin \beta) \cdot (0.134 \cdot \sin |\phi| + 0.0290 \cdot C_V + 0.0199 \cdot L/B) \quad (2.12)$$

Table 2.3: Range of applicability of Brown and Klosinski's formulae.

Parameter	Range
$C_{\Delta}$	0.4375
$L/b$	1 – 5
$\tau^o$	0 – 6
$\phi^o$	$\pm 15$
$\beta^o$	10 – 20
$C_V$	1.5 – 4.0

Where:

- $I_{yy}$  is roll moment of inertia [*slug – ft.sq*].
- $B_{\phi}$  is roll damping coefficient [*lb – ft/rps*].
- $\phi$  is roll angle [ $^{\circ}$ ].
- $C_V$  is speed coefficient.

Note that these formulae are expressed in imperial units, with limitations presented in Table 2.3.

Rosén and Garne (2006) carried out in CEHIPAR (Canal de Experiencia Hidrodinámica de El Pardo), Madrid, experiments of a planing hull model in towed condition allowing to heave, roll and pitch. The model was tested measuring pressure distribution on the hull, heave, roll and pitch motions in different sea condition from calm water; regular; and irregular head waves including oblique regular waves. The tests were performed at three different speeds with the maximum speed of 4.5 *m/s*. They concluded that the top speed of 4.5 *m/s* is not corresponding to the ideal planing conditions, still the three different model speeds show significant differences in the pressure at the transom. The variation of sea conditions fulfilled the purpose of well-defined situations of increased level of complexity and severity. In the most severe sea state, the model occasionally leaves the water indicating that the combination of speed and sea state constitutes the operational limit of planing boat.

## 2.3 2D Strip Theory Approach

Regarding strip theory based method, it is on the basis of the assumption of slenderness. The fully 3D model characteristics are simplified to the summation of 2D strips. That means a force acting on each cross section of the hull will be evaluated, and then integrated to obtain total force. The use of strip theory should be under the assumption that the wavelength must be large in comparison to the vessel length, and the wave

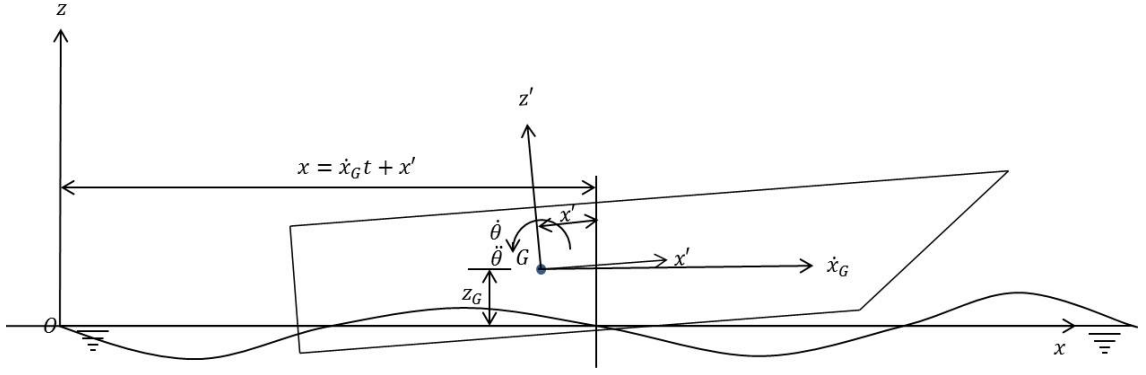


Figure 2.1: Korvin-Kroukovski definition.

slope should be small. Strip theory is proved to be very powerful when the study of seakeeping is necessary in both conventional displacement ships and high-speed planing craft. A typical strip theory of heave and pitch motions is presented here by the approach of [Korvin-Kroukovsky and Jacobs \(1957\)](#). They first defined two coordinate systems called earth-fixed:  $Oxyz$  and body-fixed:  $Gx'y'z'$ . As can be seen in Figure 2.1, the cross section under consideration is located at  $x'$  and can be expressed in earth-fixed coordinate system as:  $x' = x - x_G t$ , and consequently,  $\dot{x}' = -\dot{x}_G$ .

The relative vertical velocity of the cross section at the position  $x'$  as well as the displacement and acceleration are expressed in the following forms:

$$h = z_G - x'\theta - \zeta \quad \text{displacement} \quad (2.13)$$

$$\dot{h} = \dot{z}_G - x'\dot{\theta} + \dot{x}_G\theta - \dot{\zeta} \quad \text{velocity} \quad (2.14)$$

$$\ddot{h} = \ddot{z}_G - x'\ddot{\theta} + 2\dot{x}_G\dot{\theta} - \ddot{\zeta} \quad \text{acceleration} \quad (2.15)$$

Where  $\zeta$  is local wave elevation. Then, the sectional hydrodynamic force is defined by:

$$f = -\frac{d}{dt} (m_a \dot{h}) - b_d \dot{h} - 2\rho g y_w h \quad (2.16)$$

Where:

- $m_a$  is sectional added mass.
- $b_d$  is sectional damping.
- $y_w$  is half water line beam of section.

The first term on the right-hand side of Equation 2.16 is the result of slender body theory, the second term is damping associated with the generation of wave surface and the third is hydrostatic force due to the vertical displacement of the particular section. In linear strip theory approximation, the time derivative of the first term can be written as:

$$\frac{dm_a}{dt} = \frac{dm_a}{dx'} \frac{dx'}{dt} = -\dot{x}_G \frac{dm_a}{dx'} \quad (2.17)$$

Consequently, Equation 2.16 can be rewritten as:

$$f = -m_a \ddot{h} - \left( b_d - \dot{x}_G \frac{dm_a}{dx'} \right) \dot{h} - 2\rho g y_w h \quad (2.18)$$

Following the 2<sup>nd</sup> law of Newton, the equations of heave and pitch motions with forward speed  $\dot{x}_G$  in head waves is expressed as:

$$M \ddot{z} = \int_L (f_1 + f_2 + f_3) dx' \quad \text{heave} \quad (2.19)$$

$$I_{yy} \ddot{\theta} = - \int_L (f_1 + f_2 + f_3) x' dx' \quad \text{pitch} \quad (2.20)$$

In which:

$$f_1 = -2\rho g y_w (z_G - x' \theta - \zeta) \quad (2.21)$$

$$f_2 = -b_d (\dot{z}_G - x' \dot{\theta} + \dot{x}_G \theta - \dot{\zeta}) \quad (2.22)$$

$$\begin{aligned} f_3 &= -\frac{d}{dt} m_a (\dot{z}_G - x' \dot{\theta} + \dot{x}_G \theta - \dot{\zeta}) \\ &= -m_a (\ddot{z}_G - x' \ddot{\theta} + 2\dot{x}_G \ddot{\theta} - \ddot{\zeta}) + \dot{x}_G \frac{dm_a}{dx'} (\dot{z}_G - x' \dot{\theta} + \dot{x}_G \theta - \dot{\zeta}) \end{aligned} \quad (2.23)$$

The wave elevation and its velocity and acceleration are:

$$\zeta = \zeta_a e^{-kT} \cos(kx' + \omega_e t) \quad (2.24)$$

$$\dot{\zeta} = -\zeta_a \omega_e e^{-kT} \sin(kx' + \omega_e t) \quad (2.25)$$

$$\ddot{\zeta} = -\zeta_a \omega_e^2 e^{-kT} \cos(kx' + \omega_e t) \quad (2.26)$$

Then, by integrating the sectional forces components  $f_1$ ,  $f_2$  and  $f_3$  along the ship length, the equations of motions will be evaluated to:

$$A_{33}\ddot{z} + B_{33}\dot{z} + C_{33}z - A_{35}\ddot{\theta} - B_{35}\dot{\theta} - C_{35}\theta = F_{3a} \cos(\omega_e t + \epsilon) \quad (2.27)$$

$$A_{53}\ddot{\theta} + B_{53}\dot{\theta} + C_{53}\theta - A_{55}\ddot{z} - B_{55}\dot{z} - C_{55}z = F_{5a} \cos(\omega_e t + \epsilon) \quad (2.28)$$

Where  $F_{3a}$  and  $F_{5a}$  are heave force and pitch moment amplitude respectively. The coefficient  $A_{ij}$ ,  $B_{ij}$  and  $C_{ij}$  are total hydrodynamic coefficients evaluated from previous equations.

Equations 2.27 - 2.28 are the so-called ‘‘Ordinary Strip Theory Method’’ containing only sectional values for added mass and damping and their time derivative with forward speed effect. The results obtained from this method are generally good when small motions are considered, due to the fact that the values of hydrodynamic coefficients are constant. For high-speed planing craft, the nonlinear effects become predominant, and a modification of ordinary strip theory is necessary to be developed. Among those who carried out strip theory for planing hull, [Zarnick \(1978\)](#)’s work appears to be the most pioneering at the beginning of development of that so-called 2.5D strip theory.

According to the point of view of fluid mechanics, 2D sectional hull geometry partially penetrated in the water is a complex problem due to the free surface boundaries between the hull and the water, as well as between water surface and the air, that is continuously altered from the hull motions. The first simplification is the assumption of potential flow which are inviscid, incompressible and irrotational. The complex 3D problem has been reduced to 2D shape problem under the assumption of slender body theory previously mentioned. Due to geometrical similarity, the sectional hull of high-speed planing craft can be assumed to be a wedge shape geometry, see [Figure 2.2](#), and the vessel moving with forward speed is simulated as a wedge penetrating into the water. The pressure distribution, as well as the total force, are necessary to be evaluated. The 2D wedge penetrating into the water can be replaced by a flat lamina following the assumption that the fluid accelerations are much larger than gravity ([von Karman, 1929](#); [Wagner, 1931, 1932](#)). The flat lamina is expanding at the same rate as the sectional wedge increasing in the undisturbed water. The most significant contribution can be found in the investigation of seaplane landing of [von Karman \(1929\)](#) and [Wagner \(1931, 1932\)](#).

Starting from the potential function,  $\varphi$ , of vertical falling lamina:

$$\varphi = -V\sqrt{c^2 - x^2}, \quad |x| < c(t) \quad (2.29)$$

The pressure distribution derived from potential flow theory can be expressed as:



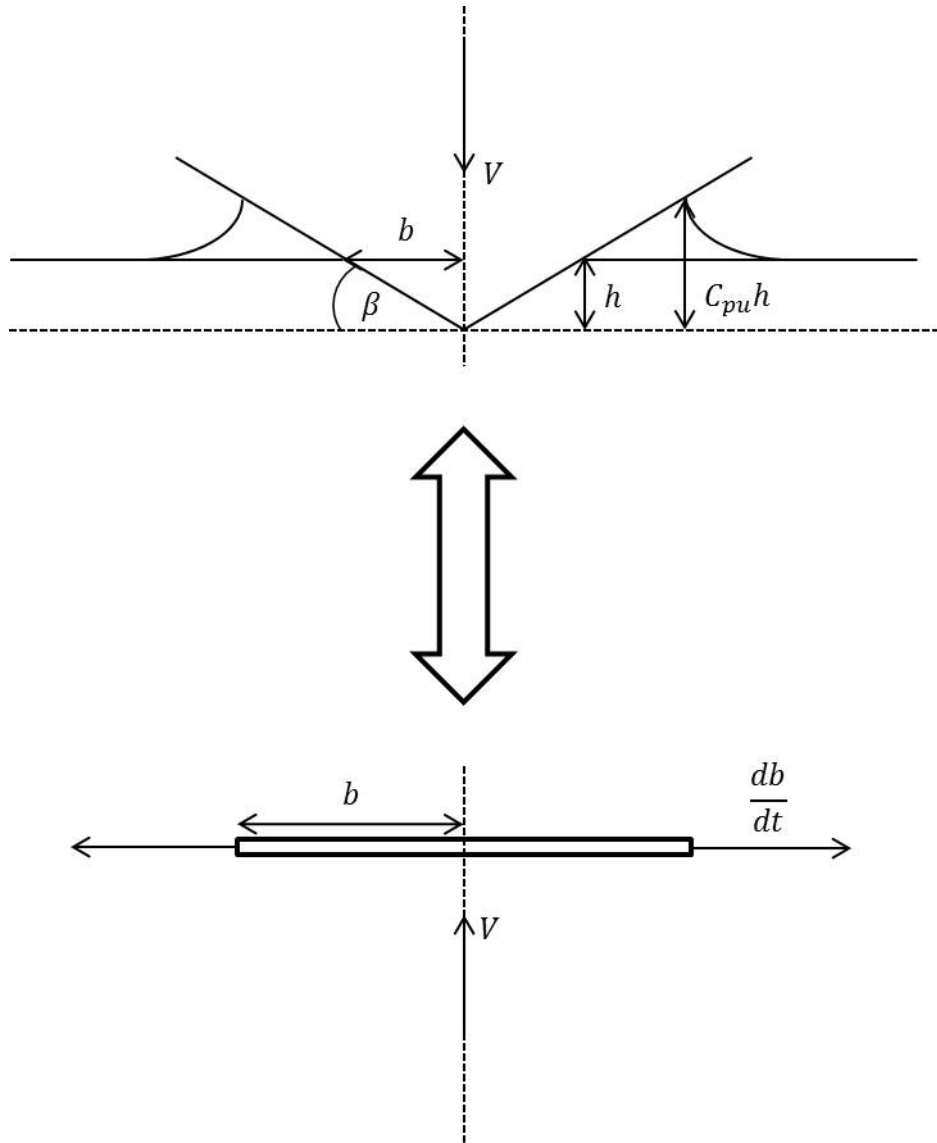


Figure 2.2: Wedge penetrating into water and equivalent flat plate.

$$\begin{aligned}
 p - p_a &= -\rho \frac{\partial \phi}{\partial t} \\
 &= \rho V \frac{c}{\sqrt{c^2 - x^2}} \frac{dc}{dt} + \rho \frac{dV}{dt} \sqrt{c^2 - x^2}
 \end{aligned} \tag{2.30}$$

Where  $c$  is the edge of the lamina from the mid point. Then, deriving the 2D vertical force acting on the impacting body gives:

$$\begin{aligned}
f_3 &= \int_{-c}^c p dx \\
&= \rho V c \frac{dc}{dt} \int_{-c}^c \frac{dx}{\sqrt{c^2 - x^2}} + \rho \frac{dV}{dt} \int_{-c}^c \sqrt{c^2 - x^2} dx \\
&= \rho \pi V c \frac{dc}{dt} + \rho \frac{\pi}{2} c^2 \frac{dV}{dt} \\
&= V \frac{da_{33}}{dt} + a_{33} \frac{dV}{dt} \\
&= \frac{d}{dt} (a_{33} V)
\end{aligned} \tag{2.31}$$

Wagner included a water pile-up correction term with the value of  $\pi/2$  in order to account for the water pile-up phenomenon when the wedge shape penetrates into the water. Following the expression of sectional force in Equation 2.31, it can translate to vertical force or heave force phenomena, in which by multiplying by the lever arm, the pitch moment can be obtained. The term of 2D added mass is expressed as  $a_{33} = (\pi/2)\rho c^2$ . This is so called the “high frequency added mass” derived from the free surface condition  $\phi = 0$ . Zarnick (1978) and later many researchers i.e. Akers (1999), Keuning (1994) and Deyzen (2008) used this expression in their mathematical model. It is necessary to apply an “added mass coefficient”,  $C_m$ , to correct the added mass term for different simulations. The detail and examples of the use of  $C_m$  are explained along the thesis. The sectional hydrodynamic force used by Zarnick (1978) is in the following form:

$$\frac{d}{dt} (a_{33} V) = a_{33} \dot{V} + \dot{a}_{33} V - U \frac{\partial}{\partial x'} (a_{33} V) \tag{2.32}$$

Payne (1992) presented an approximation of the added mass variation with chines immersed and a conventional cross-flow drag hypothesis as an additional lift component as well as in the computational models of both Zarnick (1978) and Keuning (1994). He discovered that the lift increment due to the chines immersed added mass is the same as the one due to the cross-flow drag, so that adding the two together results in chines immersed dynamic force which is twice the real value. Payne (1981) also suggested that the value of  $\pi/2$  of the water pile-up correction factor is too high when comparing the impact load with experiments. Later, in 1994 (Payne, 1994), he found that the results originally found by Pierson and Leshnover (1950), in which they expressed the pile-up correction factor as a function of deadrise angle, gave very good agreement with the results of Zhao et al., 1996. The expression of pile-up correction factor in function of deadrise angle is  $C_{pu} = (\pi/2) - \beta(1 - (2/\pi))$  whose maximum value is  $\pi/2$ .

When the sectional force has been found, the next step to perform is integrating these forces along the ship length. In the early period of investigation of planing hull motions, most researchers concentrated only on the coupled heave and pitch motions due to the availability of hydrodynamic coefficients obtained from wedge penetrating into the water analogy, in which the wedge falls vertically and is associated to the heave motion. [Martin \(1976a\)](#) evaluated a linear mathematical model capable of simulating heave and pitch motions instability in calm water called porpoising, then, in the same year ([Martin, 1976b](#)), the same mathematical model was modified by adding wave excitation force based on the model experiments of [Fridsma \(1969\)](#). The results showed good agreement with the experiments. [Martin \(1976b\)](#) shows that nonlinear effects are more severe at higher speeds, principally because of the reduction of the damping ratio of the boat when increasing the speed, and the consequential increase in motions in the vicinity of the resonant encounter frequency. It is concluded that the linear theory can provide simple and fast means of determining the effect of various parameters such as trim, deadrise, loading and speed, on the damping, natural frequency and linearised responses in waves. Nevertheless, the linear frequency domain model could not reproduce accelerations accurately enough, thus the problem should be solved by nonlinear equations of motions. [Martin \(1976b\)](#) suggested time domain analysis which is presented later by [Zarnick \(1978, 1979\)](#). The nonlinear mathematical model developed by him is solved in the time domain. His model is based on 2D strip theory and the sectional forces and moments are determined by the wedge penetrating into the water theory. His simulations are based on [Fridsma \(1969\)](#)'s model configurations. A simplified model base on Fridma's experiments is used as input data to the computer programme and then compared with the result from the model experiments. According to his results, the comparison of computed pitch and heave motions and phase angles with the corresponding experimental data is notably significant. As well as the comparison of bow and centre of gravity vertical accelerations is quite good. This pioneering work formed the theoretical basis for the simulation model developed by [Akers \(1999\)](#) and above all, the present research. After obtaining the total forces and moments by integrating the sectional forces along the ship length, the equations of motions generally will translate to the following form:

$$M(\dot{x}, x) \cdot \ddot{x} = F(\dot{x}, x) \quad (2.33)$$

Where  $M(\dot{x}, x)$  is a matrix of components associated to the accelerations including ship mass and added mass.  $x$  is a displacement vector in considered degrees of freedom, as well as its time derivation to velocities and accelerations and  $F(\dot{x}, x)$  is a matrix of the rest of force and moment components. Supposing that the initial values of  $x$  and  $\dot{x}$  turn the problem to be a system of linear equations with  $\ddot{x}$  as unknowns. Using Gaussian elimination to solve the system,  $\ddot{x}$  can be obtained. All of the process mentioned until

now are the procedures within each time step, now knowing  $\ddot{x}$  applying numerical integration,  $\dot{x}$  and  $x$  can be obtained, and used now as input data for the next time step. The numerical integration could be basically implicit or explicit method but [Zarnick \(1978\)](#) suggested Runge-Kutta-Merson method to solve, in order to get the precision of results as high as possible. Iterating the process over time will give time history of ship motions. The precision of results depends also on the relevant controlling parameters such as the number of sections,  $N_s$  and the size of time step,  $\Delta t$ . The issue related to the controlling parameters was not mentioned in details in the report of [Zarnick \(1978\)](#). Appropriate number of section,  $N_s$  and size of time step,  $\Delta t$  are important parameters needed in order to obtain the optimal use of the computation, as varying these parameters affects the time of calculation.

The linear and nonlinear forms of equations of motions corresponding to the modified strip theory, presented by [Martin \(1976b\)](#) and [Zarnick \(1978\)](#) comparing to the ordinary strip theory are shown as follows:

### Linear Equations of Motions

$$A \cdot \ddot{x}(t) + B \cdot \dot{x}(t) + C \cdot x(t) = \overline{F}(t) \quad (2.34)$$

Note: Solved in frequency domain

### Linearized Equations of Motions: [Martin \(1976a,b\)](#)

$$A(\tau, \lambda) \cdot \ddot{x}(t) + B(\tau, \lambda) \cdot \dot{x}(t) + C(\tau, \lambda) \cdot x(t) = \overline{F}(\tau, \lambda, t) \quad (2.35)$$

Note: Solved in frequency domain or time domain

### Nonlinear Equations of Motions: [Zarnick \(1978, 1979\)](#), [Keuning \(1994\)](#), [Akers \(1999\)](#)

$$\begin{aligned} M(\dot{x}(t), \overline{x}(t)) \cdot \ddot{x}(t) &= \overline{F}(\dot{x}(t), \overline{x}(t)) \\ \ddot{x}(t) &= M^{-1}(\dot{x}(t), \overline{x}(t)) \cdot \overline{F}(\dot{x}(t), \overline{x}(t)) \end{aligned} \quad (2.36)$$

Note: Solved in time domain

Where  $A$ ,  $B$  and  $C$  denote matrices of hydrodynamic coefficients.

The linearized mathematical model of [Martin \(1976b\)](#) is based on the equations of motions for dynamical stability. Knowing dynamic trim and sinkage parameters,  $\tau$  and  $\lambda$ , small perturbation motions are assumed, consequently, the equations of motions can be solved in frequency domain, following the classical solution of 2<sup>nd</sup> order non-homogeneous ordinary differential equation. While the mathematical model of [Zarnick \(1978\)](#), following the 2<sup>nd</sup> Law of Newton, is in fully nonlinear form. The assumption of conventional sinusoidal solution is no longer valid and needs to be solved in time domain.

Then, [Zarnick \(1979\)](#) presented the simulation of ship motions in irregular seas using the modified and extended version of the mathematical model used in case of regular seas. The irregular seas used in the simulation were created by the superposition of ten regular wave components of different amplitudes and frequencies. The wave components were selected from the energy distribution of a Pierson-Moskowitz Spectrum for a fully developed sea. The simulations were also based on [Fridsma \(1971\)](#)'s experiment and analysed statistically following the same manner. The comparison of [Zarnick \(1979\)](#)'s simulations with the experiments indicates that the mathematical model could predict ship motions with reasonably quantitative accuracy in moderate operating conditions. In severe operating conditions, however, the amplitudes of the computed vertical accelerations, which included impacts, are a half of the experimental value. [Blake \(2000\)](#) performed experiments and computational simulations also based on [Fridsma \(1969, 1971\)](#) and used in simulations, Bretschneider Spectrum instead of the Pierson-Moskowitz one, due to the fact that the later one is of only one parameter and the accuracy of generated seas could be less comparing to the multi-parameters spectrum.

[Chiu and Fujino \(1989\)](#) presented a mathematical model similar to [Zarnick \(1978\)](#)'s model comparing the results solved by linear and nonlinear models. Their linear model is based on the assumption that the hydrodynamics coefficients associated with calm water simulation are the same as those used in head wave simulations.

[Keuning \(1994\)](#) implemented [Zarnick \(1978\)](#)'s model adding a semi-empirical tool for estimating the calm water running attitude in order to determine correction terms to the further unsteady procedure. He performed an in-depth investigation approaching added mass behaviours and its time dependency. The model was finally implemented into a software named "Fastship". In the similar approach, [Deyzen \(2008\)](#), following the basis of [Zarnick \(1978\)](#) and [Keuning \(1994\)](#), extended the model to three degrees of freedom allowing the surge motion to take place. The simulations can be carried out with either a constant forward speed or constant thrust. His model is also capable of simulating calm water behaviours of another hull geometry different from [Fridsma \(1969\)](#)'s configurations. He suggested the simulations in three degrees of freedom by adding thrust force allowing the surge motion to be simulated comparing to the classical towed condition (no surge motion).

Garne and Rosén (2003), Garne (2004a, 2005) and Rosén and Garne (2006) studied the pressure distribution on the hull of planing craft in calm water, regular head and oblique waves and irregular waves. Also, Garne (2005) formulated a correction operating on both the hydrostatic and hydrodynamic terms of the load distribution. He based his correction on the assumption that the pressure is atmospheric at the dry transom stern. A strictly 2D analysis of the lift distribution on the planing ship overestimates the lift near to the transom. Further, it is assumed that the difference between the 2D lift distribution and the actual pressure is largest aft and decreases as it goes forward. The correction approach is to multiply the 2D force distribution by a reduction function that presents a value of 0 at transom and approaches to 1 at forepart. The near transom correction factor will be showed with more detail in Chapter 3. Garne (2005) validated the reduction function on basis of the model test measurements of the near transom pressure, and on published model data on running attitude. This correction improves the simulation in both calm water and in waves for a wider range of forward speeds. His mathematical model also allows the evaluation of hydrodynamic load distribution along the ship length in different running attitudes which can be further useful to the study of the structural strength of planing craft.

Faltinsen and Sun (2010, 2011) suggested that any of previously mentioned work account for the fully nonlinear phenomena. They presented a mathematical model based on 2.5D theory applying boundary element method (BEM) to solve 2D body-wave interaction problems derived from the 3D problem. Notable numerical procedure of the application of BEM in planing craft dynamics field was found in Zhao et al. (1996). A 2D domain of fluid is considered to be infinitely extended in horizontal direction, limited by a horizontal and waterproof bottom at the lower boundary, and limited by free surface and hull surface at the upper boundary. The potential flow assumption is applied in which the fluid is supposed to be incompressible, inviscid and irrotational. According to the consideration of irrotational flow and continuity condition, the velocity vector can be expressed in the form  $\nabla^2\varphi = 0$ . The boundary conditions are defined on the lower bottom of the fluid domain, on the free surface and on the body, and the solution of the problem will be:

$$\begin{cases} \nabla^2\varphi = 0 & \text{in the fluid domain} \\ \frac{\partial\varphi}{\partial n} = V \cdot n & \text{on the body} \\ \varphi = 0 & \text{on the free surface} \end{cases} \quad (2.37)$$

The velocity potential is found numerically by solving the integral equation obtained from applying the 2<sup>nd</sup> identity of Green to the potential  $\varphi$  and a Green's function  $G$  as follows:

$$2\pi\varphi = \int_S \left( \frac{\partial\varphi}{\partial n} \cdot G - \varphi \cdot \frac{\partial G}{\partial n} \right) dS \quad (2.38)$$

Green's 2<sup>nd</sup> identity can be solved numerically by dividing the surfaces previously defined into straight elements. The numerical solution procedure solves the velocity potential  $\varphi_i$  and its normal derivative  $\partial\varphi_i/\partial n_i$  on all boundary elements.  $\varphi_i$  and  $\partial\varphi_i/\partial n_i$  are used to solve the pressure distribution and the total force on the body at each time step.

The principal advantage of using BEM is that it is often more accurate than the simplified solutions. They compared the results with those from the simplified method and found that the comparison gives reasonably good agreement with the model tests. Then they extended their model to be capable of simulating more complex flow phenomena such as jet and spray. The study of influence of gravity as well was performed in calm water and was found that in comparison of results at high speed and moderate speed, the gravity not only affects the free-surface profile around the hull, but also influences the hydrodynamic force on the hull surface. In summary, a certain number of investigations performed by [Sun and Faltinsen \(2006\)](#), [Faltinsen and Sun \(2007, 2010, 2011\)](#) has proved itself to be capable of simulating in more detail than the simplified method but still with limitation in longitudinal plane motions and the high time consumption.

[Lewis et al. \(2007\)](#) and [Lewis et al. \(2010\)](#) presented a novel technique applied to 2D strip method by using 3D CFD with RANS solver to solve 2D water entry problem instead of the classical potential based boundary value problem. A series of falling wedge experimental tests was carried out in order to prove the hypothesis of the technique. The results from 2D wedge water entry were used as a database when applying in 2D strip method. A correction factor is necessary in order to comply the influence of forward speed when integrating the total force along the hull length.

The nonlinear approach mentioned previously is almost limited to longitudinal vertical plane motions especially the coupled heave and pitch in both calm water and in waves, due to the fact that the simplification of sectional hydrodynamic force is dependent on sectional heave added mass. In order to extend the investigation to transverse plane motions, others added mass components are necessary to be evaluated. Unlike the ordinary strip theory, due to the complexity of flow around planing hull, nonlinear and unsteady hydrodynamic coefficients in other directions are complicated to define. [Sebastiani et al. \(2008\)](#) and [Ruscelli \(2009\)](#) presented a mathematical model based on [Zarnick \(1978\)](#)'s model with extension to be capable of predicting roll motion. Apart from the strip sections along the ship length, they divided each section into port and starboard sides. Each side is considered as a particular section and by applying heave added mass  $a_{33}$ , it is possible to evaluate roll motions sufficiently. A lateral section can no longer considered as symmetric wedge but asymmetry will be considered instead. The

pressure distribution along the 2D asymmetric falling wedge was presented by [Toyama \(1993\)](#) based on [Wagner \(1931\)](#)'s work and have been extended also by [Hua et al. \(2000\)](#), [Seif et al. \(2004\)](#) and [Algarín and Tascón \(2011\)](#).

In order to evaluate sectional lift force associated to each section side appropriately, the following assumption was made by [Ruscelli \(2009\)](#). Considering the tilted section as being composed of two independent symmetrical wedges: starboard side having deadrise equal to geometric deadrise “minus” the instantaneous roll angle, port side having deadrise equal to geometric deadrise “plus” the instantaneous roll angle. Each symmetrical wedge contributes to one half of the total. It is assumed to enter the water with a vertical velocity equal to the vertical velocity of the centre of pressure of the wedge resulting from the combination of the roll velocity and the vertical velocity of the section. [Ruscelli \(2009\)](#) validated his model with full scale ship trials which gave a good agreement. Another possible way to study more degrees of freedom is applied linear mathematical model. However, it still under limitation and assumption of small motion perturbation.

Regarding the extension to transverse plane motion, it is of interest to carry out an appropriate investigation not only in waves but as well in calm water. Apart from longitudinal plane instability in calm water or porpoising, the roll instability could become a pronounced factor for both human operability and ship strength itself. The roll instability is that so-called “chine walking”. [Xu et al. \(2008\)](#) used a vortex distribution method to analyse water entry of a heeled 2D section with flow separation from hard chines. The deadrise angle is assumed small, and boundary conditions are transferred to a horizontal line. The possibility of transverse flow separation from the keel is incorporated. This method does not include the hydrostatic pressure, rudders, propulsion, and possible effects of cavitation and ventilation. [Ikeda and Katayama \(2000\)](#) presented the measurement  $\overline{GZ}$  of a planing craft on a straight line course in calm water as a function of heel angle  $\phi$ . They found that  $\overline{GZ}$  curve depends significantly on the trim angle at high speed which can translate to that in the case of unsteady motion in wave, roll-restoring moment will be a function of pitch. [Toxopeus et al. \(1997\)](#) presented a time domain computer simulation program to predict the dynamic stability and manoeuvrability of planing craft in still water for six degrees of freedom. The formulation used in the program were based on experimental data and additional coefficients taken from literature. The added mass coefficients in six directions were determined based on modified ordinary potential flow theory.

## 2.4 3D CFD Solvers

Recently, 3D CFD has become another alternative choice for investigations of ship motions due to its more realistic solutions comparing to 2D assumption. Generally, in 3D



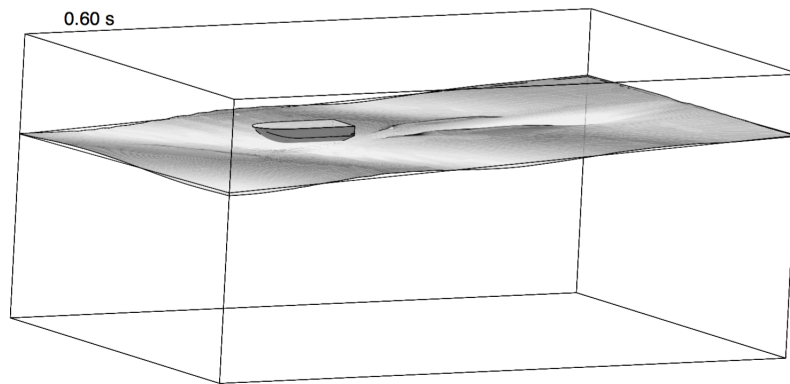


Figure 2.3: Power boat model jumping in oblique waves at  $9\text{ m/s}$  (Azcueta et al., 2003).

CFD method, the full Navier-Stokes equation is solved for the flow in a fluid domain. Azcueta (2003) and Azcueta et al. (2003) used a commercial software based on RANSE (Reynolds Averaged Navier-Stokes Equation) named COMET to simulate a high-speed planing vessel both the running attitude in calm water and the motions in waves. The comparison with the results from Savitsky (1968)'s formulae is generally acceptable. Su et al. (2012) applied RANSE to solve the running attitude and hydrodynamic performance of the planing vessel at a high speed. The results demonstrated that such an approach predicts those parameters accurately as compared to available experiment data. The difference between calculated and experimental results was small. Akers (1999) reviewed 3D Panel Method, as mentioned before, although 3D CFD appears to be the most realistic simulations, he found a number of difficulties with using panel method to predict the flow around planing hulls. First, the free surface location is a function of a solution of the problem, which means iterative solutions are required to estimate the free surface location as a function of fluid velocity potential as a function of the free surface location. Secondly, the geometry of the problem is a function of the solution to the problem, the location of the panels and their resulting normal vectors is a function of the fluid velocity potential which is a function of the geometry, implying again the iterative method. The third problem is that velocity potentials cannot be used directly to model viscous boundary layers to pressure from spray jets. Empirical methods are typically used to create effective geometries that take into account boundary layer, and to model spray pressures. Azcueta et al. (2003) reviewed results from calculations performed with a commercial CFD code solving RANSE in both calm water and in waves cases. The authors concluded that the steady state solution for the regular waves cases was achieved after around 33 hours and planing in irregular waves was out of scope. Comparing to the steady state motions in regular waves solutions obtained with the simplification of 2D approach, which the results were achieved after only about 8 minutes, if the results give sufficient good agreement with the experimental results, the 3D CFD can be considered impractical from the point of view of an ordinary design.

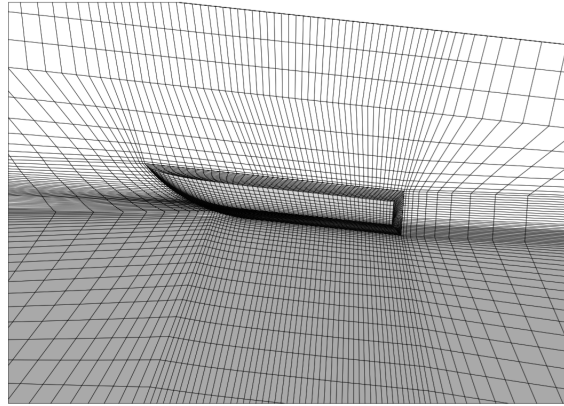


Figure 2.4: Numerical mesh around hull ([Azcueta et al., 2003](#)).

Regarding the modern techniques in CFD application, over the past decades, a state of art of CFD code called “Numerical Fluid Analysis: NFA” has been intensively developed. It is a turnkey tool of CFD allowing a possibility to investigate the complexity of multiphase flow as well as to model breaking waves around a ship, including both plunging and spilling breaking waves. As stated in [Dommermuth et al. \(2004\)](#), [Dommermuth et al. \(2006\)](#) and [Dommermuth et al. \(2007\)](#), NFA solver uses a combination of Cartesian-grid formulation with immerse body and volume-of-fluid (VOF) method. The governing equations are formulated on a Cartesian grid thereby eliminating complications associated with body-fitted grid. The sole geometric input into NFA is a surface panelization of the ship hull. No additional gridding beyond what is already used in potential flow methods and hydrostatics calculations is required. [Fu et al. \(2013\)](#) made a comparison of NFA ability to predict pressure distribution and flow characteristics of a free falling wedge to the corresponding model experiments. Application of NFA to a deep-V monohull planing hull comparing with POWRSEA and model experiments were presented by [Fu et al. \(2011\)](#). Although the more complex flow phenomena can be modelled, the disadvantage is identical to the other CFD modelling, which is the requirement of performing in supercomputers.

## 2.5 Aircraft Ditching

The original analysis carried out by [von Karman \(1929\)](#) and [Wagner \(1931\)](#) was involved with load prediction of seaplane landing. Those methodologies were successfully and widely referred as the basis of water entry problem. As the geometry employed in that analysis was wedge shape, possibility to apply in different geometry such as the semi-circular shape of the real fuselage is proposed.

The capability of an aircraft to survive an emergency landing into the water is mandatory in the early stage of design. This undesired situation could be extremely dangerous due to the loads and their effects at and after the moment of impact. This capability

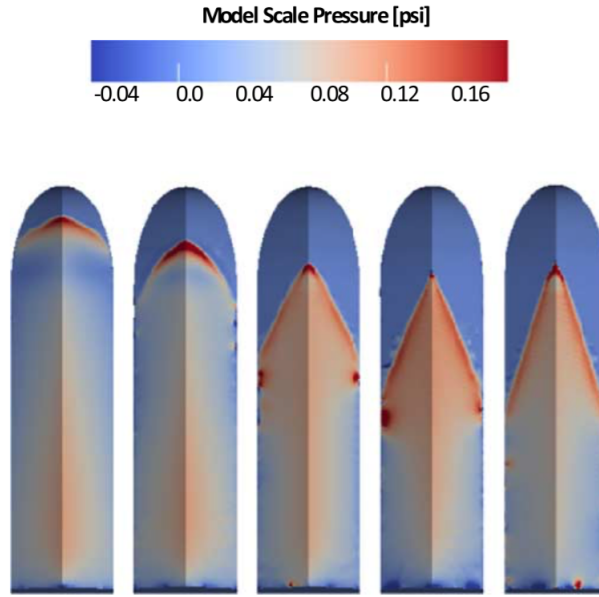


Figure 2.5: Pressure hull for  $C_{\Delta} = 0.608$   $L/B = 4$  and  $\beta = 20^0$  speed raio = 2, 3, 4, 5, 6 (from left to right) (Fu et al., 2013).

should be included in the flight manual to guide the pilot when facing this event. The important parameters to be considered can be the trim angle and landing speed. They could lead to different effects in impact loads and motions after impact. Therefore, related investigations have been carried out along the history of aviation.

Historically, due to the difficulty in achieving a correct scaling of all of the physical parameters, the relevant experiments found in the literature are carried out at full scale by aircraft manufacturers. This leads to a complication in resource limitation of the present research. Model scale experiments will be carefully planned.

Nevertheless, there are some notable investigations related to model scale ditching experiment. The first one is that of Smith et al. (1952). They made reviews of ditching experimental techniques taken place during both world wars by various institutions. The tests carried out during that periods can be classified into two main techniques. The first one is guided towing, and the other is free launching with similar three main parameters, which are touchdown speed, angle of descent at touchdown and attitude at touchdown. The advantage of guided towing technique is that the impact load acting on the fuselage can be measured. However, as the model is towed, it is not allowed to move freely after impact and cannot give the response trajectory. While the free launching technique can fulfil this but there is no way to measure forces on the hull without reference points. Later, towards the end of the wars, an investigation was started into pressure loads likely to be encountered in a fuselage bottom during an impact. In other words, how the pressure is distributed along the fuselage. This measurement of pressure distribution can be achieved by free launching technique and as well as the time histories of motions after impact.

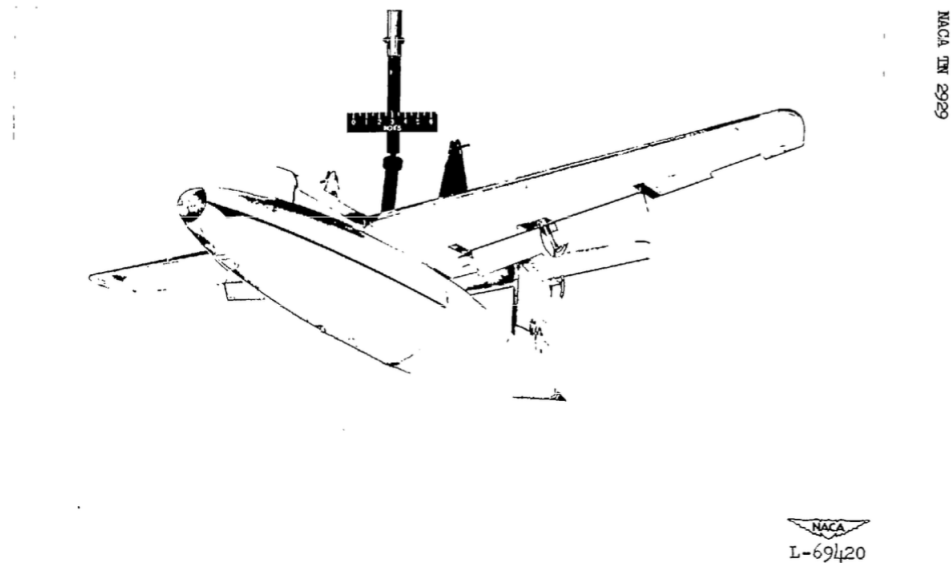


Figure 2.6: Three-quarter bottom view of the model of fineness ratio 6 in basic configuration (McBride and Fisher, 1953).

In the same period, McBride and Fisher (1953) carried out an experimental investigation on the effect of rear fuselage shape on ditching behaviour with model scale tests and then extrapolated the results to the full scale. The basic model fuselage was a streamline body of revolution with the maximum width at 50% of the length and fineness ratio of 6 and 9. By sweeping up the centreline, the longitudinal curvature of the bottom is increased, and by sweeping down, it decreases. The technique they used was a combination of guided towing and free launching. The model was accelerated firstly in guided rail to predefined launching speeds. At the end of the rail, the model dropped into the water allowing it to move freely after the impact. Time histories of speed, attitude and height of CG above water were recorded and compared. Note that there was no measurement of load or pressure distribution available in these tests.

The most recent and relevant experimental activity found in the literature is that of SMAE-FP7 project at CNR-INSEAN led by Iafrati (Siemann et al. (2012), Iafrati and Calcagni (2013) and Iafrati et al. (2014)). The project consists of an in-depth investigation of water entry of an object with a high horizontal velocity in order to achieve a better comprehension and more reliable simulation tools for the aircraft ditching phase. The first part of the study focused on the ditching of a flat plate. Due to the scaling problem mentioned previously, a facility capable of carrying out this such experiments was built and installed at the end of towing tank 1 of CNR-INSEAN. The tests were performed on aluminium plate 0.50 m wide and 1.00 m length. Similar experiments had been done by Smiley (1951) but this campaign was planned for higher horizontal and vertical velocities of full scale (from 30 to 50 m/s and 1.5 m/s respectively), and more detailed measurement involving pressure, accelerations, strain and loads. Then,

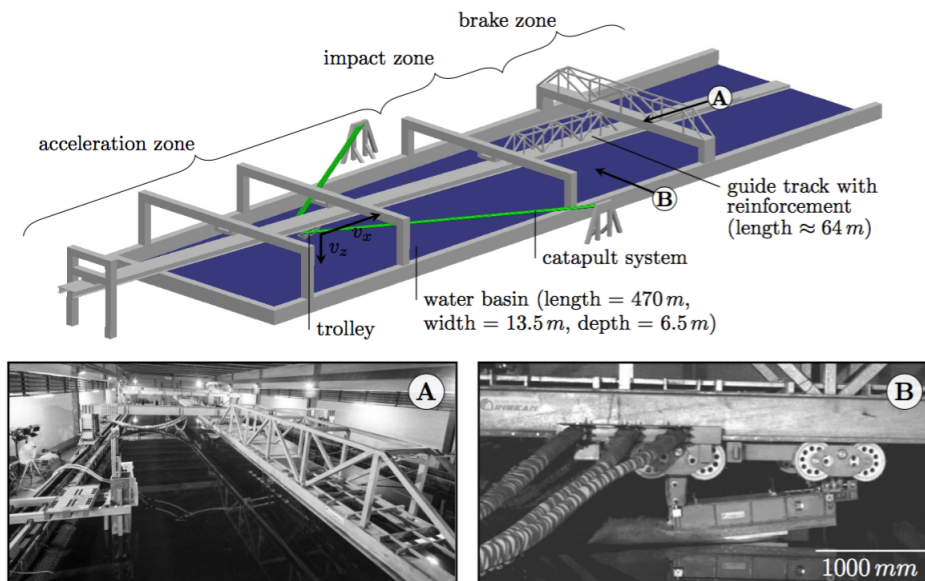


Figure 2.7: Guided ditching experimental test facility at INSEAN (Siemann et al., 2012).

Siemann et al. (2012) in the same project performed numerical and experimental simulations using rigid sub-scale aircraft CN235 and A321. The assumption of Froude similarity scaling was used to scale down the fuselages and assessed in both simulations.

Alternatively, with the development and capability of computational calculation, numerical simulations have turned to be widely used in the real world and are capable of eliminating the complication of full scale and model experiments. The most interesting computational methodology developed lastly by many researchers is CFD simulations. In the last decade, many authors have improved and tested the CFD models for aircraft ditching analysis based on both classical RANS models (Streckwall et al., 2007) and more innovative Smooth Particle Hydrodynamic (SPH) model (Climent et al., 2006). The comparison between the inclusion and exclusion of sectional forces at the tail location was presented. Another notable work of CFD investigation approaching to aircraft ditching problem is that of Streckwall et al. (2007). They follow the tests of McBride and Fisher (1953) using the identical configurations for simulations and make a comparison of results showing fair to good agreement.

Regarding the actual work, a possible methodology is derived from high-speed planing craft dynamic investigations, as its behaviours seem to be similar to the aircraft ditching problem after the moment of impact. The methodology is the combination of strip theory and wedge water impact theory presented by Martin (1976b) and Zarnick (1978). The fundamental principle of this methodology is dividing the fuselage into sections and evaluating sectional load individually by mean of the rate of change of fluid momentum. The most notable advantage of this method is small computational time with an acceptable accuracy of results.

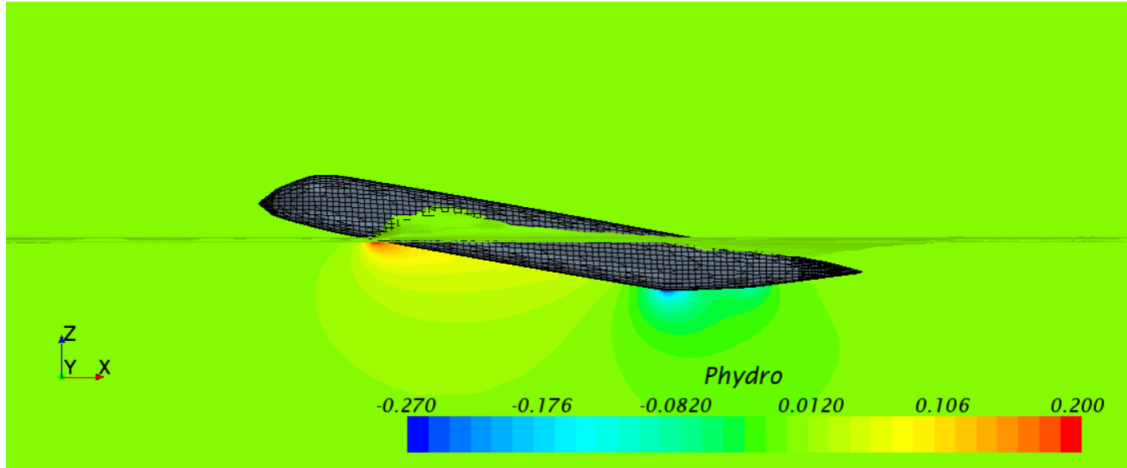


Figure 2.8: CFD (VOF) model used to simulate airframe loads for steady conditions ([Bonanni et al., 2015](#)).

Following the motivation and the aim of the research mentioned in Chapter 1 together with the reviews presented in this chapter, the methodology chosen to use as the main tool of investigation is 2D strip theory method considering its advantages and disadvantages over the others. Details of investigations approaching the aim of the research are presented further in Chapter 3.



## Chapter 3

# Verification and Validation of Mathematical Model of Calm Water and Regular Wave Simulations

Complete verification and validation of numerical models of natural systems are impossible. This is because natural systems are never closed and because model results are always non-unique. Models can be confirmed by the demonstration of agreement between observation and prediction, but confirmation is inherently partial. Complete confirmation is logically precluded by the fallacy of affirming the consequences and by incomplete access to natural phenomena. Models can only be evaluated in relative terms, and their predictive value is always open to question. The primary value of the model is heuristic.

**Definition of Verification:** According to American Institute of Aeronautics and Astronautics, Committee on Standard on Computational Fluid Dynamics definition [AIAA \(1998\)](#), Verification is a process of determining that a model implementation accurately represents the developer's conceptual description of the model and the solution to the model.

Verification is now commonly divided into two types:

- Code Verification: Verification activities directed toward:
  - Finding and removing mistakes in the source code.
  - Finding and removing errors in numerical algorithms.
  - Improving software using software quality assurance practices.



- Solution Verification: Verification activities directed toward:
  - Assuring the accuracy of input data for the problem of interest.
  - Estimating the numerical solution errors.
  - Assuring the accuracy of output data for the problem of interest.

**Definition of Validation:** Validation is the process of determining the degree to which a model is an accurate representation of the real world from the perspective of the intended uses of the model.

In summary, Verification provides evidence that the computational model is solved correctly and accurately. While Validation provides evidence that the mathematical model accurately relates to experimental measurements.

In this chapter, the system of equations of motions will be developed on the basis of principal of strip theory following [Zarnick \(1978\)](#). The system is developed initially to be capable of predicting only in two degrees of freedom in longitudinal plane motions (heave and pitch motions). This implies that the planing model is in towed condition with constant forward speed (not allowed to surge). The system is developed from evaluation of sectional forces to total force and moment. The final deliverable of the chapter will be the system of equations of motions in matrix form together with the verification and validation of the model.

### 3.1 Coordinate Systems

Classically, the coordinate system used in strip theory consists of three components shown in Figure [3.1](#).

- Earth-Fixed Coordinate System:  $Oxyz$  : The origin is fixed in a certain point at non-disturbed water level. The positive  $x$ ,  $y$  and  $z$  directions point toward to the direction of travel, toward to starboard side and downward to the water respectively.
- Ship-Fixed Coordinate System:  $Sx_sy_s z_s$  : This coordinate system is travelling with the ship with the origin fixed to the calm water level.  $x_s$  axis is pointing positively to ship travel direction, while  $y_s$  and  $z_s$  are pointing toward starboard and downward vertically to the water respectively.
- Body-Fixed Coordinate System:  $Gx'y'z'$  : The origin of this system is located at the  $CG$  of the ship.  $x'$  axis is parallel to the keel and points toward to the bow as positive direction, while  $y'$  and  $z'$  point toward to starboard side and downward perpendicularly to the keel respectively.

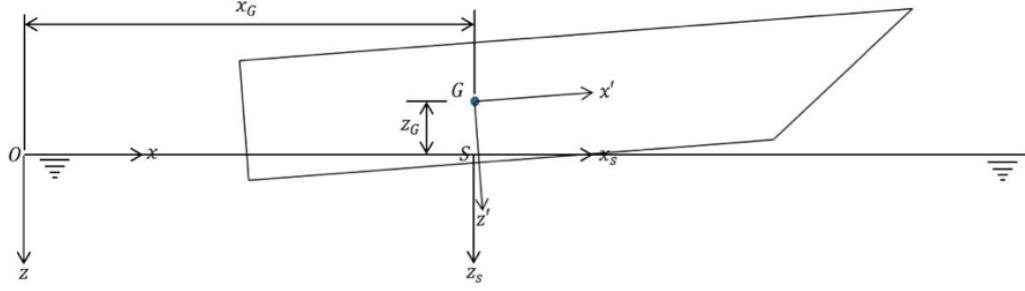


Figure 3.1: Coordinate systems.

- $x_G, y_G, z_G, \phi, \theta$  and  $\psi$  are ship's displacements (position) in the earth-fixed coordinate system.
- $\dot{x}_G, \dot{y}_G, \dot{z}_G, \dot{\phi}, \dot{\theta}$  and  $\dot{\psi}$  are ship's velocities in the earth-fixed coordinate system.
- $\ddot{x}_G, \ddot{y}_G, \ddot{z}_G, \ddot{\phi}, \ddot{\theta}$  and  $\ddot{\psi}$  are ship's accelerations in the earth-fixed coordinate system.

As the first simplification of the present project is simulations in towed condition, the surge motion does not engage,  $Sx_sy_sz_s$  can be omitted simplifying the equations of motions to involve in only the remaining two coordinate systems.

## 3.2 System of Equations of Motions

The system of equations of motions is derived from the 2<sup>nd</sup> Law of Newton and by reducing to two degrees of freedom (heave and pitch), it can be expressed in the following form: (See Figure 3.2).

$$M\ddot{z}_G = -(F_h + F_{cfd}) \cos \theta - F_b + D \sin \theta + W \quad (3.1)$$

$$I_{yy}\ddot{\theta} = M_h + M_{cfd} + M_b - Dx_D \quad (3.2)$$

Where  $\ddot{z}_G$  and  $\ddot{\theta}$  are accelerations corresponding to heave and pitch motions.  $F_h, F_{cfd}, M_h$  and  $M_{cfd}$  are hydrodynamic and cross-flow drag forces and moments respectively.  $D$  is skin friction or drag force.  $F_b$  and  $M_b$  are hydrostatic or buoyancy force and moment respectively, and finally,  $W$  is the weight of the craft.

Following the strip method, the total hydromechanics and hydrostatic forces in the system of equations of motions are derived into sectional forces in the following forms:

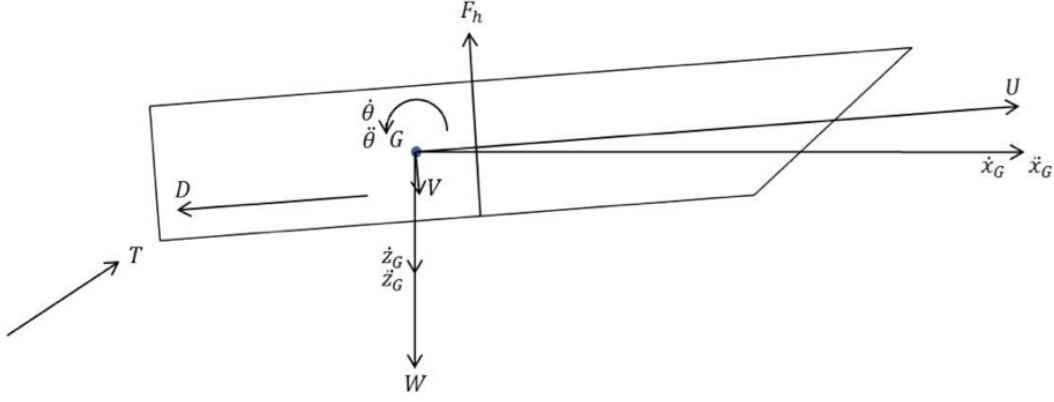


Figure 3.2: Free body diagram of forces, velocities and accelerations.

$$F_h = \int_L C_{tr} f_h dx' \quad (3.3)$$

$$M_h = \int_L C_{tr} f_h x' dx' \quad (3.4)$$

$$F_{cfd} = \int_L C_{tr} f_{cfd} dx' \quad (3.5)$$

$$M_{cfd} = \int_L C_{tr} f_{cfd} x' dx' \quad (3.6)$$

$$F_b = \int_L C_{tr} f_b dx' \quad (3.7)$$

$$M_b = \int_L C_{tr} f_b x' dx' \quad (3.8)$$

Due to flow separation phenomenon at the transom, a correction factor called “Near Transom Correction Factor:  $C_{tr}$ ” presented by Garne (2005) has been applied to the equations of motions in all of hydrodynamic and hydrostatic force terms. The aim of this additional factor is to correct the pressure distribution in transom zone where the pressure reduces to atmospheric. This factor is expressed as:

$$C_{tr} = \tanh \left[ \frac{2.5}{0.34 \cdot B_m \cdot C_v} \cdot (x' - x'_{tr}) \right] \quad (3.9)$$

In which  $B_m$  is full breadth at main section.  $C_v$  is breadth Froude Number and  $x'_{tr}$  is body-fixed coordinate of the transom.

Following the principle of Wagner (1931), sectional hydrodynamic forces are determined according to the theory of a wedge shape section penetrating into the water. The 2D penetrating wedge is replaced by a flat lamina by the assumption that the fluid accelerations are much larger than gravity. The flat lamina is expanding with the identical constant

rate at which the intersection width between the wedge and the water is increasing in the undisturbed water surface.

By solving boundary values problems, the sectional hydrodynamic force can be defined as “Rate of Change of Fluid Momentum” and written in the following form:

$$f_h = \frac{D}{Dt} (m_a V) = \dot{m}_a V + m_a \dot{V} - U \frac{\partial}{\partial x'} (m_a V) \quad (3.10)$$

With:

$$U = \dot{x}_G \cos \theta - (\dot{z}_G - w_w) \sin \theta \quad (3.11)$$

$$V = \dot{x}_G \sin \theta - (\dot{z}_G - w_w) \cos \theta \quad (3.12)$$

$$\dot{V} = \ddot{x}_G \sin \theta + (\ddot{z}_G - \dot{w}_w) \cos \theta + \dot{\theta} [\dot{x}_G \cos \theta - (\dot{z}_G - w_w) \sin \theta] \ddot{\theta} x' \quad (3.13)$$

Where  $m_a$  is sectional added mass,  $U$  and  $V$  are velocities parallel and perpendicular to the keel respectively.  $\dot{V}$  is time derivative of  $V$ ,  $w_w$  and  $\dot{w}_w$  are wave vertical orbital velocity and acceleration respectively.

[Wagner \(1931\)](#) solved a boundary value problem of an equivalent expanding flat plate and deduced expressions of sectional added mass and its time derivative as follows:

$$m_a = C_m \frac{\pi}{2} \rho b^2 \quad (3.14)$$

$$\dot{m}_a = C_m \pi \rho b \dot{b} \quad (3.15)$$

Where  $C_m$  is the sectional added mass coefficient, which is a function of sectional geometry. [Payne \(1994\)](#) suggested the dependency of deadrise angle of sectional added mass coefficient as:

$$C_m = \left(1 - \frac{\beta}{2\pi}\right)^2 \quad (3.16)$$

The half beam  $b$  is related to the section submergence  $h$  by  $b = h / \tan \beta$ . As mentioned in the previous section, the water pile-up phenomenon influences significantly to the alteration of the half beam, the expression of this factor found by [Payne \(1994\)](#) is shown as follows:

$$C_{pu} = \frac{\pi}{2} - \beta \left(1 - \frac{2}{\pi}\right) \quad (3.17)$$

And then, the corrected half beam including pile-up phenomena becomes  $b = C_{pu}h / \tan \beta$ . Thus, the expression of sectional added mass and its time derivative are expressed as functions of section submergence as follows:

$$m_a = C_m \cdot \frac{\pi}{2} \cdot \rho \cdot \left(\frac{C_{pu}h}{\tan \beta}\right)^2 \quad (3.18)$$

$$\dot{m}_a = C_m \cdot \pi \cdot \rho \cdot h \cdot \left(\frac{C_{pu}}{\tan \beta}\right)^2 \frac{dh}{dt} \quad (3.19)$$

This makes the sectional added mass and its time derivative being functions of  $\beta$  and  $h$ . Both can be expressed as functions of  $x'$  in body-fixed coordinate as:

$$\beta = \beta(x') \quad (3.20)$$

$$\begin{aligned} h &= h(x') \\ &= z'_k + \left(\frac{z_G - x' \sin \theta}{\cos \theta}\right) - \frac{r}{\cos \theta} \end{aligned} \quad (3.21)$$

$$\begin{aligned} \dot{h} &= \dot{h}(x') \\ &= \frac{dh(x')}{dt} \\ &= \left(\frac{\left(\dot{z}_G - x' \cos \theta \dot{\theta}\right) + (z_G - x' \sin \theta) \sin \theta \dot{\theta}}{\cos^2 \theta}\right) - \left(\frac{\dot{r} \cos \theta + r \sin \theta \dot{\theta}}{\cos^2 \theta}\right) \end{aligned} \quad (3.22)$$

Where  $z'_k$  is the coordinate of the keel in ship-fixed coordinate system,  $r(x')$  and  $\dot{r}(x')$  are wave elevation and its time derivative at each time step respectively.

The expression of wave elevation and its time derivative, wave vertical orbital velocity and acceleration are functions of time and space. As the present calculation procedure is in each time step, the functions are reduced to be only space dependent in earth-fixed coordinate system  $x$  as follows:

$$r = r_0 \cos(kx - \omega t) \quad (3.23)$$

$$\dot{r} = -r_0(k\dot{x} + \omega) \sin(kx + \omega t) \quad (3.24)$$

$$w_w = r_0 \omega \sin(kx + \omega t) \quad (3.25)$$

$$\dot{w}_w = r_0 \omega(k\dot{x} + \omega) \cos(kx + \omega t) \quad (3.26)$$

Then, it can be elaborated into functions of space dependent in body-fixed coordinate system ( $x'$ ):

$$r(x') = r_0 \cos[k(x_G + x' \cos \theta - (z_G - x' \sin \theta) \tan \theta) + \omega t] \quad (3.27)$$

$$\dot{r}(x') = \frac{d}{dt} r(x') \quad (3.28)$$

$$w_w(x') = -r_0 \omega \sin[k(x_G + x' \cos \theta - (z_G - x' \sin \theta) \tan \theta) + \omega t] \quad (3.29)$$

$$\dot{w}_w(x') = \frac{d}{dt} w_w(x') \quad (3.30)$$

Substituting Equations 3.27 - 3.30 into Equations 3.18 - 3.19, the sectional added mass,  $m_a$  and its time derivative,  $\dot{m}_a$  are functions of only ship length coordinate at each instance (stopped time) as the rest of variables in Equations 3.20 - 3.22 are fixed, and subsequently updated at the next time step.

The additional lift term due to the cross-flow drag on the surface of a wedge penetrating into the water is expressed as:

$$f_{cfd} = C_{D,C} \cos \beta \rho b V^2 \quad (3.31)$$

Or in term of submergence as:

$$f_{cfd} = C_{D,C} \cos \beta \rho \left( \frac{C_{pu} h}{\tan \beta} \right) V^2 \quad (3.32)$$

Where  $C_{D,C}$  is sectional cross-flow drag coefficient with the value of 1.33 suggested by Keuning (1994).

Sectional buoyancy is expressed as:

$$f_b = a_{bf} \rho g A \quad (3.33)$$

With  $a_{bf}$  as sectional buoyancy coefficient. Its value is fixed at 0.5 as the simulations are always in towed condition with high Froude Number.

Finally, the drag force or frictional resistance is determined by:

$$D = \frac{1}{2} \rho C_F S_w U^2 \quad (3.34)$$

The frictional resistance is strongly dependent on three fully nonlinear parameters,  $U$ ,  $S_w$  and  $C_F$ . Wetted surface area is obtained by integrating sectional wetted curve along the ship length. Frictional coefficient is approximated by using ITTC 1957 correlation line. Note that the drag force has small influence in the equations of motions, as the system is reduced to two degrees of freedom implying towed condition. The horizontal component of drag does not affect to the response motions leaving only vertical component to do that role.

After evaluating the system of equations of motions by substituting the terms previously mentioned, it can be expressed in the following matrix forms:

$$M \cdot \ddot{\vec{x}} = \sum F \quad (3.35)$$

Thus:

$$\ddot{\vec{x}} = M^{-1} \cdot \sum F \quad (3.36)$$

Where:

$$\ddot{\vec{x}} = \begin{pmatrix} \ddot{z}_G \\ \ddot{\theta} \end{pmatrix} \quad (3.37)$$

As well as  $M$  and  $\sum F$  are matrices of mass and total forces minus terms associated to the motion accelerations.

For the further reference in this thesis, the system of equations of motions is fully developed in Appendix A with coefficient assignments to be referred in further contents.

The desired results of the present project are time histories of ship's displacements, velocities and accelerations. The system of equations of motions derived in the previous section gives firstly, the ship's accelerations for a given time step. This can lead to the velocities and consequently the displacements by time marching integration of equations of motions according to the dynamic principle. Generally, an equation of motions in a dynamical process appears to be "Linear 2<sup>nd</sup> Order Non-Homogeneous Ordinary Differential Equations" with time as principal variable. This can be solved simply by analytical solutions which is that so-called "Exact Solutions". Nevertheless, the present mathematical model is instead the fully nonlinear one; the exact solutions are mostly impossible to deal with. The only way to solve this kind of ODE is by using numerical analysis. However, the numerical analysis can only give an approximation of exact solutions always with unavoidable errors. Therefore, it is essential to select the most suitable numerical methods, in order to minimize these errors.

The explanation about the choices of numerical integration methods is presented. Other numerical methods such as numerical differentiation used in each particular term in the equations of motions are explained in detail in Appendix A. All of the numerical methods are verified in order to be appropriately selected. Once the model is verified, it is validated with some existing experimental data which will be explained in the further sections.

### **3.3 Verification of the Mathematical Model**

Due to its fundamental behaviours, the present mathematical model is considered as a dynamic process. Verification for such a process consists of analysing the relevant controlling parameters influenced on performance of the mathematical model, leading also to the adequate selection of numerical methods. To fulfil this aim, "Hypothesis of Accuracy of Time Histories" is proposed.

#### **3.3.1 Hypothesis of Accuracy of Time Histories**

Supposing that, when a mathematical model has been created to simulate a physical phenomenon, an ideal condition can be explained by a corresponding mathematical expression and by adding some environmental factors, the reality can be simulated with accuracy. The first process of the dynamic phenomenon is to evaluate the total force acting on an object and consequently, the acceleration caused by that force is found. The following process is to evaluate the corresponding velocity and displacement knowing the acceleration by integration over time. In all dynamic physical phenomena, the force



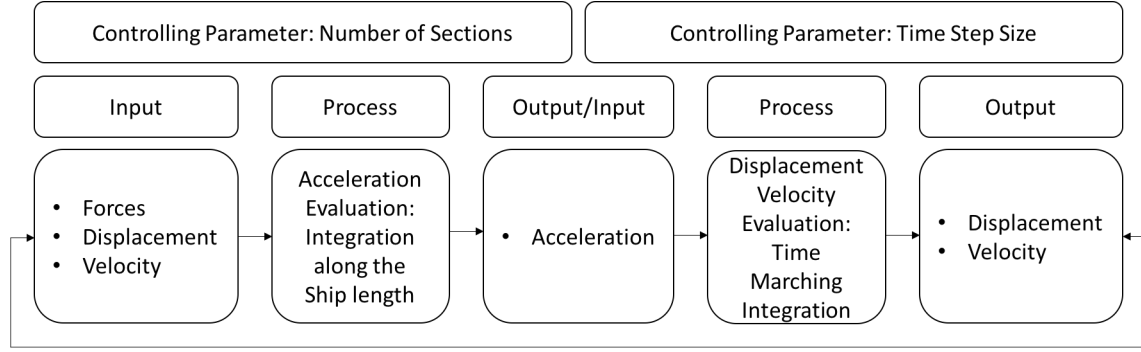


Figure 3.3: Dynamic process in the present mathematical model.

acting on the object at each instant is state-space dependent. This implies that if the velocity and displacement at each instant are not adequately evaluated, the force and acceleration corresponding to the next will be inaccurate. Similar to the process of evaluating force and acceleration, if they are not accurately defined, the effect will be an inaccurate velocity and displacement. The time history resulting from an inaccurate mathematical model will produce an inaccurate time history and will not converge if the parameters of accuracy are not appropriately applied.

The “**Hypothesis of Accuracy of Time Histories**” is defined as that, when increasing the resolution of controlling parameters influenced in the dynamical process, resulting time histories should converge to a single asymptote value. As the exact solution is not available, the results obtained by using maximum resolution parameters are taken as the “**highest fidelity**” or “**superior data**” corresponding to that asymptote. The dynamic process corresponding to the present mathematical model is explained in Figure 3.3. The controlling parameter influenced in force and acceleration evaluation is the resolution of hull sections or **Number of Sections**,  $N_s$ . Then, the other influenced in velocity and displacement evaluation in time flowing step is **Time Step Size**,  $\Delta t$ .

### 3.3.2 Pressure Distribution Evaluation

The present mathematical model is an implementation to the original Zarnick (1978)’s work that allows the pressure distribution to be represented by mathematical model rather than experimental results (see Figure 3.4). Once receiving the data of accelerations, velocities and displacements at each instant as input data, evaluation of sectional forces along the hull length is carried out. In other words, it is the representation of particular sectional force along the length.

As it can be seen in Figures 3.5 - 3.6, the pressure distribution is accounted only in locations where particular sections are under the water surface. The integral evaluation along the hull length appears not to be constantly evaluable considering the physical

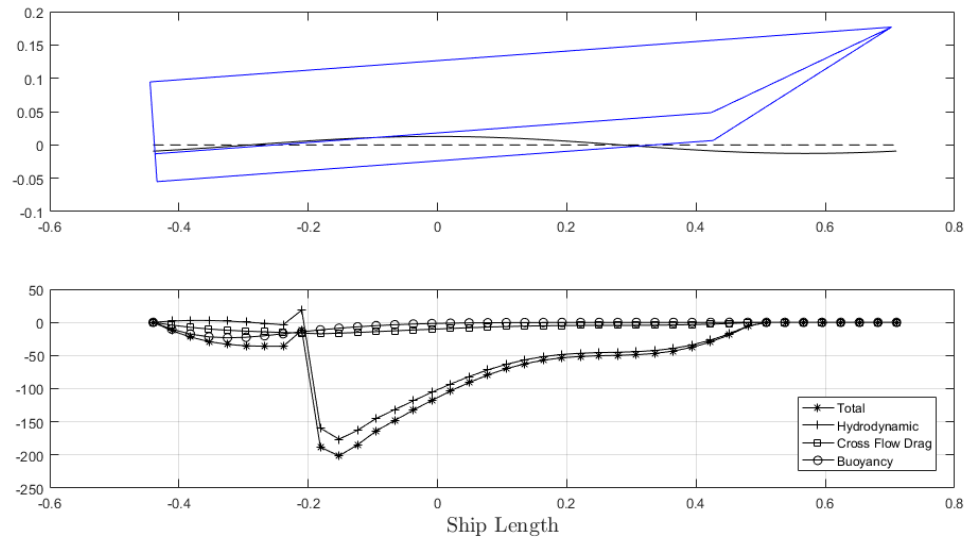


Figure 3.4: Pressure distribution along the ship length.

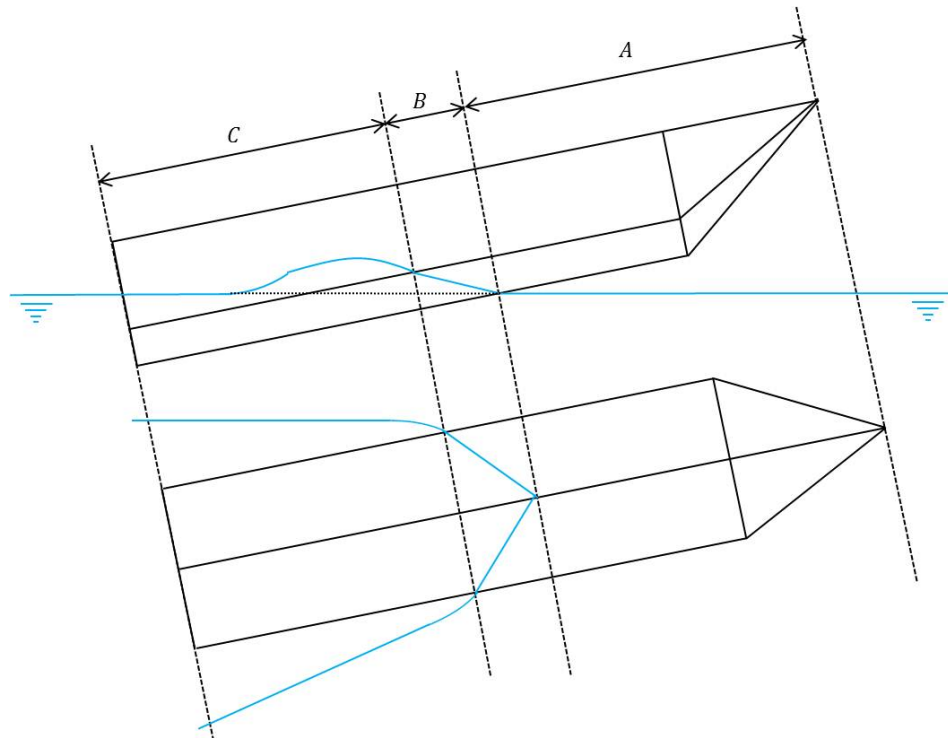


Figure 3.5: Flow - hull characteristic zones (longitudinal).

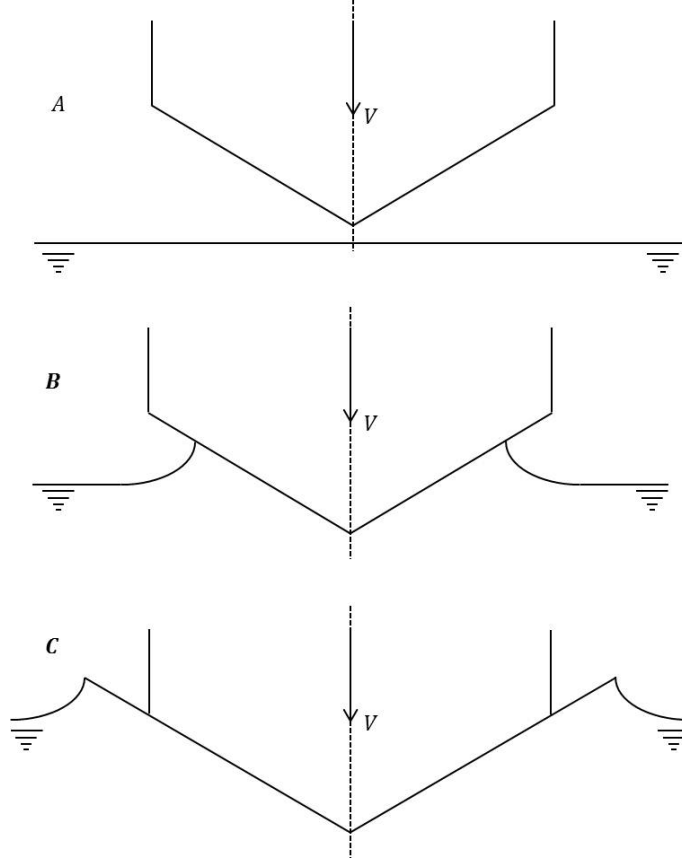


Figure 3.6: Flow-hull characteristic (transverse).

characteristic of particular sectional flow. Following [Martin \(1976a\)](#), [Zarnick \(1978\)](#), and [Akers \(1999\)](#), the flow characteristic can be divided into three zones:

- Zone A: Dry keel.
- Zone B: Wetted keel but dry chine.
- Zone C: Wetted chine.

The largest magnitude of each component takes place in zone B due to the strong rate of change of fluid momentum. In calm water case, the last term of sectional hydrodynamic force expression (Equation 3.10) plays a very important role as the other terms are of small magnitude due to its steady state situation. Moreover, by the influence of  $C_{tr}$ , all of the force components die out to zero at the transom as the consequence of flow separation.

### 3.3.3 Methodologies of Convergence Analysis and Optimization Consideration

In order to analyse the convergence of resulting time histories, root mean square errors, RMSE, of a pair of data between each actual and the highest fidelity data are evaluated. This result should show the points of corresponding value of the controlling parameters where the time histories begin to converge, as their RMSE should be as small as possible. Firstly, the heave and pitch responses are normalized by wave height,  $H$  and  $2\pi H/\lambda$  respectively, while CG and bow accelerations are normalized by the gravity. Then, every time history corresponding to different pairs of  $N_s$  and  $\Delta t$  are compared to the highest fidelity data, in order to calculate RMSE. Then, by following the definition of Hypothesis of Accuracy of Time Histories, when increasing or decreasing both  $N_s$  and  $\Delta t$ , RMSE should decrease and converge to an asymptote implying the accuracy of time histories.

Apart from the consideration of small RMSE, computation time is also considered in order to determine the optimal use of the model. As the advantage of the present methodology (Strip Theory + Wedge Water Entry) is the economic time consumption in calculation, **Pareto Efficiency Analysis** will be used in further contents of this thesis when considering computational time,  $T_c$  together with RMSE of time histories to find the optimal controlling parameters. The objective functions of the actual consideration are minimizing computational time and minimizing RMSE comparing to the highest fidelity data. The pairs of objective functions in the Pareto Front of optimal time consumption and accuracy will represent and reflect back to the pairs of controlling parameters,  $N_s$  and  $\Delta t$ .

### 3.3.4 Time Integration Numerical Solvers Verification

The simulations are set to perform using corresponding static stability conditions as initial conditions. The planing models are moving with a constant forward speed (towed condition). This condition does not exist in reality due to the fact that when an object is starting to move, a corresponding acceleration is applied to bring the object to achieve that desired velocity. If the object suddenly commences to move from the repose condition to a velocity, a large acceleration is applied and the problem is therefore of an impulsive start. This causes an extreme response motions but later it can restore to set itself to the equilibrium. Once all parameters at the present time step are obtained (stopped time process), in order to continue the simulation to the next time step, the acceleration of present time step needs to be integrated to evaluate velocity and displacement. The equations of motions are classified as  $2^{nd}$  order non-homogeneous ODE. This kind of equations can be solved numerically by several methods. The choices of numerical method such as Euler, Predictor-corrector and several kinds of Runge-Kutta

methods are analysed in order to compare with the numerical method used by [Zarnick \(1978\)](#) and deduce the optimal one.

### 3.3.4.1 Fixed Step Solver and Variable-Step Solver

A dynamical system is simulated by computing its states at successive time steps over a specified time span, using information provided by the model. The size of this time interval is called the step size. The process of computing the successive states of a system from its model is known as solving the model. No single method of solving a model suffices for all systems. Accordingly, a set of programs, known as solvers, is provided that each embody a particular approach to solving a model. Solvers are broadly classified using these criteria:

- The type of step size used in the computation:
  - Fixed-step solvers solve the model at a single step size from the beginning to the end of simulation. The step size can be specified or let the solver choose the step size. Generally, decreasing the step size increase the accuracy of the results and increases the time required to simulate the system.
  - Variable-step solvers vary the step size during the simulation, they change the step size to maintain accuracy as the state of a model changes. Computing the step size adds to the computational overhead at each step. However, it can reduce the total number of steps, and hence the simulation time required to maintain a specified level of accuracy for models with piecewise continuous or rapidly changing states.
- The nature of states in the model:
  - Continuous solvers use numerical integration to compute continuous states of a model at the current time step based in the states at previous time steps and the state derivatives. Continuous solvers rely on individual blocks to compute the values of the discrete states of the model at each time step.
  - Discrete solvers are primarily for solving purely discrete models. They compute only the next simulation time step for a model. When they perform this computation, they rely on each block in the model to update its individual discrete state. They do not compute continuous states.

Fundamentally, the use of variable step solver is necessary as the convergence of simulations can be proved by it. Originally, [Zarnick \(1978\)](#) used variable step Runge-Kutta-Merson solver to evaluate time histories of response motions and accelerations. The maximum initial time step size he used was 0.1 s and halved it constantly until the tolerance was small (around 1%) and converged. In order to prove the convergence of

Table 3.1: Convergence criteria of variable steps solver.

$\Delta t_i$ (s)	$\epsilon$
0.100	> 10%
0.050	5% - 10%
0.025	2% - 5%
0.020	< 1%
0.010	< 1%

the present mathematical model, a series of simulations are carried out. A particular hull configuration and sea condition is evaluated varying number of section  $N_s$ , initial time step size  $\Delta t_i$  and maximum tolerance  $\epsilon$ . The results of simulations are summarized in Table 3.1.

It can be seen that when  $\Delta t_i < 0.01$  s, the tolerance is smaller than 1% in any step, in other words, the simulation converges with  $\Delta t_i$  without iterating to the smaller  $\Delta t$  within that corresponding step. This leads to the deduction that when using  $\Delta t < 0.01$  s, Runge-Kutta family solver gives converged results and are equivalent to fixed step solver. The detail of accuracy of this solver is explained in the following section.

In summary, the variable step solver allows an analysis of convergence within the actual time history. The fixed step solver leads to the next level of convergence analysis that is a convergence between different time histories of the same sea condition but varying controlling parameters.

### 3.3.4.2 Comparison and Verification of Time Integration Methods

Several numerical time marching integration are compared in order to find the most appropriate as well corresponding  $\Delta t$ . These methods are:

- Adam's predictor-corrector method: PCA.
- Euler's predictor-corrector method: PCE.
- Runge-Kutta method: RK.
- Runge-Kutta-Merson method: RKM.
- Runge-Kutta-Fehlberg method: RKF.

The detailed algorithm are explained in Appendix B. The optimal ones should be that of the least time consumption and accurately convergence. The hull chosen to be simulated is of  $\beta = 20^\circ$ . It is towed freely to heave and pitch with constant forward speed of  $V/\sqrt{L} = 6.0$ . The simulations are carried out by five different numerical integration

methods and five different  $\Delta t$ ; 0.01 s, 0.002 s, 0.001 s, 0.0005 s and 0.0002 s. As the exact analytical solution for this kind of equations of motions does not exist, the criteria of convergence is supposed to be that, by decreasing time step size, time history results should converge to an asymptote.

### 3.3.4.3 Influence of Time Step Size: $\Delta t$

Figures 3.7 - 3.8 represent samples of time histories of normalized response motions and impact accelerations of different time step sizes and integration methods. The normalization consists of dividing the response motions by the wave height. While in the same manner, the accelerations are normalized by the gravity. The simulations have been carried out again for a planing model of  $\beta = 20^\circ$  and  $V/\sqrt{L} = 6.0$ . Actually, the verification is focusing on the influence of  $\Delta t$ , as  $N_s$  is supposed to be appropriate enough to give the accurate total force.

First of all, time histories of results from three different Runge-Kutta methods and two predictor-corrector methods are analysed statistically and presented in Figure 3.10. As it can be seen, the standard deviation of heave maxima calculating by Runge-Kutta family methods are small, although it is larger when using  $\Delta t = 0.01$  s, the rest of  $\Delta t$  have similar standard deviation and also the other statistics. While the standard deviation of motions obtained by predictor-corrector methods are significantly larger than the Runge-Kutta ones. This could imply less stability when using predictor-corrector method with larger  $\Delta t$ . The Runge-Kutta methods give the convergence when  $\Delta t < 0.002$  s is used. In summary, when varying controlling parameters, the results get closer to the values when using the highest resolution (smallest  $\Delta t$ ).

Then the time histories of results are compared by mean of RMSE analysis. The reference values for RMSE are deduced from statistical analysis to be those when using the highest resolution of controlling parameters, as it can be seen from a sample of heave maxima analysis in Figure 3.10. The error metrics of the normalized heave are represented in Figure 3.9.

Once the optimum numerical integration is chosen to be Runge-Kutta methods, computational times in simulation varying both controlling parameters ( $N_s$  and  $\Delta t$ ) are shown in Table 3.2 using a personal computer (1.7GHz Intel Core i7, 8GB 1600MHz DDR3 RAM). The data is represented in the amount of times of the least duration or computational time ratio,  $T_{cs} = T_c/T_{cmin}$ . The most influential parameter in computational time is  $\Delta t$ . It can be seen that for any  $\Delta t$ , the largest  $N_s$  consumes less computational time than the smallest  $N_s$  for the next smaller  $\Delta t$ . Note that the computational language used in the present research is MATLAB (Versions 2012 - 2016), using other languages could also affect to computational times depending on the mechanism of the languages.

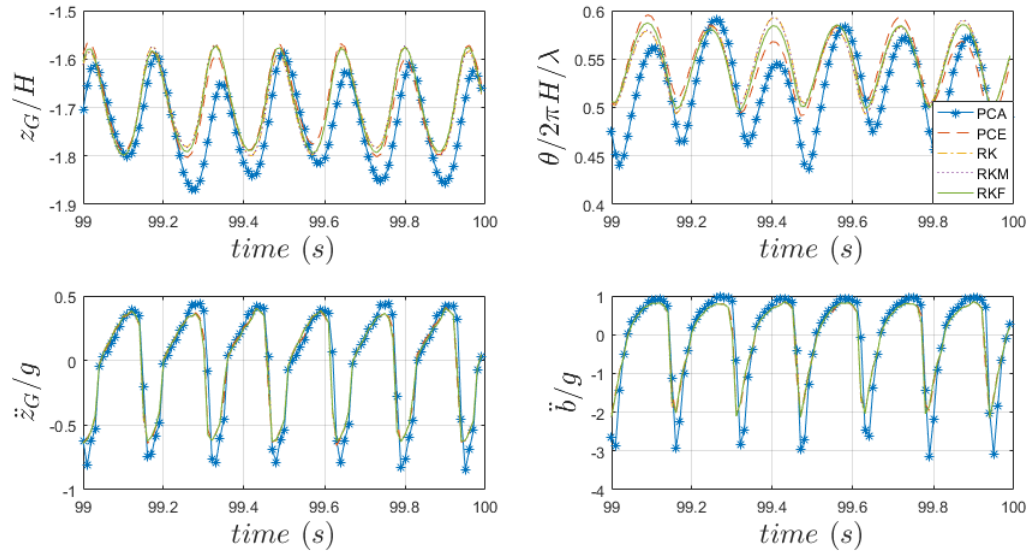


Figure 3.7: Time histories of accelerations and motions using different solvers with  $\Delta t = 0.01$  s.

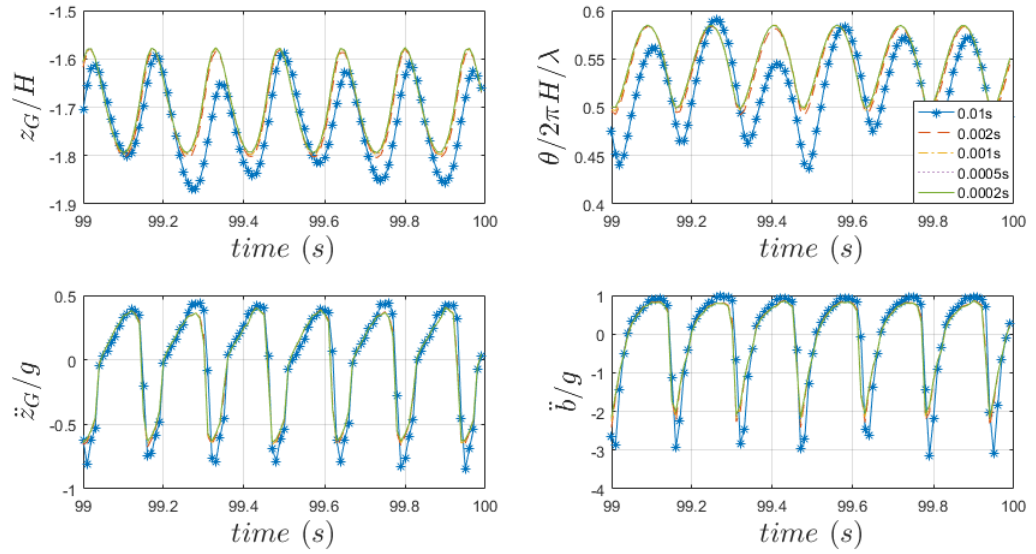


Figure 3.8: Time histories of accelerations and motions using PCA solvers with different  $\Delta t$ .

Table 3.2: Computational times of Runge-Kutta integration methods varying  $N_s$  and  $\Delta t$ .

$N_s / \Delta t(s)$		0.01	0.002	0.001	0.0005	0.0002
40	$T_{cs} = 1.00$	4.64	9.20	19.10	47.97	
80		1.04	4.82	9.55	20.01	49.53
120		1.07	5.00	9.96	20.52	51.33
160		1.10	5.17	10.28	21.14	52.94
200		1.12	5.30	10.97	21.85	54.54



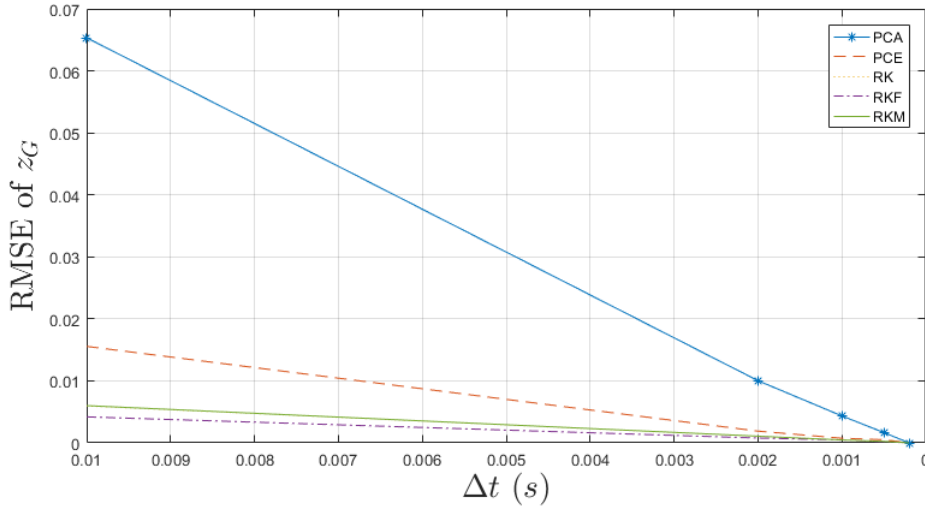


Figure 3.9: Error metrics representation of normalized heave motion comparing different integration methods.

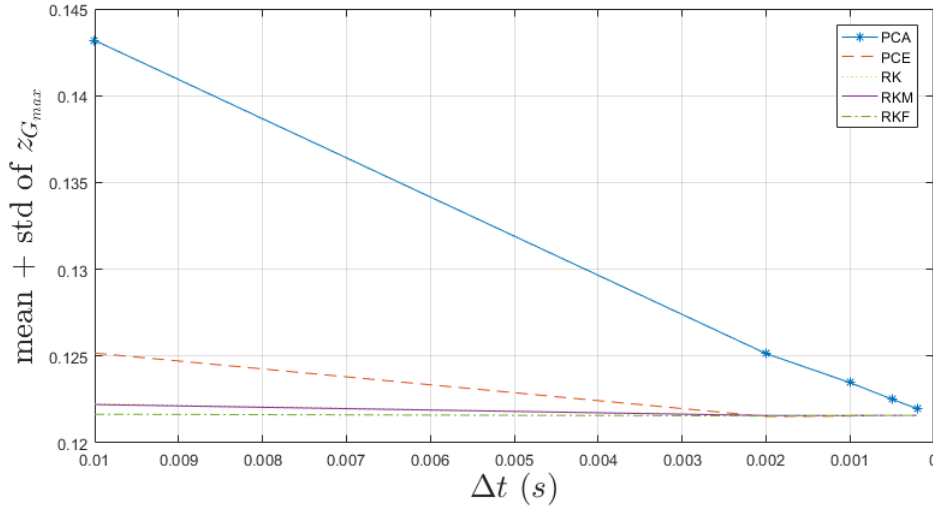


Figure 3.10: Statistical representation of normalized heave motion comparing different integration methods.

### 3.3.5 Limitations and Optimization of Mathematical Model in Time History Evaluations

The case of moderate deadrise hull has been used to verify the effectiveness of time marching integration. Nevertheless, though the optimal  $\Delta t$  is known, it cannot guarantee the accuracy of time history if the force is not evaluated accurately. Influence of controlling parameter involved in a certain time step which is  $N_s$  is analysed focusing on sectional added mass and its derivative terms, as it is the most predominant component of the overall hydrodynamic forces. Note that the terms  $m_a$ ,  $\dot{m}_a$  associated and  $\partial m_a / \partial x'$

associated are represented in form of the integral coefficients  $C_A$ ,  $C_E$  and  $C_F$  defined in Appendix A.

### 3.3.5.1 Influence of Number of Sections: $N_s$ on Sectional Added Mass and Its Associated Terms

The distribution of sectional added mass and its associated terms along the ship length (of  $\beta = 10^\circ$ ,  $20^\circ$  and  $30^\circ$ ) evaluated by different  $N_s$  are presented in Figure 3.11. It shows that the distribution curves using small  $N_s$  (continuous curves) do not fit the to other using larger  $N_s$ , especially the case of  $\beta = 10^\circ$ . Also it can be seen that the distribution of  $\dot{m}_a$  is zero when  $m_a$  is constant. This implies that the sudden change of  $\dot{m}_a$  from zero to a high value causes a sharply discontinuous function. The function of the distribution is represented numerically by a discrete function. The main cause of variation of this function (varying  $N_s$ ) is that if the discrete points corresponding to a certain  $N_s$  do not fit closely to the sharp points of the distribution, the discrete representation will not be accurately defined. Consequently, when being multiplied by the component of relative velocity perpendicular to the keel,  $V$ , the effect of magnitude of this product is magnified. Due to the dependency of wave vertical orbital velocity,  $w_w$ , in any instant that a particular section hits the position corresponding to high  $w_w$ , the order of magnitude of  $C_E$  will be extremely high compared with  $C_F$ . Obviously if the distribution functions are not evaluated appropriately, the integral or the area under the distribution ( $C_A$ ,  $C_E$  and  $C_F$ ) will not be obtained accurately. Considering the principle of strip theory, each particular section is considered as a wedge penetrating into calm water with different local relative velocity to the water level. In case of short wavelength and large wave amplitude (large wave slope), if  $N_s$  is not sufficiently large, the distribution of any terms along the ship length will be inaccurate. While in the case of small wave slope, this occurrence does not happen due to the smoothness of relative impact phenomenon. Regarding the influence of deadrise angle,  $\beta$ , the cases of moderate and large  $\beta$  suffer small effect of variation of  $N_s$ , due to the fact that the vertical projection distance from the keel to the chine is sufficiently far. This could avoid the sudden and frequent flow separation that causes the sharp discontinuous distribution and consequently the associated derivative. While in the case of small  $\beta$ , the discontinuous distribution is unavoidable and requires larger  $N_s$  in order to achieve the better fit of the distribution.

### 3.3.5.2 Influence of Number of Sections: $N_s$ and Time Step Size: $\Delta t$ in Full Time History Evaluations

The analysis of influence of  $N_s$  in stopped time has been done previously. In order to prove the hypothesis of accuracy of time histories, the full length of time histories of the results will be explained in term of  $N_s$  and  $\Delta t$ . The planing hull models of constant

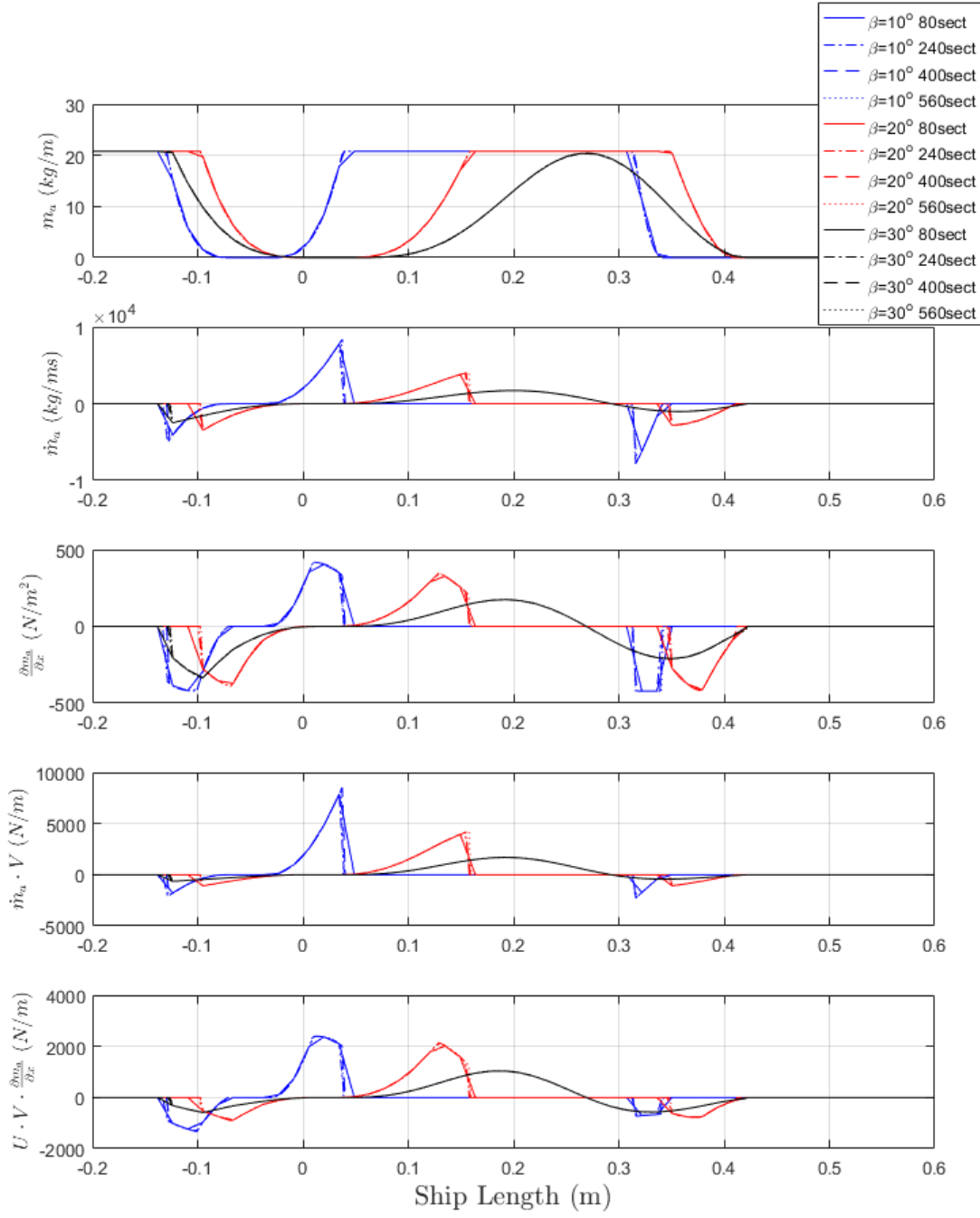


Figure 3.11: Variation of sectional added mass and its associated terms with different  $N_s$  along the ship length.

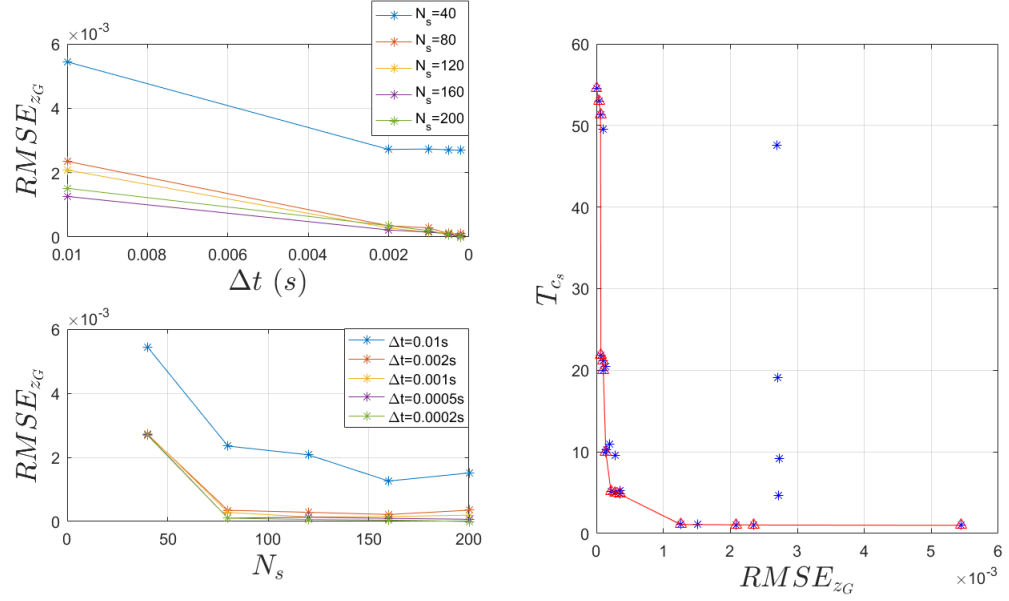


Figure 3.12: Error metrics of time histories and Pareto front line of heave motion of planing hull model  $\beta = 20^\circ$ ,  $\lambda/L = 4.0$ ,  $H/B = 0.1$ .

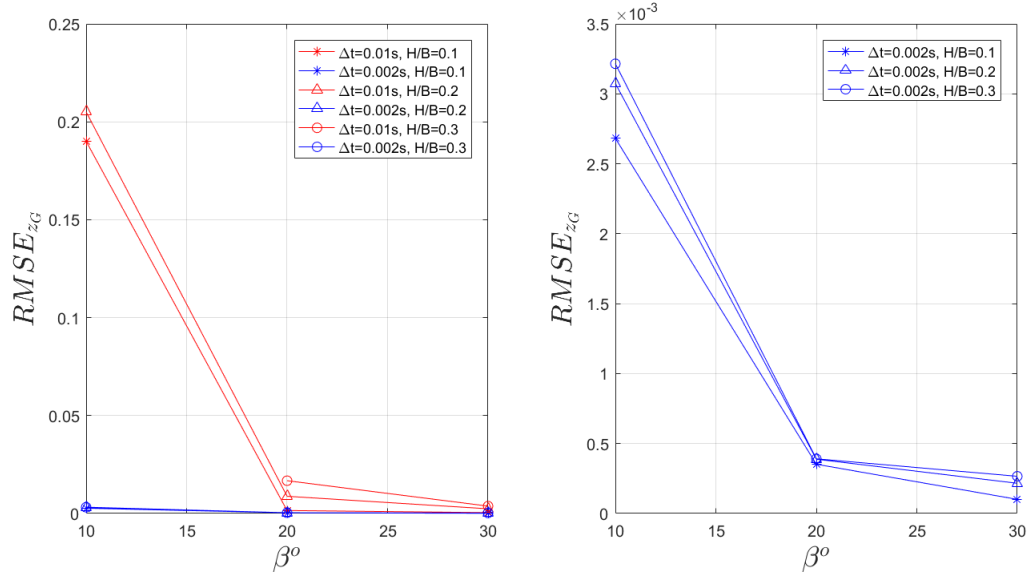


Figure 3.13: Comparison of  $RMSE_{z_G}$  of different  $\beta$  and  $H/B$  at  $\lambda/L = 4.0$  with  $N_s = 200$ .

10, 20 and 30 degrees deadrise angles are simulated by the present mathematical model in regular waves varying wavelength between  $\lambda/L = 1.0$  and  $\lambda/L = 6.0$  and wave amplitudes between  $H/B = 0.1$  and  $H/B = 0.3$  in order to verify limitations and accuracy of the model. The results of response motions and accelerations are analysed in the same manner used in time marching integration analysis. Samples of statistical analysis and the comparison of error metrics are shown in Figure 3.12.

Similar to the verification of time integration methods, the reference data for RMSE

metrics are when using highest resolution controlling parameters. It can be deduced that for  $\beta = 20^\circ$  and  $\beta = 30^\circ$  hulls, the response motions and accelerations can be predicted with good accuracy using any  $N_s$  with  $\Delta t < 0.002$  s in the whole range of wavelength and wave amplitudes. Although some larger errors happen in the zone of natural frequency, in which RMSE of the responses is significantly high when using any  $N_s$  with  $\Delta t = 0.01$  s comparing to the other using smaller  $\Delta t$ . In other words,  $N_s$  has a small influence in the convergence when  $\Delta t < 0.002$  s, although some notable differences of RMSE can be observed between the cases of  $N_s = 40$  and  $N_s = 80$ . On the other hand, as mentioned in Section 3.3.4.3, when considering computational time issue, using  $\Delta t = 0.01$  s with larger  $N_s$  gives similar order accuracy but slightly increases calculation time.

While in the case of  $\beta = 10^\circ$ , in high frequency waves and large wave amplitudes, the response motions are irregular with constant frequency (equal to frequency of encounter) and do not fit one to each other when varying  $N_s$ . This implies the inaccuracy of force prediction and consequently, an un-identical (un-fit) time history. Nevertheless, time histories when using larger  $N_s$  and smaller  $\Delta t$  are closer to each other and imply that the case of  $\beta = 10^\circ$ , higher resolution in integration along the ship length and over the time is necessary in order to achieve accurately the total force acting on the hull. To represent this fact, Figure 3.13 shows the comparison of  $RMSE_{z_G}$  using  $\Delta t = 0.01$  s and  $\Delta t = 0.002$  s in different  $\beta$  and  $H/B$ . It can be seen that when using  $\Delta t < 0.002$  s, time histories convergence appears to fit better although it is not quantitatively the same as in the cases of  $\beta = 20^\circ$  and  $\beta = 30^\circ$ . Due to the fact that when using large  $\Delta t$ , the peaks of accelerations would not be detected, consequently, velocities and motions would not be precisely integrated.

In some circumstance, this effect is small, as the peak acceleration duration is small, the motions can be also considered as a slight fluctuation. Moreover, when simulating in the zone of natural frequency, this case cannot be completed using low-resolution integrations. With small  $N_s$ , the total force evaluated appears to be of exaggerated order and with large  $\Delta t$ ; the acceleration lasts too long and resulting inappropriate velocity and displacement.

Nevertheless, note that the discrete variation of  $\Delta t$  shifts significantly between the first and the second point ( $\Delta t = 0.01$  s to  $\Delta t = 0.002$  s). As the overall convergence appears appropriately at the second point ( $\Delta t = 0.002$  s), it is of interest and recommended to further investigate the influence of  $\Delta t$  in convergence between those points, and consequently, a more economic computational time could be achieved.

### 3.3.5.3 Optimal Parameters for Time History Simulations

In order to deduce the optimal parameters for the simulations by the present mathematical model, it is essential to consider the accuracy (RMSE) of the calculation together with the computational time. Tables 3.3 - 3.8 represent the accuracy by mean of RMSE, alongside with the computational time ratio,  $T_{cs}$ . The LHS of each particular cell of the tables shows  $T_{cs}$  as shown in Table 3.2 and the RHS shows the magnitude order of RMSE. The optimal parameters are analysed by mean of Pareto Efficiency. Sample of Pareto Line representation is presented graphically together with RMSE in Figure 3.12. Two objective functions are applied. The first one is minimizing RMSE. As in order to fulfil the hypothesis of accuracy of time histories, RMSE of time histories need to be minimized. The other is minimizing computational time:

$$RMSE_{min} = f(N_s, \Delta t) \quad (3.38)$$

$$T_{c_{min}} = g(N_s, \Delta t) \quad (3.39)$$

The points on the front's line show the optimal pair of RMSE and  $T_{cs}$  that leads to the pair of  $N_s$  and  $\Delta t$  as shown in Tables 3.3 - 3.8 respectively. In cases of  $\beta = 20^\circ$  and  $\beta = 30^\circ$ , the optimal parameters can be obtained at the point where  $T_{cs}$  is small and decreasing  $\Delta t$  does not increase significantly the accuracy (decreasing RMSE). While in cases of  $\beta = 10^\circ$ , the acceptable accuracy (where the convergence occurs) is seen at the points where  $T_{cs}$  is considerably high.

In summary, the overall optimal selection of controlling parameters considering the same order of accuracy ( $10^{-4}$  of RMSE) can be deduced as follows:

- For  $\beta = 10^\circ$ :
  - $N_s > 200$  and  $\Delta t < 0.0005$  s when  $H/B = 0.1$ .
  - $N_s > 120$  and  $\Delta t < 0.0002$  s when  $H/B = 0.2$ .
  - $N_s > 120$  and  $\Delta t < 0.0002$  s when  $H/B = 0.3$ .
- For  $\beta = 20^\circ$ ,  $N_s > 80$  and  $\Delta t < 0.002$  s in all of sea conditions.
- For  $\beta = 30^\circ$ ,  $N_s > 80$  and  $\Delta t < 0.002$  s in all of sea conditions.

However, some particular considerations could be made when accuracy issue is of higher importance than computational time.

Table 3.3: RMSE VS  $T_{cs}$  of planing hull model  $\beta = 20^\circ$ ,  $\lambda/L = 4.0$ ,  $H/B = 0.1$ .

$\Delta t(s)$	0.01		0.002		0.001		0.0005		0.0002	
$N_s$	RMSE	Tcs	RMSE	Tcs	RMSE	Tcs	RMSE	Tcs	RMSE	Tcs
40	<b>0.005442</b>	<b>1.00</b>	0.002721	4.64	0.002734	9.20	0.002709	19.10	0.002690	47.55
80	<b>0.002352</b>	<b>1.04</b>	<b>0.000349</b>	<b>4.82</b>	0.000283	9.55	<b>0.000103</b>	<b>20.01</b>	0.000101	49.53
120	<b>0.002081</b>	<b>1.07</b>	<b>0.000286</b>	<b>5.00</b>	<b>0.000141</b>	<b>9.96</b>	0.000133	20.52	<b>0.000062</b>	<b>51.33</b>
160	<b>0.001261</b>	<b>1.10</b>	<b>0.000218</b>	<b>5.17</b>	0.000151	10.28	<b>0.000096</b>	<b>21.14</b>	<b>0.000041</b>	<b>52.94</b>
200	0.001514	1.12	0.000352	5.30	0.000197	10.97	<b>0.000068</b>	<b>21.85</b>	<b>0.000000</b>	<b>54.54</b>

Table 3.4: RMSE VS  $T_{cs}$  of planing hull model  $\beta = 20^\circ$ ,  $\lambda/L = 4.0$ ,  $H/B = 0.3$ .

$\Delta t(s)$	0.01		0.002		0.001		0.0005		0.0002	
$N_s$	RMSE	Tcs	RMSE	Tcs	RMSE	Tcs	RMSE	Tcs	RMSE	Tcs
40	<b>0.015650</b>	<b>1.00</b>	<b>0.001110</b>	<b>4.64</b>	0.000767	9.20	0.000466	19.10	0.000395	47.55
80	<b>0.015617</b>	<b>1.04</b>	<b>0.000770</b>	<b>4.82</b>	<b>0.000333</b>	<b>9.55</b>	0.000294	20.01	0.000214	49.53
120	<b>0.014897</b>	<b>1.07</b>	<b>0.000516</b>	<b>5.00</b>	0.000351	9.96	<b>0.000172</b>	<b>20.52</b>	<b>0.000131</b>	<b>51.33</b>
160	<b>0.014671</b>	<b>1.10</b>	0.000604	5.17	<b>0.000299</b>	<b>10.28</b>	<b>0.000151</b>	<b>21.14</b>	<b>0.000073</b>	<b>52.94</b>
200	0.016741	1.12	<b>0.000391</b>	<b>5.30</b>	<b>0.000249</b>	<b>10.97</b>	<b>0.000147</b>	<b>21.85</b>	<b>0.000000</b>	<b>54.54</b>

Table 3.5: RMSE VS  $T_{cs}$  of planing hull model  $\beta = 30^\circ$ ,  $\lambda/L = 4.0$ ,  $H/B = 0.1$ .

$\Delta t(s)$	0.01		0.002		0.001		0.0005		0.0002	
$N_s$	RMSE	Tcs	RMSE	Tcs	RMSE	Tcs	RMSE	Tcs	RMSE	Tcs
40	<b>0.001294</b>	<b>1.00</b>	<b>0.000341</b>	<b>4.64</b>	0.000287	9.20	0.000274	19.10	0.000263	47.55
80	<b>0.000641</b>	<b>1.04</b>	<b>0.000163</b>	<b>4.82</b>	<b>0.000092</b>	<b>9.55</b>	0.000068	20.01	0.000057	49.53
120	0.000942	1.07	<b>0.000104</b>	<b>5.00</b>	<b>0.000061</b>	<b>9.96</b>	<b>0.000040</b>	<b>20.52</b>	<b>0.000020</b>	<b>51.33</b>
160	<b>0.000462</b>	<b>1.10</b>	0.000113	5.17	0.000066	10.28	<b>0.000035</b>	<b>21.14</b>	<b>0.000012</b>	<b>52.94</b>
200	<b>0.000444</b>	<b>1.12</b>	<b>0.000101</b>	<b>5.30</b>	<b>0.000053</b>	<b>10.97</b>	<b>0.000030</b>	<b>21.85</b>	<b>0.000000</b>	<b>54.54</b>

Table 3.6: RMSE VS  $T_{cs}$  of planing hull model  $\beta = 30^\circ$ ,  $\lambda/L = 4.0$ ,  $H/B = 0.3$ .

$\Delta t(s)$	0.01		0.002		0.001		0.0005		0.0002	
$N_s$	RMSE	Tcs	RMSE	Tcs	RMSE	Tcs	RMSE	Tcs	RMSE	Tcs
40	<b>0.003965</b>	<b>1.00</b>	<b>0.000573</b>	<b>4.64</b>	0.000516	9.20	0.000510	19.10	0.000471	47.55
80	0.004004	1.04	<b>0.000364</b>	<b>4.82</b>	<b>0.000236</b>	<b>9.55</b>	<b>0.000118</b>	<b>20.01</b>	0.000073	49.53
120	<b>0.003910</b>	<b>1.07</b>	<b>0.000296</b>	<b>5.00</b>	<b>0.000194</b>	<b>9.96</b>	<b>0.000114</b>	<b>20.52</b>	0.000063	51.33
160	<b>0.003791</b>	<b>1.10</b>	<b>0.000267</b>	<b>5.17</b>	<b>0.000127</b>	<b>10.28</b>	<b>0.000062</b>	<b>21.14</b>	<b>0.000055</b>	<b>52.94</b>
200	0.003779	1.12	<b>0.000266</b>	<b>5.30</b>	0.000167	10.97	0.000091	21.85	<b>0.000000</b>	<b>54.54</b>

Table 3.7: RMSE VS  $T_{cs}$  of planing hull model  $\beta = 10^\circ$ ,  $\lambda/L = 4.0$ ,  $H/B = 0.1$ .

$\Delta t(s)$	0.01		0.002		0.001		0.0005		0.0002	
$N_s$	RMSE	Tcs	RMSE	Tcs	RMSE	Tcs	RMSE	Tcs	RMSE	Tcs
40	<b>0.174615</b>	<b>1.00</b>	<b>0.010175</b>	<b>4.64</b>	0.012185	9.20	0.010637	19.10	0.011180	47.55
80	<b>0.138059</b>	<b>1.04</b>	<b>0.004790</b>	<b>4.82</b>	0.002970	9.55	0.002167	20.01	0.002354	49.53
120	0.216803	1.07	<b>0.003222</b>	<b>5.00</b>	<b>0.001630</b>	<b>9.96</b>	0.001166	20.52	0.000711	51.33
160	<b>0.135081</b>	<b>1.10</b>	<b>0.002700</b>	<b>5.17</b>	<b>0.001443</b>	<b>10.28</b>	<b>0.000756</b>	<b>21.14</b>	<b>0.000297</b>	<b>52.94</b>
200	0.190055	1.12	<b>0.002682</b>	<b>5.30</b>	<b>0.001038</b>	<b>10.97</b>	<b>0.000451</b>	<b>21.85</b>	<b>0.000000</b>	<b>54.54</b>

Table 3.8: RMSE VS  $T_{cs}$  of planing hull model  $\beta = 10^\circ$ ,  $\lambda/L = 4.0$ ,  $H/B = 0.3$ .

$\Delta t(s)$	0.01		0.002		0.001		0.0005		0.0002	
$N_s$	RMSE	Tcs	RMSE	Tcs	RMSE	Tcs	RMSE	Tcs	RMSE	Tcs
40			<b>0.004235</b>	<b>4.64</b>	<b>0.002654</b>	<b>9.20</b>	0.001719	19.10	0.001588	47.55
80			<b>0.003737</b>	<b>4.82</b>	<b>0.001798</b>	<b>9.55</b>	<b>0.000790</b>	<b>20.01</b>	<b>0.000333</b>	<b>49.53</b>
120			<b>0.003153</b>	<b>5.00</b>	<b>0.000991</b>	<b>9.96</b>	<b>0.000540</b>	<b>20.52</b>	0.000344	51.33
160			0.003311	5.17	0.001095	10.28	<b>0.000511</b>	<b>21.14</b>	<b>0.000222</b>	<b>52.94</b>
200			0.003215	5.30	<b>0.000902</b>	<b>10.97</b>	<b>0.000363</b>	<b>21.85</b>	<b>0.000000</b>	<b>54.54</b>

### 3.3.5.4 Effects on Variable Deadrise Angles Hull

Practically, the constant  $\beta$  hull is not widely applicable and leads to poor characteristics when navigating in calm water. Moreover, for planing application in waves, variable  $\beta$  hull appears to be more realistic and give better performance. Comparing to the planing hull models based on Fridsma (1969)'s experiments that are of constant  $\beta$  with the prismatic body occupies more than 80% of the length overall, the number of sections,  $N_s$ , is assumed to be the predominant controlling parameter, as the hull cross sections

of variable  $\beta$  vary along the length and consequently cause non uniformly constant sectional added mass distribution. Inadequate resolution of the hull could cause inaccurate integration results and consequently inaccurate convergence of time histories.

Table 3.9: Model configuration of variable  $\beta$  hull (Rosén and Garne, 2006).

Dimension	Outlined	Measured	Comment
$L_{oa}$ [m]	1.050	1.110	Length overall
$L_{wl}$ [m]	0.950		Length waterline, idle
$B_{wl}$ [m]	0.250	0.250	Beam waterline, idle
$T_{lcf}$ [m]	0.055		Draft, idle
$\beta$ [°]	22.000	22.000	Deadrise
$\tau$ [°]	1.500	1.500	Trim, idle
$\Delta$ [kg]	6.500	6.500	Displacement
$LCG$ [m]	0.360	0.360	Longitudinal CG from transom
$VCG$ [m]	0.092	0.092	Vertical CG from keel
$r_x$ [m]	0.082	0.087	Roll radius of gyration
$r_y$ [m]	0.270	0.270	Pitch radius of gyration
$r_z$ [m]	0.270	0.270	Yaw radius of gyration

Therefore, it is of interest to investigate the effect of variable  $\beta$  hull form when varying controlling parameters similarly to the cases of constant  $\beta$  hulls. A variable  $\beta$  planing hull based on a series of experimental test carried out by Rosén and Garne (2006) is chosen to use in this analysis. The fundamental characteristics of the model are shown in Table 3.9. Wave conditions used are also similar to those used in constant  $\beta$  cases with the range of waves length from  $\lambda/L = 2.0$  to  $\lambda/L = 6.0$  and wave height  $H/B = 0.1$  to  $H/B = 0.3$ . A sample of an identical error metrics analysis of accuracy by RMSE is presented together with the corresponding Pareto lines in Figures 3.14 - 3.15.

Fundamentally, the corresponding computational times are identical to the cases of the constant  $\beta$  hull, as the computational code is only modified to use predefined hull data of variable  $\beta$ . The original code is already created to handle with the predefined data. The convergence of time histories (small RMSE) of most waves conditions appear when using  $\Delta t < 0.002$  s and  $N_s$  disengages from being predominant parameters. Note that the minimum  $\beta$  of this model is approximately  $20^\circ$ , which gives the similar simulation behaviours as the case of constant moderate deadrise hull ( $\beta = 20^\circ$ ).

In summary, it can be concluded that variable  $\beta$  has no effect on accuracy and convergence when simulating with the present mathematical model, providing the same accuracy behaviour as the equivalent constant  $\beta$  with the identical minimum  $\beta$ . The most important consideration for this kind of hull is that of the minimum value of  $\beta$ .



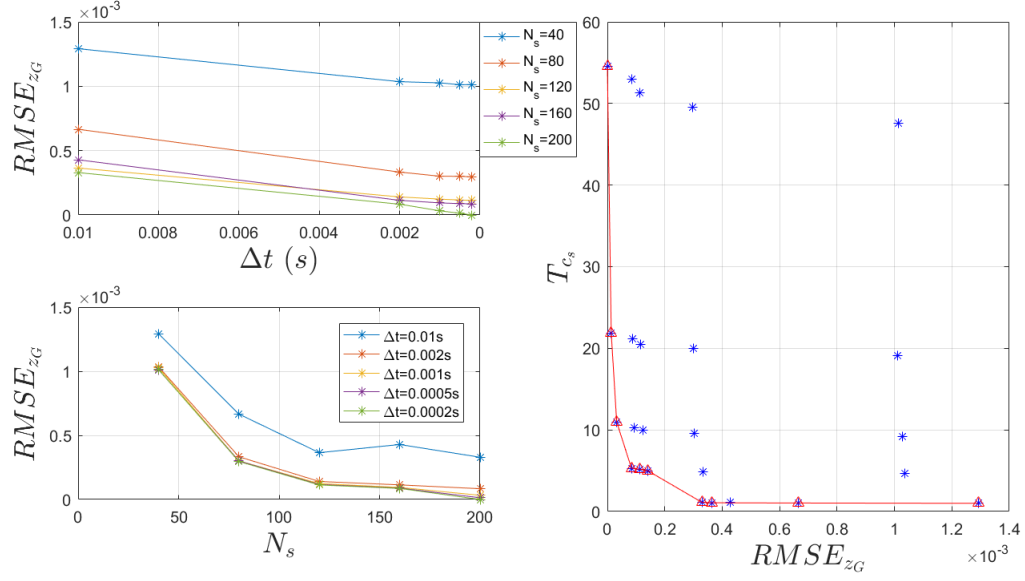


Figure 3.14: Error metrics of time histories and Pareto front line of heave motion of planing hull model with variable  $\beta$ .

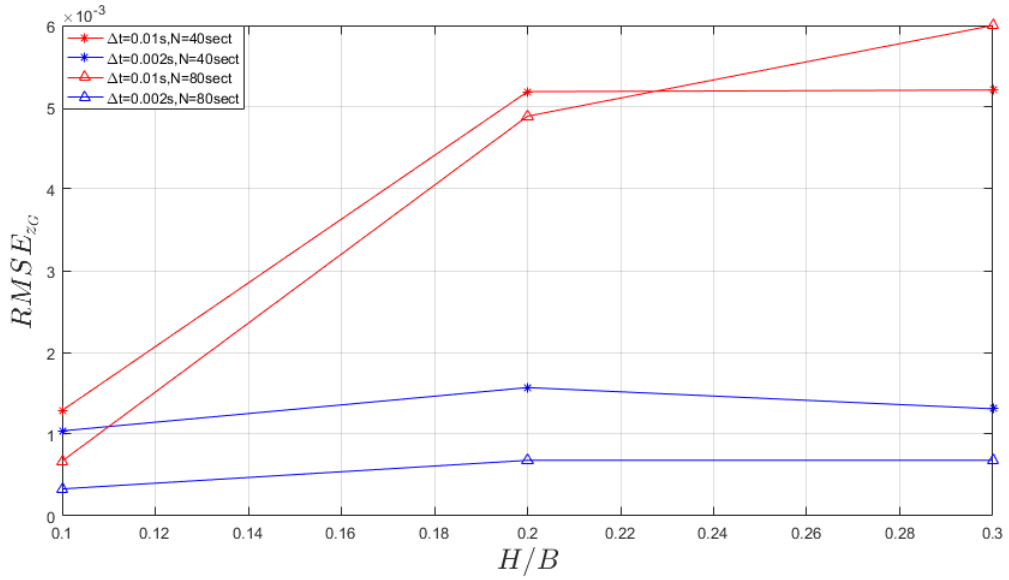


Figure 3.15: Comparison of  $RMSE_{z_G}$  of variable  $\beta$  hull at  $\lambda/L = 4.0$ .

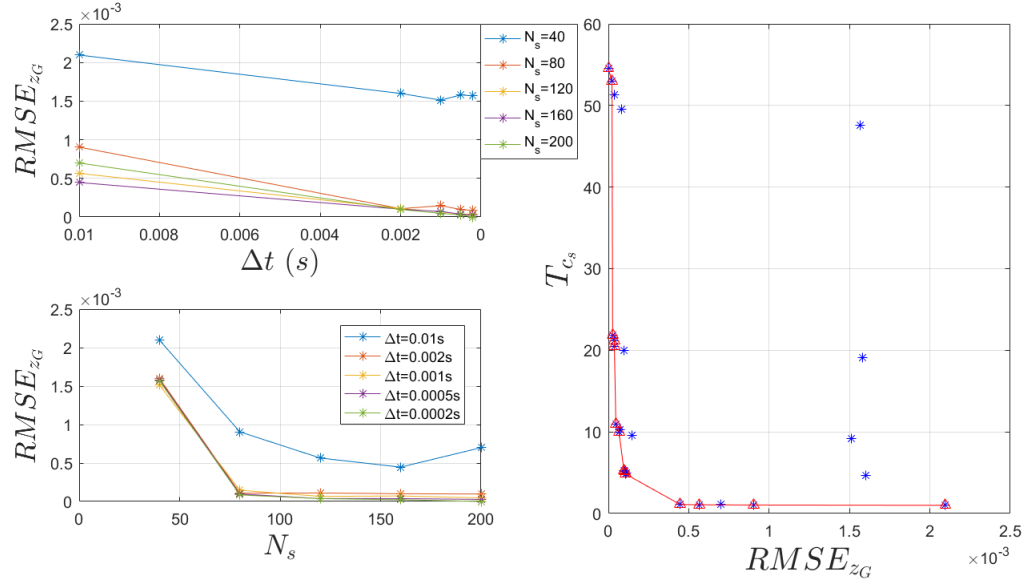


Figure 3.16: Error metrics of time histories and Pareto front line of heave motion of planing hull model  $\beta = 20^\circ$ ,  $\lambda/L = 4.0$  and  $H/B = 0.1$  with 10 times scaled-up.

### 3.3.5.5 Scale Effects

In order to conclude the full-range availability of the present mathematical model, it is also of interest to verify its efficiency when applying with other hull dimensions. Three-dimensional scale-up hull simulations are carried out with scale factor,  $scale = 5$  and  $scale = 10$ . All range of constant deadrise angles ( $\beta = 10^\circ$ ,  $\beta = 20^\circ$  and  $\beta = 30^\circ$ ) are scaled-up together with all waves characteristics (both  $H/B$  and  $\lambda/L$ ). Forward speed is scaled-up by Froude scaling ( $\dot{x}_{G_{ship}} = \sqrt{scale} \cdot \dot{x}_{G_{model}}$ ) and the model weight by the cube law ( $\Delta_{ship} = scale^3 \cdot \Delta_{model}$ ). A sample of a similar error metrics analysis of accuracy by RMSE is presented together with the corresponding Pareto Lines in Figure 3.16. The pair of controlling parameters ( $N_s$  and  $\Delta t$ ) varies identically to the cases of  $scale = 1$  that would make comparison and analysis more devoted.

It can be seen also in Figures 3.16 - 3.17 that comparing to the cases of  $scale = 1$  model, the scaled model simulations have a very similar convergence behaviour. When using  $\Delta t < 0.002$  s, RMSE of time histories converges to an asymptote in better order. Including the case of  $\beta = 10^\circ$ , RMSE is smaller comparing to the identical  $\beta$  with  $scale = 1$ , as well as its better convergence behaviours. Moreover, it is found that increasing  $scale$  decreases slightly but notably order of RMSE.

These behaviours are supposed to be the effect of mass scaling. It is shown in Figure 3.18 that the orders of CG accelerations of the three scales are mostly identical. The remaining relevant parameter is obviously the mass of the different model scales that causes a direct impact on force and moment at each instant. On the other hand,

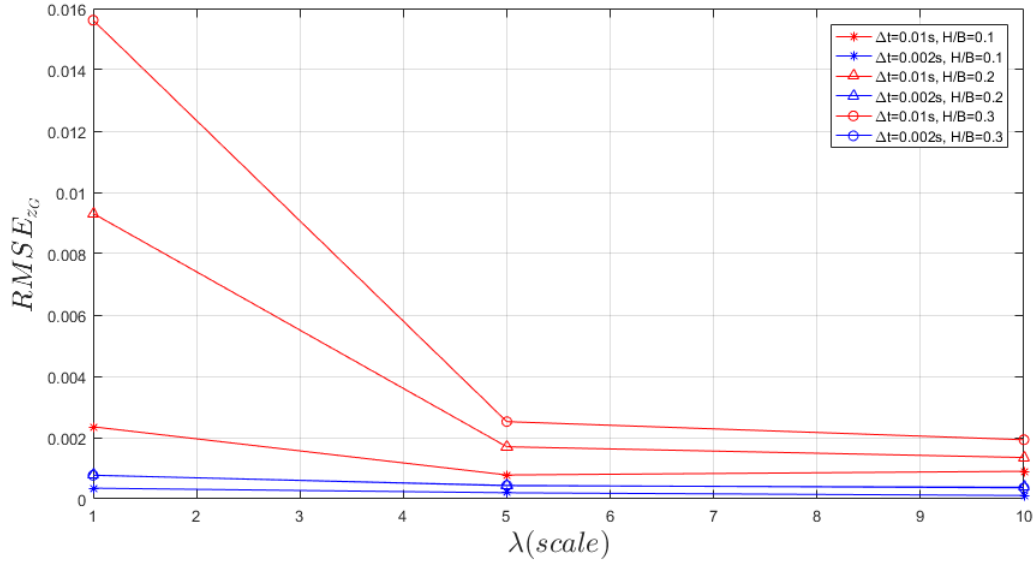


Figure 3.17: Comparison of  $RMSE_{z_G}$  of  $\beta = 20^\circ$  planing hull at  $\lambda/L = 4.0$  varying  $H/B$  and scales.

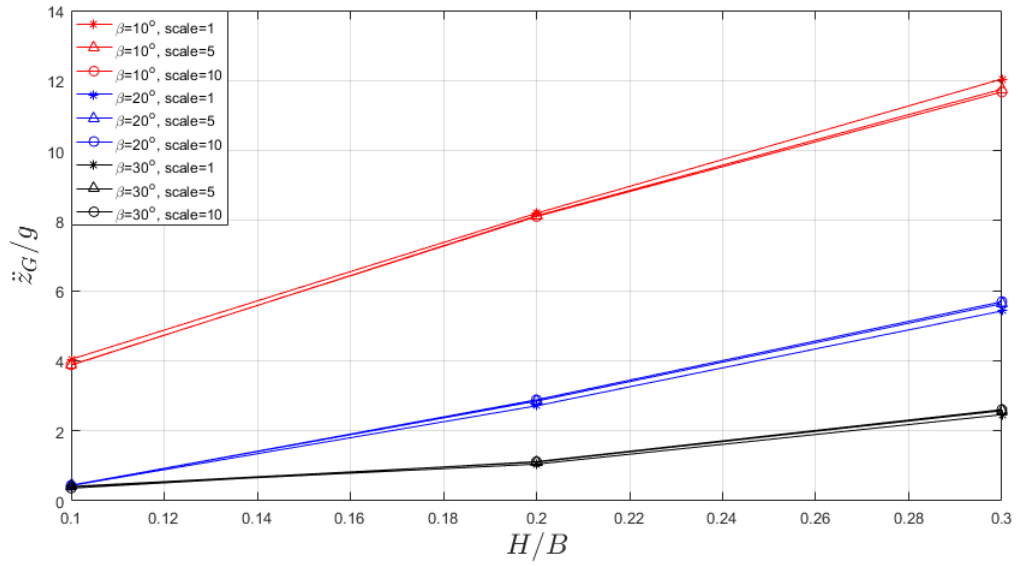


Figure 3.18: Comparison of CG's accelerations at  $\lambda/L = 4.0$  with different  $\beta$  and scales.

as the present mathematical model is governed by potential theory, the lack of viscous component could also cause this slight effect on RMSE behaviours.

This could lead to the conclusion that, in the range of  $scale = 1$  to  $scale = 10$ , the scale has no significant impact in the convergence behaviour of the present mathematical model. Nevertheless, it is still subjected to investigate the effect of some larger or smaller scale out of the range mentioned previously, in order to confirm the full validity of the range of applicability of the present mathematical model in different scales.

### 3.4 Validation

Following the experiments of [Fridsma \(1969\)](#) and the numerical simulations of [Zarnick \(1978\)](#), once verifying and choosing the optimum parameters influenced in numerical calculation, the present mathematical model is used to simulate different cases of the performance of high speed planing boat in both calm water and regular waves.

Table 3.10: Model Configurations for Regular Seas Validation.

CONFIGURATIONS				
$\nabla = 0.0074m^3, L_{OA} = 1.15m, VCG = 0.06m, B = 0.23m$				
Model	$V/\sqrt{L}$	$\beta^\circ$	LCG (m from transom)	$k_{yy}$ (m)
A	4.0	20	0.44	0.29235
B	6.0	20	0.44	0.29235
J	6.0	10	0.37	0.3013
M	6.0	30	0.45	0.2852

#### 3.4.1 Calm Water Simulations

Planing hull models with three different configurations defined in Table 3.10 ( $\beta = 10^\circ$ :J,  $20^\circ$ :B and  $30^\circ$ :M) are simulated. The results of performance in calm water that are dynamic trim, dynamic sinkage and resistance are represented in function of forward speed (speed to length ratio,  $V/\sqrt{L}$ ) in Figure 3.19 comparing to those data calculated using [Savitsky \(1964\)](#)'s Formulae and [Fridsma \(1969\)](#)'s experiments. The range of these ratios is of high speed ( $V/\sqrt{L} = 4.0$  to  $V/\sqrt{L} = 6.0$ ), as the present mathematical model does not include wave resistance component that is predominant part for the low speed range. In most cases, the model is capable of predicting good agreement results. The case of small  $\beta$  delivers sufficiently good real physical phenomena, such as porpoising at high speed. Porpoising can be detected by the present mathematical model with the model J at  $V/\sqrt{L}$  within a range of LCG similar to [Fridsma \(1969\)](#). Further detailed investigations and validations of porpoising simulation are recommended, as it can be also useful for the designer comparing to the existing design charts.

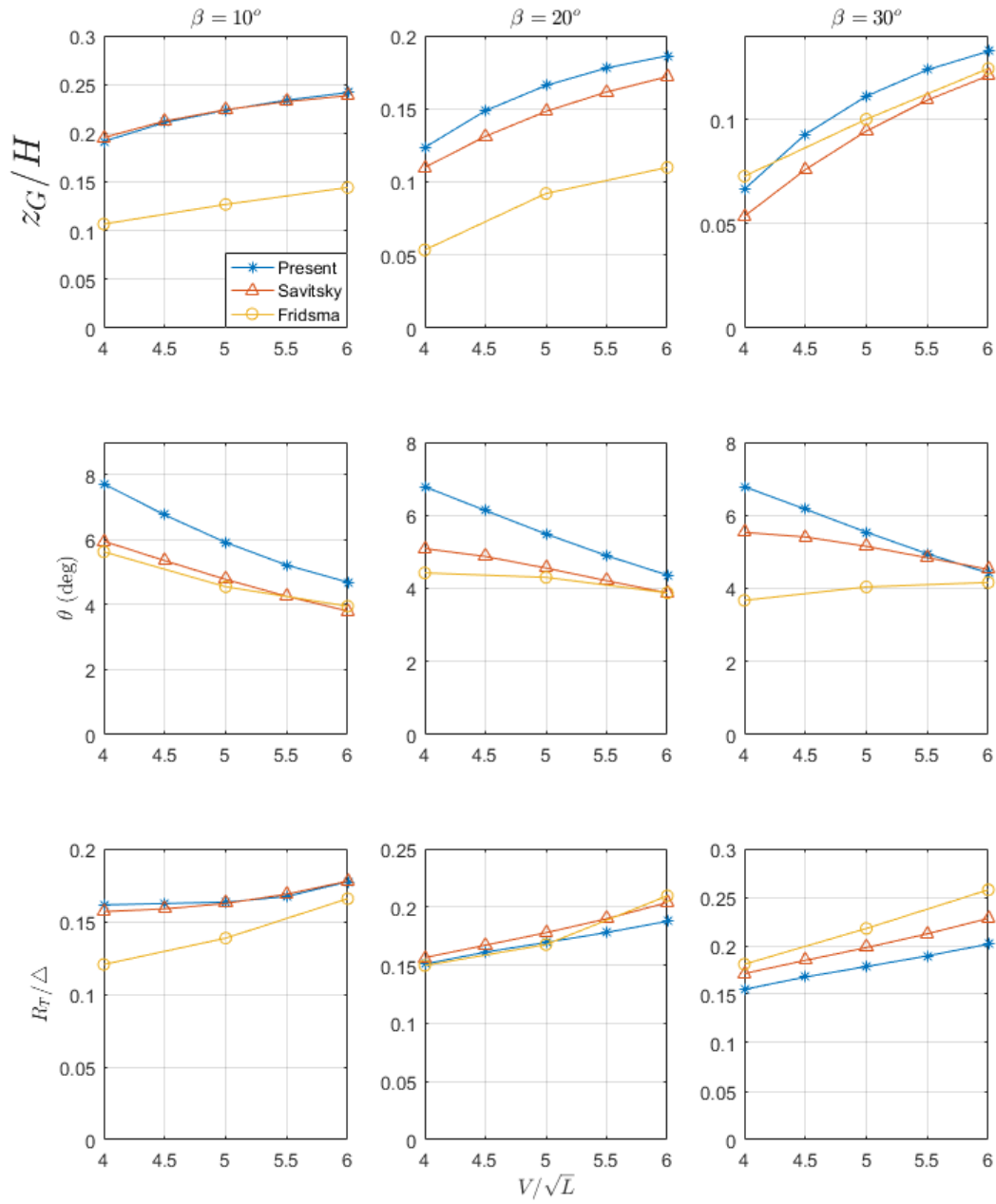


Figure 3.19: Comparison of running attitude in calm water showing sinkage, trim and resistance.

### 3.4.2 Regular Waves Simulations

Simulations of heave and pitch motions and CG and bow accelerations have been carried out for comparison with the experimental results of Fridsma (1969). Fridsma tested a series of constant  $\beta$  models of various lengths in regular seas to define effects of deadrise, trim, loading, speed, length to beam ratio and wave proportions on the added resistance, heave and pitch motions and accelerations at the bow and CG. The configurations of the model are identical to that used by Zarnick (1978) and is shown in Table 3.10. Most of cases have been carried out at  $V/\sqrt{L} = 4.0$  and  $V/\sqrt{L} = 6.0$ , however, no comparison has been made at  $V/\sqrt{L} = 2.0$ , as at this speed, the model operates in the displacement mode for which the present mathematical model is not valid, due to the lack of appropriate component within the model.

Simulation of each case was run in range of 500 s of time history which is sufficiently long to assume that its convergence behaviour should be clarified within this range. The simulations were carried out using  $N_s = 80$ ,  $\Delta t = 0.002$  s for configurations A, B and M, and  $N_s = 200$ ,  $\Delta t = 0.0005$  s for configuration J as per suggested in Section 3.3.5.3.

Figures 3.20 - 3.23 show comparisons of the results evaluated by the present model, Zarnick's model and the experimental results of Fridsma. The response data are collected from the stabilized time histories taking the mean values of peak to peak (wave height) of the signal in the stable interval, as they are close to sinusoidal. Heave responses are normalized by wave height,  $H$  and pitch responses are normalized by  $2\pi H/\lambda$ . Accelerations of response are collected from their peak values and normalized by the gravity. The response data are represented as a function of wavelength to ship length ratio  $\lambda/L$  varying from 1.0 to 6.0. The graphic representation of the resulting motions forms the so-called Response Amplitude Operator, RAO. This RAO represents motion behaviours in three different ranges in term of frequencies of encounter (Journée and Massie, 2001):

- The low-frequency region, with motions dominated by restoring force associated terms. The model tends to follow the wave as the frequency decrease (large wavelength). The RAO tends to 1.0 and the phase lag tends to 0.0.
- The natural frequency region, with motions dominated by damping associated terms. A high resonance can be expected in case of small damping component. A phase shift of  $\pm\pi$  could occur around the natural frequency.
- The high-frequency region, with motions dominated by mass associated terms. The waves are losing their influence on the behaviour of the hull.

It can be seen in cases of  $\beta = 20^\circ$  and  $\beta = 30^\circ$  that the computational results from the present model give very good agreement compared with Fridsma (1969)'s experiments

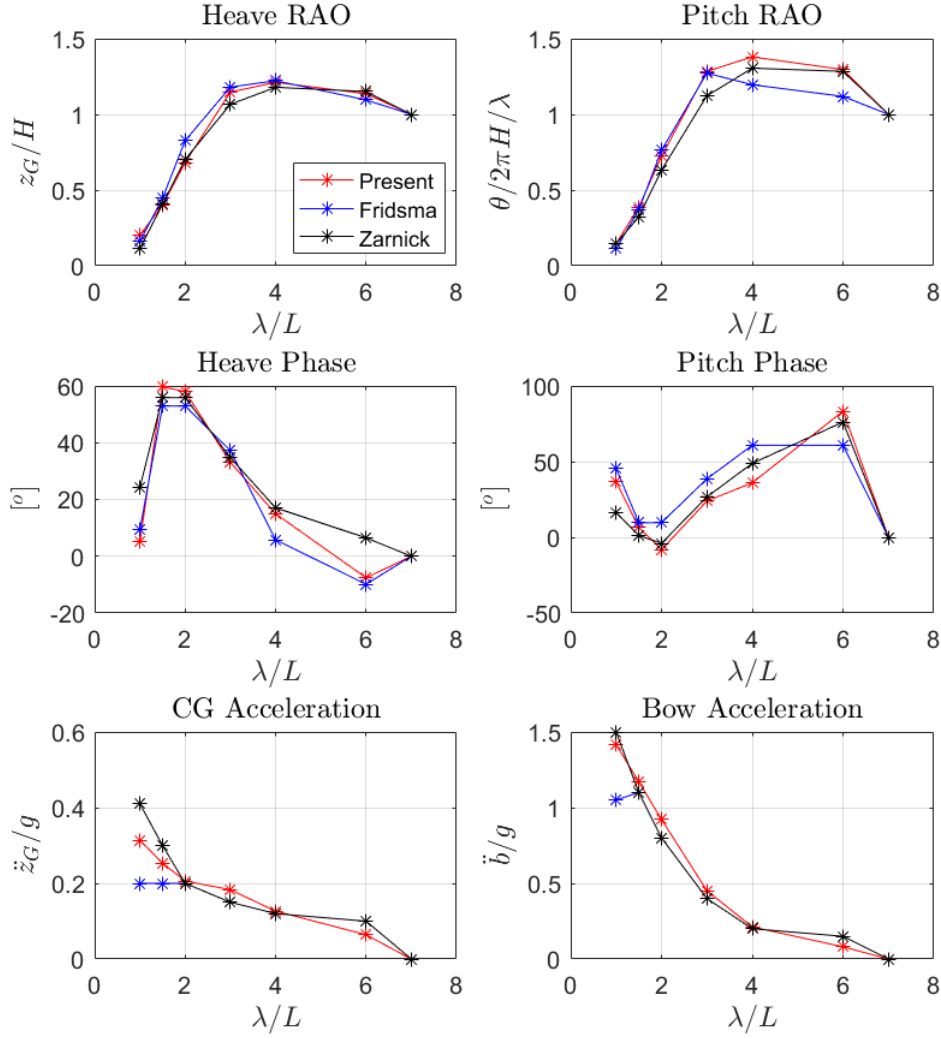


Figure 3.20: Response motions and accelerations of planing hull model  $\beta = 20^\circ$ ,  $V/\sqrt{L} = 4.0$ ,  $H/B = 0.1$ .

and Zarnick (1978)'s simulations. Except in natural frequency region, the present mathematical model slightly over predicts the resonant motions. This could be because of the assumption of only geometry dependent of added mass coefficient  $C_m$  (Payne, 1992), that in reality it is also frequency dependent. This leads to further in-depth investigation of  $C_m$  in term of frequency of encounter. The case of  $\beta = 10^\circ$  gives good agreement results in high frequency region, although at the very high frequency (wavelength equal to ship length), the boat skips over waves (as occurred in Fridsma's experiments). This leads to unidentifiable frequency of encounter, as the frequency of encounter of waves and frequency of response motions are different. Moreover, in natural frequency and low frequency region, the response motions form irregular signal but identical to the frequency of encounter. The data treatment uses the statistic mean to represent signal

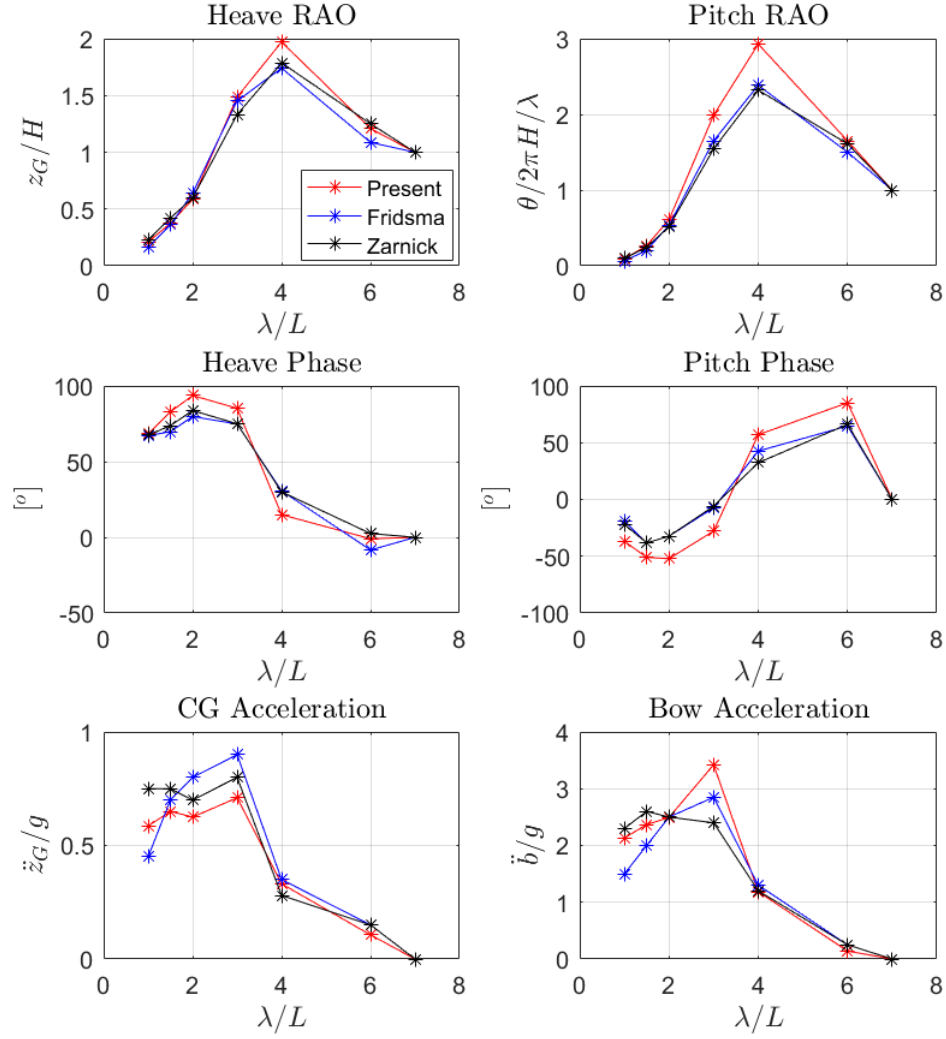


Figure 3.21: Response motions and accelerations of planing hull model  $\beta = 20^\circ$ ,  $V/\sqrt{L} = 6.0$ ,  $H/B = 0.1$ .

wave height of the response motions during the time histories when the motions are already stabilized. The trend of RAO in this case shows fairly good agreement comparing to the experiments but still of larger magnitude in natural frequency region and it is subjected to be analysed in more details on added mass influence.

Regarding the accelerations, the data treatment uses the mean of acceleration peaks when they are stabilized instead of highest peak used by Zarnick (1978). The results of  $\beta = 20^\circ$  and  $V/\sqrt{L} = 4.0$  are of very good agreement in both trend and order of magnitude for all frequency region. When increasing forward speed to  $V/\sqrt{L} = 6.0$ , the magnitudes of both CG and bow accelerations are slightly over predicted from natural to low frequency region. As well as in the case of  $\beta = 10^\circ$ , the trend of both CG and bow accelerations are similar to Fridsma's experiments and Zarnick's simulations. The



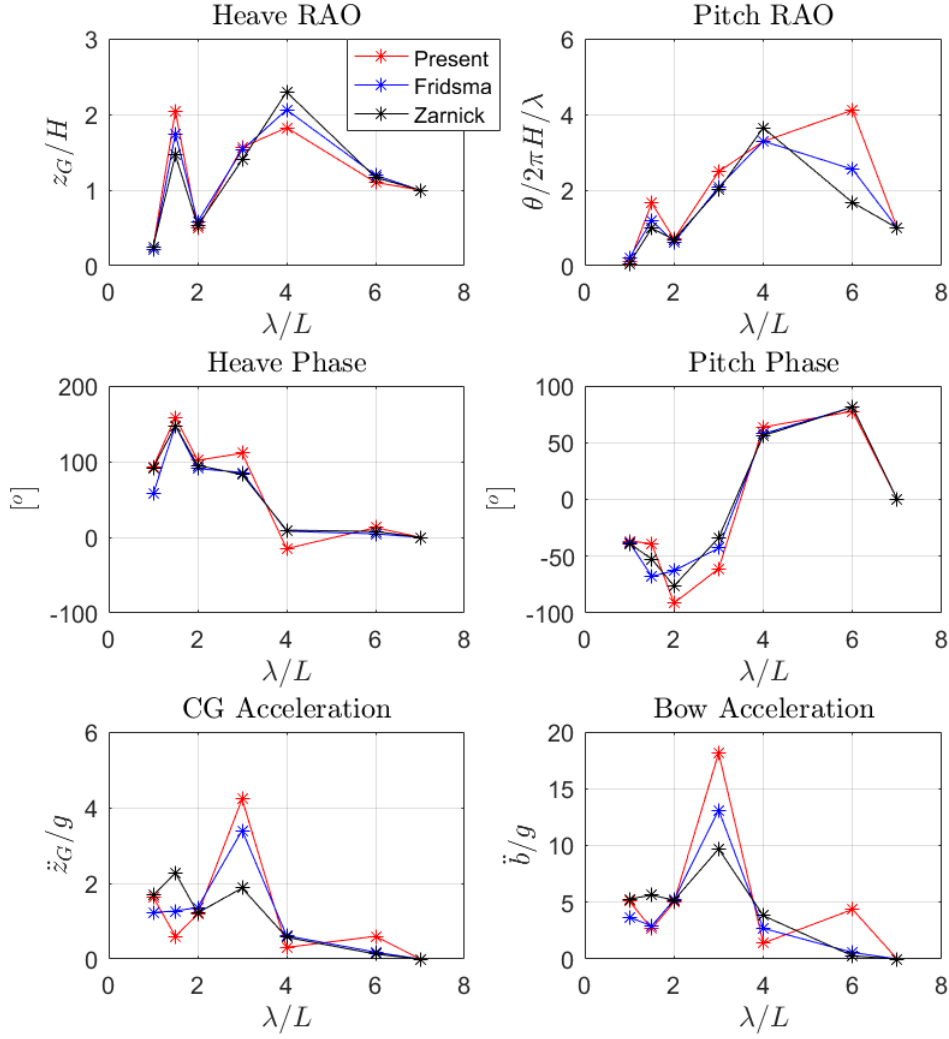


Figure 3.22: Response motions and accelerations of planing hull model  $\beta = 10^\circ$ ,  $V/\sqrt{L} = 6.0$ ,  $H/B = 0.1$ .

order of magnitude of bow acceleration is closer to the reference while CG acceleration is larger in natural to low frequency region. Finally, the case of  $\beta = 30^\circ$  gives very good agreement of CG acceleration and slightly different in order of magnitude but similar trend of bow acceleration.

In summary, the verification and validation processes for calm water and regular waves cases are discussed successfully in this chapter. The present mathematical model will be used as the basis of investigation throughout the further chapters.

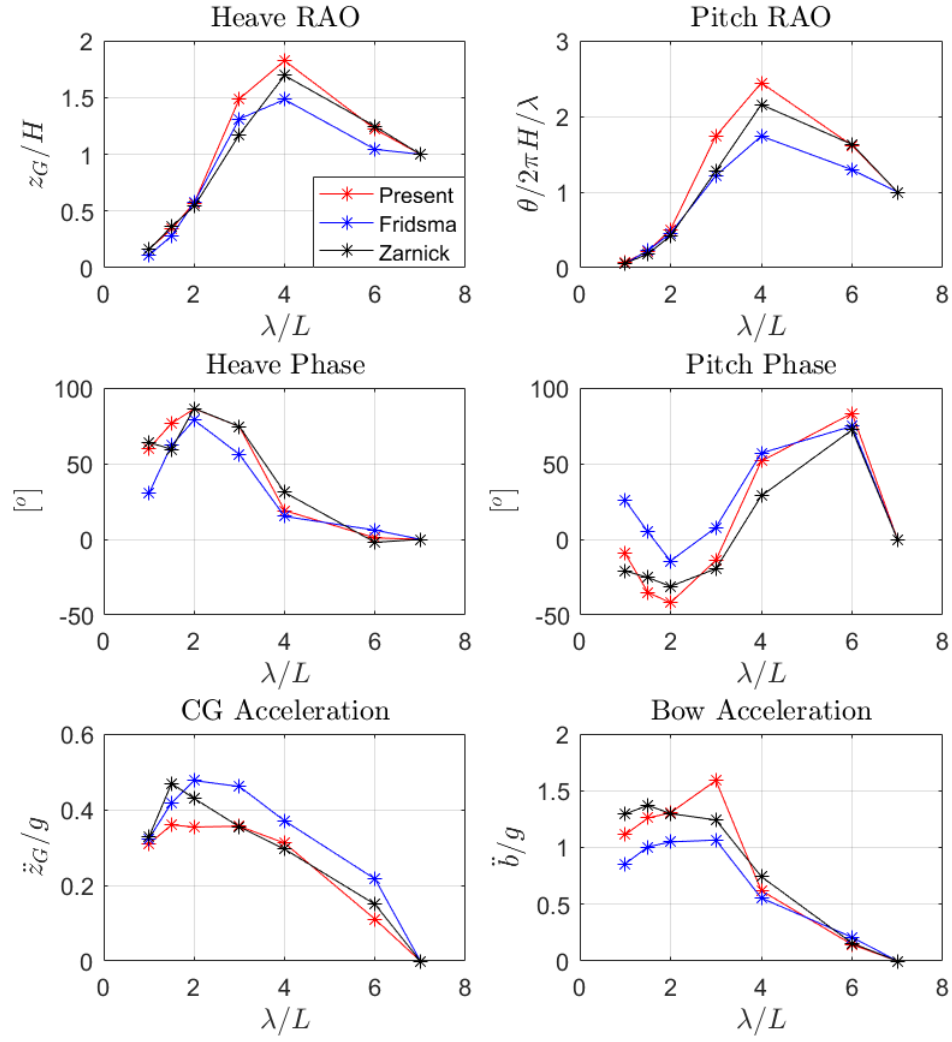


Figure 3.23: Response motions and accelerations of planing hull model  $\beta = 30^\circ$ ,  $V/\sqrt{L} = 6.0$ ,  $H/B = 0.1$ .



## Chapter 4

# Verification and Validation of Simulations in Irregular Waves

Due to the limitations of the present mathematical model mentioned in Chapter 3, the simulations in case of short wavelength and large wave amplitude need to be carefully investigated. This implies that when performing simulations of motions in irregular waves, similar in-depth investigation is necessary as the short wavelength component in irregular sea will be found inevitably. Nevertheless, before carrying out the simulations, appropriate irregular waves need to be generated and verified.

### 4.1 Irregular Waves Generations

In the early stage of simulations, following the work of [Blake \(2000\)](#), the irregular waves are generated using standard wave energy spectra.

#### 4.1.1 Fourier Series

The generation or decomposition of irregular waves can be carried out by the principle of superposition. This leads to the application of a Fourier series due to the fact that the irregular waves are the sum of a certain number of regular waves with various amplitudes and frequencies.

#### 4.1.2 Wave Energy Spectrum

The amount of energy stored in an irregular sea system is considered as a fundamental concept of its analysis. Once a unit area of the sea surface of certain number of components is taken, the proportion of energy corresponding to that area can be defined

in a range of frequencies. The wave energy spectrum is then defined so that the area bound by the frequency range  $\omega$  and  $\omega + d\omega$  is proportional to the total energy of all the components within that range of frequency. The integration of the energy spectrum from  $\omega = 0$  to  $\omega = \infty$  will provide a total proportional to the energy contained in that unit area.

$$A = \int_0^{\infty} S_r(\omega) d\omega \quad (4.1)$$

In this manner, the relative importance of component sine waves that make up an irregular sea can be quantified. The wave energy spectrum therefore provides frequencies required for the Fourier series and the corresponding amplitudes from the wave energy spectral ordinate.

The statistical quantities such as variance and standard deviation of the irregular sea elevation can be obtained from the wave energy spectrum. The variance is described as being equal to the area enclosed by the wave energy spectrum, and as such is the 0<sup>th</sup> moment of area under the spectrum which can be expressed as:

$$m_0 = \int_0^{\infty} S_r(\omega) d\omega \quad (4.2)$$

[Cartwright and Longuet-Higgins \(1956\)](#) show that the significant wave height  $H_{1/3}$  can be expressed as a 4 times the standard deviation for a Rayleighian distribution of wave amplitude:

$$H_{1/3} = 4\sqrt{m_0} \quad (4.3)$$

In more general terms, the  $n^{th}$  moment of the wave energy spectrum about  $\omega = 0$  can be expressed as:

$$m_n = \int_0^{\infty} \omega^n S_r(\omega) d\omega \quad (4.4)$$

### 4.1.3 Choices of Wave Spectra

By a suitable selection of spectrum  $S_r$ , a specific sea state can be created from which the distribution of maxima and minima ( $X_{max}$  and  $X_{min}$ ) should follow a random probability

density distribution fit. It is truly representative of the sea surface. Depending upon the spectral width parameter  $\varepsilon$ , and the non-dimensional maxima and minima of the statistics associated with, the probability distributions are known to be represented by the limits of a Gaussian ( $\varepsilon = 1$ ) or Rayleigh ( $\varepsilon = 0$ ) distribution. Various spectra have been developed, each with their own characteristics and a brief outline of some are given on the paragraphs below, for example, Pierson and Moskowitz (1964), Bretschneider (1952), Bretschneider (1957) and JONSWAP (Hasselmann et al., 1973).

**Pierson-Moskowitz Spectrum:** Pierson and Moskowitz (1964) selected certain spectral measures based upon a large amount of oceanographic records and then grouped those spectra into a family of five wind speeds. From this spectral family, an idealized sea spectrum representing fully developed seas was formed with no frequency elements associated with swell generated from far-off sources.

This method loses its applicability in ship design since it is based on a single parameter of wind strength and fully developed seas created by very high winds are known to be rare (Lewis, 1988), as duration and fetch are insufficient for spectral stability.

**Bretschneider Spectrum:** The Bretschneider spectrum (Bretschneider (1952) and Bretschneider (1957)) is based on two parameters which allow significant wave period and wave height to be assigned separately. These two parameters can be directly related to the extensive data available on observed wave heights and periods.

The Bretschneider spectral form is assumed to adequately represent any seaway but in reality, multi-modal spectra are commonly found. Also, swell from distant storms is found in measured data, the components of which are limited in high frequency since those components take longer to arrive at the observation point. The Bretschneider spectrum however has very well defined high-frequency limits so that there is a significant contribution to the total energy within the system supplied by high frequency components. This could lead to ship high-frequency responses greater than that which would physically occur (St Denis, 1980). If the deviations in form between the Bretschneider and the measured spectra are collectively small, then, the Bretschneider spectrum can lead to a good measure of ship performance.

**Ochi 6-Parameters Spectrum:** In an attempt to improve the Bretschneider spectrum in its basic form, Ochi and Hubble (1976) introduced a shape parameter  $\lambda$  which when it is equal to 1.0, it produces the Bretschneider form. The uni-modal spectrum thus had three parameters based upon frequency, wave height and  $\lambda$ . Adding this spectrum to another which covered higher frequency components led to a 6-parameters multi-modal spectrum which could have much better agreement with the real sea spectra depending on the assignment of values to the parameters.

**JONSWAP:** The limited fetch conditions found in areas such as the North Sea led to the need for a better representation of sea states currently offered by other spectra. The Joint North Sea Wave Project was set up to provide extensive oceanographic measurements in the attempt to meet this need. The subsequent spectral fit found that the sort of spectrum created is simply of a Bretschneider form.

**ITTC Spectrum:** The 15<sup>th</sup> International Towing Tank Conference recommend the use of a form of the Bretschneider spectrum for average rather than fully-developed seas since this allowed for a more realistic representation of the sea surface when more specifically appropriate spectral forms are unknown.

#### 4.1.4 Representation of the Seaway

The seaway in general can be represented by an infinite sum of sine waves with random phase but acceptable results can be obtained with a limited number which [Lloyds \(1998\)](#) recommends a maximum of 50. In this study, principally following [Zarnick \(1979\)](#), the irregular seaway is represented by the discrete sum of ten harmonic waves with random phase varying from 0 to  $2\pi$  radians. It can be expressed on the earth-fixed coordinate system as follows:

$$r = \sum_{i=1}^{10} r_{0i} \cos [k_i (x_G + x' \cos \theta - (z_G - x' \sin \theta) \tan \theta) + \omega_i t + \epsilon_i] \quad (4.5)$$

Where:

- $r_{0i}$ : Components of wave amplitude.
- $k_i$ : Component of wave number.
- $\omega_i$ : Corresponding frequency of each component.
- $\epsilon_i$ : Corresponding random phase.

For the purpose of this study, the simplest representation of a random seaway is used. Use is made of, by following [Zarnick \(1979\)](#), the energy distribution in a Pierson-Moskowitz Spectrum for a fully developed sea. The Pierson-Moskowitz formulation for a continuous spectrum can be written as:

$$S_r = \frac{A \cdot g^2}{\omega^5} \cdot \exp \left( \frac{-B}{\omega^4} \right) \quad (4.6)$$

Where:

- $A = 8.1 \cdot 10^{-3}$
- $g = 9.81 \text{ m/s}^2$
- $B = 4 \cdot A \cdot g^2 / H_{1/3}^2$

The constant  $B$  is also related to the peak frequency  $\omega_p$  of the spectrum by:

$$B = \frac{5}{4} \cdot \omega_p^4 \quad (4.7)$$

Which can be confirmed in the point that the differentiation of the spectrum expression is equal to zero. Normalizing the frequencies by the peak frequency leads to a non-dimensional spectrum  $\bar{S}_r$  which is related to the dimensional spectrum by:

$$\bar{S}_r(\Omega) = \frac{5}{\Omega^5} \exp\left(-\frac{5}{4\Omega^4}\right) \quad (4.8)$$

Where  $\Omega = \omega/\omega_p$ , and:

$$\int_0^\infty \bar{S}_r(\Omega) d\Omega = 1 \quad (4.9)$$

The discrete frequencies representing the spectrum varied from  $\Omega = 0.8$  to  $\Omega = 2.6$  in nearly equal increment  $\Delta\Omega = 0.2$ . A slight random perturbation is given to each frequency to avoid precise integer multiple frequencies, thereby increasing the fundamental repetition period of the computed time history. Each discrete amplitude is adjusted so that its energy corresponds to that contained in a bandwidth  $\Delta\Omega$  centred about its frequency in the continuous spectrum:

$$r_{0i} = \frac{H_{1/3}^2}{8} \cdot \int_{\Omega_i - \Delta\Omega/2}^{\Omega_i + \Delta\Omega/2} \bar{S}_r(\Omega) d\Omega \quad (4.10)$$

The bandwidth are equally spaced between frequencies except for the first and last frequencies which lump all of the remaining energy at the beginning and end of the spectrum. Table 4.1 presents a list of the amplitude for each non-dimensional frequency in terms of significant wave height.



Table 4.1: Wave representing discrete spectrum.

$r_0/H_{\frac{1}{3}}$	$\Omega$
0.1364	0.795
0.1861	1.000
0.1657	1.183
0.1302	1.403
0.0999	1.602
0.0771	1.795
0.0604	2.004
0.0482	2.194
0.0390	2.392
0.0626	2.612

Table 4.2: Planing hull model configurations for irregular waves simulations.

Run	Symbol	$\beta$ (degree)	LCG (%L)	$K_{yy}$ (% L)	$V/\sqrt{L}$	$H_{1/3}/B$
1	M	20	64.0	24.8	6	0.222
2	M	20	64.0	24.8	6	0.444
3	M	20	64.0	24.8	6	0.666
4	O	20	66.8	25.0	4	0.666
5	C	10	68.0	25.0	6	0.444
6	G	30	62.1	25.0	6	0.444

## 4.2 Model Simulations

The mathematical model used in simulations of cases of coupled heave and pitch motions in regular seas is modified to be capable of simulating the cases of irregular seas. These simulations follow the configurations and conditions of [Zarnick \(1979\)](#) that will be used as validation reference. Table 4.2 presents the characteristic of the model craft for those conditions selected for the comparison. Numerical methods used in differentiation and integration terms are assumed to be already verified from Chapter 3. Nevertheless, due to the limitations mentioned before, for the simulations in irregular seas, it appears to be that, at any instance, the short wavelength and large wave amplitude will be found unavoidably and time histories of results will not fit one to the others when varying the number of model sections. Therefore, time history simulations using different  $N_s$  and different  $\Delta t$  are simulated and compared in order to perform the necessary verification. Procedure of analysis of response data will be explained in the following sections:

### 4.2.1 Generated Irregular Waves Analysis

[Zarnick \(1979\)](#) performed model simulations in three different sea conditions. Each condition is characterized by significant wave height  $H_{1/3}$  represented in non-dimensional

form normalized by model's breadth. These sea conditions are  $H_{1/3} = \{0.2, 0.4, 0.6\}$ . Each case of significant wave height  $H_{1/3}$  is generated firstly in a long range of time history. Each generation of irregular sea by a certain input significant wave height gives different time history due to the random phases. The significant wave height of generated wave is evaluated in a certain number of runs and compared to the input significant wave height until the most appropriate range of time history is found. Once the most appropriate time history is found, it will be analysed statistically in a small interval of time in order to find the shortest time range to be used in model simulation. Nevertheless, the number of response cycles should be sufficient to be used in statistical analysis of response motions which is recommend to be 100 cycles (Zarnick, 1979). The irregular seas corresponding to each condition have been evaluated firstly for 1,200 s. Then they have been analysed statistically in various segments of the time history. 100 cycles of wave crests are found in approximately 70 s of time history, moreover, statistic of this shorter range is close to that of the whole time history. This implies the validity of this range of time history of the generated waves. Note that the Pierson-Moskowitz spectrum is of one parameter, it would be preferable to perform the generation of irregular seas with multiple parameters in order to generate more realistic irregular seas.

#### 4.2.2 Response Data Analysis

The output of the present mathematical model is the time histories of heave and pitch motions and bow and CG acceleration. Time histories of response motions and accelerations evaluated using variations of controlling parameters ( $N_s$  and  $\Delta t$ ) are compared. In order to facilitate the comparison, the analysis procedures in this chapter have been carried out following Fridsma (1971) and Zarnick (1979). The amplitudes, maxima and minima of the heave and pitch motions about the mean are assumed to be described as the so-called "Cartwright and Longuet-Higgins Distribution" (Cartwright and Longuet-Higgins, 1956) which is expressed as:

$$p(y) = \frac{1}{\sqrt{2\pi}} \left( \epsilon \cdot e^{\left(-\frac{1}{2} \frac{y^2}{\epsilon^2}\right)} + \left(\sqrt{1-\epsilon^2}\right) \cdot y \cdot e^{\left(\frac{1}{2} y^2\right)} \cdot \int_{-\infty}^{y(\sqrt{1-\epsilon^2})/\epsilon} e^{\left(-\frac{1}{2} x^2\right)} dx \right) \quad (4.11)$$

Where  $y$  is maxima or minima normalized by the standard deviation:

$$y_i = \frac{X_i}{\sqrt{m_0}} \quad (4.12)$$

And the parameter  $\epsilon$ :

$$\epsilon = \sqrt{1 - (1 - 2r)^2} \quad (4.13)$$

$r$  is proportion of negative maxima to total maxima or positive minima to total minima.

To fit the data to this distribution, the maxima and minima relative to the mean value are first determined from the time histories of the response motions. The mean value is defined as halfway between the average maxima and average minima value. The maxima or minima data ( $X_i$ ) are sorted in ascending order and grouped into fifteen bins and plotted in histogram. At the same time, the proportion  $r$  of negative maxima to total maxima or positive minima to total minima is determined. The cumulative frequency and corresponding probability that a maxima or minima is less than or equal to the interval value is computed. From the probability and  $r$  values, the theoretical value of the normalized amplitude  $y$  is calculated. A plot of  $X_i$  versus corresponding  $y_i$  values is compared with a line drawn through  $X = y = 0$ , and the point,  $X = \bar{X}$ ,  $y = \bar{y}$ , which is indicative of the fit of the theoretical distribution function of the data. The values of  $X$  and  $y$  are the observed average value of the first moment and the theoretical average value (normalized) respectively.

The acceleration data was assumed to follow the simple exponential distribution:

$$p(\eta) = \frac{1}{\bar{\eta}} \exp\left(\frac{-\eta}{\bar{\eta}}\right) \quad (4.14)$$

For this distribution, the probability,  $P$  of the acceleration peak  $\eta$  being less than a given value is:

$$P(\eta) = 1 - \exp\left(\frac{-\eta}{\bar{\eta}}\right) \quad (4.15)$$

Where  $\bar{\eta}$  is average peak acceleration.

Only the negative peak acceleration (impact spikes as well as wave induced) were analysed. The data was sorted and grouped into a fifteen bins histogram similar to the motion data analysis and the probability was plotted with respect to  $\eta$  on inverted semi-log paper. For a good fit, the data should follow a straight line through the point ( $P = 0.368, \eta = \bar{\eta}$ ) and the origin.

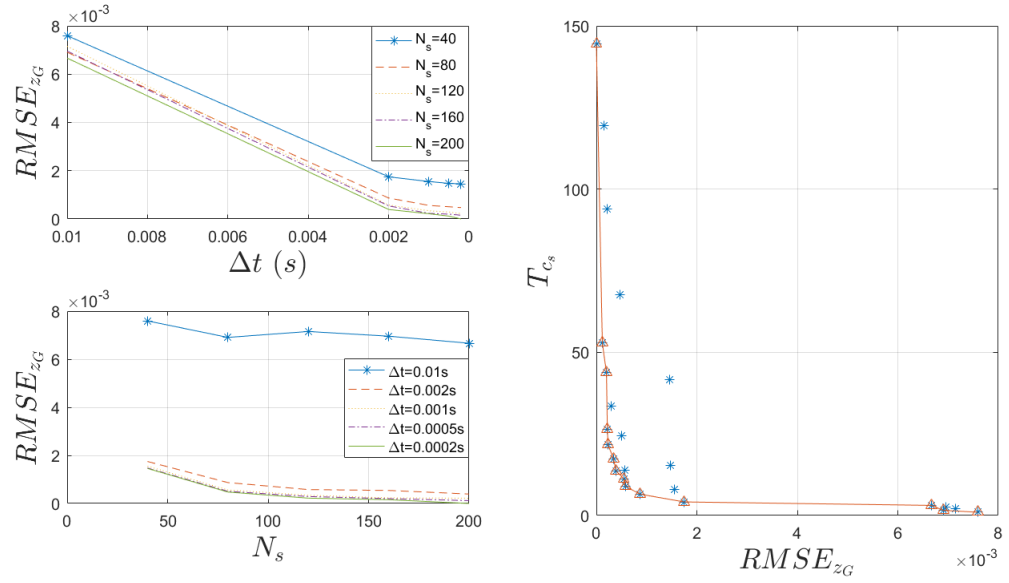


Figure 4.1: Error metric of time histories and Pareto front line of heave motion of planing hull model  $\beta = 20^\circ$ ,  $V/\sqrt{L} = 6.0$ ,  $H_{1/3}/B = 0.2$ .

### 4.3 Verification of the Mathematical Model

The limitations of the present mathematical model discussed in Chapter 3 have direct impacts when it is used to simulate motions in irregular seas. It works well when the wavelength is equal to the model length at the smallest value. However, due to the fact that generated irregular seas are a superposition of a number of sinusoidal waves varying the amplitudes and frequencies, the wavelength of the component corresponding to the largest frequency (smallest wavelength), defined by the actual wave energy spectra used, is around  $0.3 \cdot L_{oa}$ . That value of wavelength could cause inaccurate variation of sectional added mass  $m_a$  and its associated terms when varying the number of sections,  $N_s$ . The optimal number of sections,  $N_s$  and time step sizes,  $\Delta t$  are then analysed in the same manner as in regular wave simulations.

#### 4.3.1 Influence of Number of Section $N_s$ and Time Step Size $\Delta t$ in Different Deadrise Angle and Sea Conditions

Similar to the regular wave simulations, three different  $\beta$  planing models ( $10^\circ$ ,  $20^\circ$  and  $30^\circ$ ) are simulated in three different sea conditions ( $H_{1/3} = \{0.2, 0.4, 0.6\}$ ). Time histories of all of the cases are normalized in the same manner as in cases of regular waves. Sample of error metrics of time histories is presented graphically in Figure 4.1.

The RMSE together with the computational time ratio,  $T_{c_s}$  are also represented in Tables 4.3 - 4.10 by highlighting the points on Pareto front line. The comparison gives a similar deduction as in cases of regular waves simulations. Time histories of moderate

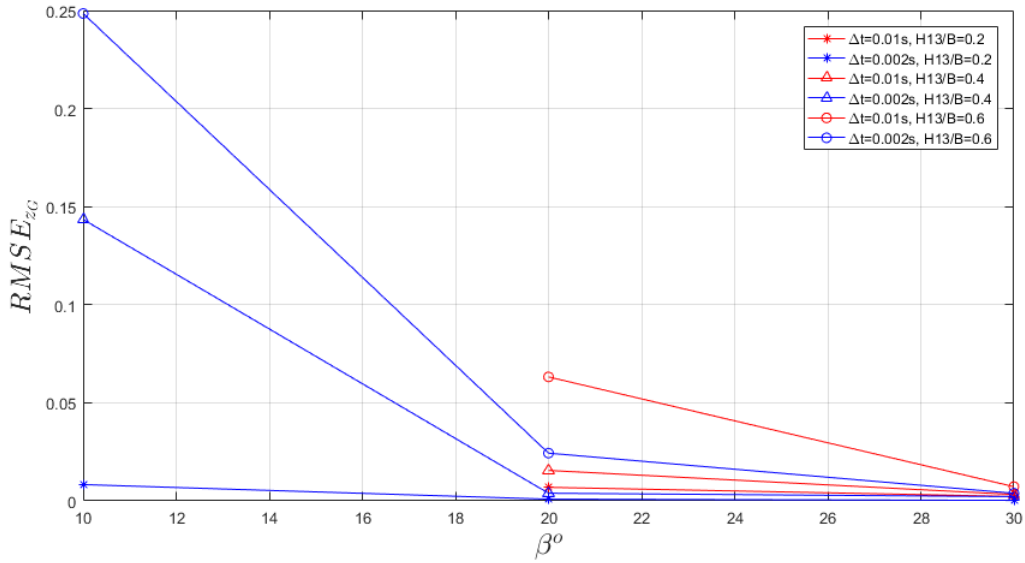


Figure 4.2: Comparison of  $RMSE_{z_G}$  of different  $\beta$  and  $H_{1/3}/B$  at  $\lambda/L = 4.0$ .

and large  $\beta$  hulls converge when  $\Delta t < 0.002$  s in most sea conditions. Figure 4.2 shows the comparison of  $RMSE_{z_G}$  using  $\Delta t = 0.01$  s and  $\Delta t = 0.002$  s in different  $\beta$  and  $H_{1/3}/B$ . However, smaller  $\Delta t$  can be considered efficient if variation of accuracy is acceptable as it can be seen from Pareto front line. The case of small deadrise angle needs more dedicated selection of controlling parameters. Its resulting time histories do not converge and are numerically unstable when using  $\Delta t = 0.01$  s. This is also proved by analysing with variable steps solver and the convergence does not happen even after a considerable number of iterations. The optimal  $\Delta t$  appears to be 0.002 s for simulations in small and moderate significant wave height conditions. Although using smaller  $\Delta t$  may give better accuracy, consideration of computational time as mentioned previously should be accounted for. The extreme seas (large significant wave height) simulations give significantly large fluctuation of time histories when varying controlling parameters. The best convergence appears after  $\Delta t < 0.0001$  s implying very large computational time.

When considering the same order of RMSE, the overall optimal selection of controlling parameters can be summarised as follows:

- For  $\beta = 10^\circ$ :
  - $N_s > 200$  and  $\Delta t < 0.0002$  s when  $H_{1/3}/B = 0.2$ .
  - $N_s > 200$  and  $\Delta t < 0.0002$  s when  $H_{1/3}/B = 0.4$ .
  - $N_s > 200$  and  $\Delta t < 0.0001$  s when  $H_{1/3}/B = 0.6$ .
- For  $\beta = 20^\circ$ ,  $N_s > 200$  and  $\Delta t < 0.002$  s in all of sea conditions.
- For  $\beta = 30^\circ$ ,  $N_s > 200$  and  $\Delta t < 0.002$  s in all of sea conditions.

Note that the order of RMSE considered in the cases of irregular waves is larger than the cases of regular waves, as the fluctuation of time histories is higher.

Table 4.3: RMSE VS  $T_{cs}$  of planing hull model  $\beta = 20^\circ, H_{1/3}/B = 0.2, V/\sqrt{L} = 4.0$ .

$\Delta t(s)$	0.01		0.002		0.001		0.0005		0.0002	
$N_s$	RMSE	Tcs	RMSE	Tcs	RMSE	Tcs	RMSE	Tcs	RMSE	Tcs
40	<b>0.003701</b>	<b>1.00</b>	<b>0.002010</b>	<b>4.16</b>	0.001892	7.87	0.001882	15.31	0.001885	41.59
80	<b>0.002691</b>	<b>1.57</b>	<b>0.000735</b>	<b>6.53</b>	0.000729	13.96	0.000694	24.51	0.000692	67.71
120	<b>0.002622</b>	<b>2.07</b>	<b>0.000439</b>	<b>8.96</b>	0.000424	17.31	0.000415	33.58	0.000415	93.86
160	<b>0.002501</b>	<b>2.58</b>	<b>0.000356</b>	<b>11.24</b>	0.000306	21.72	0.000289	43.75	0.000290	119.50
200	<b>0.002456</b>	<b>3.09</b>	<b>0.000137</b>	<b>13.74</b>	<b>0.000076</b>	<b>26.49</b>	<b>0.000053</b>	<b>52.82</b>	<b>0.000000</b>	<b>144.52</b>

Table 4.4: RMSE VS  $T_{cs}$  of planing hull model  $\beta = 20^\circ, H_{1/3}/B = 0.6, V/\sqrt{L} = 4.0$ .

$\Delta t(s)$	0.01		0.002		0.001		0.0005		0.0002	
$N_s$	RMSE	Tcs	RMSE	Tcs	RMSE	Tcs	RMSE	Tcs	RMSE	Tcs
40	<b>0.048773</b>	<b>1.00</b>	<b>0.004307</b>	<b>4.16</b>	<b>0.002166</b>	<b>7.87</b>	0.002519	15.31	0.002537	41.59
80	<b>0.018006</b>	<b>1.57</b>	<b>0.002454</b>	<b>6.53</b>	0.001318	13.96	0.000898	24.51	0.000801	67.71
120	<b>0.014653</b>	<b>2.07</b>	<b>0.001797</b>	<b>8.96</b>	<b>0.000871</b>	<b>17.31</b>	<b>0.000629</b>	<b>33.58</b>	0.000528	93.86
160	0.017665	2.58	<b>0.001234</b>	<b>11.24</b>	<b>0.000676</b>	<b>21.72</b>	<b>0.000473</b>	<b>43.75</b>	0.000369	119.50
200	0.023900	3.09	0.001437	13.74	0.000900	26.49	<b>0.000318</b>	<b>52.82</b>	<b>0.000000</b>	<b>144.52</b>

Table 4.5: RMSE VS  $T_{cs}$  of planing hull model  $\beta = 20^\circ, H_{1/3}/B = 0.2, V/\sqrt{L} = 6.0$ .

$\Delta t(s)$	0.01		0.002		0.001		0.0005		0.0002	
$N_s$	RMSE	Tcs	RMSE	Tcs	RMSE	Tcs	RMSE	Tcs	RMSE	Tcs
40	<b>0.007595</b>	<b>1.00</b>	<b>0.001747</b>	<b>4.16</b>	0.001552	7.87	0.001475	15.31	0.001457	41.59
80	<b>0.006908</b>	<b>1.57</b>	<b>0.000869</b>	<b>6.53</b>	0.000563	13.96	0.000506	24.51	0.000475	67.71
120	0.007154	2.07	<b>0.000578</b>	<b>8.96</b>	<b>0.000341</b>	<b>17.31</b>	0.000288	33.58	0.000222	93.86
160	0.006959	2.58	<b>0.000542</b>	<b>11.24</b>	<b>0.000233</b>	<b>21.72</b>	<b>0.000201</b>	<b>43.75</b>	0.000156	119.50
200	<b>0.006665</b>	<b>3.09</b>	<b>0.000393</b>	<b>13.74</b>	<b>0.000218</b>	<b>26.49</b>	<b>0.000119</b>	<b>52.82</b>	<b>0.000000</b>	<b>144.52</b>

Table 4.6: RMSE VS  $T_{cs}$  of planing hull model  $\beta = 20^\circ, H_{1/3}/B = 0.6, V/\sqrt{L} = 6.0$ .

$\Delta t(s)$	0.01		0.002		0.001		0.0005		0.0002	
$N_s$	RMSE	Tcs	RMSE	Tcs	RMSE	Tcs	RMSE	Tcs	RMSE	Tcs
40	<b>0.067816</b>	<b>1.00</b>	0.060571	4.16	0.048412	7.87	0.046461	15.31	0.045675	41.59
80	<b>0.063187</b>	<b>1.57</b>	<b>0.024330</b>	<b>6.53</b>	0.020257	13.96	0.009294	24.51	0.006399	67.71
120	0.080141	2.07	<b>0.018139</b>	<b>8.96</b>	0.018085	17.31	<b>0.006287</b>	<b>33.58</b>	0.005084	93.86
160	0.077935	2.58	<b>0.015616</b>	<b>11.24</b>	<b>0.008751</b>	<b>21.72</b>	0.034330	43.75	0.002951	119.50
200	<b>0.053288</b>	<b>3.09</b>	0.021263	13.74	<b>0.007595</b>	<b>26.49</b>	<b>0.002467</b>	<b>52.82</b>	<b>0.000000</b>	<b>144.52</b>

Table 4.7: RMSE VS  $T_{cs}$  of planing hull model  $\beta = 30^\circ, H_{1/3}/B = 0.2, V/\sqrt{L} = 6.0$ .

$\Delta t(s)$	0.01		0.002		0.001		0.0005		0.0002	
$N_s$	RMSE	Tcs	RMSE	Tcs	RMSE	Tcs	RMSE	Tcs	RMSE	Tcs
40	<b>0.002364</b>	<b>1.00</b>	<b>0.000663</b>	<b>4.16</b>	0.000627	7.87	0.000596	15.31	0.000587	41.59
80	<b>0.002273</b>	<b>1.57</b>	<b>0.000258</b>	<b>6.53</b>	0.000231	13.96	0.000198	24.51	0.000190	67.71
120	<b>0.002124</b>	<b>2.07</b>	<b>0.000183</b>	<b>8.96</b>	0.000141	17.31	0.000112	33.58	0.000103	93.86
160	<b>0.002078</b>	<b>2.58</b>	<b>0.000172</b>	<b>11.24</b>	<b>0.000101</b>	<b>21.72</b>	0.000082	43.75	0.000070	119.50
200	0.002107	3.09	<b>0.000140</b>	<b>13.74</b>	<b>0.000064</b>	<b>26.49</b>	<b>0.000038</b>	<b>52.82</b>	<b>0.000000</b>	<b>144.52</b>

### 4.3.2 Validation of Irregular Waves Simulations

The model configuration of the simulations to be validated is shown in Table 4.2. They were carried out using the pair of controlling parameters as per suggested in Section 4.3.1. Table 4.11 presents comparisons of statistics of the results using the present mathematical model to those of Zarnick (1979) and Fridsma (1971), the results are also presented graphically in Figures 4.3 - 4.4. The tabulated values for the heave and pitch are those

Table 4.8: RMSE VS  $T_{cs}$  of planing hull model  $\beta = 30^\circ, H_{1/3}/B = 0.6, V/\sqrt{L} = 6.0$ .

$\Delta t(s)$	0.01		0.002		0.001		0.0005		0.0002	
$N_s$	RMSE	Tcs	RMSE	Tcs	RMSE	Tcs	RMSE	Tcs	RMSE	Tcs
40	<b>0.015196</b>	<b>1.00</b>	<b>0.004779</b>	<b>4.16</b>	0.004366	7.87	0.003866	15.31	0.003827	41.59
80	<b>0.007250</b>	<b>1.57</b>	<b>0.003864</b>	<b>6.53</b>	0.001444	13.96	0.001309	24.51	0.001226	67.71
120	0.014946	2.07	<b>0.001218</b>	<b>8.96</b>	0.001455	17.31	0.000843	33.58	0.000513	93.86
160	<b>0.006631</b>	<b>2.58</b>	<b>0.001046</b>	<b>11.24</b>	<b>0.000513</b>	<b>21.72</b>	0.000550	43.75	<b>0.000263</b>	<b>119.50</b>
200	<b>0.005757</b>	<b>3.09</b>	0.001219	13.74	0.000822	26.49	<b>0.000417</b>	<b>52.82</b>	<b>0.000000</b>	<b>144.52</b>

Table 4.9: RMSE VS  $T_{cs}$  of planing hull model  $\beta = 10^\circ, H_{1/3}/B = 0.2, V/\sqrt{L} = 6.0$ .

$\Delta t(s)$	0.01		0.002		0.001		0.0005		0.0002	
$N_s$	RMSE	Tcs	RMSE	Tcs	RMSE	Tcs	RMSE	Tcs	RMSE	Tcs
40	-	-	<b>0.013173</b>	<b>4.16</b>	0.010415	7.87	0.011455	15.31	0.009524	41.59
80	-	-	<b>0.008311</b>	<b>6.53</b>	<b>0.003644</b>	<b>13.96</b>	0.002855	24.51	0.002802	67.71
120	-	-	<b>0.005667</b>	<b>8.96</b>	<b>0.002449</b>	<b>17.31</b>	<b>0.001481</b>	<b>33.58</b>	0.001350	93.86
160	-	-	<b>0.004913</b>	<b>11.24</b>	0.002942	21.72	<b>0.001457</b>	<b>43.75</b>	0.001649	119.50
200	-	-	0.016916	13.74	0.005643	26.49	<b>0.001187</b>	<b>52.82</b>	<b>0.000000</b>	<b>144.52</b>

Table 4.10: RMSE VS  $T_{cs}$  of planing hull model  $\beta = 10^\circ, H_{1/3}/B = 0.6, V/\sqrt{L} = 6.0$ .

$\Delta t(s)$	0.01		0.002		0.001		0.0005		0.0002	
$N_s$	RMSE	Tcs	RMSE	Tcs	RMSE	Tcs	RMSE	Tcs	RMSE	Tcs
40	-	-	-	-	-	-	-	-	-	-
80	-	-	<b>0.2484638</b>	<b>6.53</b>	0.2493804	13.96	0.3048835	24.51	0.3090574	67.71
120	-	-	-	-	-	-	-	-	-	-
160	-	-	0.2563004	11.24	0.2769489	21.72	<b>0.3236768</b>	<b>43.75</b>	0.3113237	119.50
200	-	-	0.2558897	13.74	0.292542	26.49	0.2909403	52.82	0	144.52

with a 50% and 90% probability of not being exceeded. The response motions are normalized in the same manner as in the cases of regular waves. It can be seen that the case of moderate  $\beta$  model in all speed range the present mathematical model gives very good agreement results comparing to the references. In some cases, such as heave maxima and minima and pitch maxima and minima of Run 2 are closer to Frisma's experiments than Zarnick's simulations. Run 6 gives fairly good agreement except the heave minima. Although it is different from the experiments, it is still closed to Zarnick's simulations. As well as the accelerations, all cases give very good agreement except Run 6 but still closed to Zarnick's simulations. Run 5 is the most extreme case, as it is of small  $\beta$  hull, the impact effect is extremely high. Moreover, from the verification of convergence, the fluctuation of time histories is still of high level, although a very small  $\Delta t$  is used.

Nevertheless, using a ten-component wave model could cause a difficulty of catching an appropriate statistical process, due to the risk of a short return period. It is recommended for further investigation to use a more realistic and complete wave model.

Once the present mathematical has been verified its optimal use and validated in irregular waves, it can be concluded that the simulations in longitudinal plane motions can be carried out effectively. It is of interest to extend the model to another degree of freedom on the basis of the actual strip principal. The first extension is roll motion which is detailed in Chapter 5.

Table 4.11: Statistic Comparison of Irregular Waves Simulations.

Run	Methods	Pitch (Degrees)				Heave				Acceleration (Gs)	
		Maxima		Minima		Maxima		Minima			
		$\theta_{50}$	$\theta_{90}$	$\theta_{50}$	$\theta_{90}$	$z_{G50}/2B$	$z_{G90}/2B$	$z_{G50}/2B$	$z_{G90}/2B$	$\ddot{b}$	$\ddot{z}_G$
1	Present	2.12	4.00	1.62	3.20	0.11	0.21	0.07	0.15	3.47	0.95
	Zarnick	0.69	1.67	0.82	1.75	0.03	0.06	0.03	0.09	1.74	0.47
	Fridsma	0.90	2.13	0.88	1.78	0.03	0.07	0.04	0.08	2.10	0.68
2	Present	2.56	5.90	2.08	4.49	0.16	0.36	0.10	0.24	4.53	1.51
	Zarnick	1.83	3.93	1.72	3.85	0.08	0.21	0.10	0.22	2.90	0.82
	Fridsma	2.25	5.51	2.20	4.34	0.14	0.27	0.15	0.39	5.33	1.77
3	Present	3.51	8.18	2.88	6.68	0.25	0.55	0.19	0.42	5.59	2.32
	Zarnick	2.47	5.53	2.38	5.45	0.21	0.41	0.17	0.39	3.29	1.06
	Fridsma										
4	Present	4.34	8.85	3.37	7.21	0.20	0.47	0.16	0.37	4.98	1.43
	Zarnick	3.14	6.71	2.45	6.27	0.14	0.37	0.18	0.39	3.02	0.78
	Fridsma	3.92	8.18	3.86	7.47	0.20	0.45	0.20	0.40	5.50	1.68
5	Present	3.67	7.37	2.56	5.47	0.19	0.39	0.13	0.28	6.86	2.24
	Zarnick	1.60	3.66	1.75	3.63	0.09	0.21	0.11	0.26	2.05	0.69
	Fridsma	1.76	3.98	1.76	3.91	0.12	0.23	0.12	0.26	3.05	1.00
6	Present	2.49	5.08	2.00	4.19	0.15	0.34	0.11	0.23	3.12	1.15
	Zarnick	2.15	4.72	2.13	4.70	0.11	0.25	0.12	0.25	3.40	1.15
	Fridsma	2.39	5.78	2.36	4.87	0.13	0.26	0.14	0.42	7.20	2.40



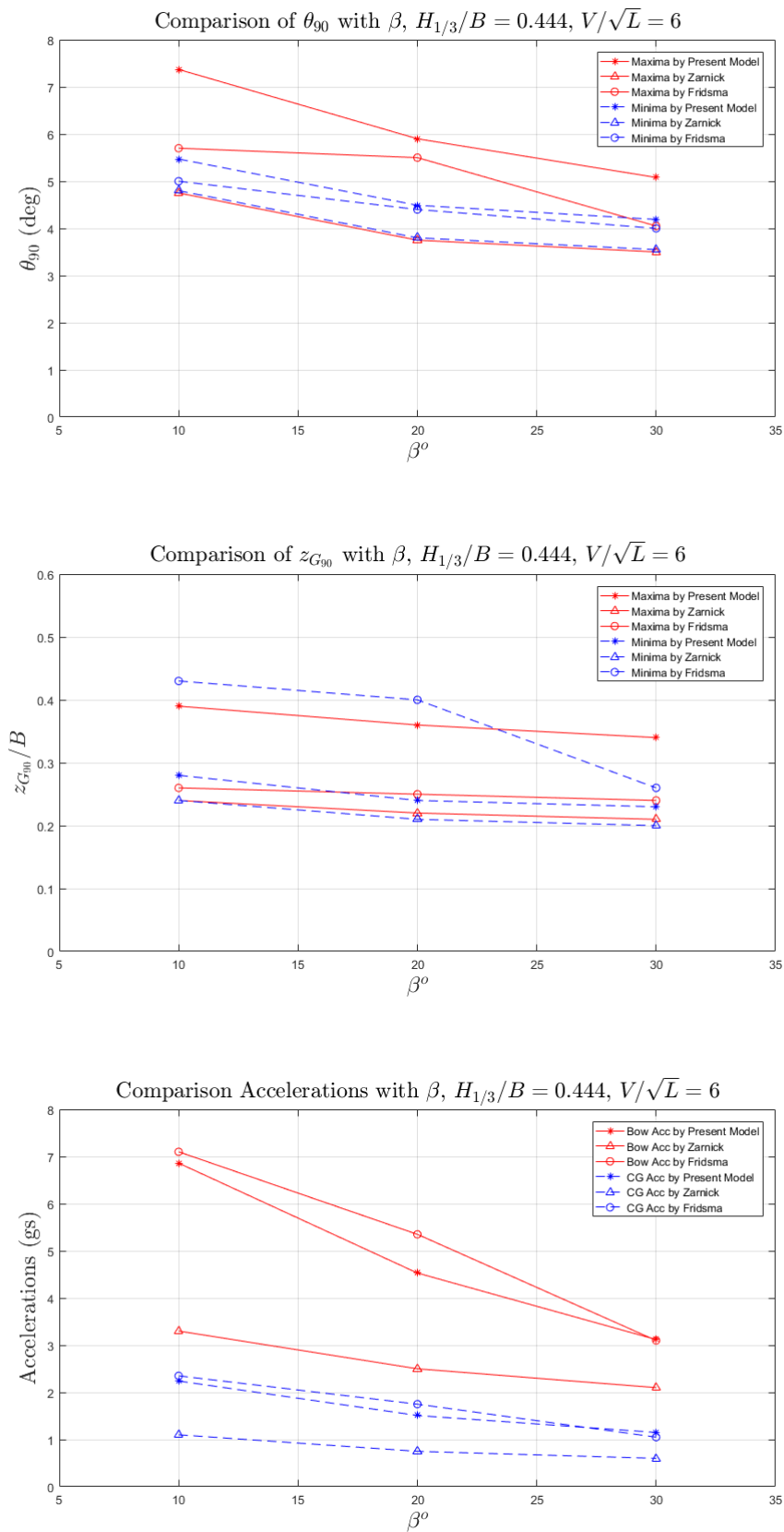
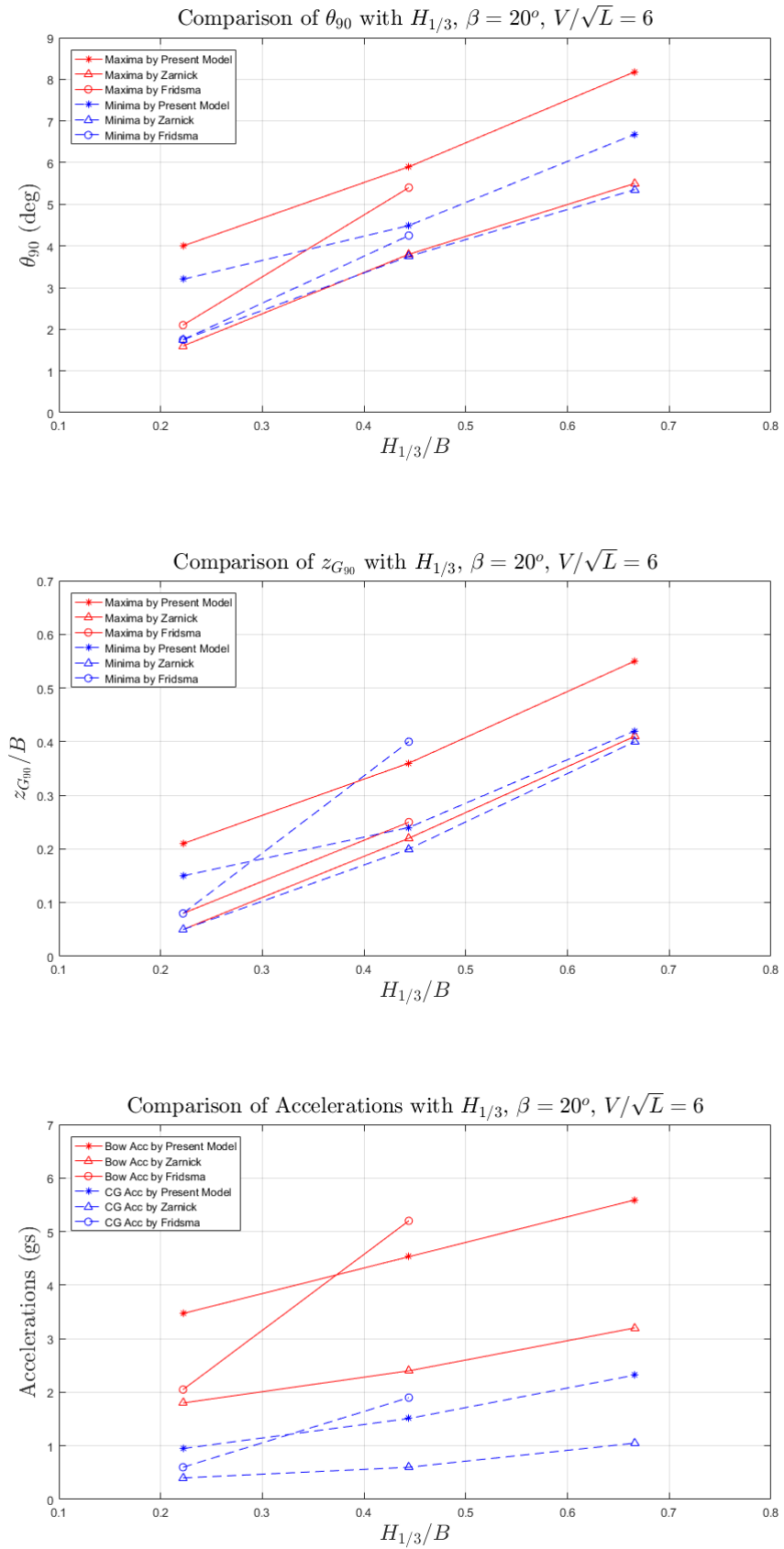


Figure 4.3: Statistic of response motions of different  $\beta$  hulls with  $H_{1/3}/B = 0.4$ ,  $V/\sqrt{L} = 6.0$ .

Figure 4.4: Statistic of response motions of  $\beta = 20^\circ$  hulls varying  $H_{1/3}/B$ .



## Chapter 5

# Extension to Transverse Asymmetric Motions

The mathematical developed in Chapter 3 is capable of simulating only the longitudinal plane motions. The water entry principle used is valid only for symmetrical geometries. This leads to the restriction of application to be capable of predicting in only coupled heave and pitch motions in upright planing dynamics. Practically, although a planing craft is likely to experience more significantly heave and pitch motions when sailing in calm water and waves, some situations such as empty side tanks could occur and cause asymmetric conditions even in calm water. Above all, when travelling in 3D irregular waves or oblique waves, asymmetric excitation forces are unavoidable causing roll motion. Therefore, it is of interest to perform investigations approaching these asymmetric situations.

A number of researchers have been working on this approach. [Algarín and Tascón \(2011\)](#) and [Algarín et al. \(2011\)](#) investigated pressure distribution of an asymmetric wedge falling into the water implementing the original work of [Ikeda and Katayama \(2000\)](#). The pressure distribution and total force evaluated by their methodologies are included in linear equations of motions fulfilling the external force and moment components. Hydrodynamic coefficients are necessary to be included in this kind of system of equations. [Ruscelli \(2009\)](#) and [Sebastiani et al. \(2008\)](#) modified the original [Zarnick \(1978\)](#)'s model eliminating the necessity of predefined hydrodynamic coefficients. Moreover, this simplification allows the mathematical model to be evaluated using only sectional added mass due to the heave motion, assumed to be valid in this coupled situation. Nevertheless, Ruscelli still considered the conventional roll damping components including in his model.

The present work is developed following the assumption of Ruscelli, simplifying some aspects to fulfil its aims to reduce computational efforts. Validation are performed with the existing experimental data in various situations of asymmetric planing conditions.

Due to the roll motion, considered as the rotation of the boat around the body fixed  $x'$  axis, the symmetry of section disappears. The loss of symmetry influences the calculation of hydrodynamic forces and moments. The original Zarnick's model was limited to vertical motions, and it was dedicated to symmetrical wedge shape water entry problem. When the roll motion is coupled, such a hypothesis is no longer applicable. Therefore, the extension to asymmetrical wedge shape is attempted in order to evaluate the total asymmetric hydrodynamic forces and moments of the hull.

Following this approach, each section of the hull is divided into 2 sides characterized by:

- Different equivalent deadrise angles defined as the sum of the effective deadrise angle  $\beta$  corresponding to a certain section and the roll angle  $\phi$ .
- Different values of the relative vertical velocities, properly calculated as a function of the effective submerged geometry of the model.

The total sectional force is considered as the sum of forces corresponding to port and starboard equivalent side acting on the corresponding part of the section and calculated separately section by section. The momentum theory (implemented by means of Strip Theory) is applied again for two different part of each section as described in the following expression:

$$f_{hyd_P} = \frac{1}{2} \left( \frac{D}{Dt} (m_{a_P} \cdot V_P) \right) \quad (5.1)$$

$$f_{hyd_S} = \frac{1}{2} \left( \frac{D}{Dt} (m_{a_S} \cdot V_S) \right) \quad (5.2)$$

Where:

- $f_{hyd_i}$ : Hydrodynamic force associated to the  $i^{th}$  port or starboard side of the hull.
- $\frac{D}{Dt}$ : Substantial derivative.
- $m_{a_i}$ : Sectional added mass associated to the  $i^{th}$  port or starboard side of the hull.
- $V_i$ : Relative velocities of section parallel to keel associated to the  $i^{th}$  port or starboard side of the hull.

Then, the total hydrodynamic force can be obtained as the sum of the integration along the ship length of each particular side:

$$F_{hyd} = \sum_{i=P,S} \int_L f_{hyd_i} dx' \quad (5.3)$$

As well as the roll moment:

$$M_{hyd_{x'}} = \sum_{i=P,S} \int_L f_{hyd_i} y'_i dx' \quad (5.4)$$

The term  $y_i$  represents the roll arm of the hydrodynamic forces acting in the port and starboard side of the section. It is defined as the centre of sectional pressure distribution following Wagner's theory, which consequently, is  $x'$  dependent.

Besides the hydrodynamic forces related to the added mass, the damping forces (neglected for the vertical plane motions) are considered due to their unavoidable influence in roll motion. However, as a first approach of the present work, damping components are initially excluded from the model, in order to observe the effects of this exclusion, simplifying the development of the mathematical model.

The nonlinear roll hydrostatic restoring forces will also be investigated. They can be calculated considering the effective wave profile on each section and evaluating section by section, the sectional area and its geometrical centre in order to evaluate the total hydrostatic buoyancy and its application point.

As a final consideration, it can be observed that the asymmetry is related to the following main aspects:

- **Asymmetric Submerged Volume Geometry:** Submerged volume and wet surface are no longer symmetrical, affecting hydrostatics and in general the points of application of forces.
- **Asymmetric Action of Fluid on Hull:** The hull in oblique sea undergoes different actions of fluid on its port and starboard side, due to different absolute wave velocities and relative ship motions relevant to roll. This aspect influences the relative vertical velocity and so the hydrodynamic forces related to the added mass.
- **Asymmetric of the Sectional Water Impact:** Due to roll, the section which impacts against water is not symmetrical. Port and starboard side are considered separately with their "Effective Equivalent Deadrise Angle", which is the resultant of the local geometrical deadrise and the roll angle in order to evaluate the added mass term.

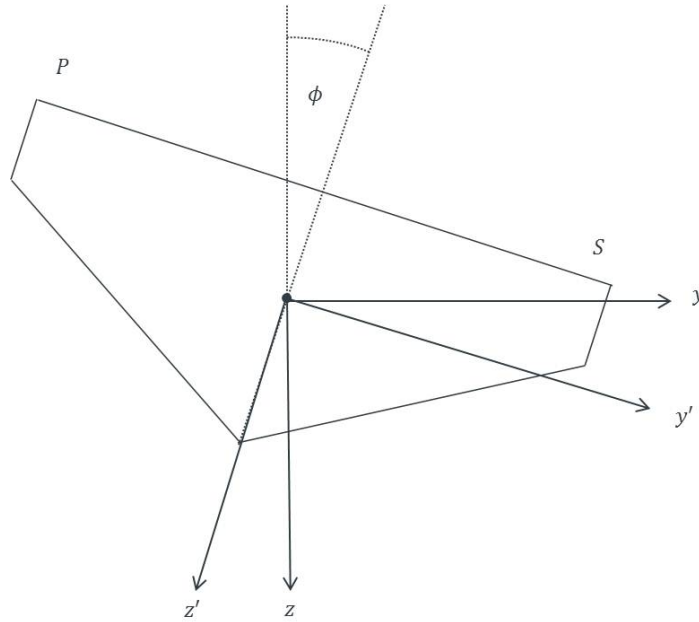


Figure 5.1: Transversal plane coordinate systems.

The theoretical and numerical models of the methodology dealing with the coupled heave, roll and pitch motions are presented in the following sections

## 5.1 Definition of Coordinate Systems

The coordinate systems are defined with the same principal as in the cases of coupled heave and pitch motions as follows:

- **Earth-Fixed Coordinate System: ( $Oxyz$ )** The origin is fixed in a certain point at non-disturbed water level. The positive  $x$ ,  $y$  and  $z$  directions point toward to the direction of the travel, toward to starboard side and downward to the water respectively.
- **Body-Fixed Coordinate System: ( $Gx'y'z'$ )** The origin of this system is located at the CG of the ship.  $x$  axis is parallel to the keel and points toward to the fore as positive direction while  $y'$  and  $z'$  point toward to starboard side and downward to the perpendicular to the keel respectively.

The coordinate systems in the transversal plane are shown in Figure 5.1:

Heave motion is so defined as the vertical distance of centre of gravity of the hull with respect to the calm water free surface. Pitch motion is defined as baseline inclination with respect to calm water level as well as roll motion is defined as the  $y'$  axis inclination. The roll angle  $\phi$  and pitch angle  $\theta$  are positive with the hull upward and heeled toward

port side respectively due to the right hand rule. The centre of pitch motion is de facto the centre of gravity while the centre of roll is also assumed to be as well the centre of gravity. In the reality, although the centre of roll varies dynamically, the experimental data used as validation reference were carried out by towing the model at its centre of gravity and allowed the model to pitch and roll only around that point.

## 5.2 Definition of Wave Characteristics

According to Figure 5.2, regular cylindrical waves are described in the earth-fixed coordinate system  $Oxyz$  by mean of:

$$x = x' \cos \mu - y' \sin \mu \quad (5.5)$$

$$y = x' \sin \mu + y' \cos \mu \quad (5.6)$$

Where  $\mu$  is heading angle varying from  $0^\circ$  to  $359^\circ$  in which  $\mu = 0^\circ$  is defined as head waves. Following the clockwise direction,  $\mu = 90^\circ$  and  $\mu = 180^\circ$  are lateral starboard waves and following waves respectively. Also in this case, with the aim to avoid sudden discontinuities in initial time of simulation (above all for heavy sea conditions), nominal wave amplitude is multiplied by a ramp functions which is 0 at the initial time marching and goes to 1 after an appropriate time interval.

Then, the wave expression to be used in this case is a modification of the wave expression defined in detail in Appendix A:

$$r_P = r_0 \cos [k (x_G + x' \cos \theta - (z_G - x' \sin \theta) \tan \theta) \cos \mu + ky'_P \sin \mu + \omega t] \quad (5.7)$$

$$r_S = r_0 \cos [k (x_G + x' \cos \theta - (z_G - x' \sin \theta) \tan \theta) \cos \mu + ky'_S \sin \mu + \omega t] \quad (5.8)$$

In general, wave elevation is a function of both longitudinal and transverse distance from the centre of gravity of the hull ( $x'$  and  $y'$  respectively). At a particular section, wave elevation corresponding to the equivalent port and starboard sides are approximated as those evaluated by assigning  $y'_P$  or  $y'_S$  to be equal to a half of the half breadth from the longitudinal plane. As the smallest wavelength used in simulation is equal to the model length, the variation of wave elevation is very small along the section and can be considered constant.

The expression of time derivative of wave elevation, wave vertical orbital velocity and its time derivative are consequently expressed as:



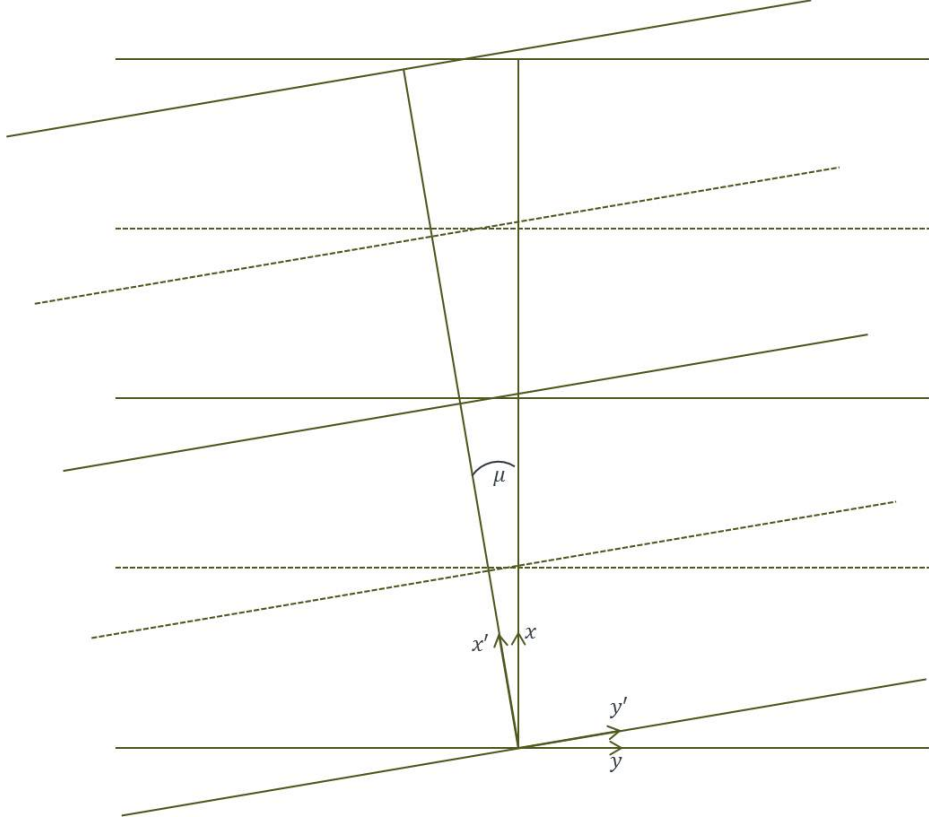


Figure 5.2: Oblique wave definition.

$$\dot{r}_P = \frac{dr}{dt} \quad (5.9)$$

$$\dot{r}_S = \frac{dr}{dt} \quad (5.10)$$

$$w_{wP} = -r_0\omega \sin [k (x_G + x' \cos \theta - (z_G - x' \sin \theta) \tan \theta) \cos \mu + ky'_P \sin \mu + \omega t] \quad (5.11)$$

$$w_{wS} = -r_0\omega \sin [k (x_G + x' \cos \theta - (z_G - x' \sin \theta) \tan \theta) \cos \mu + ky'_S \sin \mu + \omega t] \quad (5.12)$$

$$\dot{w}_{wP} = \frac{dw_w}{dt} \quad (5.13)$$

$$\dot{w}_{wS} = \frac{dw_w}{dt} \quad (5.14)$$

### 5.3 Equations of Motions of Coupled Heave, Roll and Pitch Motions

Planing hull motion laws are derived from the usual laws of dynamics. External forces considered are weight force, hydrostatic force, shaft thrust, wave force, and hydrodynamic forces. In the present model, following the same analogy as in the heave and pitch model, thrust force and drag force in the horizontal direction will be neglected due to

the definition of towed condition. The resulting system of global equations of motions are expressed as follows:

$$M \cdot \ddot{z}_G = -(F_{hyd} + F_{cfd}) \cdot \cos \theta - F_b + D \cdot \sin \theta + W \quad (5.15)$$

$$I_{xx} \cdot \ddot{\phi} = M_{hyd_{x'}} + M_{cfd_{x'}} + M_{b'_{x'}} + Dy_d + B_{\phi} \quad (5.16)$$

$$I_{yy} \cdot \ddot{\theta} = M_{hyd_{y'}} + M_{cfd_{y'}} + M_{b'_{y'}} - D \cdot x_d \quad (5.17)$$

Where the difference between the new equations of motions and the coupled heave and pitch motions are:

- $M_{i'_{x'}}: i^{th}$  moment contribution to roll.
- $M_{i'_{y'}}: i^{th}$  moment contribution to pitch.
- $B_{\phi}$ : Total roll damping.

The above-mentioned forces are computed as a variation with respect to time around the undisturbed steady equilibrium position at a specified speed.

Theoretical base for hydrodynamic force is again the “Momentum Theory”, stating that hydrodynamic force exerted by a fluid on the hull is equal and opposite to the variation of fluid momentum associated to the hull itself.

In the first appearance of the methodology, the momentum Theory is implemented by means of strip theory, considering the 3D hull as it is made of a conjunction of a number of 2D strip sections, and evaluating the total 3D forces as the summation of sectional forces acting separately on each particular section without interactions. This such principle, introduced by [Korvin-Kroukovsky and Jacobs \(1957\)](#) was fundamentally capable of evaluating only with vertical plane motions. Then, after contributions of various researchers, it was extended and implemented by [Salvesen et al. \(1970\)](#). The fundamental hypothesis is that the normal vector of each section has the longitudinal component  $n_x$  much lower than the other two components  $n_y$  and  $n_z$  as described:

$$\begin{cases} n_x & \ll n_y \\ n_x & \ll n_z \end{cases}$$

The total sectional hydrodynamic force is considered as the sum of the equivalent port and starboard forces acting on the corresponding side of the section. The evaluation is performed separately section by section through the momentum theory as described in

Equations 5.1 - 5.2. The evaluation of each term in the system of equations of motions uses the same analogy as in the case of coupled heave and pitch motions. The expressions corresponding to each term are explained as follows:

### 5.3.1 Hydrodynamic Lift Force

The hydrodynamic lift force is evaluated separately in two equivalent port and starboard side sections, and by following the principal of momentum theory, the formulation of rate of change of fluid momentum is expressed as:

$$f_{h_{P,S}} = \frac{1}{2} \left( \frac{D}{Dt} (m_{a_{P,S}} V_{P,S}) \right) = \frac{1}{2} \left( m_{a_{P,S}} \dot{V}_{P,S} + \dot{m}_{a_{P,S}} V_{P,S} - U \frac{\partial}{\partial x} (m_{a_{P,S}} V_{P,S}) \right) \quad (5.18)$$

Note that all of the sectional forces need to be halved in order to comply the assumption of equivalent wedge water entry, as the overall sectional forces are the sum of both equivalent sides.

The formulation for the sectional added mass adopted in the present mathematical is described in the following form:

$$m_{a_P} = C_m \rho \frac{\pi}{2} \left( \frac{C_{pu} h_P}{\tan(\beta - \phi)} \right)^2 \quad (5.19)$$

$$m_{a_S} = C_m \rho \frac{\pi}{2} \left( \frac{C_{pu} h_S}{\tan(\beta + \phi)} \right)^2 \quad (5.20)$$

The expressions of time derivative of sectional added mass appear to be more complicated due to the appearance of roll angle and its dynamic properties which are time dependent :

$$\dot{m}_{a_P} = C_m \rho \pi \left( \frac{h_P C_{pu}}{\tan(\beta - \phi)} \right) \frac{d}{dt} \left( \frac{h_P C_{pu}}{\tan(\beta - \phi)} \right) \quad (5.21)$$

$$\dot{m}_{a_S} = C_m \rho \pi \left( \frac{h_S C_{pu}}{\tan(\beta + \phi)} \right) \frac{d}{dt} \left( \frac{h_S C_{pu}}{\tan(\beta + \phi)} \right) \quad (5.22)$$

The time derivative in the last part of the expression of time derivative of sectional added mass can be developed as follows:

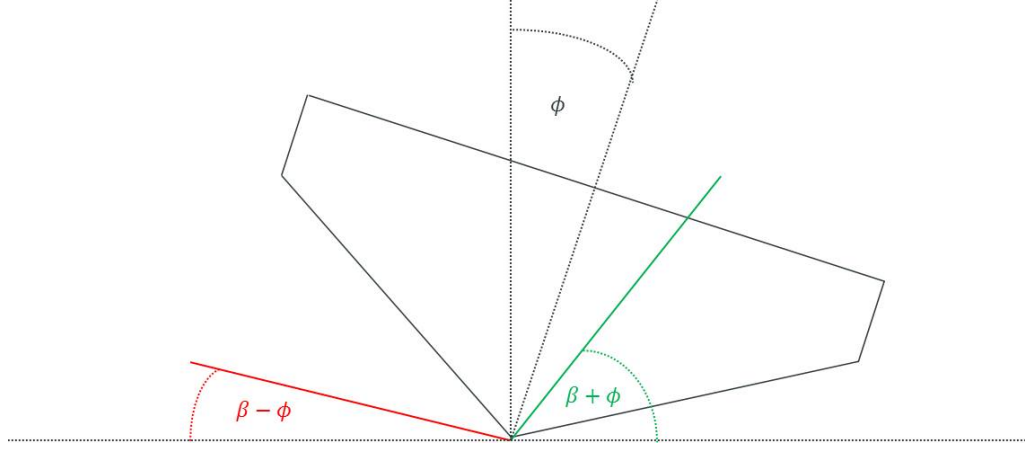


Figure 5.3: Asymmetric geometrical equivalent I.

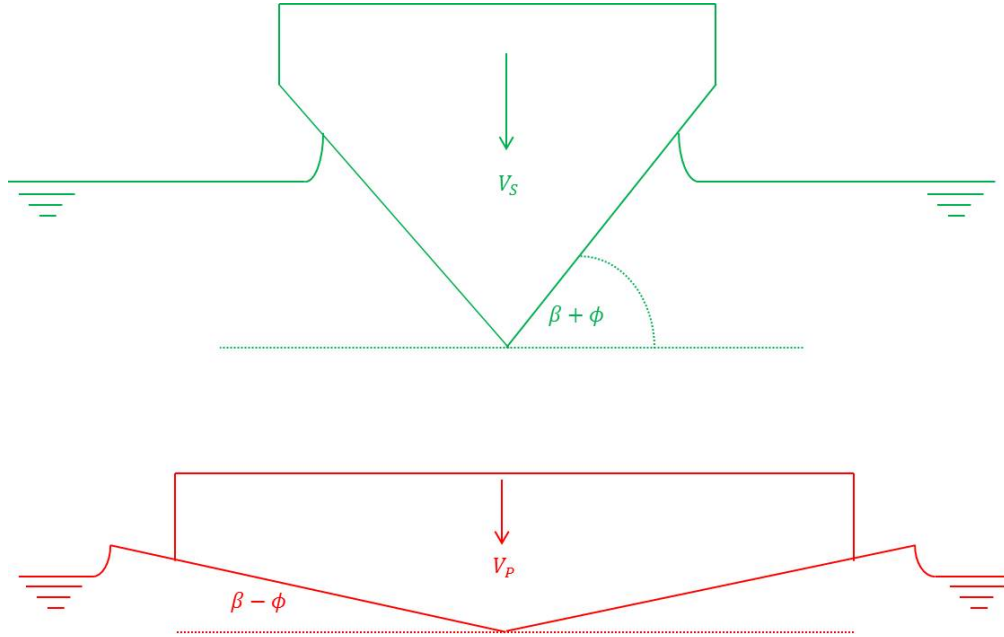


Figure 5.4: Asymmetric geometrical equivalent II.

$$\frac{d}{dt} \left( \frac{h_P C_{pu}}{\tan(\beta - \phi)} \right) = \frac{(\dot{h}_P C_{pu} + h_P \dot{C}_{pu}) \tan(\beta - \phi) + h_P C_{pu} \left[ (\tan^2(\beta - \phi)) \dot{\phi} \right]}{\tan^2(\beta - \phi)} \quad (5.23)$$

$$\frac{d}{dt} \left( \frac{h_S C_{pu}}{\tan(\beta + \phi)} \right) = \frac{(\dot{h}_P C_{pu} + h_P \dot{C}_{pu}) \tan(\beta + \phi) - h_P C_{pu} \left[ (\tan^2(\beta + \phi)) \dot{\phi} \right]}{\tan^2(\beta + \phi)} \quad (5.24)$$

Figures 5.3 - 5.4 show that the effective deadrise angle corresponding to port and starboard side are  $(\beta - \phi)$  and  $(\beta + \phi)$  respectively. The pile-up correction factor  $C_{pu}$  in this case is assumed to be that corresponding to the side of larger effective deadrise angle:

$$C_{pu} = \frac{\pi}{2} - (\beta + |\phi|) \left(1 - \frac{2}{\pi}\right) \quad (5.25)$$

And its time derivative:

$$\dot{C}_{pu} = \left(\frac{2}{\pi} - 1\right) \cdot \dot{\phi} \quad (5.26)$$

The section submergence is now necessary to account for the different effective deadrise angle:

$$h_P = z'_k \cos \phi + \left(\frac{z_G - x' \sin \theta}{\cos \theta}\right) - \frac{r_P}{\cos \theta} \quad (5.27)$$

$$h_S = z'_k \cos \phi + \left(\frac{z_G - x' \sin \theta}{\cos \theta}\right) - \frac{r_S}{\cos \theta} \quad (5.28)$$

Consequently, their time derivatives are expressed as:

$$\dot{h}_P = -\sin \phi \dot{\phi} + \left(\frac{(\dot{z}_G - x' \cos \theta \dot{\theta}) + (z_G - x' \sin \theta) \sin \theta \dot{\theta}}{\cos^2 \theta}\right) - \left(\frac{\dot{r}_P \cos \theta + r_P \sin \theta \dot{\theta}}{\cos^2 \theta}\right) \quad (5.29)$$

$$\dot{h}_S = -\sin \phi \dot{\phi} + \left(\frac{(\dot{z}_G - x' \cos \theta \dot{\theta}) + (z_G - x' \sin \theta) \sin \theta \dot{\theta}}{\cos^2 \theta}\right) - \left(\frac{\dot{r}_S \cos \theta + r_S \sin \theta \dot{\theta}}{\cos^2 \theta}\right) \quad (5.30)$$

The relative sectional velocities parallel or normal to the keel are defined based on the similar analogy of the case of coupled heave and pitch motions taken into account the effect of roll motion in especially the normal velocity  $V$ . Each equivalent port and starboard side section with corresponding effective deadrise angle is actually affected by roll velocity  $\dot{\phi}$  and are expressed as follows:

$$U = \dot{x}_G \cdot \cos \theta - (\dot{z}_G - w_w) \sin \theta \quad (5.31)$$

$$V_P = \dot{x}_G \cdot \sin \theta + (\dot{z}_G - w_{w_S}) \cos \theta - \dot{\theta} \cdot x' - \dot{\phi} \cdot y'_P \quad (5.32)$$

$$V_S = \dot{x}_G \cdot \sin \theta + (\dot{z}_G - w_{w_P}) \cos \theta - \dot{\theta} \cdot x' - \dot{\phi} \cdot y'_S \quad (5.33)$$

$$\dot{V}_P = \ddot{x}_G \cdot \sin \theta + (\ddot{z}_G - \dot{w}_{w_P}) \cos \theta + \dot{\theta}(\dot{x}_G \cos \theta - (\dot{z}_G - w_{w_P}) \sin \theta) - \ddot{\theta} \cdot x' - \ddot{\phi} y'_P \quad (5.34)$$

$$\dot{V}_S = \ddot{x}_G \cdot \sin \theta + (\ddot{z}_G - \dot{w}_{w_S}) \cos \theta + \dot{\theta}(\dot{x}_G \cos \theta - (\dot{z}_G - w_{w_S}) \sin \theta) - \ddot{\theta} \cdot x' - \ddot{\phi} y'_S \quad (5.35)$$

The roll lever arms  $y'_P$  and  $y'_S$  are defined in the case hydrodynamic lift force as centre of pressure corresponding to each equivalent side section following the theory of wedge shape water entry of [Wagner \(1931\)](#).

$$y'_P = \frac{\frac{\pi}{(\beta-\phi)} \left(1 - \sqrt{1 - y'^2_{0_P}}\right) + \frac{1}{2} \ln(1 - y'^2_{0_P}) + \frac{1}{2} y'^2_{0_P}}{\frac{\pi}{(\beta-\phi)} \arcsin y'_{0_P} + \frac{1}{2} \ln\left(\frac{1-y'_{0_P}}{1+y'_{0_P}}\right) + y'_{0_P}} \quad (5.36)$$

$$y'_S = \frac{\frac{\pi}{(\beta+\phi)} \left(1 - \sqrt{1 - y'^2_{0_S}}\right) + \frac{1}{2} \ln(1 - y'^2_{0_S}) + \frac{1}{2} y'^2_{0_S}}{\frac{\pi}{(\beta+\phi)} \arcsin y'_{0_S} + \frac{1}{2} \ln\left(\frac{1-y'_{0_S}}{1+y'_{0_S}}\right) + y'_{0_S}} \quad (5.37)$$

Where  $y'_{0_{P,S}}$  are the abscissa where pressure distribution is equal to zero and expressed as:

$$y'_{0_P} = \sqrt{1 - \left(\frac{\sqrt{\pi^2 - 4(\beta - \phi)^2} - \pi}{2(\beta - \phi)}\right)^2} \quad (5.38)$$

$$y'_{0_S} = \sqrt{1 - \left(\frac{\sqrt{\pi^2 - 4(\beta + \phi)^2} - \pi}{2(\beta + \phi)}\right)^2} \quad (5.39)$$

This definition of roll lever arms is valid only for hydrodynamic forces, the roll arm for hydrostatic force is explained subsequently.

### 5.3.2 Cross-Flow Drag:

The expression of sectional cross-flow drag adopted to equivalent port and starboard sides are expressed as:

$$f_{cfd_P} = \frac{1}{2} C_{D,c} \cos(\beta - \phi) \rho \left( \frac{C_{pu} h_P}{\tan(\beta - \phi)} \right) V_P^2 \quad (5.40)$$

$$f_{cfd_S} = \frac{1}{2} C_{D,c} \cos(\beta + \phi) \rho \left( \frac{C_{pu} h_S}{\tan(\beta + \phi)} \right) V_S^2 \quad (5.41)$$

### 5.3.3 Buoyancy:

As it can be seen in Figure 5.5, physical submerged geometry of a particular section with instantaneous heel angle is a composition of various sub-geometry. Generally it can be divided into two equivalent port and starboard sides, nevertheless, in this case, the geometry can be evaluated only in half section form. The geometry of sections can be grouped into two main ranges of flow characteristic. In the dry chine range, the submerged geometry is a simple triangle while in the wetted chine range, it is composed of a triangle and a trapezoid. The expressions are as follows:

If  $0 < h_{P,S} < a$

$$A_P = h_P^2 \cot(\beta - \phi) \quad (5.42)$$

$$A_S = h_S^2 \cot(\beta + \phi) \quad (5.43)$$

If  $h_{P,S} > a$

$$A_P = \frac{1}{2} a_P^2 \cot(\beta - \phi) + \frac{1}{2} (h_P - a_P) [2a_P \cot(\beta - \phi) + (h_P - a_P) \tan \phi] \quad (5.44)$$

$$A_S = \frac{1}{2} a_S^2 \cot(\beta + \phi) + \frac{1}{2} (h_S - a_S) [2a_S \cot(\beta + \phi) - (h_S - a_S) \tan \phi] \quad (5.45)$$

Where:

- $b = B/2$ : The half beam.
- $a = b \tan \beta$
- $a_S = b \sin(\beta + \phi) / \cos \beta$
- $a_P = b \sin(\beta - \phi) / \cos \beta$

The roll moment of buoyancy is evaluated with a different lever arm defined previously for hydrostatic force which is the centre of pressure acting on each section. In this

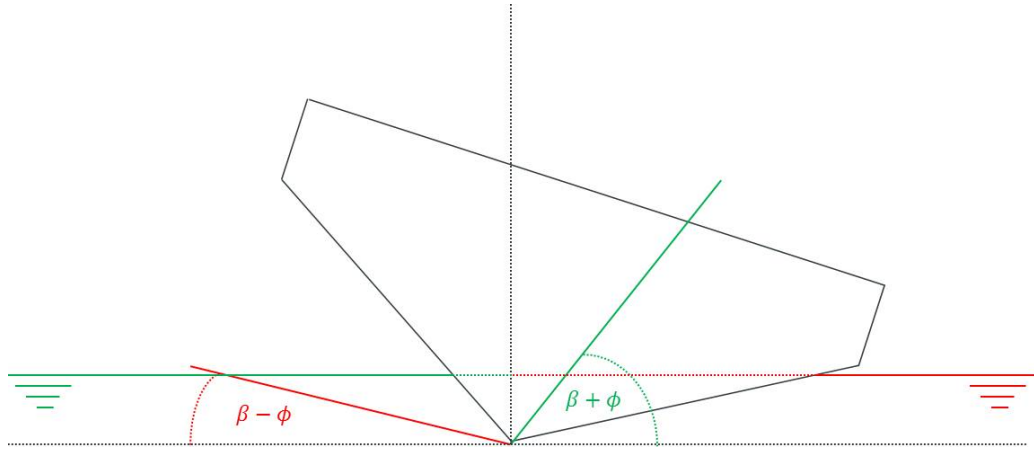


Figure 5.5: Asymmetric geometrical of buoyancy.

case, the centre of application of buoyancy force corresponding to each equivalent port and starboard side sections is defined as the centre of mass of the submerged geometry respect to the centre of roll motion (in this case the VCG). In case of a simple triangle, it can be assumed as  $1/3$  of the triangle base. The expression of centre of geometry of a trapezoid can be found in literature as  $y' = (a^2 + ab + b^2) / 3 (a + b)$

#### 5.3.4 Total Forces and Moments

Once obtaining the sectional forces corresponding to each equivalent port and starboard side, by integrating along the ship length, the total forces and moments of each side are obtained. Finally, by summing both sides, the total forces and moments acting on the hull are obtained. They are explained in the following expressions:



$$F_h = \sum_{i=P,S} \int_L f_{h_i} dx' = \sum_{i=P,S} \frac{1}{2} \int_L m_{a_i} \dot{V}_i + \dot{m}_{a_i} V_i - U \frac{\partial}{\partial x'} (m_{a_i} V_i) dx' \quad (5.46)$$

$$F_{cfd} = \sum_{i=P,S} \int_L f_{cfd_i} dx' = \sum_{i=P,S} \frac{1}{2} \int_L C_{D,C} \cos \beta \rho b_i V_i^2 dx' \quad (5.47)$$

$$F_b = \sum_{i=P,S} \int_L f_{b_i} dx' = \sum_{i=P,S} \frac{1}{2} \int_L a_{bf} \rho g A_i dx' \quad (5.48)$$

$$M_{h_{y'}} = \sum_{i=P,S} \int_L f_{h_i} x' dx' = \sum_{i=P,S} \frac{1}{2} \left[ \int_L m_{a_i} \dot{V}_i + \dot{m}_{a_i} V_i - U \frac{\partial}{\partial x'} (m_{a_i} V_i) \right] x' dx' \quad (5.49)$$

$$M_{cfd_{y'}} = \sum_{i=P,S} \int_L f_{cfd_i} x' dx' = \sum_{i=P,S} \frac{1}{2} \int_L C_{D,C} \cos \beta \rho b_i V_i^2 x' dx' \quad (5.50)$$

$$M_{b_{y'}} = \sum_{i=P,S} \int_L f_{b_i} x' dx' = \sum_{i=P,S} \frac{1}{2} \int_L a_{bf} \rho g A_i x' dx' \quad (5.51)$$

$$M_{h_{x'}} = \sum_{i=P,S} \int_L f_{h_i} y'_i dx' = \sum_{i=P,S} \frac{1}{2} \left[ \int_L m_{a_i} \dot{V}_i + \dot{m}_{a_i} V_i - U \frac{\partial}{\partial x'} (m_{a_i} V_i) \right] y'_i dx' \quad (5.52)$$

$$M_{cfd_{x'}} = \sum_{i=P,S} \int_L f_{cfd_i} y'_i dx' = \sum_{i=P,S} \frac{1}{2} \int_L C_{D,C} \cos \beta \rho b_i V_i^2 y'_i dx' \quad (5.53)$$

$$M_{b_{x'}} = \sum_{i=P,S} \int_L f_{b_i} y'_i dx' = \sum_{i=P,S} \frac{1}{2} \int_L a_{bf} \rho g A_i y'_i dx' \quad (5.54)$$

Substituting and developing all terms of the expression of the total forces and moments in the global equations of motions, and following the same methodology as in the case of coupled heave and pitch motions, and taken into account the influence of Near Transom Correction Factor,  $C_{tr}$ , the system can be elaborated into the following form using the coefficient assignment defined in Appendix A:

$$\begin{aligned} M\ddot{z}_G = & - \left( C_A \cos \theta \dot{x}_G \dot{\theta} + C_A \cos \theta \ddot{z}_G - C_A \sin \theta \dot{z}_G \dot{\theta} - C_B \cos \theta + C_C \sin \theta \dot{\theta} - C_{D1} \ddot{\theta} - C_{D2} \ddot{\phi} \right. \\ & \left. + C_E - C_F + C_G \cos \theta + C_{H1} \dot{\theta} + C_{H2} \dot{\phi} - F_{cfd} \right) \cos \theta - F_b + D \sin \theta + W \end{aligned} \quad (5.55)$$

$$\begin{aligned} I_{xx} \ddot{\phi} = & C_{D2} \cos \theta \dot{x}_G \dot{\theta} + C_{D2} \cos \theta \ddot{z}_G - C_{D2} \sin \theta \dot{z}_G \dot{\theta} - C_S \cos \theta + C_T \sin \theta \dot{\theta} - C_{N2} \ddot{\theta} - C_U \ddot{\phi} \\ & + C_{O2} - C_V + C_W \cos \theta + C_{X1} \dot{\theta} + C_{X2} \dot{\phi} + M_{cfd} + M_b - D y_d \end{aligned} \quad (5.56)$$

$$\begin{aligned}
I_{yy}\ddot{\theta} = & C_{D1} \cos \theta \dot{x}_G \dot{\theta} + C_{D1} \cos \theta \ddot{z}_G - C_{D1} \sin \theta \dot{z}_G \dot{\theta} - C_K \cos \theta + C_M \sin \theta \ddot{\theta} - C_{N1} \ddot{\theta} - C_{N2} \ddot{\phi} \\
& + C_{O1} - C_P + C_Q \cos \theta + C_{R1} \dot{\theta} + C_{R2} \dot{\phi} + M_{cfd} + M_b - Dx_d
\end{aligned} \tag{5.57}$$

Moving the terms associated to accelerations to the left hand side and reorder the system:

$$\begin{aligned}
(M + C_A \cos^2 \theta) \ddot{z}_G - C_{D2} \cos \theta \ddot{\phi} - C_{D1} \cos \theta \ddot{\theta} = & - \left( C_A \cos \theta \dot{x}_G \dot{\theta} - C_A \sin \theta \dot{z}_G \dot{\theta} - C_B \cos \theta \right. \\
& + C_C \sin \theta \ddot{\theta} + C_E - C_F + C_G \cos \theta + C_{H1} \dot{\theta} \\
& \left. + C_{H2} \dot{\phi} - F_{cfd} \right) \cos \theta - F_b + D \sin \theta + W
\end{aligned} \tag{5.58}$$

$$\begin{aligned}
-C_{D2} \cos \theta \ddot{z}_G + (I_{xx} + C_U) \ddot{\phi} + C_{N2} \ddot{\theta} = & C_{D2} \cos \theta \dot{x}_G \dot{\theta} - C_{D2} \sin \theta \dot{z}_G \dot{\theta} - C_S \cos \theta \\
& + C_T \sin \theta \ddot{\theta} + C_{O2} - C_V + C_W \cos \theta + C_{X1} \dot{\theta} \\
& + C_{X2} \dot{\phi} + M_{cfd} + M_b - Dy_d
\end{aligned} \tag{5.59}$$

$$\begin{aligned}
-C_{D1} \cos \theta \ddot{z}_G + C_{N2} \ddot{\phi} + (I_{yy} + C_{N1}) \ddot{\theta} = & C_{D1} \cos \theta \dot{x}_G \dot{\theta} - C_{D1} \sin \theta \dot{z}_G \dot{\theta} - C_K \cos \theta \\
& + C_M \sin \theta \ddot{\theta} + C_{O1} - C_P + C_Q \cos \theta + C_{R1} \dot{\theta} \\
& + C_{R2} \dot{\phi} + M_{cfd} + M_b - Dx_d
\end{aligned} \tag{5.60}$$

Then turn the system into the matrix form:

$$A \cdot \ddot{\vec{x}} = B \tag{5.61}$$

Where:

$$A = \begin{pmatrix} M + C_A \cos^2 \theta & -C_{D2} \cos \theta & -C_{D1} \cos \theta \\ -C_{D2} \cos \theta & I_{xx} + C_U & C_{N2} \\ -C_{D1} \cos \theta & C_{N2} & I_{yy} + C_{N1} \end{pmatrix} \quad (5.62)$$

$$\ddot{\vec{x}} = \begin{pmatrix} \ddot{z}_G \\ \ddot{\phi} \\ \ddot{\theta} \end{pmatrix} \quad (5.63)$$

$$B = \begin{pmatrix} F'_z + D \sin \theta + W \\ F'_\phi - D y_d \\ F'_\theta - D x_d \end{pmatrix} \quad (5.64)$$

The system is solved in a similar manner to the case of coupled heave and pitch motions.

## 5.4 Simulations and Validations

Once the mathematical model has been modified, it is essential to verify its performance. As the modification is involved only in separate evaluation of sectional load in each corresponding equivalent lateral loads, verification of the influence of controlling parameters is assumed to be done and identical to the process done in Chapter 3. The remaining verification is to identify if it is capable of roll motions. A set of initial simulations has been carried out applying to a planing craft travelling in oblique seas. Sample time histories of heave, roll and pitch motions simulated in  $15^\circ$  and  $30^\circ$  oblique seas are shown in Figure 5.6. It can be seen that the present mathematical model gives reasonable results, as increasing angle of wave direction, amplitude of roll responses increase.

### 5.4.1 Fixed Heel Angle Simulations

When a planing craft is sailing with an empty lateral tank, the craft is facing unavoidably heel situation. It is obviously essential to assess the craft's performance in such kind of situation. The modified mathematical model applied to asymmetric sectional wedge shape load evaluations is used to simulate fixed heel angles situations. The simulations follow the experimental tests carried out by Li (2014). The model configuration is identical to Fridsma's model configuration B. The test has been carried out in three different heel angles, upright condition,  $5^\circ$  and  $10^\circ$  heels ( $\phi = \{0^\circ, 5^\circ, 10^\circ\}$ ). Regarding the sea conditions, wavelength to ship length ratio varies from  $\lambda/L = 1.5$  to  $\lambda/L = 4.0$  with only  $H/B = 0.1$ . The resulting data is treated in the identical manner as in cases done in Chapter 3, and represented in form of RAO. The results of experimental tests and numerical simulations are compared in Figure 5.7. It can be seen that the present mathematical model gives the results with the same trend as the experimental

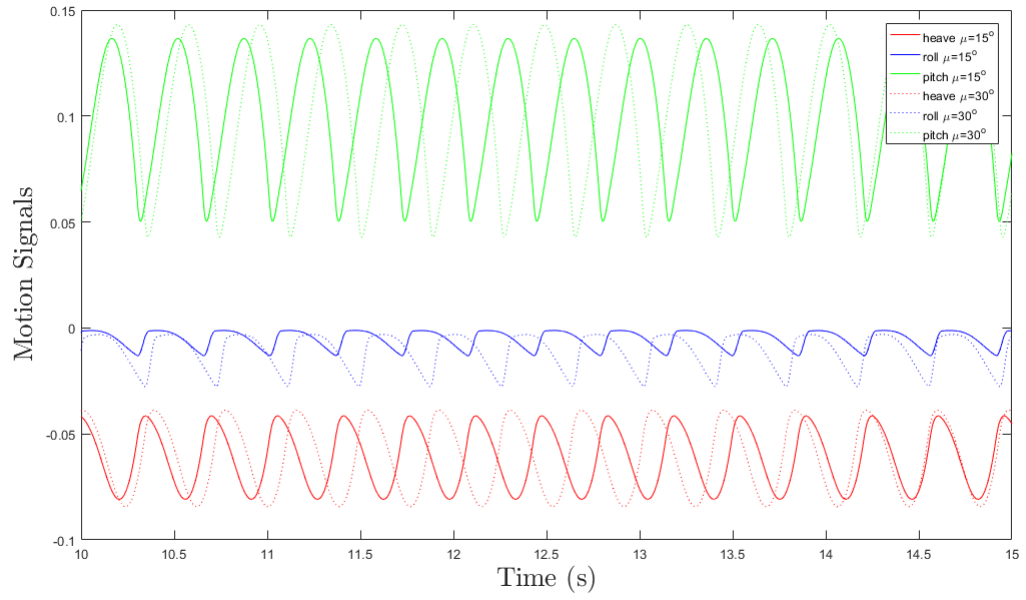


Figure 5.6: Sample of time histories of response motions in  $\lambda/L = 2.0$ .

tests but slightly over-predicts the magnitudes of both heave and pitch responses. The difference of the resulting magnitudes between the tests and the simulations appears to be constantly uniform. This could imply an existence of a missing component in the equations of motions. An inclusion of a constant factor would fit the response motions of the simulations to the tests. Note that the lack of roll damping components does not affect these cases. As the model is not allowed to roll freely, the damping component is evidently not the predominant term in case of only coupled heave and pitch motions. Note that the present mathematical model simplifies geometrical characteristics of the asymmetrical wedge by only the superposition of two equivalent symmetrical ones. As per suggested by [Ruscelli \(2009\)](#), the lateral equivalent sectional load predicted by momentum theory should be analysed and compared with existing asymmetric wedge falling vertically into the water in order to achieve the appropriate factor. Nevertheless, this simplification seems to be acceptable once the appropriate factor is verified.

#### 5.4.2 Coupled Heave, Roll and Pitch Motions Simulations

It is difficult to find validation reference of planing roll motion in literature. The most related to the plan of the present work is that of [Ruscelli \(2009\)](#) and [Rosén and Garne \(2006\)](#). Rosén and Garne performed a series of experiments of planing hull model with variable deadrise angles. The model was towed at its CG and allowed to heave, roll and pitch with a range of forward speed in regular head and oblique waves. The results are represented in the classical form of response amplitude operator, RAO. The present mathematical model in extension to roll motion is assumed to be already verified due to the original of this modification is that of the case of coupled heave and pitch

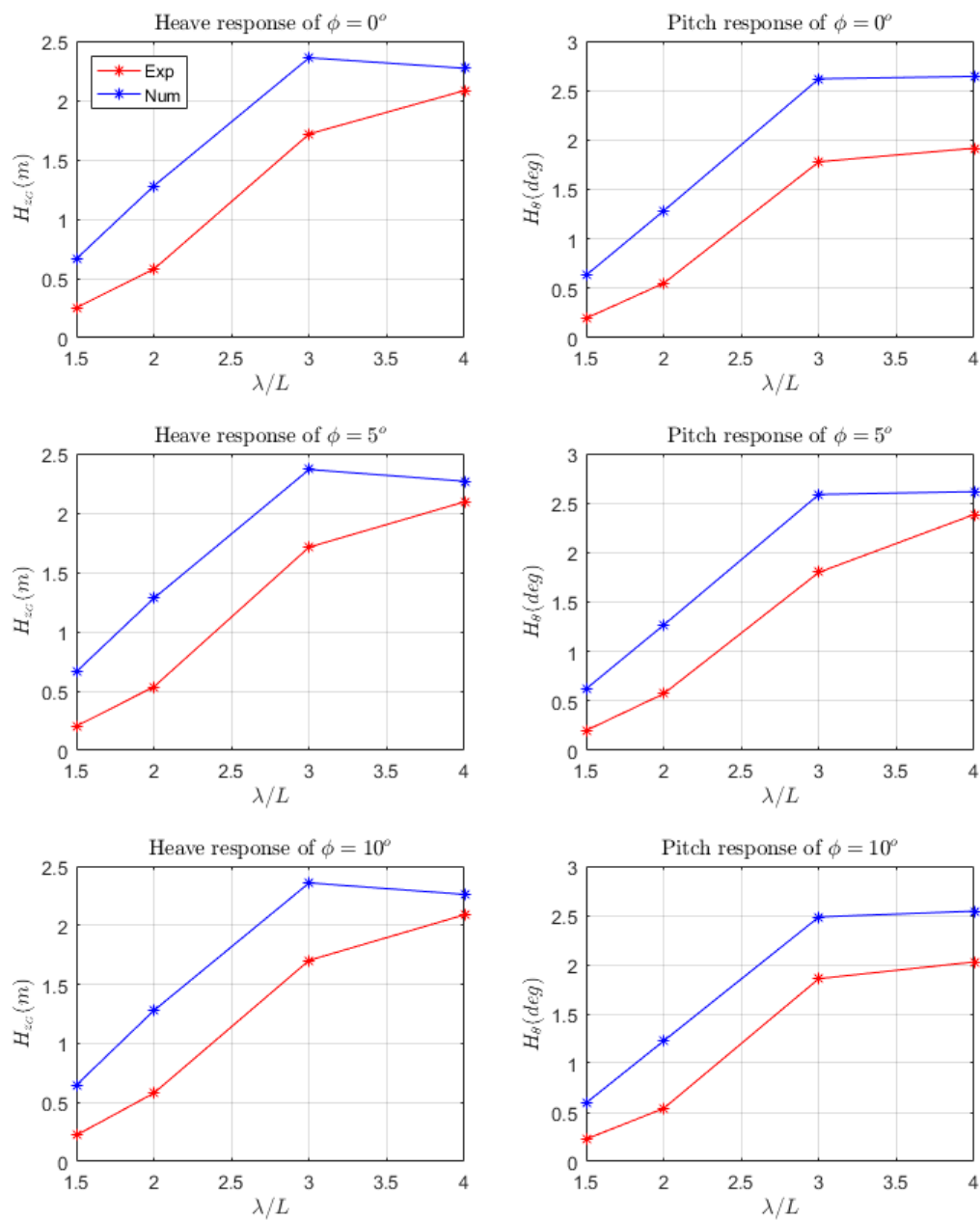


Figure 5.7: Comparison of response motions of fixed heel simulations.

which is already verified in Chapter 3. Actually, the mathematical model is simplified to simulate only in coupled heave, roll and pitch motion and planned to extend further to the remaining degrees of freedom. The damping components although have been neglected in heave and pitch motions, it is difficult to confirm the validity using the same hypothesis in roll motion. The damping components are still subjected to be developed and will be incorporated as a recommended implementation for the future work.

Table 5.1: Model configuration used by [Rosén and Garne \(2006\)](#).

Dimension	Outlined	Measured	Comment
$L_{oa}[m]$	1.050	1.110	Length overall
$L_{wl}[m]$	0.950		Length waterline, idle
$B_{wl}[m]$	0.250	0.250	Beam waterline, idle
$T_{lcf}[m]$	0.055		Draft, idle
$\beta[degree]$	22.000	22.000	Deadrise
$\tau[degree]$	1.500	1.500	Trim, idle
$\Delta[kg]$	6.500	6.500	Displacement
$LCG[m]$	0.3600	0.360	Logitudinal CG from transom
$VCG[m]$	0.092	0.092	Vertical CG from keel
$r_x[m]$	0.082	0.087	Roll radius of gyration
$r_y[m]$	0.270	0.270	Pitch radius of gyration
$r_z[m]$	0.270	0.270	Yaw radius of gyration

The model configuration used in the initial simulation following the experiments of Rosén and Garne is shown in Table 5.1. The response motions and accelerations are treated and compared in the form of RAO and shown in Figures 5.8 - 5.11.

For all of the response motions, the present mathematical model gives extreme values at  $\lambda/L = 3.0$ , in any direction of waves and especially for the lowest wave height ( $H/B = 0.1$ ). This is the effect of the natural frequency area of RAO that the damping associated term is predominant. The absence of damping component in the equations of motions leads to these extreme motions compared with the resulting response of experimental tests. For heave and pitch motions, when the frequencies of encounter are higher than that natural frequency area, the present mathematical model is capable of predicting the response motions closer to the experimental tests. When considering the response roll motion, the present mathematical model gives generally slight under predicted results, but still closer to the experiments after that natural frequency area. The largest difference occurs at the lowest wave height, and decreases nonlinearly when increasing the wave height. This could confirm the nonlinear behaviour of the response roll motion with the wave height property of the environments. The overall bow accelerations are of good agreement between the prediction and the experiments. Except the natural frequency area but the order of difference is not significantly notable.

The overall capability of this modification to asymmetrical motion simulations seems to be effective when simulating in higher frequencies of encounter over the natural frequency

area. In other words, due to the lack of damping component in the equations of motions, the simulations in that damping predominant zone cannot be adequately carried out. The present mathematical model needs further implementation and inclusion of this appropriate component, in order to comply with the application to any wave conditions.

With the implementation presented in this chapter, the mathematical model can be considered as a useful tool and partially effective for simulating asymmetric plane motions. It can also be used as a base model for further extensions to the remaining degrees of freedom.

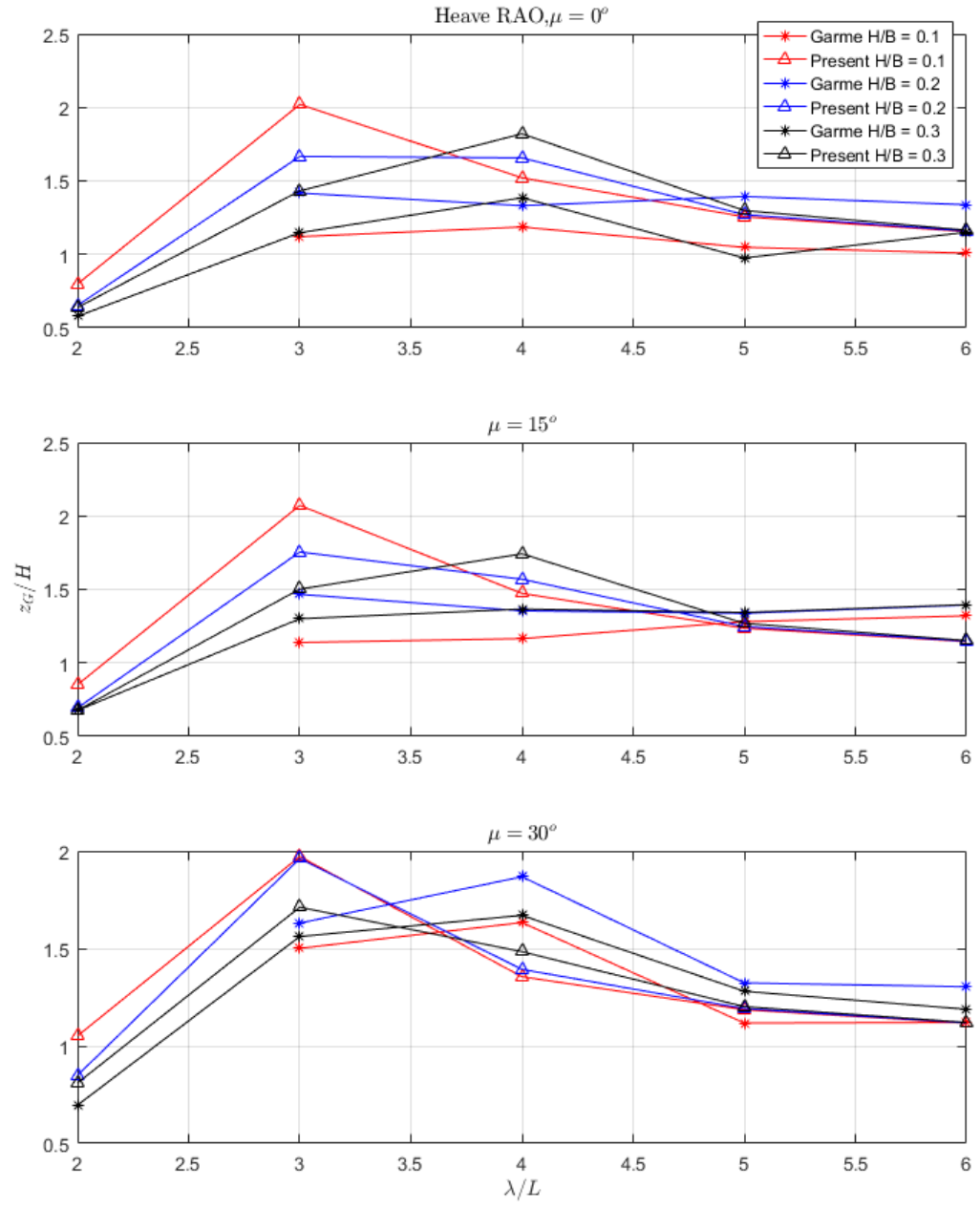


Figure 5.8: Comparison of response heave motions.



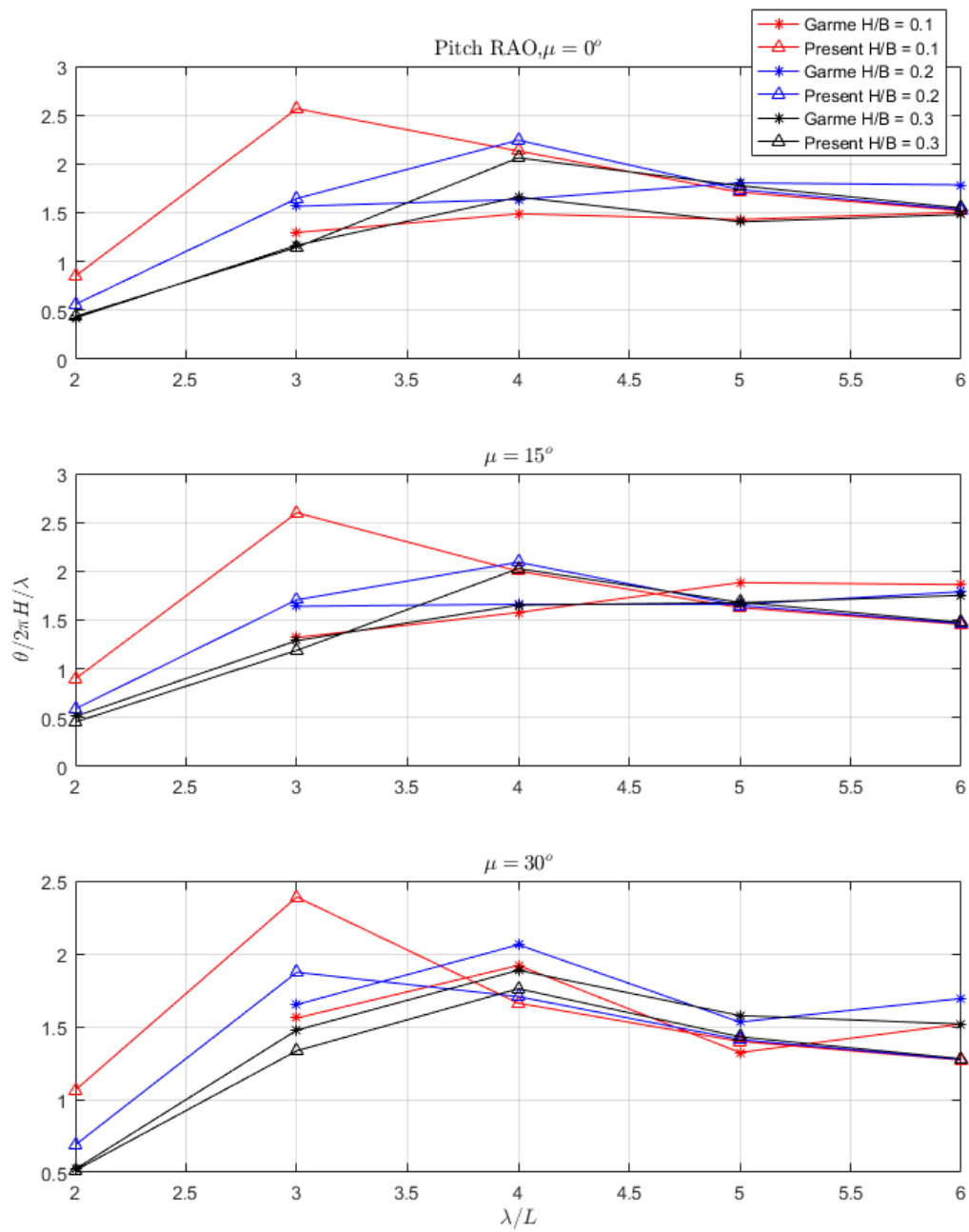


Figure 5.9: Comparison of response pitch motions.

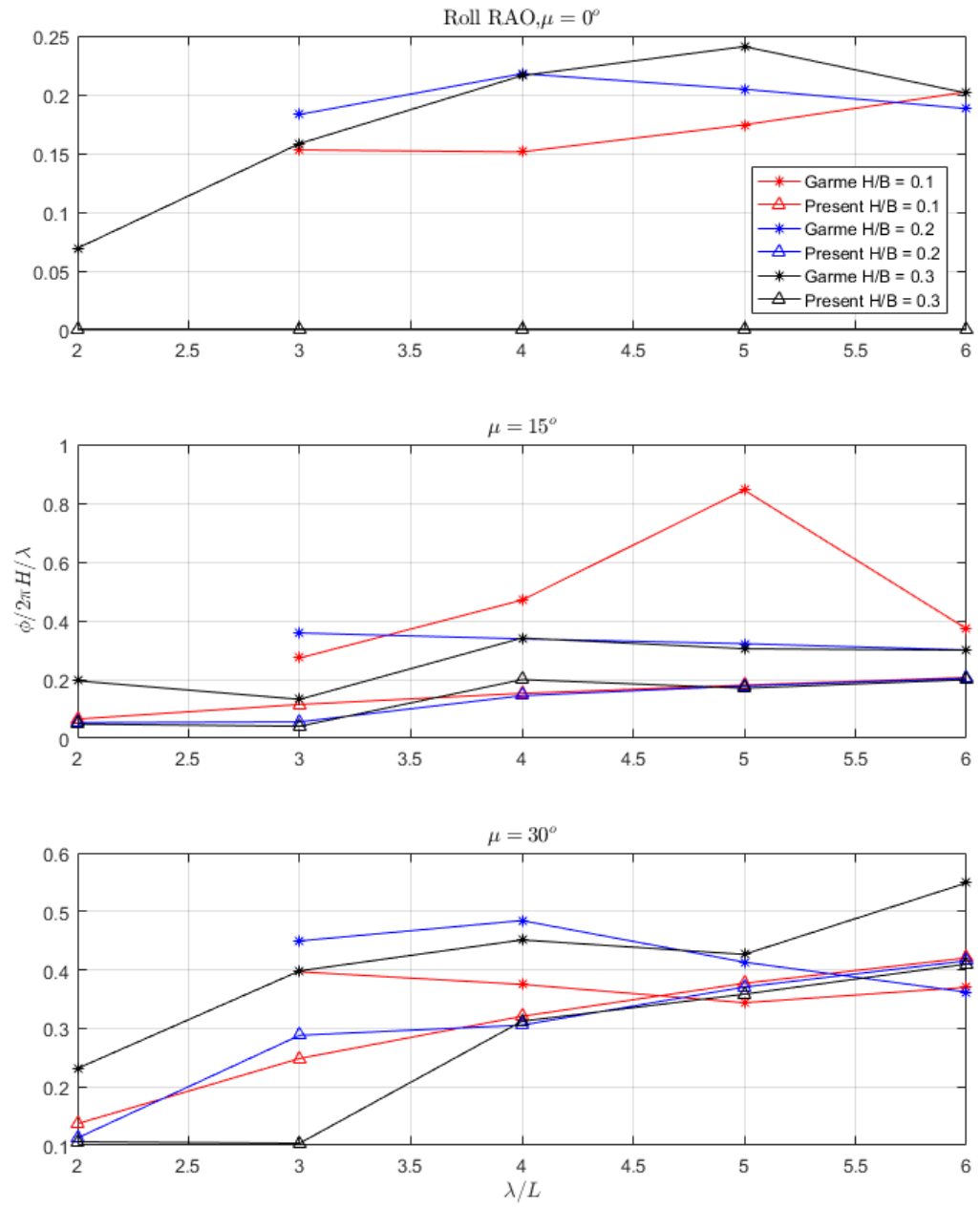


Figure 5.10: Comparison of response roll motions.

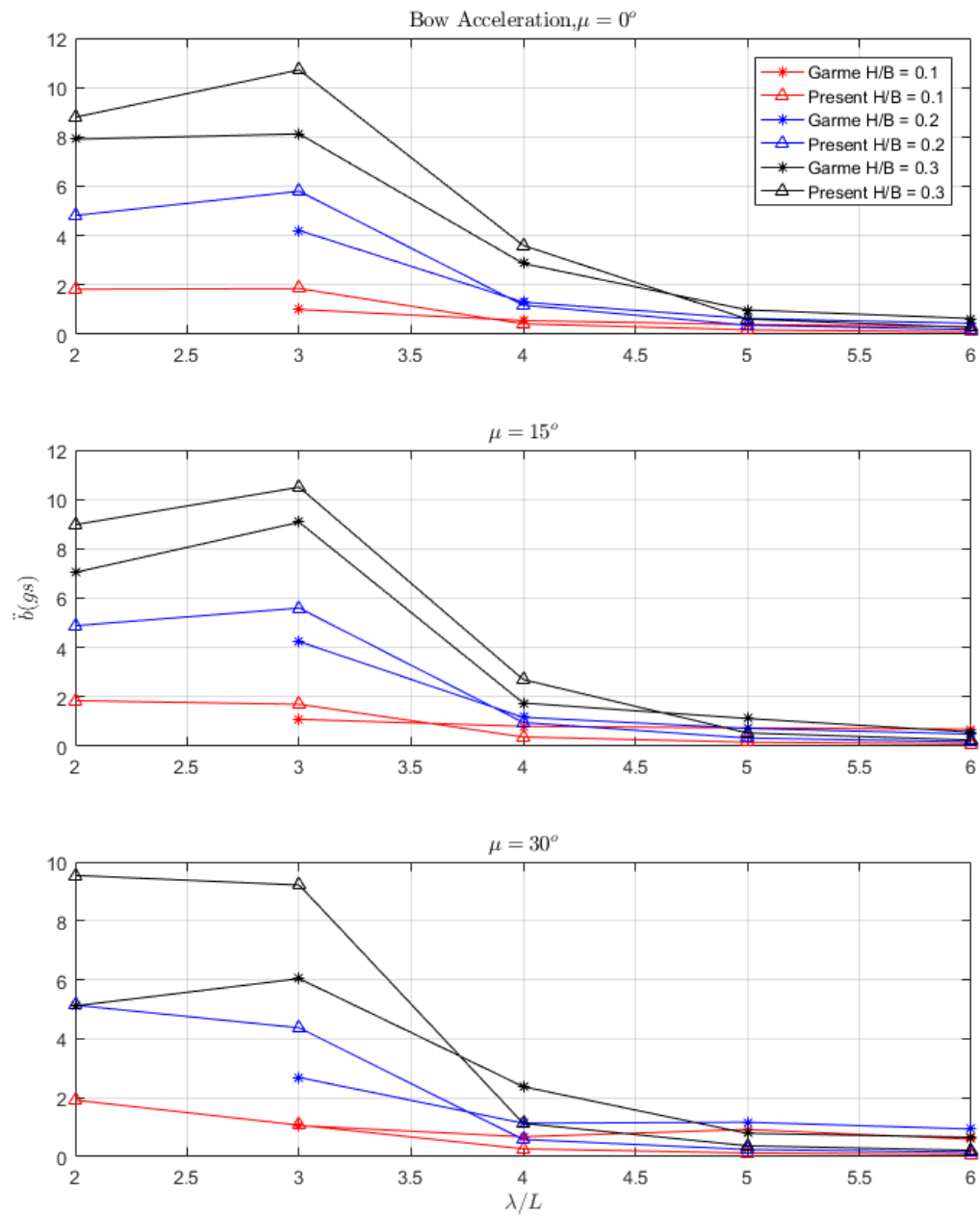


Figure 5.11: Comparison of bow accelerations.

## Chapter 6

# Application to Aircraft Ditching: Development and Verification of Mathematical Model

As mentioned previously in Chapter 2, another possible useful application of the present mathematical model is aircraft ditching. The original application of the theory was applied to seaplane landing load prediction, the application to aircraft ditching load prediction has been chosen as an interesting application to investigate.

It is of interest to find a robust and reliable technique to predict the loads on the fuselage of an air plane ditching into the water. There is a similar simulation in literature that is the famous seaplane landing load analysis performed by [Wagner \(1931\)](#). His research led to a number of applications and implementations by many researchers in order to simulate loads and motions of high-speed planing craft, as due to his principal, the impact load on the cross section of the craft can be calculated by a falling 2D wedge. Loads on 2D wedge shape geometry can be evaluated applying potential theory and boundary value problems. This led to the evaluation of expression of sectional force on the geometry which appears in the form of rate of change of fluid momentum.

Regarding the methodologies of investigating high-speed planing dynamics presented in Chapters 1 - 2. The 2D strip theory method has been chosen to apply in this project due to its very low computational effort in simulations. Moreover, it has been proven to be efficient to predict both impact loads on hull and response motions. For further literature review on the typical evaluation methods for high-speed planing craft, see [Kanyoo et al. \(2015\)](#). The 2D ordinary strip theory simplifies the 3D problems by dividing the ship hull into sections, and by using the potential flow principal, sectional pressure acting on each section can be evaluated.

The fundamental system of equations of motions is identical to that developed in Chapter 3. Initially, simulations of a hard chine hull form free falling into water have been carried out. The aim of the simulations was to verify the suitability of the mathematical model developed by Kanyoo et al. (2015) and determine whether it could be valid for this new application. The mathematical model has been developed based on the pioneering work of Zarnick (1978) and later modified, implemented, verified and optimized by Kanyoo et al. (2015) to be valid for the simulation of high speed planing hard chine travelling in both calm water and in waves.

The results from the initial simulations done by Kanyoo et al. (2014) appear to be reasonable from the perspective of pressure distributions along the hull at instants of impact. The first five instants (five time steps during the impact) can sufficiently represent the highest impact load on the hull. The optimal parameters in simulation (number of strip sections,  $N$  and time step sizes,  $\Delta t$ ) have been used. It is of interest as well to compare the results evaluated by the optimal parameter with those of higher resolution and this is subject to carry out in the further stage of the work. Furthermore, in order to guarantee its validity, it is necessary to perform as well an appropriate validation process.

The subsequent stage of the investigation is to modify the present mathematical model to be capable of simulating hull forms that are more representative of an aircraft fuselage (semi-circular shape). This modification needs more in-depth analysis of sectional added mass of semi-circular shape. In order to achieve this approach, a hypothesis of sectional added mass expression for semi-circle is proposed. It consists of determining whether the sectional added mass coefficient derived by Lewis transformation is equivalent to that derived by Payne (1994), sectional added mass expression of semi-circular section could be replaced by an expanding flat lamina as well as in the case of wedge shape section, and the use of sectional added mass coefficient derived from Lewis transformation could be valid for the case of semi-circular shape. More details of the modification and implementation of the mathematical model to be capable of predicting sectional load on semi-circular shape will be explained in the further section.

In summary, the aim and objectives of this chapter are to find a novel technique based upon the mathematical model of high-speed planing dynamics to predict aircraft ditching loads and motions. Note that once the mathematical model is adequately implemented, apart from the principal application to predict the impact load in ditching event, this modified tool could be also applicable for other load prediction situation such as, the loads of a Unmanned Air Vehicle (UAV) landing on to the water, impact load of torpedo launching into the water, etc. It is then cross-validated with other two techniques provided by Stirling Dynamics Ltd. (Bonanni et al., 2015; Vandewaeter et al., 2015) in order to confirm the initial validity. One of these techniques, the high fidelity CFD tool is used as the main references.

## 6.1 Application to Aircraft Fuselage Form

Following the principle of strip theory used in the mathematical model developed previously, the sectional hydrodynamic load is evaluated from the rate of change of fluid momentum. The fundamental parameter of this principle is the added mass of the fluid when it is interacting with an object. Sectional added mass expression for wedge shape geometry has been successfully applied to high-speed planing craft. A modification of the original model is necessary in order to be able to apply to a semi-circular shape.

### 6.1.1 Sectional Added Mass Coefficient

The accurate solutions of the system of equations of motions are very much dependent on the accurate evaluation of the hydrodynamic coefficients. The hydrodynamic coefficients themselves require the evaluation of the added mass terms.

Wagner (1932) derived a mathematical theory for describing the time history of the impact pressure at the surface of a body during vertical water entry. This theory, which was introduced by von Karman (1929) as the flat plate theory was based on the impact of a flat plate with varying width on a horizontal flat water surface. The width as function of time determined the geometry of the object's surface. The fluid was assumed irrotational and incompressible, thus, viscous effects could be neglected.

According to Wagner (1932), a 2D wedge shape section falling into the water can be replaced by a flat plate lamina expanding in the water surface with an identical rate of change of its geometrical beam. This problem is solved by the principle of potential flow theory and boundary value problem and results in the expression of sectional added mass as represented in Chapter 3 (Equations 3.14 - 3.15). The sectional added mass coefficient  $C_m$  is geometry dependent and varies differently in various geometrical parameters. There are several expressions of sectional added mass coefficients for wedge shape geometry available in literature. Originally, Zarnick (1978) used constant value for  $C_m$ . He assumed it to be equal to 1. Keuning (1994) showed that Zarnick's method is only applicable to very high forward speed, because of the constant values he used for hydrodynamic coefficient.

Some expressions of sectional added mass coefficient are presented as follows:

**Sectional Added Mass Coefficient Suggested by Payne (1994):**

$$C_m = \left(1 - \frac{\beta}{2\pi}\right)^2 \quad (6.1)$$

**Sectional Added Mass Coefficient Suggested by [Vorus \(1996\)](#):**

$$C_m = \frac{\pi^2}{4} \cdot \left( 1 - \frac{\beta}{90} \cdot 0.4 \cdot (1 - KAR) \right) \quad (6.2)$$

Where  $KAR$  is an added mass correction factor. Using  $KAR = 0.1$  is equivalent to using added mass coefficient of Wagner, while  $KAR = 0.0$  roughly matches the added mass coefficient curve of Vorus.

**Sectional Added Mass Suggested by [Faltinsen \(2000\)](#):**

$$m_a = \frac{\rho b^2}{\tan \beta} \cdot \left( \frac{\pi}{\sin \beta} \cdot \frac{\Gamma \left( 1.5 - \frac{\beta}{\pi} \right)}{\Gamma^2 \left( 1 - \frac{\beta}{\pi} \right) \Gamma \left( 0.5 + \frac{\beta}{\pi} \right)} - 1 \right) \quad (6.3)$$

Where  $b$  is half beam and  $\Gamma$  is the gamma function.

**Sectional Added Mass Evaluated using Lewis Conformal Mapping:** Lewis Conformal Mapping is widely used to evaluate hydrodynamic coefficients for ship motions investigation. It consists of transforming a ship's section shape into a semi-circular shape and applying potential theory to assess corresponding pressure, and leads to the achievement of sectional added mass quantity. According to [Blake \(2000\)](#), the sectional added mass coefficient expression derived from Lewis Conformal Mapping is:

$$C_m = \frac{m_a}{\pi \rho B^2 / 8} = \frac{|(1 + a_1)^2 + 3a_3^2|}{(1 + a_1 + a_3)^2} \quad (6.4)$$

Equation 6.4 describes the added mass coefficient from a two parameter conformal mapping, valid for the infinite frequency of encounter. [Payne \(1994\)](#) simplifies this expression for a wedge form into a dependency upon the deadrise angle (see Equation 6.1).

Note that Payne's approximation is based on potential flow theory results of Wagner's equivalent flat plate. Due to this flat plate approach, it is supposed to be valid only in the case of small deadrise angles.

**6.1.2 Sectional Added Mass of Semi-Circular Shape**

Following the literature review of [Ghadimi et al. \(2012\)](#), they state that a limited number of investigations approaching the water entry problem of semi-circular shapes have been carried out. According to [Sun and Faltinsen \(2006\)](#), a 2D problem in the cross plane

can be considered if the variation along the length of the cylinder is discounted. Some researchers attempted to implement Wagner solution as his model is not capable of describing the in-depth details of the impact process. Nevertheless, this classical model is still significant due its simplicity. Significant implementations and corrections were made by [Armand and Cointe \(1987\)](#), [Howison et al. \(1991\)](#), [Oliver \(2002\)](#), [Logvinovich \(1969\)](#) and [Korobkin \(2004\)](#). They are capable of predicting the loads on a body as it enters the water with higher accuracy compared with the original model of Wagner. [Zhao et al. \(1996\)](#) solved the boundary value problem (BEM) and numerically obtained the distribution of vertical velocity on the free surface to evaluate the shape of the free surface and the splash-up height for the next time instant. Due to the existence of flow singularity at the intersection points, the nonlinear Bernoulli equation evaluates negative pressures close to these points. [Zhao et al. \(1996\)](#) suggested integration of the hydrodynamic pressure distribution only over the wetted surface where the pressure is positive. With the same approach, analytical results were also obtained by [Mei et al. \(1999\)](#) for the water entry of a wedge shape, circular cylinder and ship sections of Lewis form. This is for the problems with known conformal mapping of Schartz-Christoffel that maps the flow domain into a half-plane. The boundary value problems of the generalized Wagner solution are much simpler than those within the original formulation making the approach significantly more practical. [Vorus \(1996\)](#) developed another analytical model of water entry problems. He neglected the geometrical nonlinearity of the problem but still considered that of the boundary conditions. Then, positions of the intersection points can be evaluated using this condition at the point of intersection where the hydrodynamic pressure is zero. The results obtained by [Xu \(1998\)](#) based on Vorus' model were of good agreement with the experimental data.

Accounting for the semi-circular shape, the impact pressure of this shape on entry into the water varies significantly. As considering the analogy of wedge shape, the deadrise angle changes as the submergence increases. This also could be the effects of many phenomena, such as, air cavity, flow separation and breaking waves. In order to find the accurate solution of the problem with fully nonlinear free surface conditions, numerical methods will be used. [Greenhow \(1988\)](#) studied the water entry of a rigid circular cylinder using a BEM based on Cauchy's theorem. Nevertheless, the calculations needed to be refined, and the flow separation model needed to be accounted for. [Zhu et al. \(2006\)](#) also investigated the water entry of a rigid circular cylinder using a constrained interpolation profile (CIP) method. It gave a good prediction of the time history of the body motion due to the infinite rate of change of wetted surface. [Sun and Faltinsen \(2006\)](#) developed a 2D boundary element code to simulate the water flow and pressure distribution during the water impact of the horizontal circular cylinder. They satisfied the exact free surface boundary conditions. The non-viscous flow separation on the curved surface of the cylinder was simulated by merging a local analytical solution with the numerical method.



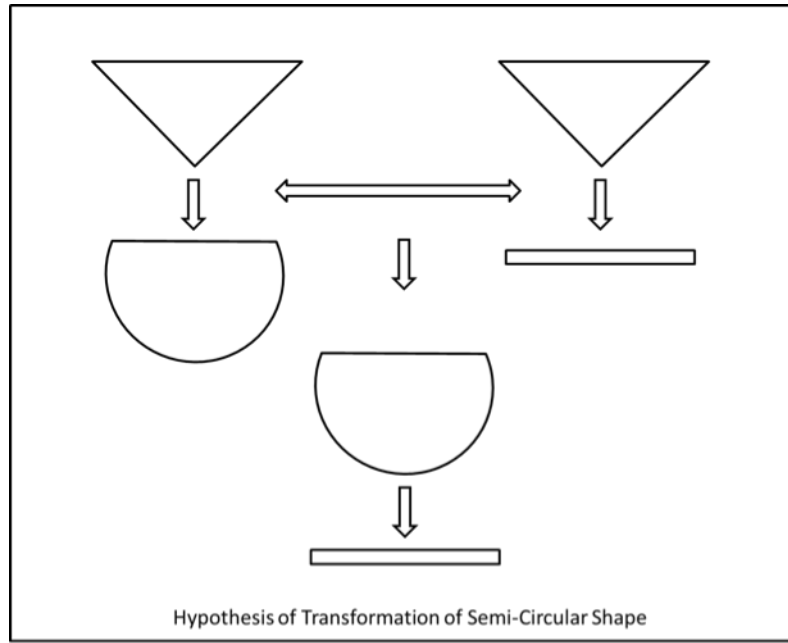


Figure 6.1: Hypothesis of transformation of semi-circular shape.

The present work is planned to follow the expression of wedge water entry of [Wagner \(1931\)](#) but finding the most appropriate added mass coefficient corresponding to the actual semi-circular shape rather than that of a wedge shape. A hypothesis is proposed, verified and validated with the details explained in the following sections.

#### 6.1.2.1 Hypothesis

It can be seen previously that the expression of sectional added mass presented by [Wagner \(1931\)](#) is valid for a wedge shape section. It is of interest to verify and determine whether it is valid for the case of sectional hull of the airplane, which is a semi-circle. By using a two parameter conformal mapping of Lewis, wedge shape geometry can be transformed to a semi-circle of unit radius. The proposed hypothesis is that if the sectional added mass coefficient derived by Lewis transformation is equivalent to that derived by Payne, sectional added mass expression of semi-circular section could be replaced by an expanding flat lamina as well as in the case of wedge shape section and the use of sectional added mass coefficient derived from Lewis transformation could be valid for the case of semi-circular shape, see [Figure 6.1](#).

#### 6.1.2.2 Verification of Sectional Added Mass Coefficient

In order to verify the validity of sectional added mass expression used in the case of wedge shape, two different sectional added mass coefficients will be normalized and verified.

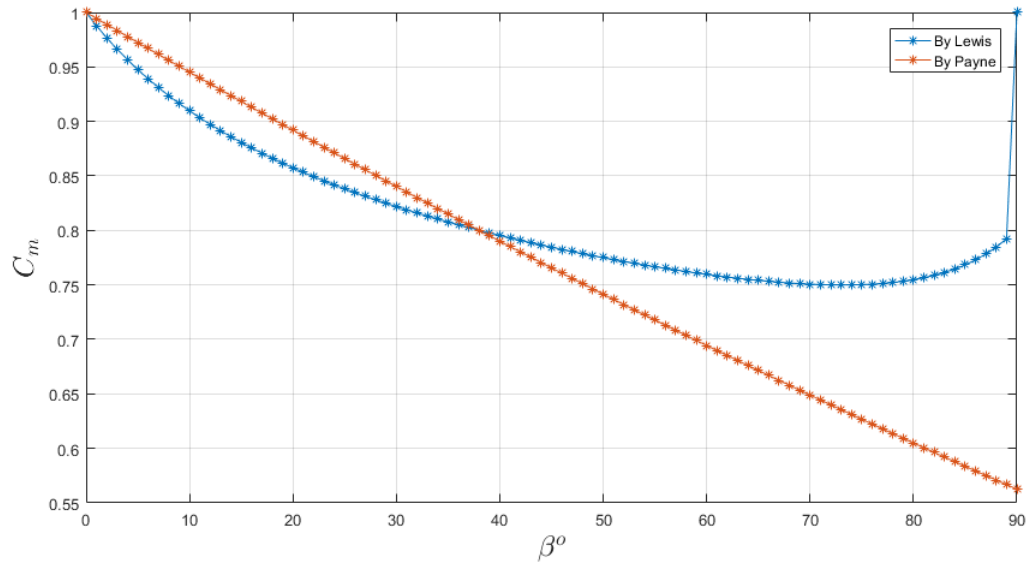


Figure 6.2: Comparison of variation sectional added mass coefficients between wedge shape and semi - circular shape in term of deadrise angle.

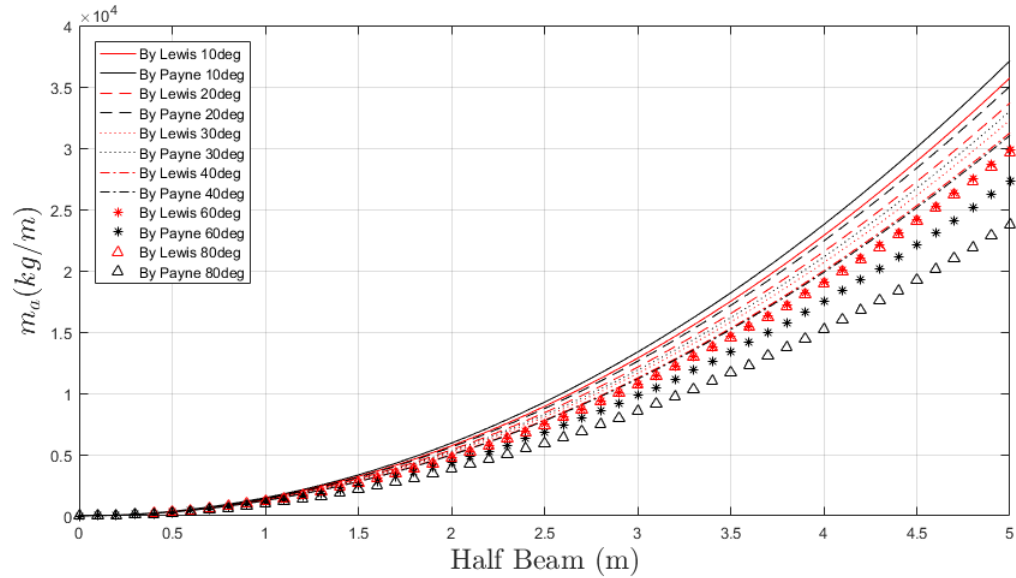


Figure 6.3: Comparison of sectional added mass evaluated by Lewis and Payne's methodologies.

One can be seen as a transformation from a wedge shape to a unit radius semi-circle and the other as a transformation of wedge shape to a lamina flat plate.

Sectional added mass coefficients evaluated by Lewis mapping (wedge shape to semi-circle) and that evaluated by Payne (wedge shape to flat lamina) are compared in Figure 6.2. It is also of interest to represent a comparison of the sectional added mass evaluated by those two different added mass coefficients, see Figure 6.3.

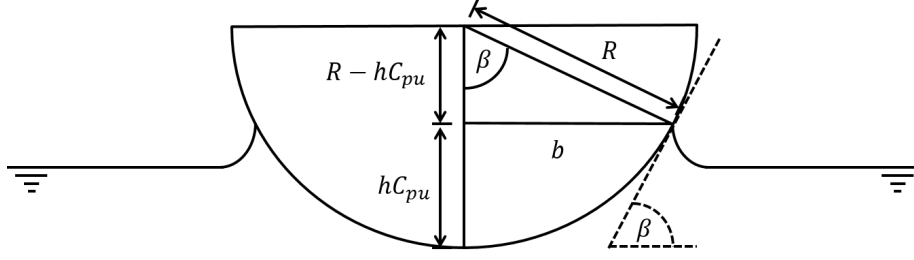


Figure 6.4: Geometry definition of 2D semi-circular shape.

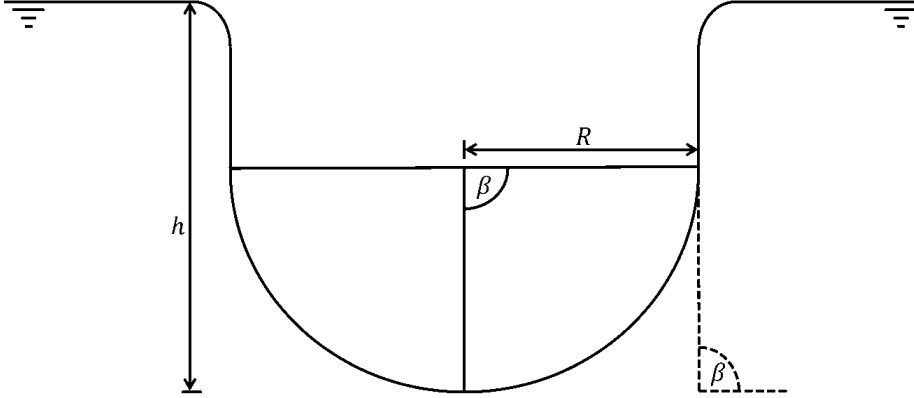


Figure 6.5: Geometry definition of 2D semi-circular shape after flow separation.

It can be seen in Figures 6.2 - 6.3 that the sectional added mass and its coefficient are similar using Lewis mapping and Payne expression in the range of  $\beta \leq 40^\circ$ . This can confirm a statement mentioned in the previous section that Payne's sectional added mass coefficient approximation is only valid for range of small  $\beta$ . Once  $\beta$  is larger, the sectional added mass coefficients evaluated by those different methods start to diverge.

This could lead to the deduction that sectional added mass coefficient evaluated by Lewis transformation could be more suitable than that by Payne when simulating semi-circular shape. As its effective  $\beta$  varies in function of section submergence and reaches the value of 90 degree when its chine is fully submerged. As well as the other suggestions of sectional added mass coefficient are subjected to the limitation of  $\beta$  up to around 50 degrees. The  $C_m$  evaluated by Lewis transformation has a curve form in function of  $\beta$ . It starts to be close to the unit when  $\beta$  approaches zero, and reaches a minimum value around 0.75 at around 70 degree. It starts to increase again but very slightly from 70 to 90 degree. At the same time, the  $C_m$  expressed by the other methods has quasi-linear form and keeps decreasing with increasing  $\beta$  until reaching a very small value of around 0.5 at 90 degree. This could lead to an under-prediction of sectional added mass and consequently, the sectional force, as well as the acceleration.

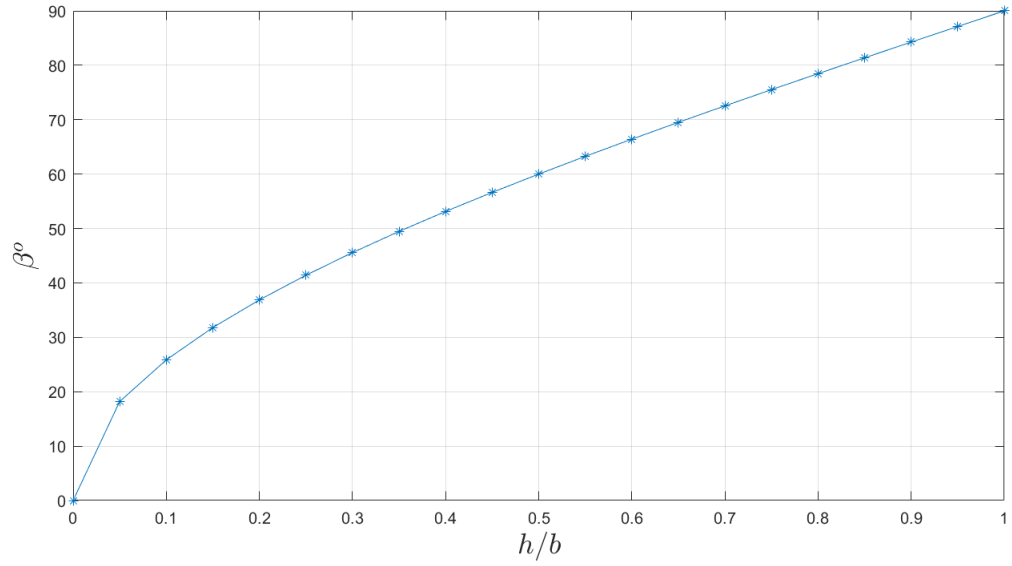


Figure 6.6: Equivalent deadrise angle in term of submergence to half beam ratio.

### 6.1.2.3 Expression of Sectional Added Mass of Semi-Circular Shape

As it can be seen previously in this thesis, the sectional added mass of semi-circular shape may be approximated accurately by Wagner's expression when using appropriate expression of sectional added mass coefficient. It is deduced in the previous section that the expression of  $C_m$  derived from Lewis transformation seems to be the most suitable. Nevertheless, this still needs to be validated.

The corresponding expression for evaluation of sectional added mass of semi-circular shape following the principle of expanding flat laminar is developed as follows:

The general expression of 2D section arbitrary shape is:

$$m_a = C_m \frac{\pi}{2} \rho b^2 \quad (6.5)$$

Where  $b$  is the half beam,  $b = R \sin \beta$ . Due to physical geometry of circular shape of the fuselage shown in Figure 6.4, the half beam is expressed as:

$$b = \sqrt{R^2 - (R - hC_{pu})^2} = \sqrt{2RhC_{pu} - h^2C_{pu}^2} \quad (6.6)$$

Where  $R$  is radius of the fuselage,  $h$  is section submergence and  $C_{pu}$  is pile-up correction factor.

In the case of a circular shape, there is no apparent deadrise angle as in the case of wedge shape section. It varies in term of section submergence and expressed as an equivalent deadrise angle. This angle is defined as the angle between calm water line and tangential line at the intersection point of the section and the water, as can be seen in Figure 6.4:

$$\beta = \cos^{-1} \left( \frac{R - hC_{pu}}{R} \right) \quad (6.7)$$

Nevertheless, pile-up correction factor is deadrise dependent:

$$C_{pu} = \frac{\pi}{2} - \beta \left( 1 - \frac{2}{\pi} \right) \quad (6.8)$$

Substituting Equation 6.7 into Equation 6.8 resulting in:

$$\beta = \cos^{-1} \left( \frac{R - h \left( \frac{\pi}{2} - \beta \left( 1 - \frac{2}{\pi} \right) \right)}{R} \right) \quad (6.9)$$

This can be evaluated numerically by iteration method for each particular section submergence.

Time rate of change of sectional added mass is the time derivative of sectional added mass expression:

$$\begin{aligned} \frac{dm_a}{dt} &= \dot{m}_a \\ &= C_m \frac{\pi}{2} \rho \left[ 2R \left( \dot{h}C_{pu} + h\dot{C}_{pu} \right) - \left( 2h\dot{h}C_{pu}^2 + 2h^2C_{pu}\dot{C}_{pu} \right) \right] + \dot{C}_m \frac{\pi}{2} \rho \left[ 2RhC_{pu} - h^2C_{pu}^2 \right] \end{aligned} \quad (6.10)$$

Unlike the case of wedge shape section, here  $C_{pu}$  and  $C_m$  are functions of  $\beta$ . They vary along the time marching, as equivalent deadrise angle is section submergence dependent. The time derivatives corresponding to those parameters are:

$$\dot{C}_{pu} = \dot{\beta} \left( \frac{2}{\pi} - 1 \right) \quad (6.11)$$

As it can be seen in Figure 6.6, the sectional added mass coefficient  $C_m$  is expressed as a polynomial function by interpolating in term of  $\beta$  as follows:

$$C_m = p_1\beta^6 + p_2\beta^5 + p_3\beta^4 + p_4\beta^3 + p_5\beta^2 + p_6\beta + p_7 \quad (6.12)$$

Where  $p_1 - p_7$  are polynomial coefficients. Thus, its time derivative is expressed as:

$$\dot{C}_m = \dot{\beta} (6p_1\beta^5 + 5p_2\beta^4 + 4p_3\beta^3 + 3p_4\beta^2 + 2p_5\beta + p_6) \quad (6.13)$$

And:

$$\dot{\beta} = \frac{\dot{h} \left[ \frac{\pi}{2} - \beta \left( 1 - \frac{2}{\pi} \right) \right]}{R \sqrt{1 - \left[ \frac{R - h \left[ \frac{\pi}{2} - \beta \left( 1 - \frac{2}{\pi} \right) \right]}{r} \right]^2} - h \left( \frac{\pi}{2} - 1 \right)} \quad (6.14)$$

Finally, by substituting Equations 6.6 - 6.14 into the expression of sectional hydrodynamic force, the final expression can be obtained:

$$f_h = \frac{D}{Dt} (m_a V) = \dot{m}_a V + m_a \dot{V} - U \frac{\partial}{\partial x'} (m_a V) \quad (6.15)$$

For the initial simulation in validation process, a semi-circular section shape will be penetrating into the water with constant vertical velocity, Equation 6.15 can be reduced to:

$$f_h = \dot{m}_a V \quad (6.16)$$

The expressions developed above are applicable only in the range of section submergence not larger than the radius of the fuselage. Similar to the case of wedge section shape, once the section submergence reaches the value of the radius, the half beam increment also reaches its maximum value identical to the radius. Beyond this point, due to the physical geometry of the circular shape, the half beam will be decreasing when section submergence is increasing. The equivalent deadrise angle at maximum half beam is the right angle, and due to the decrement of half beam since that point, flow separation

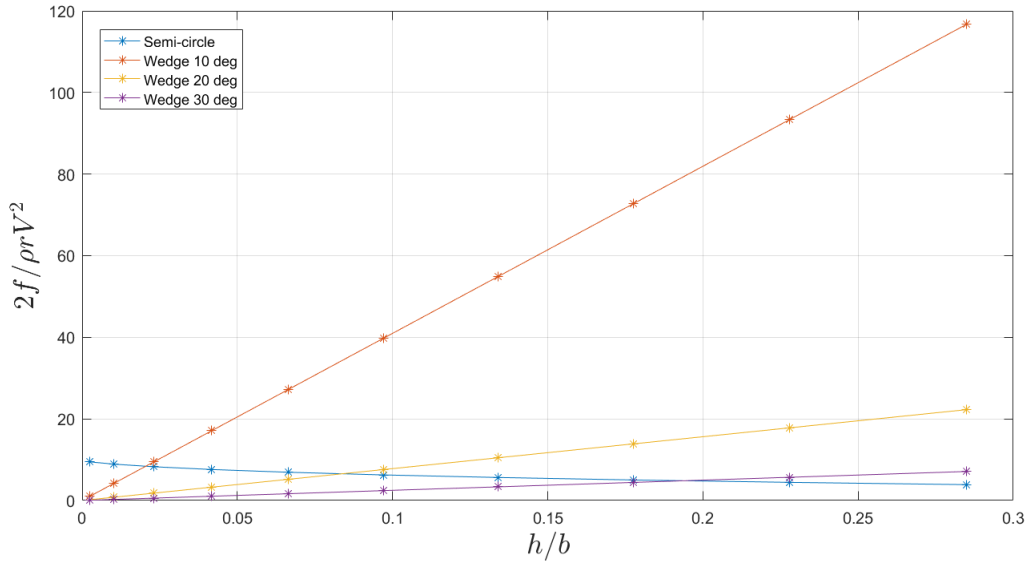


Figure 6.7: Normalized sectional forces of different geometries in term of submergence to half beam ratio.

phenomenon occurs at high vertical speed and this implies the need to evaluate another applicable expression of sectional added mass.

As it can be seen in Figure 6.5, due to flow separation, the equivalent deadrise angle beyond that point remains constantly at 90 degrees. The pile-up correction factor is 1 at that point and remains 1 until the section is fully submerged. Similar to the case of wedge shape section, after flow separation point, the sectional added mass remains constant and leads to the annulment of its time derivative expression.

Figure 6.7 shows comparison of normalized sectional force  $f/\frac{1}{2}\rho r V^2$  of different sectional geometries as a function of normalized section submergence  $h/b$ . Sectional force corresponding to the circular shape is compared to those of the wedge shape of 10, 20 and 30 degree deadrise angles. Initially, at the moment of impact, the sectional force acting on circular shape is of large magnitude due to the relative small equivalent deadrise angle (approximately zero). When increasing submergence, it decreases convexly as the equivalent deadrise angle increases logarithmically with submergence, see Figure 6.6. Generally, the magnitudes of sectional force on circular shape are above those of wedge shape at the range of 0.00 - 0.10 normalized submergence and turn to be of smaller magnitude under those of wedge shape when the submergence keeps growing. While the forces acting on the wedge shape increase linearly, as the deadrise angles are constant. Typically, the wedge shape geometry of small deadrise angle (10 degree) experiences larger impact force comparing to those of larger  $\beta$ . Although at the moment of impact, the impact force is of smaller magnitude comparing to that of circular shape, it ends up being of significantly larger magnitude. While those corresponding to 20 and 30 degree deadrise run around that of circular shape. The critical equivalent deadrise angle of

circular shape where the impact forces turn to be of smaller magnitude than that of the wedge shape are approximately 15, 30 and 45 degree comparing to the wedge shape of 10, 20 and 30 degree respectively.

#### 6.1.2.4 Validation of the Expression

The 2D circular cylinder used in this validation has a radius of 5.5 *m*. It is dropped with a constant vertical velocity of 10 *m/s*. The numerical results, together with the published experimental and analytical results are shown in Figure 6.8. The impact force and the submergence of the cylinder are normalized in order to get a non-dimensional representation.

In Figure 6.8, the normalized impact force called the slamming coefficient is represented in term of the non-dimensional submergence. As shown in this figure, theoretical model of von Karman (1929) indicates an initial slamming coefficient  $C_{f0} = \pi$ , whereas that of Wagner (1931) and Fabula (1957) is  $C_{f0} = 2\pi$ . The coefficients  $C_{f0}$  obtained by the experiments exhibit a considerable degree of scatter. Based on experimental data, Campbell and Weynberg (1980) proposed an empirical formulation for the slamming coefficient as shown in Figure 6.8. The numerical results evaluated by Arai and Matsunaga (1989) are closed to those of Von Karman in the range of  $h/b > 0.2$ , while in the region of  $h/b < 0.2$ , the numerical results of Arai have sharper gradient and tend to Campbell's empirical curve. The present mathematical model shows good agreement with the numerical results of Arai, with small difference in the region of small values of sectional penetration. This could lead to the deduction of the validity of the model to the problem of semi-circular shape falling into the water.

Note that the limitation of using strip theory is that of the thin body condition. Once the sectional hydrodynamic force is obtained, the total loads on the fuselage at freeze time step will also be obtained.

### 6.1.3 Other Force Components

#### 6.1.3.1 Expression of Sectional Cross-Flow Drag

The cross-flow drag is an additional lift presented in case of planing hard chine form when the chine is completely submerged. This statement is deduced from the fact that in the case of planing craft sailing in calm water, once the chine is fully submerged, there should not be any hydrodynamic force due to the fact that there is no rate of change of sectional added mass since the chine is under water. In practice, there is some component of the hydrodynamic force, and it is deduced to be that of cross-flow drag. The physical meaning of the cross-flow drag is simply that of drag force of the



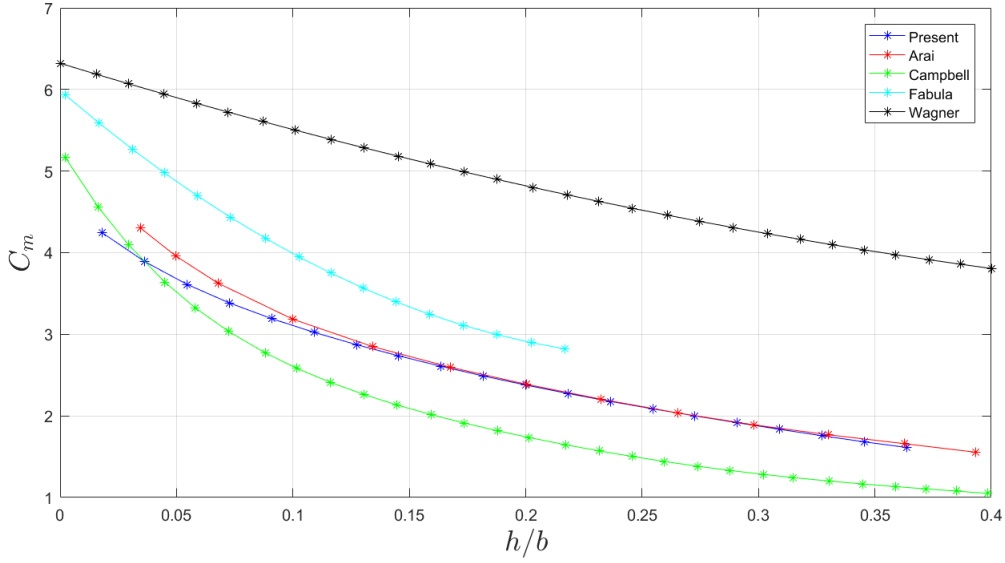


Figure 6.8: Comparison of sectional added mass coefficient of different methodologies in term of submergence to half beam ratio.

flow around a particular section in normal direction to the keel, which is different from the frictional drag force. The expression of sectional cross-flow drag of a wedge shape section widely used by many researchers is as follows:

$$f_{cfd} = C_{D,C} \cos \beta \rho b V^2 \quad (6.17)$$

Remember that the expression of  $b$  and  $\beta$  used are as defined in Equation 6.6 and Equation 6.9 respectively.

As mentioned above, this expression is valid for the wedge shape section but it is subjected to be verified in the case of semi-circular shape section. Nevertheless, at the present stage of the work, it is supposed to be valid, as the magnitude of sectional cross flow drag is notably small comparing to that of the hydrodynamic force.

### 6.1.3.2 Expression of Sectional Buoyancy

The buoyancy force needs to be evaluated very carefully due to the form of aircraft fuselage and flow separation phenomenon. Generally, the buoyancy is evaluated by taking the product of water density and the submerge volume of the object. In the case of aircraft fuselage, due to its semi-circular shape cross section, the flow separation location is assumed to take place at the maximum submerged breath, which is the maximum radius of the fuselage. Beyond the point of flow separation, the area of submerged section is no longer only the arc of a portion of the semi-circle but a complete

semi-circle plus the upper cross section of water above the fuselage, as it can be seen in Figure 6.5. The section submerged area can be expressed in two different conditions:

Before flow separation:

$$A_{sub} = \frac{R^2}{2} [2\beta - \sin 2\beta] \quad (6.18)$$

After flow separation:

$$A_{sub} = \frac{\pi R^2}{2} + 2R(h - R) \quad (6.19)$$

### 6.1.3.3 Global Equations of Motions

Initially, the simulations were planned to be carried out in towed condition, in other words, the model will be moving with constant forward speed without horizontal acceleration, and consequently, no surge motion is accounted for in these cases. The system of global equations of motions can be reduced to only two equations with two unknowns. Following the 2<sup>nd</sup> law of Newton, the system is represented as expressed in Equations 3.1 - 3.2, as well as the matrix form in Equations 3.35 - 3.37.

## 6.2 Numerical Experiments

Following the aim and the objective of the present work, Stirling Dynamics Limited; SDL and University of Southampton; UoS (led by the Author) develop numerical models and evaluate the load prediction together using different methodologies in order to carry out the later cross-validation. The mathematical model developed by UoS has been mentioned previously. Description of the other methods developed by SDL and the high fidelity CFD setting are explained in Appendix C.

A series of numerical experiments has been carried out in order to perform a cross-validation using high fidelity CFD results as the superior data. At the present stage of the work, all of the test cases are carried out for steady state simulations. The model is forced to move with constant velocities or accelerations. This implies the validity of the results to be effective only at the instant of impact and the infinitesimal interval after impact. The full natural motions after impact are subjected to be investigated once the validation of current study is satisfied. Note that the work contained in this thesis will be further refereed as “UoS’s model”. The configurations of a series of simulations are presented in the following section:

### 6.2.1 Test Configurations

A series of cases have been simulated by UoS's model, SDL's model and CFD tools. Two geometries have been used, an "infinite" cylinder and a fuselage geometry described in Appendix C. Different test configurations are presented in Tables 6.1 - 6.4.

A typical landing descent rate of an Airbus A320 is in the range of 0.9  $m/s$ , and the landing speed of 130 – 140 *knots*. The vertical impact speeds for the drop tests documented in Tables 6.1 - 6.4 are therefore well above the limits to be expected in a ditching event. The horizontal velocity of the steady hydrodynamic load test is within the limits to be expected in a ditching event.

Table 6.1: Steady cases.

$\theta$ ( $^{\circ}$ )	$\dot{x}_G$ ( $m/s$ )	$\dot{z}_G$ ( $m/s$ )	$\ddot{z}_G$ ( $m/s^2$ )	$h@t=0$ ( $m$ )	$t_{max}$ ( $s$ )	$t_{imp}@h=0$ ( $s$ )
0	10	0	0	0	N/A	N/A
5	10	0	0	0	N/A	N/A
10	10	0	0	0	N/A	N/A
0	50	0	0	0	N/A	N/A
5	50	0	0	0	N/A	N/A
10	50	0	0	0	N/A	N/A

Table 6.2: Constant speed drop test cases.

$\theta$ ( $^{\circ}$ )	$\dot{x}_G$ ( $m/s$ )	$\dot{z}_G$ ( $m/s$ )	$\ddot{z}_G$ ( $m/s^2$ )	$h@t=0$ ( $m$ )	$t_{max}$ ( $s$ )	$t_{imp}@h=0$ ( $s$ )
0	0	2	0	2	3	1
5	0	2	0	2	3	1
10	0	2	0	2	3	1
0	0	2.83	0	2	2	0.71
5	0	2.83	0	2	2	0.71
10	0	2.83	0	2	2	0.71
0	0	4	0	2	2	0.5
5	0	4	0	2	2	0.5
10	0	4	0	2	2	0.5

Table 6.3: Accelerated drop test cases.

$\theta$ ( $^{\circ}$ )	$\dot{x}_G$ ( $m/s$ )	$\dot{z}_G$ ( $m/s$ )	$\ddot{z}_G$ ( $m/s^2$ )	$h@t=0$ ( $m$ )	$t_{max}$ ( $s$ )	$t_{imp}@h=0$ ( $s$ )
0	0	2.83	2	2	3	1.41
5	0	2.83	2	2	3	1.41
10	0	2.83	2	2	3	1.41
0	0	4	4	2	2	1
5	0	4	4	2	2	1
10	0	4	4	2	2	1

Table 6.4: Accelerated drop test + forward speed cases.

$\theta$	$\dot{x}_G$	$\dot{z}_G$	$\ddot{z}_G$	$h@t = 0$	$t_{max}$	$t_{imp}@h = 0$
( $^\circ$ )	(m/s)	(m/s)	(m/s <sup>2</sup> )	(m)	(s)	(s)
10	50	4	2	4	3	2

## 6.2.2 Results, Discussion and Cross Validation

The simulations described previously have been carried out, the results, discussion and cross-validation are explained as follows:

### 6.2.2.1 Cylinder Drop Simulations

The first series of simulations was carried out in a simple cylindrical geometry. The aim of these simulations is to validate the hydrodynamic loads model developed by SDL and UoS. As detailed in Appendix C, SDL's model and UoS's model consist basically of similar principle that the predominant component of the impact loads is hydrodynamic component due to the added mass. Figure 6.9 shows time histories of the cylinder falling vertically with constant speed into the water. At the instant of impact both SDL and UoS's models experience the maximum impulse load and decrease drastically in a very small instant after. Once the cylinder submergence reaches the maximum beam (half submerged), UoS's model shows constant load as the added mass remains constant and due to Equation 6.15, the load is also constant. While SDL's model and CFD show different loads trend after that situation as they included the other components within the model. Nevertheless, all of them show the same trend since the instant of impact with an acceptable difference of magnitude. This could imply the validity of the sectional added mass model used in these numerical models.

### 6.2.2.2 Constant Horizontal Speed Towed Conditions

The fuselage model is towed with a number constant forward speeds and trim angles and with CG at the water level. This series of tests could show the validity of horizontal load component predicted by vertical added mass expression (UoS's model). Figures 6.10 - 6.11 present the resulting loads acting on nine sections along the fuselage with the first section at the nose and the ninth section at the tail. Note that the force component shown here are parallel and perpendicular to the centreline, thus in any simulation, UoS's model cannot give the horizontal component, especially when  $\theta = 0^\circ$ . As its principal requires the sectional velocity vertical component  $V$  perpendicular to the centreline to evaluate the sectional load and always gives the result only perpendicular to the fuselage.

Both models show good agreement compared with CFD results. The maximum load appears at the stagnation point, in other words, the point of intersection between the

fuselage and the water line. Negative loads or suction appear at the tail part. Due to the fact that using the principle of rate of change of fluid momentum, the sectional added mass at the tail part decreasingly varies proportional to the sectional geometry, the resulting load is negative when evaluating with Equation 6.15.

### 6.2.2.3 Constant Vertical Speed Drop Simulations

This series repeats the simulations done in the first series by replacing the cylinder with a fuselage geometry, dropping the model vertically with different vertical speed and different trim angles. Figures 6.12 - 6.13 present the resulting loads at the moment that the CG coincides with the water line. The overall results show good agreement between the three methodologies. Nevertheless, the UoS's model under-predicts the impact load when  $\theta = 0^\circ$ , due to its ineffectiveness when the horizontal component of speed and load cannot be evaluated appropriately.

### 6.2.2.4 Accelerated Vertical Speed with Zero Forward Speed Simulations

As well as the previous series, this series is carried out without the forward speed but constantly accelerated and dropped vertically into the water. It can be seen in Figures 6.14 - 6.15 that the overall results also show good agreement as in the previous test series except the cases of  $\theta = 0^\circ$  that the UoS's model gives under-predicted results. This could imply the obvious limitation of the UoS's model that is ineffective when simulating  $\theta = 0^\circ$ . Moreover, although it is not obviously significant, when simulating with higher drop speed, the total load evaluated by the UoS's model has a different peak load location close to the nose section while the other methodologies present the peak close to the tail part. This could be due to the fact that the predominant load in the UoS's model is the hydrodynamic force and the inclusion of hydrostatic force is not sufficiently appropriated.

On the other hand, when considering the classical planing theory, the increment of lift force beyond the immersed chine is explained by cross-flow drag phenomenon. In this model, this phenomenon is simplified using the original expression applied in the planing craft investigation. It might not be suitable for semi-circular geometry and also ditching situation. More in-depth analysis approaching this phenomenon is recommended, in order to be able to model it more appropriately.

### 6.2.2.5 Constant Horizontal Speed with Vertical Acceleration Simulations

The final simulations series is carried out with the aim of simulating as much as possible the real ditching conditions. With this approach, the fuselage is moving with both vertical and horizontal speeds. The vertical speed is accelerated with a constant acceleration,

and the horizontal velocity remains constant and allowed to pitch freely implying the towed condition. The effect of 2D motions has direct impact in pressure distribution evaluated by UoS's model.

It can be seen in Figure 6.16 that the shape of sectional forces appears to be obviously different comparing to the other two methodologies. The preliminary assumption of this behaviour is supposed to be the effect of inappropriate "Flow separation model". This does not affect the horizontal steady and vertical drop test cases. The original UoS's model defined that flow separation phenomenon occurred after the maximum beam of the fuselage is under water. This simplification follows the original model applied in high-speed planing hull dynamics that the flow separation occurs after the chines are under water. Nevertheless, it is not valid when applied to aircraft fuselage due to the reduction of geometry at the tail part, unlike the planing hull whose aft sections are prismatic. The reduction of geometry affects directly the direction of pressure distribution, generating negative pressure or suction according to the last term of Equation 6.15. In case that the definition of original model is followed, the flow separation is defined in the manner that the water is attached to the fuselage until the maximum sectional beam locations as it is shown in Figure 6.16. Thus, the negative pressures are magnified. In other words, only vertical flow separation has been defined in the original model.

When the fuselage is moving with horizontal motion, flow separation projected in horizontal direction must be accounted for. Due to the reduction of geometry at the tail part, when the object is travelling forward with very high speed, the water is no longer attached to the object along its length. The locations of flow separation are difficult to determine, the first assumption is made by simply modelling different flow separation's locations, as can be seen in Figure 6.17. The variation of locations defines the wetted surface area at the tail starting from the original model and decreases slightly until the flow is supposed to separate beyond the point the prismatic body ends.

The comparison is made again and shown in Figure 6.18. It can be seen that the pressure distribution has a better fit at the tail part when flow separation location is supposed to be of level 4. This can prove the simplified assumption of these such locations and leads to more in-depth investigation when simulating the motions after impact. As it is dynamical process, inappropriate evaluation of loads leads to inaccurate motions.

The cross validation presented in this chapter can confirm the initial validity of the implementation of 2D strip based model to the capability of simulating aircraft ditching under some limitations mentioned previously. In order to strengthen its validity, a series of model experiments was planned and carried out with details presented in Chapter 7.

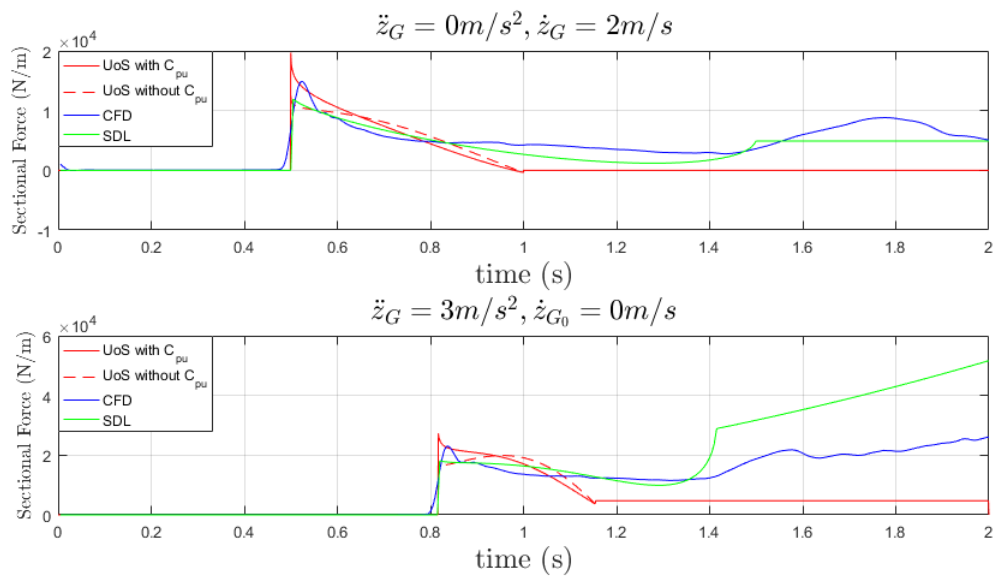


Figure 6.9: Time histories of sectional force of 2D cylinder drop tests.

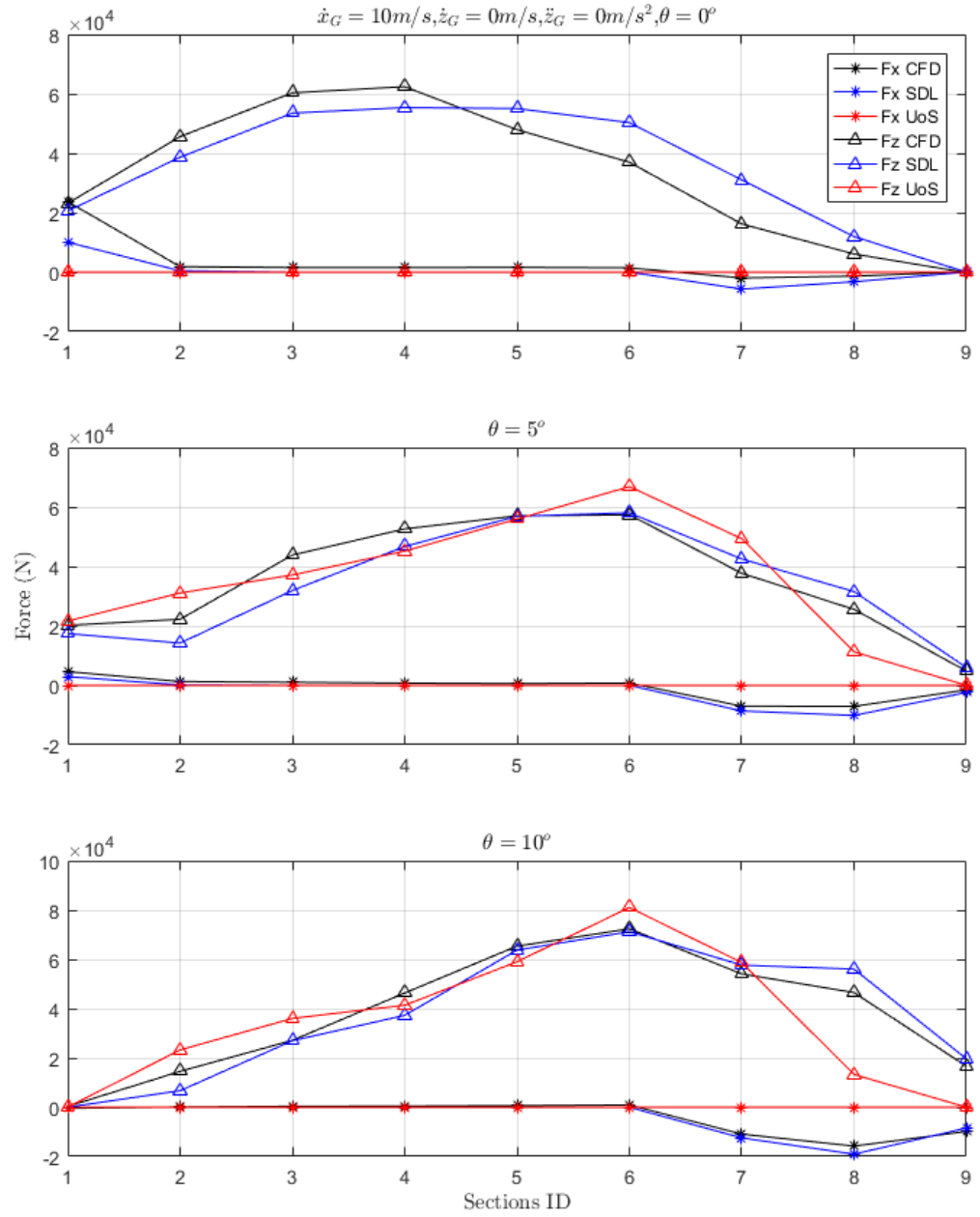


Figure 6.10: 9 sectional forces of constant horizontal speed  $\dot{x}_G = 10 \text{ m/s}$ .



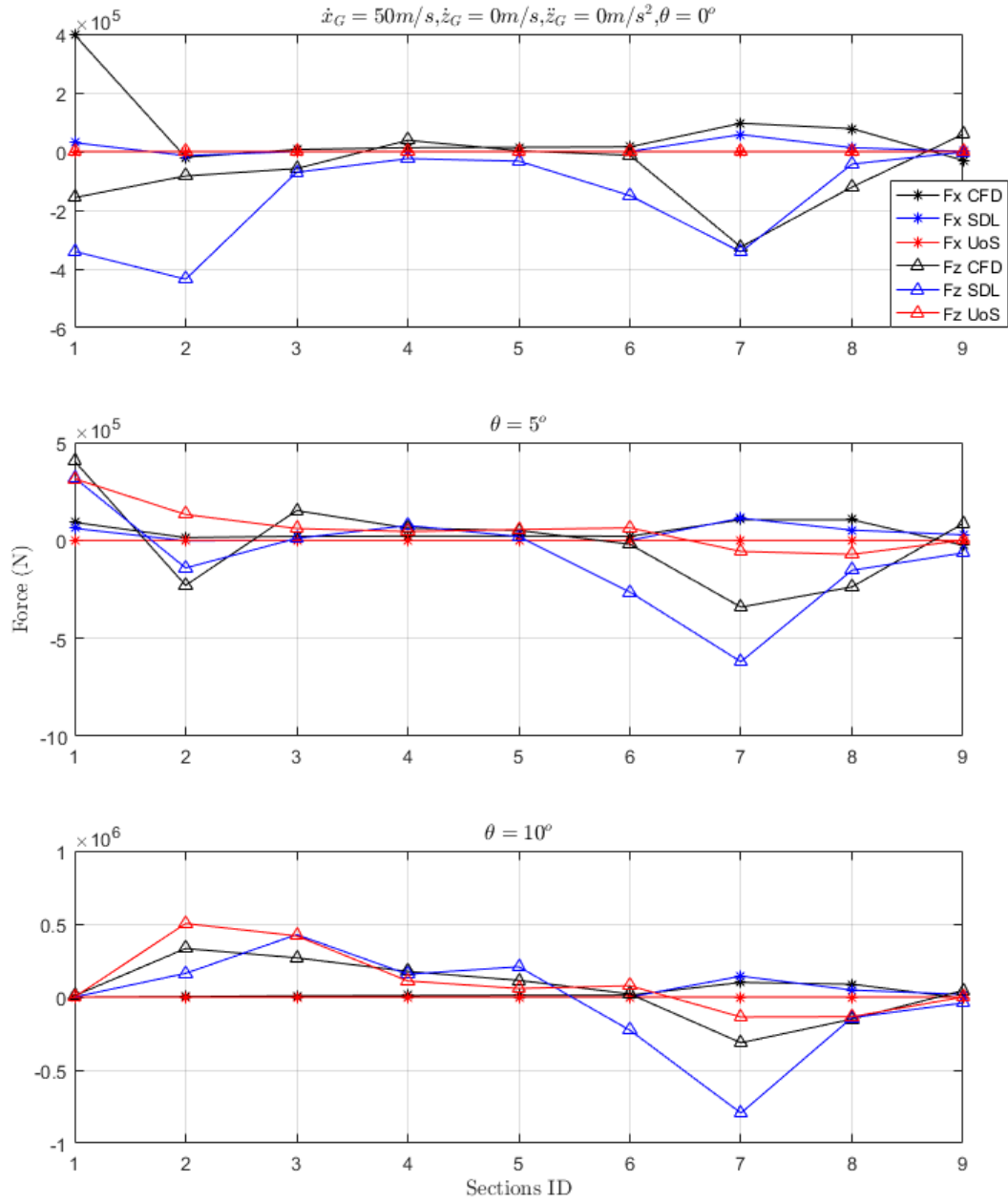


Figure 6.11: 9 sectional forces of constant horizontal speed  $\dot{x}_G = 50 \text{ m/s}$ .

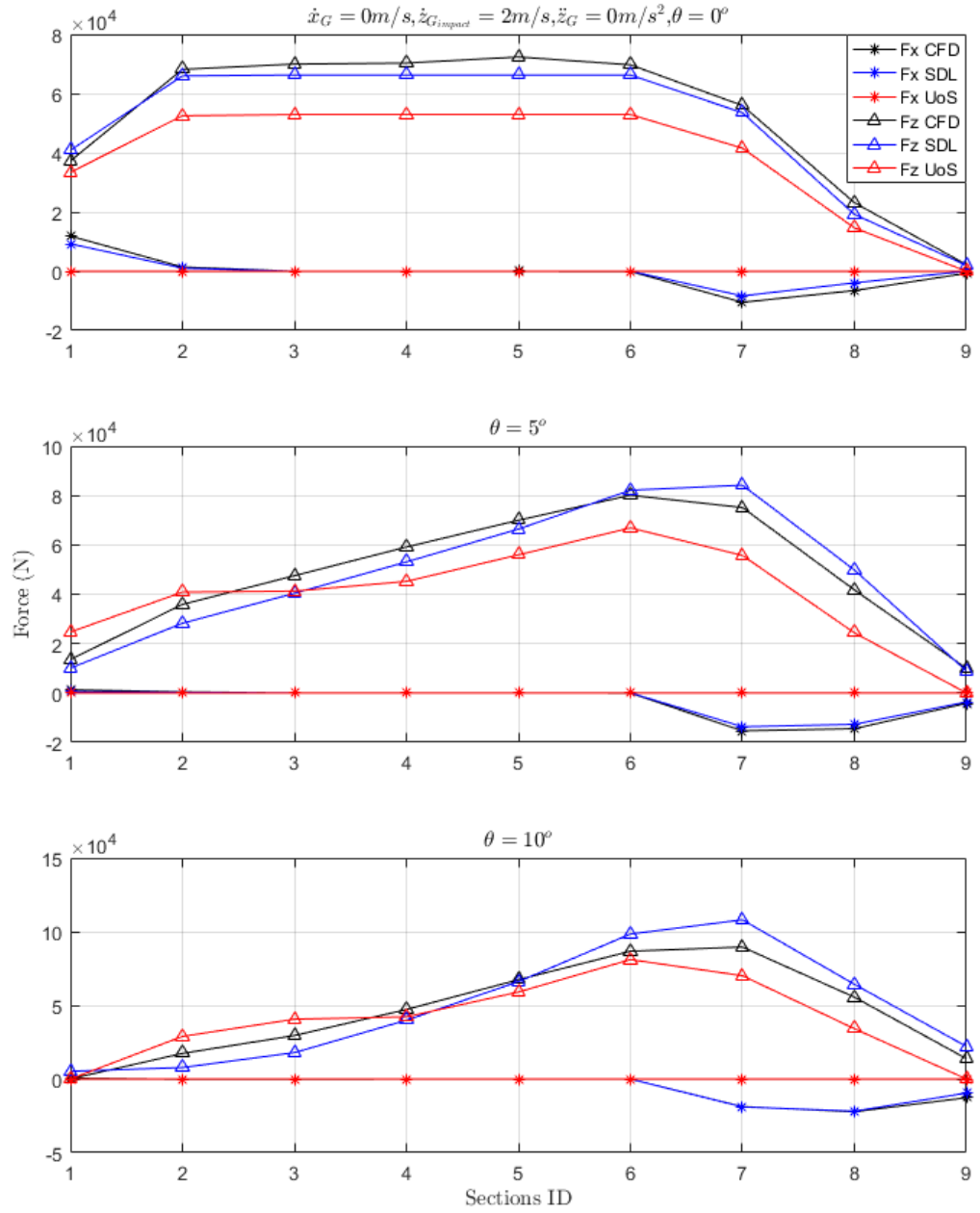


Figure 6.12: 9 sectional forces of constant drop test of vertical speed  $\dot{z}_G = 2\text{ m/s}$ .

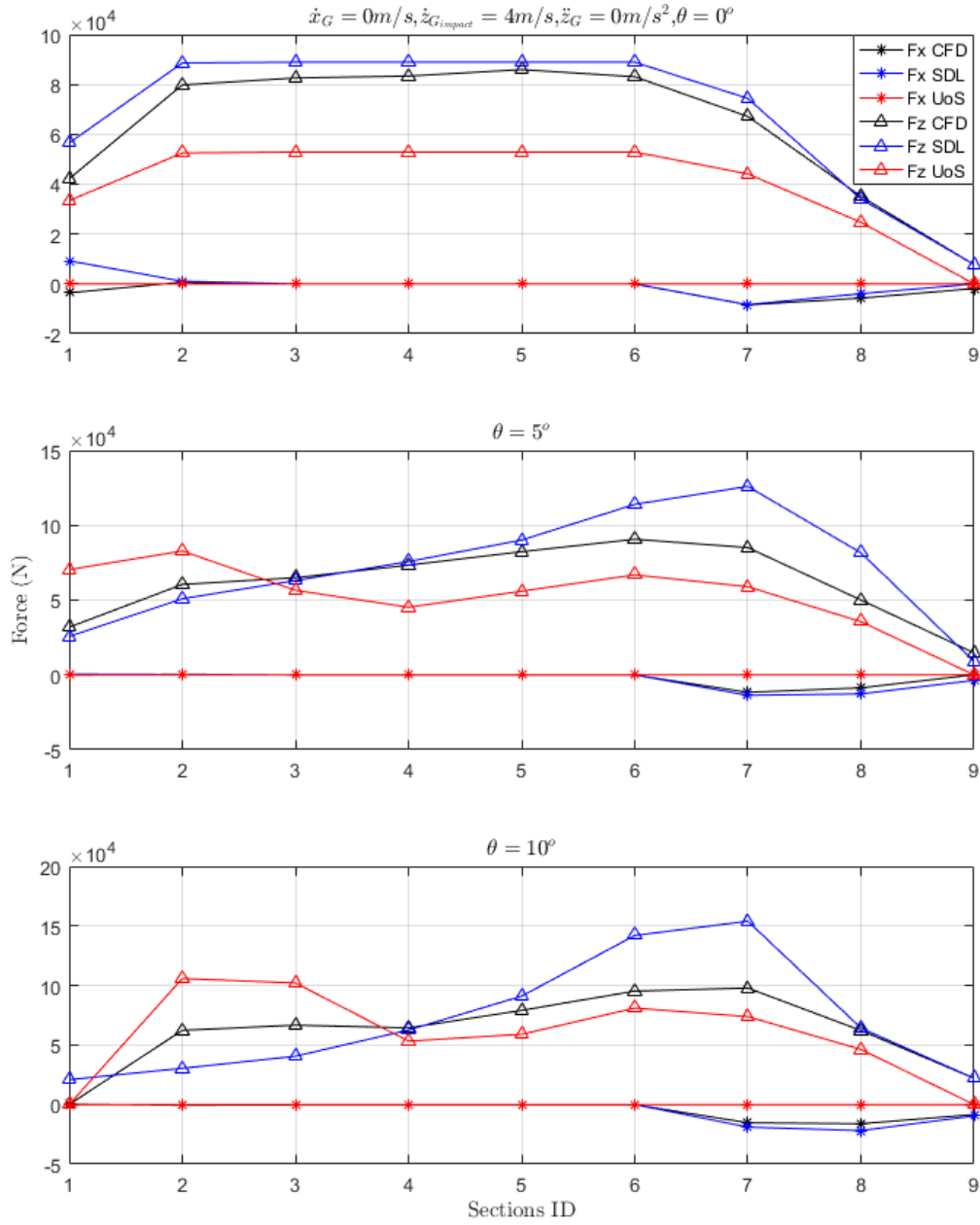


Figure 6.13: 9 sectional forces of constant drop test of vertical speed  $\dot{z}_G = 4\text{ m/s}$ .

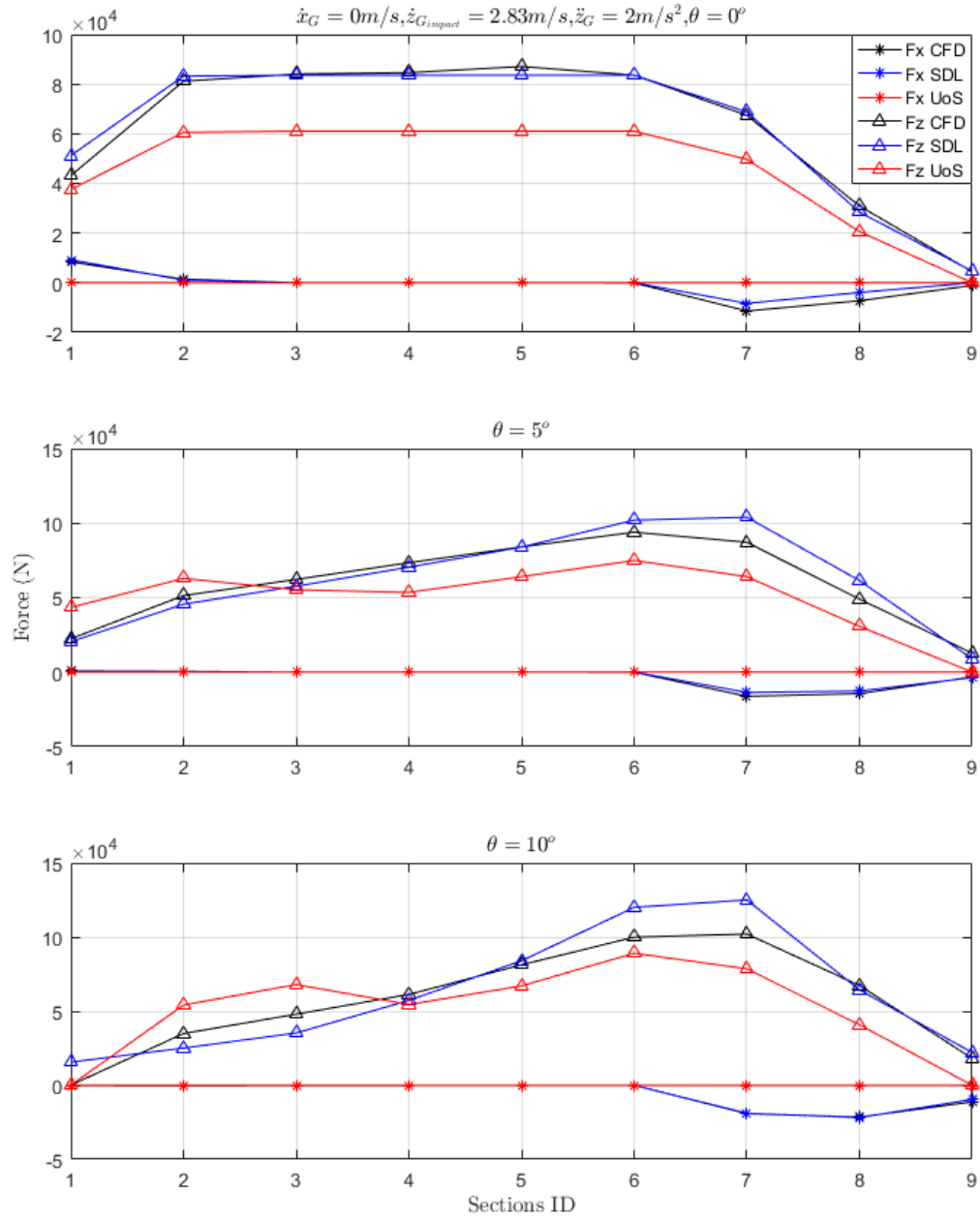


Figure 6.14: 9 sectional forces of accelerated drop test with vertical acceleration  $\ddot{z}_G = 2 m/s^2$ .

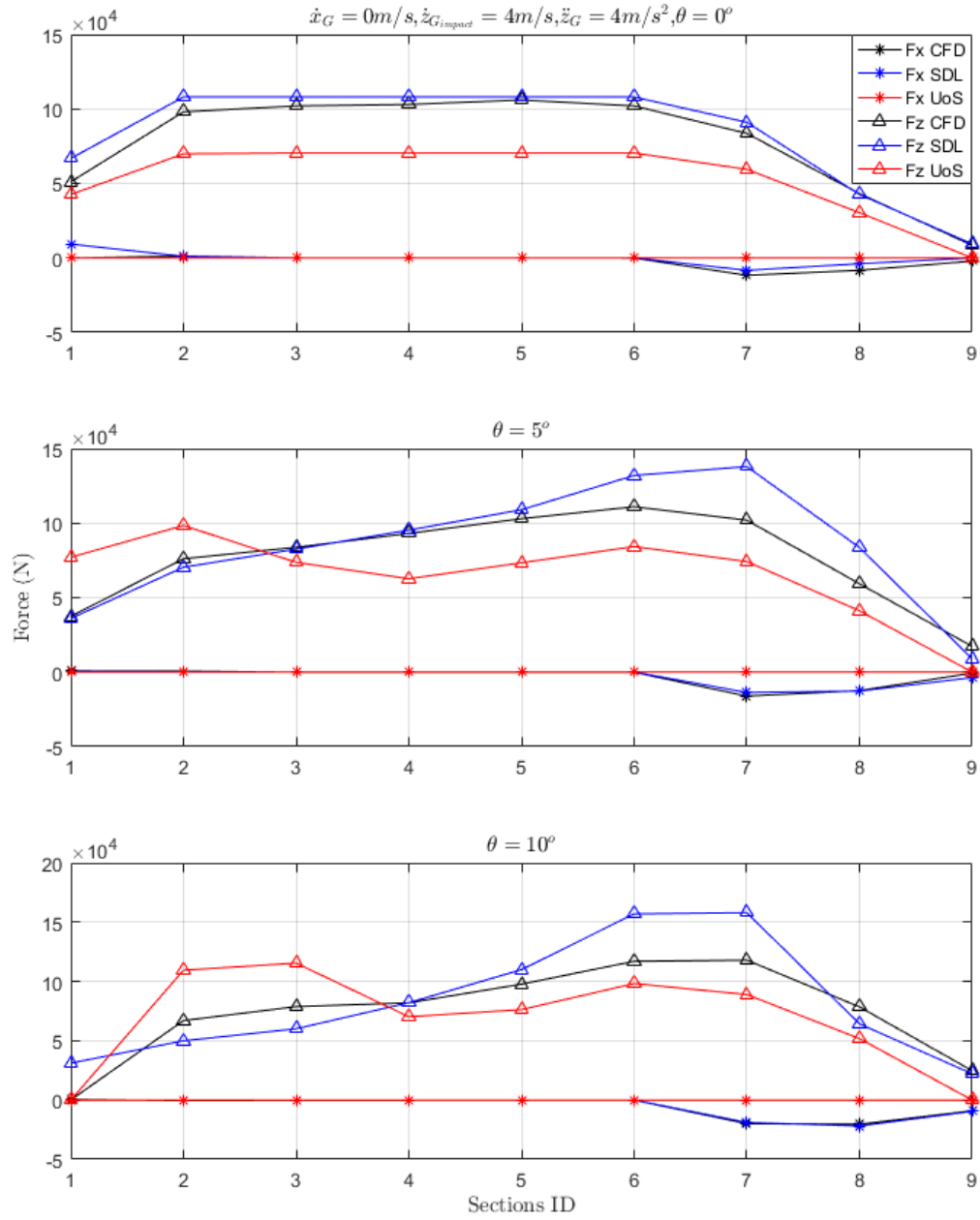


Figure 6.15: 9 sectional forces of accelerated drop test with vertical acceleration  $\ddot{z}_G = 4 \text{ m/s}^2$ .

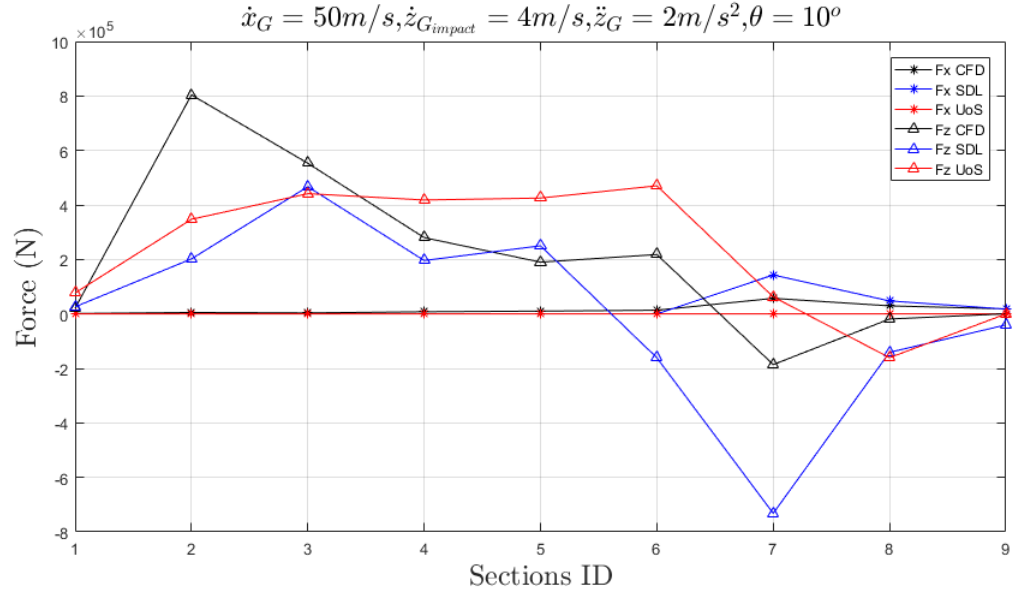


Figure 6.16: 9 sectional forces of constant horizontal speed with vertical acceleration  $\ddot{z}_G = 2 \text{ m/s}^2$ .

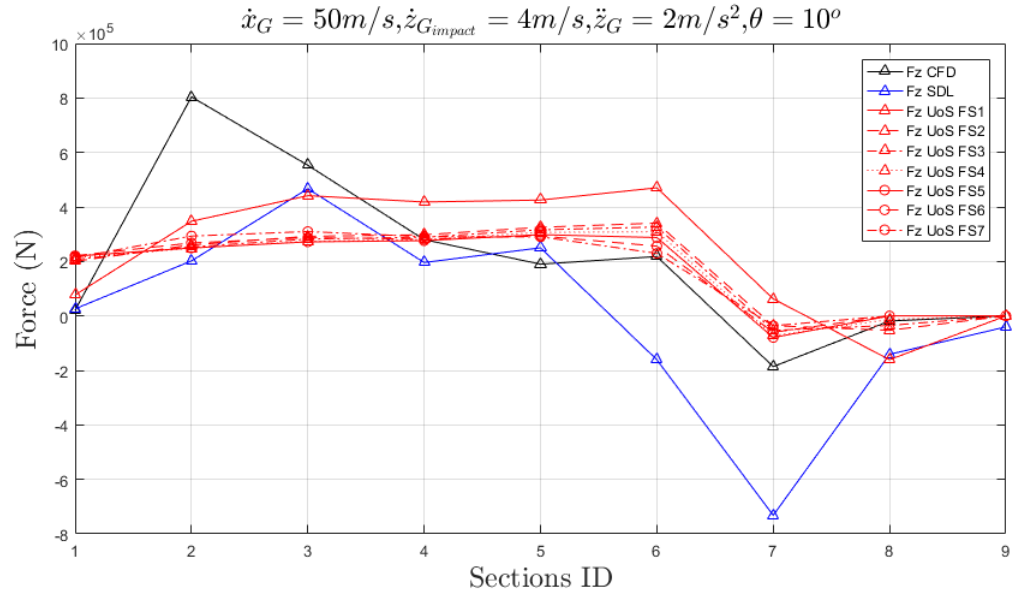


Figure 6.17: 9 sectional forces of constant horizontal speed with vertical acceleration  $\ddot{z}_G = 2 \text{ m/s}^2$  varying flow separation locations.

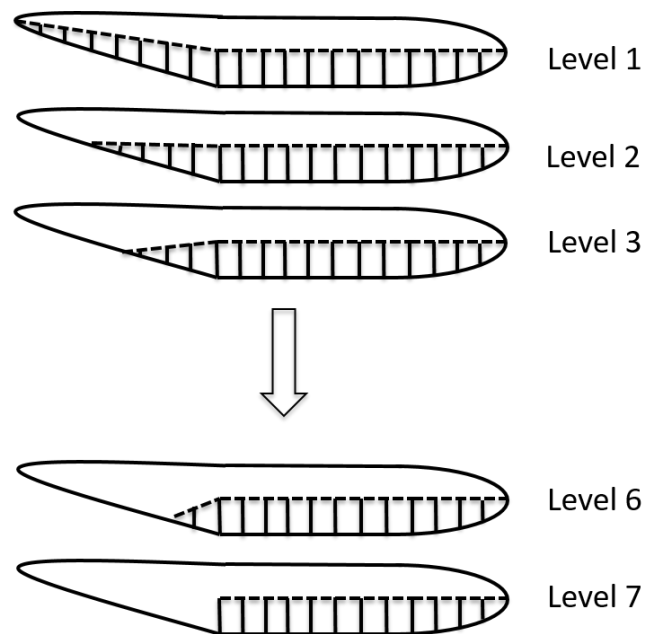


Figure 6.18: Simplified assumption of different locations of flow separation.

## Chapter 7

# Application to Aircraft Ditching: Ditching Experiments

A series of experiments are described which have been designed and conducted to validate the numerical ditching model described in Chapter 6.

### 7.1 Background

Traditionally, model experiments have been the most reliable validation reference for any kind of physical simulations. Aircraft ditching is difficult to reproduce exactly. Moreover, the relevant parameters of ditching to investigate, i.e., impact load, pressure distribution, motions and accelerations are complicated when attempting to carry them out together. Two popular techniques of ditching investigation (Smith et al., 1952) consist of different capabilities and limitations. The guided towing technique allows the measurement of the impact load, as a reference ground is necessary in order to take the value of this parameter. However, motions and accelerations are not recreated accurately. While the free launching technique is capable of recreating realistic motions and accelerations but without any means of measuring the impact loads.

Another essential consideration is that previous ditching experiments have been complex and expensive. Therefore, the present work aims to find a simple way to carry out a series of ditching experiments taking into account the availability of resources. Following the scope of the actual goal, the impact load is the first parameter to investigate; a similar guided towing technique seems to be the first alternative to follow. As it also allows the instant accelerations and motions after impact to be captured. As well as it is sufficient to use as reference data for the simulations done in Chapter 6, with the limitation of evaluating the relevant parameters in a short interval after the moment of impact.



In summary, the aim and objectives of planning this experimental campaign are, firstly, to be used as validation data for the results from the mathematical model and consequently, to implement and improve the model capability with the inclusion of appropriate correction factor.

## 7.2 Experimental Planning and Procedure

The load on the fuselage can be measured either by integrating a number of discrete pressure measurements or by measuring the total force acting on the fuselage. The measurement of pressure requires a number of small area pressure transducers. The measurement of total force acting on the fuselage is simpler and less expensive to achieve using a loadcell. Also, an accelerometer is planned to include in order to evaluate the acceleration of the model at the moment of impact.

### 7.2.1 Facility

Due to limitations of resources and facilities, it is difficult to build and install similar equipment as it was done in previous experiments. Some adaptation for available facilities is necessary. The Southampton Solent University Towing Tank is selected to use in the present work due to the actual circumstance and availability. It is equipped with a motorized carriage capable of achieving the maximum speed of  $4.2\text{ m/s}$ . The dimensions of the tank are:

- Length: 60.00 m
- Beam: 3.70 m
- Depth: 1.85 m

An important consideration is the maximum speed of the carriage used to accelerate the model. The first approach will be finding corresponding model dimension using Froude Scaling. Following the full-scale data in Table 7.1, the maximum landing speed is  $70\text{ m/s}$ , scaling the model down to the maximum speed of the carriage gives the results shown in Table 7.2:

### 7.2.2 Preliminary Simulations

Due to the similarity of the model used in Chapter 6, the fundamental length and weight of the full-scale fuselage are approximated and extracted from the commercial aircraft Bombardier G7000 as follows:

Table 7.1: Froude scaling of controlling parameters of free falling technique (1).

	$L$ (m)		$D$ (m)		$U$ (m/s)			$V$ (m/s)	
Full scale	24	2.4	30	40	50	60	70	6	
Model scale	0.88	0.09	5.74	7.66	9.57	11.49	13.4	1.15	
	1.2	0.12	6.71	8.94	11.18	13.42	15.65	1.34	
	1.5	0.15	7.5	10	12.5	15	17.5	1.5	
	1.8	0.18	8.22	10.95	13.69	16.43	19.17	1.64	
	2	0.2	8.66	11.55	14.43	17.32	20.21	1.73	
	2.64	0.26	9.95	13.27	16.58	19.9	23.22	1.99	

- Length: 24.00 m
- Basic Operating Weight: 25,764 kg
- Maximum Ramp Weight: 48,308 kg
- Maximum Take off Weight: 48,194 kg
- Maximum Zero Fuel Weight: 28,350 kg
- Maximum Fuel Weight: 21,523 kg

Table 7.2: Froude scaling of controlling parameters of free falling technique (2).

	$L$ (m)	$D$ (m)			$U$ (m/s)			$V$ (m/s)	$z_{G_0}$ (m)	$F_{max}$ (N)
Full scale	24	2.4	30	40	50	60	70	6	3	
Model scale	0.08	0.01	1.73	2.31	2.89	3.46	4.04	0.35	0.01	0.04
	0.18	0.02	2.57	3.43	4.28	5.14	5.99	0.51	0.02	0.38
	0.26	0.03	3.15	4.2	5.24	6.29	7.34	0.63	0.03	1.27
	0.35	0.04	3.63	4.84	6.06	7.27	8.48	0.73	0.04	3.02
	0.44	0.04	4.06	5.42	6.77	8.12	9.48	0.81	0.06	6.01
	0.53	0.05	4.45	5.93	7.42	8.9	10.38	0.89	0.07	10.36
	0.62	0.06	4.81	6.41	8.01	9.61	11.21	0.96	0.08	16.46
	0.7	0.07	5.14	6.85	8.56	10.28	11.99	1.03	0.09	24.69
	0.79	0.08	5.45	7.27	9.08	10.9	12.72	1.09	0.10	35.05
	0.88	0.09	5.74	7.66	9.57	11.49	13.4	1.15	0.11	47.32
	1.06	0.11	6.29	8.39	10.49	12.59	14.68	1.26	0.13	81.74
	1.23	0.12	6.8	9.06	11.33	13.59	15.86	1.36	0.15	130.94
	1.41	0.14	7.27	9.69	12.11	14.53	16.95	1.45	0.18	195.08
	1.58	0.16	7.71	10.28	12.85	15.41	17.98	1.54	0.20	279.58
	1.76	0.18	8.12	10.83	13.54	16.25	18.96	1.62	0.22	385.24

The dimensions of the model are scaled down using breadth Froude number,  $F_{n_B}$ , while the corresponding masses are scaled down using constant volumetric density. The actual  $F_{n_B}$  for this landing speed is 14.43. As it can be seen in Table 7.2, the limited speed corresponding to the full-scale maximum speed (70 m/s) leads to scaled down model of 0.08 m length with approximately 0.02 kg of mass. This size of model will not allow

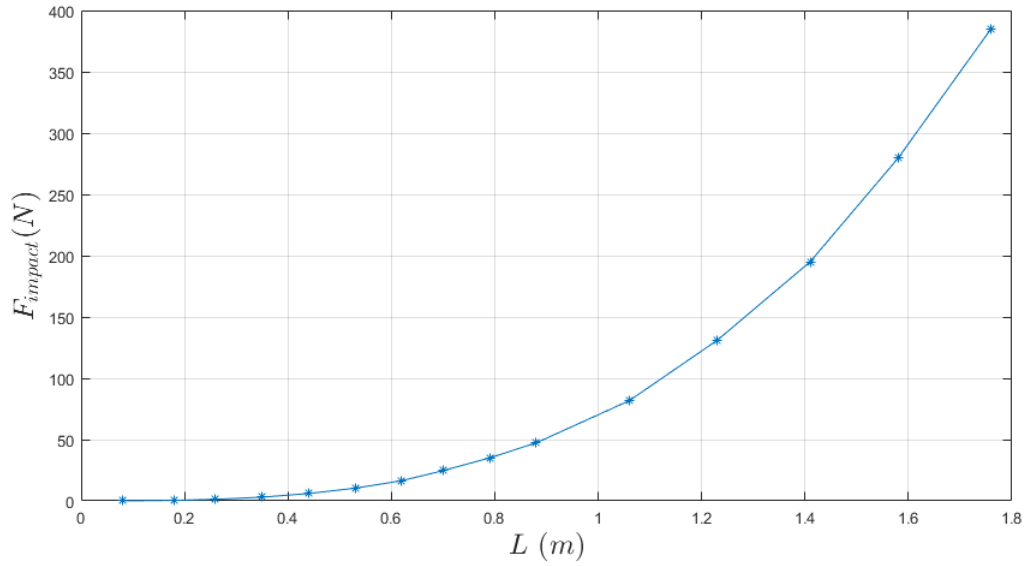


Figure 7.1: Impact force in term of model length.

any kind of instrumental equipment to be installed, as it is too small. Then, when considering the minimum full-scale landing speed ( $30 \text{ m/s}$ ), the corresponding model scale dimension is of  $0.44 \text{ m}$  length, which is still too small.

A possible solution for the actual circumstance is proposed to be the assumption that the impact forces are uniformly and directly proportional to the model dimensions. If the impact forces corresponding the low landing speed range (low  $F_{n_B}$ ) are also of the same behaviours, the high-speed range (high  $F_{n_B}$ ) should give proportionally the same results. The proof of this assumption for the actual high  $F_{n_B}$  (14.43) is evaluated by the mathematical model varying the model lengths (with corresponding landing speed), and plotting a curve of impact force as shown in Figures 7.1 - 7.2.

As mentioned previously, considering the actual Froude number, the corresponding model size is too small, and it is decided to use  $1.58 \text{ m}$  length model instead, in order to facilitate the installation of measuring equipment. Hence, the Froude number,  $F_{n_B}$ , reduces to 3.30 at the maximum speed of the carriage. Although the reduced Froude number is significantly small comparing to the original Froude number, it will be analysed in order to fulfil the assumption mentioned above. Note that at this stage of the work, parameter of interest is only the global impact force, the motions after impact are neglected implying a simplification of the tests to be fixed in pitch but free to heave.

Moreover, considering the mass of the model and applying Froude scaling to the full scale weight results that the range of model's mass is  $9 \text{ kg}$  -  $16 \text{ kg}$  corresponding to the basic operating weight and maximum weight of the full scale aircraft respectively.

The plot of impact forces in terms of low landing speed is shown in Figure 7.3.

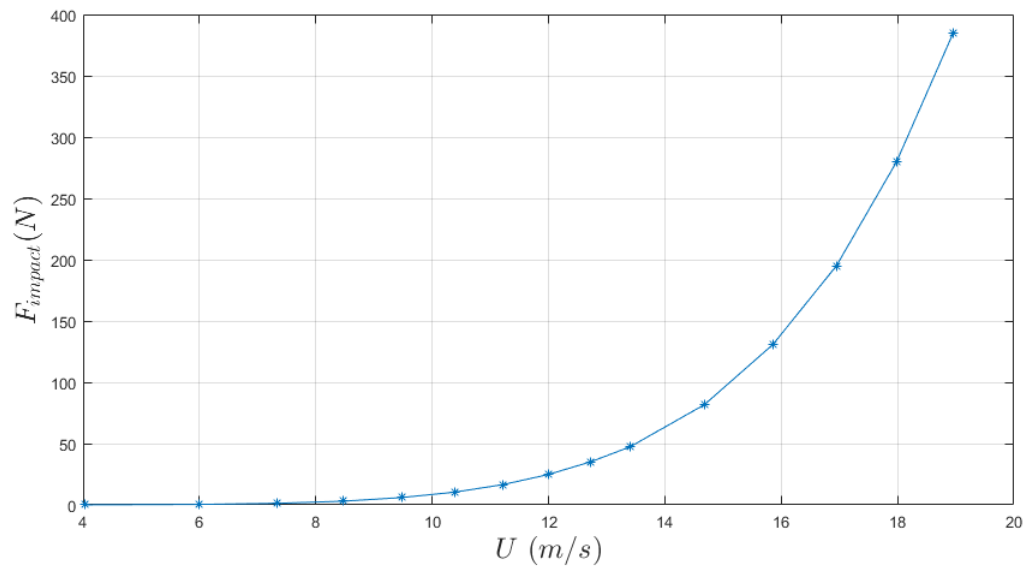


Figure 7.2: Impact force in term of landing speed.

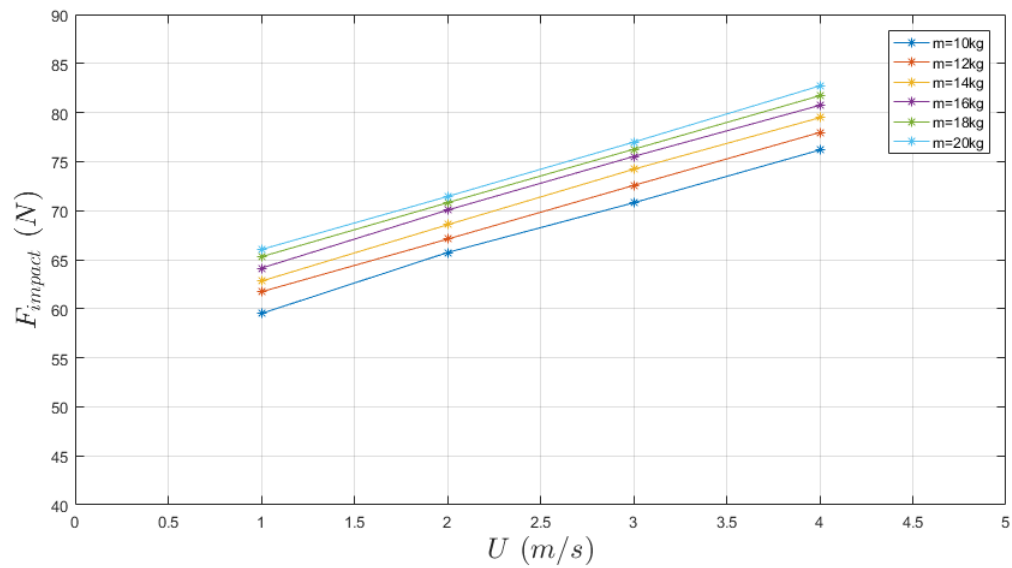


Figure 7.3: Impact force in term of low landing speed in different masses.

Obviously, the impact forces appear to be uniformly proportional to the landing speed. Nevertheless, although it seems to be linear, the landing speeds are at the low range, and this cannot be fully confirmed unless the higher speed can be evaluated.

The influence of model's mass is another issue necessary to account for. As several parts will be installed in the model, the effect of the mass on impact forces is analysed numerically by the mathematical model. It is presented in Figure 7.4 and also shown the uniform proportion when increasing the masses.

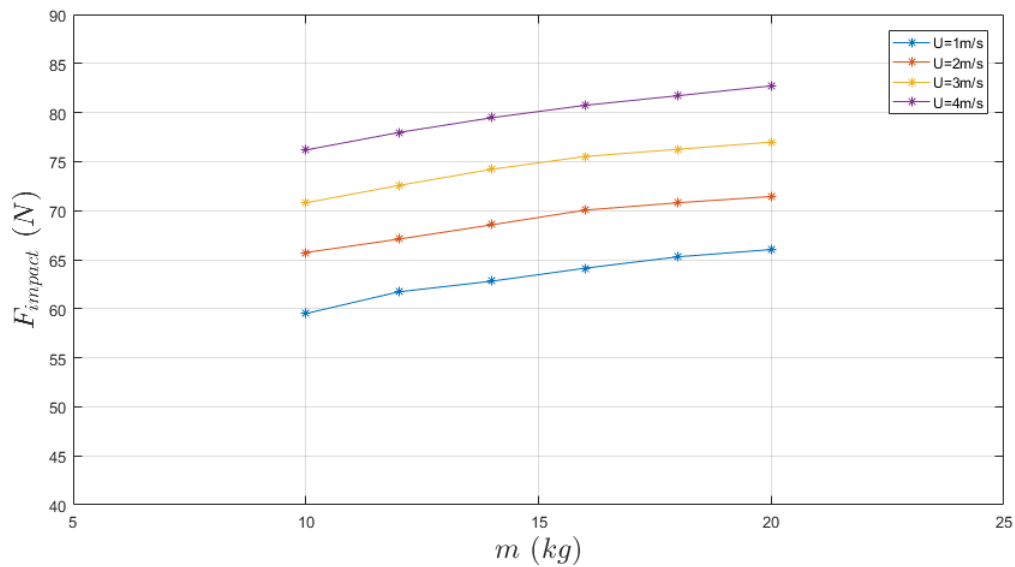
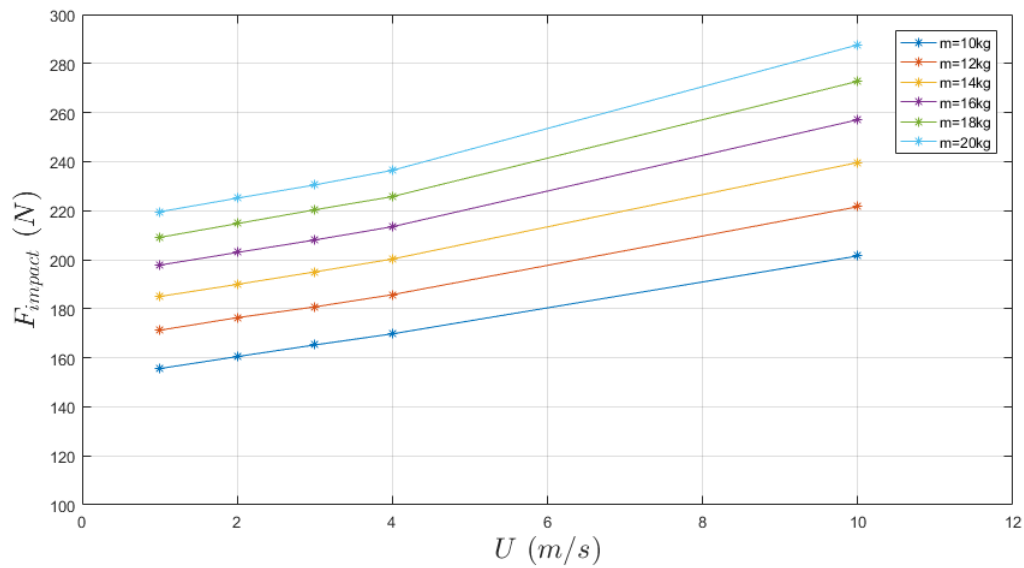


Figure 7.4: Impact force in term of model's mass.

Figure 7.5: Impact force in term of low landing speed extrapolating to 10  $m/s$ .

It is believed that when increasing the landing speed to that corresponding to the full-scale speed, the resulting total impact loads would be uniformly proportional to the landing speed extrapolating in the identical trend. A preliminary series of this extrapolation is carried out by the present mathematical model and presented in Figure 7.5.

Note that the resulting impact forces shown in Figure 7.5 are larger than those in Figures 7.1 - 7.4 because the initial height above water before impact has been raised in order to match the actual dimensions of the facility.

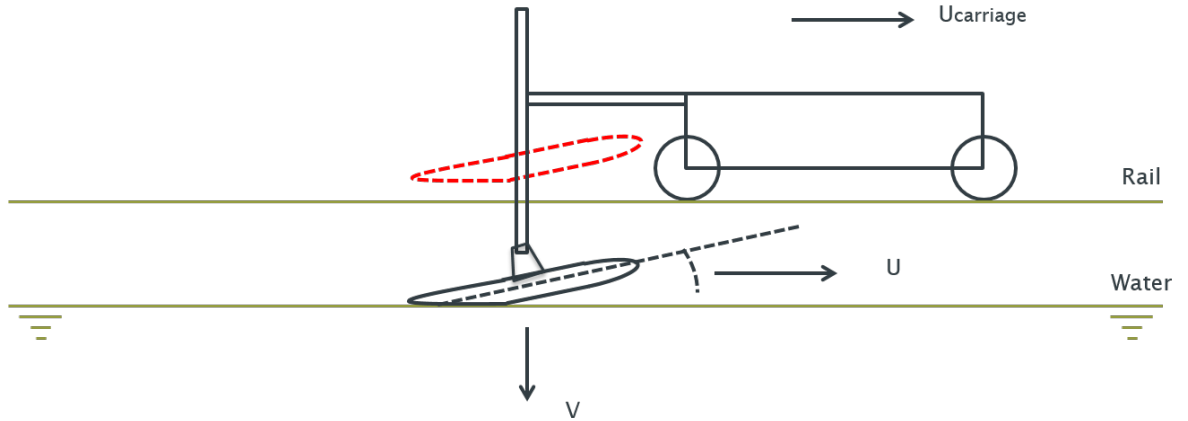


Figure 7.6: Full launching equipment.

### 7.2.3 Fuselage Model

The geometry of the fuselage used in this work is based the commercial jet Bombardier G7000, identical to that used in numerical simulations in Chapter 6. It is scaled down to 1.50 m length fulfilling the decision of model's dimension previously estimated. The core of the model is made of medium density foam dividing into three main parts; tail, cylindrical and nose part. In order to get the tail form as smooth as possible, it is split again into 5 sections to achieve a conical form. The cylindrical part is split into two part as the machine used to cut the foam has a limited length. The nose part is split into six sections although it is not necessary, as this part does not seem to be affected by the geometry-water interactions. All of the parts are joined together by epoxy resin and then coated by carbon fibre fabric. This fabric allows the core to be strengthened in order to survive the ditching impact.

### 7.2.4 Equipment

The use of launching equipment or the launching rig needs to meet the conditions of the facility and the preliminary simulations. The horizontal landing speed can be achieved by the towing speed of the tank's carriage. While the vertical motions will be restricted by a guided rail component. The whole equipment is shown schematically in Figure 7.6. Details of its components are presented in Appendix D.

### 7.2.5 Instrumentation

The parameters of interest as mention previously are the total impact force and impact acceleration. To fulfil this aim, three sensors are available covering the requirement of the further data processing. The installation is represented schematically in Figure 7.7.

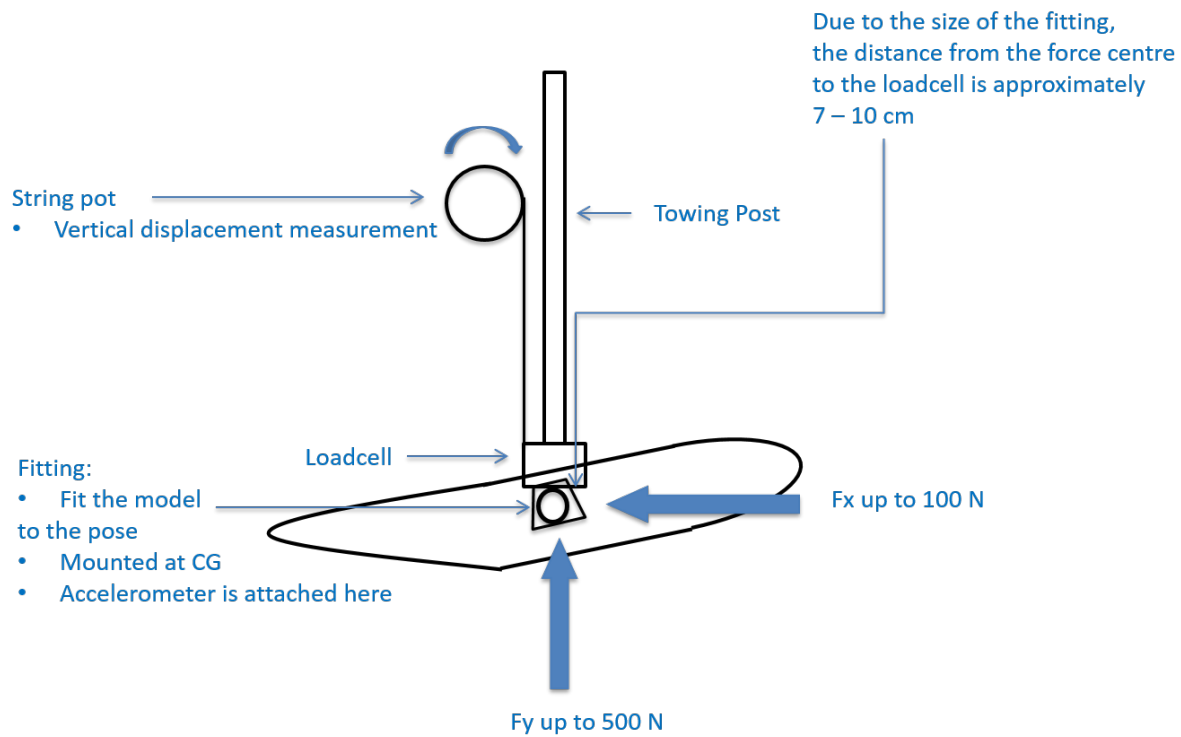


Figure 7.7: Schematic of instruments installation.

The system consists of the following instruments:

- **NOVATECH F332 2 Axis Loadcell:** The instrument is capable of acquiring bi-directional forces in two perpendicular axes. It is calibrated to the range of  $\pm 300\text{ N}$  and  $\pm 700\text{ N}$  in horizontal and vertical direction respectively.
- **PCB PIEZOTRONICS 353B31 Single Axis Accelerometer:** It operates in a range of  $\pm 100g$  providing reading in gravity scale.
- **Linear String Potentiometer PT5A:** It provides measurement of linear displacement with a range of  $0-6\text{ m}$ . The resolution is claimed to be virtually infinite with a capability of calibration into any convenient unit of measurement.
- **National Instruments CompactDAQ Controllers cDAQ-913x:** It features a multi-core processor for intense multiple processing tasks simultaneously. It operates with MS Windows 7 providing possibility of easily using LabVIEW to control and acquire the data from the other instruments.

Details of each instrument are explained in Appendix D.

### 7.2.6 Launching Technique

Regarding the launching technique, once the rig is installed in the aluminium frame of the carriage, the model was raised such that the CG was 0.42 *m* above the water. Once the carriage is up to speed, the model was released using a quick release mechanism. The model was released towards the end of the run in order to minimise the forces exerted on the model if it became fully submerged.

### 7.2.7 Uncertainty Analysis of the Instruments

Prior to commence the main experimental tests, a series of bench tests of the rig without the model are carried out, in order to analyse the experimental uncertainties associated to the instruments. The results can be used as an additional consideration when validating the mathematical model.

The tests consist of launching the sliding post (B) together with the loadcell case (C) into a foam damper (see Appendix D). The only relevant controlling parameter in these tests is the height above the floor. Each launch run is repeated until the data reading is considered stable. The time histories of all of those three instruments are recorded and analysed. Samples of the reading from the instruments are shown in Figure 7.8.

The uncertainty of the instruments is analysed quantitatively by taking the mean values of each instance in time histories. Standard deviation (STD) and mean absolute error (MAE) are then taken to represent the actual fluctuations considering the mean value as the reference. For instance, as it can be seen in Figure 7.8, in a set of the reading of displacement  $S_{ij}$  ( $i$  indicates an independent run and  $j$  indicates each particular instance in time history) at each particular instance  $j$ , the mean value of different runs  $i$  is taken as  $\bar{S}_j = \frac{1}{N} \sum_{i=1}^N S_{ij}$ , where  $N$  is the number of launching runs.

The standard deviation of  $i$  runs are then evaluated as  $\sigma_{S_i} = \sqrt{\frac{1}{n} \sum_{j=1}^n (S_{ij} - \bar{S}_j)^2}$ , where  $n$  is the number of the reading data in each particular run. This can identify the level of fluctuation from the expected value (mean) of data read from the instrument. Similarly, the mean absolute error is evaluated as  $\varepsilon_{S_i} = \frac{1}{n} \sum_{j=1}^n |S_{ij} - \bar{S}_j|$ . The uncertainty of the instruments is quantitatively represented in Table 7.3.

Each instrument committed a small magnitude of error of its reading. Considering the order of magnitude of the error between these instruments, the linear pot and the loadcell show good reliability. While the accelerometer presents the maximum percentage of error comparing to its corresponding range. In order to confirm the accuracy of the accelerometer's reading, use of the second order time derivative of the displacement reading taken from the linear pot is used and compared with the reading from the accelerometer.



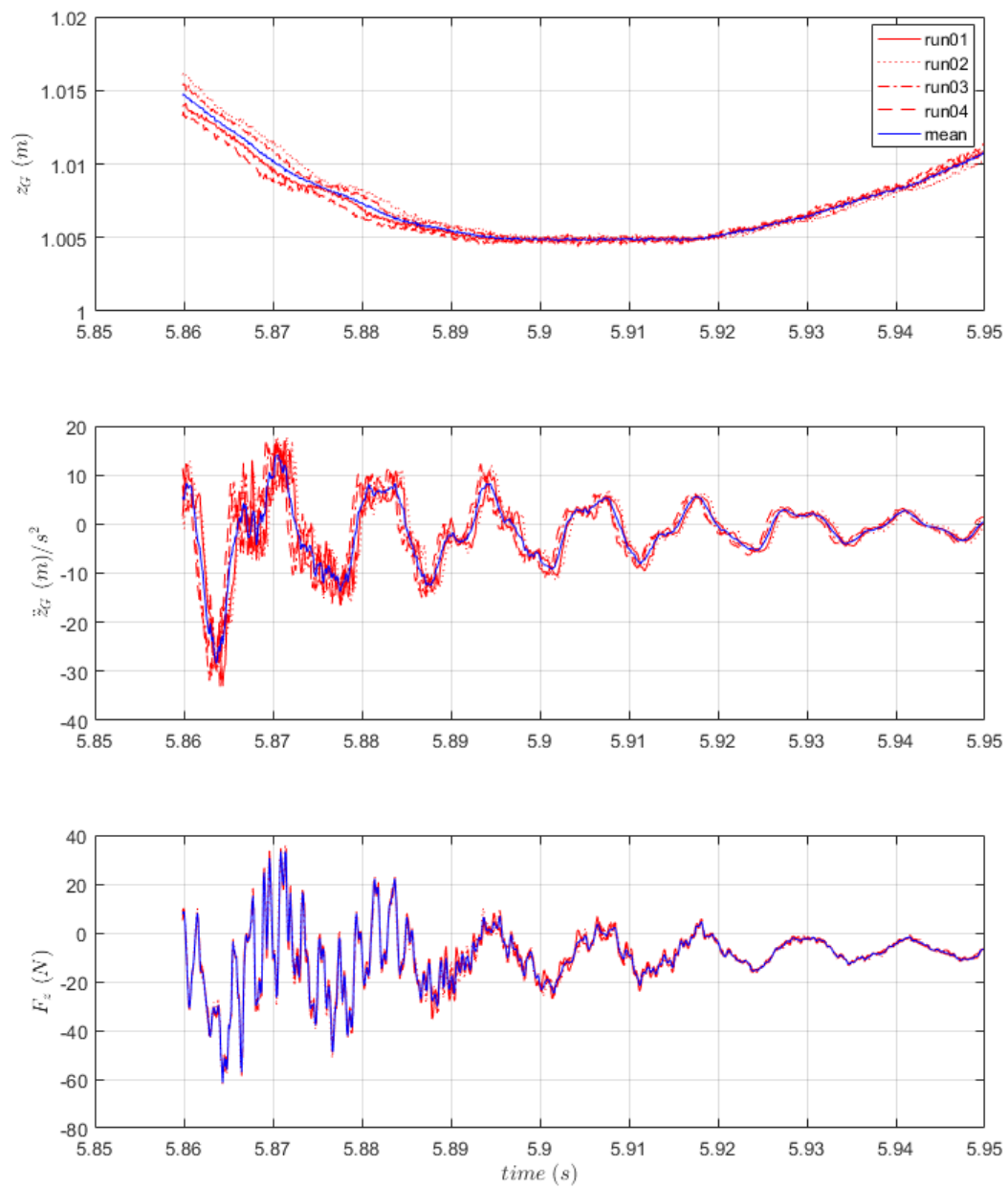


Figure 7.8: Samples of time series of repeating free falling runs.

Table 7.3: Standard deviations and mean absolute errors of the instruments.

Instruments	Run	Standard Deviation	Mean Absolute Error
Linear Pot	1	0.0393897 (m)	0.0015516 (m)
	2	0.0393897 (m)	0.0015516 (m)
	3	0.0393897 (m)	0.0015516 (m)
	4	0.0393897 (m)	0.0015516 (m)
	5	0.0094813 (m)	0.0000899 (m)
	6	0.0211978 (m)	0.0004493 (m)
	7	0.0109706 (m)	0.0001204 (m)
	8	0.0134497 (m)	0.0001809 (m)
	Average	0.0265823 (m)	0.0008808 (m)
Accelerometer	1	0.3060892 (g)	0.0936906 (g)
	2	0.3060892 (g)	0.0936906 (g)
	3	0.3060892 (g)	0.0936906 (g)
	4	0.3060892 (g)	0.0936906 (g)
	5	0.2702256 (g)	0.0730219 (g)
	6	0.2514512 (g)	0.0632277 (g)
	7	0.2699678 (g)	0.0728826 (g)
	8	0.3193071 (g)	0.1019570 (g)
	Average	0.2919135 (g)	0.0857314 (g)
Loadcell	1	1.0788852 (N)	1.1639933 (N)
	2	1.0788852 (N)	1.1639933 (N)
	3	1.0788852 (N)	1.1639933 (N)
	4	1.0788852 (N)	1.1639933 (N)
	5	0.9061310 (N)	0.8210734 (N)
	6	0.7448199 (N)	0.5547567 (N)
	7	0.9635120 (N)	0.9283554 (N)
	8	1.1523163 (N)	1.3278329 (N)
	Average	1.0102900 (N)	1.0359989 (N)

### 7.2.8 Experimental Run Log

The experimental tests have been planned to carry out as many as possible in order to cover the variation of the expected results when varying controlling parameters. The controlling parameters considered in these tests are horizontal landing speed;  $U$  and trim angles;  $\theta$ . The trim angles vary from  $6^\circ$  to  $10^\circ$ . Each trim angle is run varying the landing speeds starting from 0  $m/s$  speed fall and then moving the carriage from 1  $m/s$  to the maximum allowance of 4  $m/s$ . The run log together with the observation are presented in Table 7.4:

At the beginning of the tests, run002 to run004 are performed in order to observe the limitation of the rig security system. As well as to observe the splash flow behaviour when the model is completely floated in the water. As stated by the supplier, the loadcell is not fully waterproof, a certain quantity of water could damage the appropriate functionality of the sensor.

Table 7.4: Experimental test run log.

Run	file name	$U$ (m/s)	$\theta_{set}^\circ$	$h_0$ (m)	Remarks
1	run001	0	4	0.425	free falling
2	run002	1.01	4	0.425	towed
3	run003	1.97	4	0.425	towed
4	run004	3	4	0.425	towed
5	run005	3.71	4	0.425	launching test
6	run006	3.82	10	0.425	launching test
7	run007	0	10	0.425	free falling
8	run008	3	10	0.425	launching test
9	run009	0	10	0.425	free falling
10	run010	0	10	0.42	free falling
11	run011	3.88	10	0.42	launching test
12	run012	3	10	0.42	launching test
13	run013	1.97	10	0.42	launching test
14	run014	1.97	10	0.42	launching test
15	run015	1	10	0.42	launching test
16	run016	0	8	0.42	free falling
17	run017	3.88	8	0.42	launching test
18	run018	2.99	8	0.42	launching test
19	run019	1.97	8	0.42	launching test
20	run020	1	8	0.42	launching test
21	run021	0	6	0.42	free falling
22	run022	3.89	6	0.42	launching test
23	run023	3	6	0.42	launching test
24	run024	1.97	6	0.42	launching test
25	run025	1	6	0.42	launching test
26	run026	0	7	0.41	free falling
27	run027	3.94	7	0.41	launching test
28	run028	3	7	0.41	launching test
29	run029	1.97	7	0.41	launching test
30	run030	1	7	0.41	launching test
31	run031	0	9	0.41	free falling
32	run032	3.94	9	0.41	launching test
33	run033	3	9	0.41	launching test
34	run034	1.97	9	0.41	launching test
35	run035	1	9	0.41	launching test

The reading from run005 - run009 are discarded, as the loadcell stopped working because it got wet from spray. Then, starting from run010, the whole instrumental system resumes the appropriate working order and gives the raw data in expected form of results.

## 7.3 Signal Processing

The raw data contains a large amount of noise. These noisy signals are the results of disturbance caused by the vibration of the carriage as well as the operating frequency of its traction motor. As the sampling rate of the data acquisition is  $10,240\text{ Hz}$ , it cannot be interpreted to any representation without increasing some intervals to see those noisy spikes. By doing so, it leads to a careful consideration of selecting further appropriate filtering techniques. Moreover, the disturbance manners are fully random. It cannot be deduced with a simple assumption of a single frequency noise. Each run will be particularly analysed in order to achieve the adequate filter.

### 7.3.1 Vertical Displacement

The vertical displacement is acquired by the linear string potentiometer. According to the result of uncertainty analysis, it can be deduced that the accuracy of this instrument is good. Although most of the raw data suffers a slight disturbance during the carriage run, those noisy signals have the identical manner of spikes as shown in Figure 7.9. The spikes point into only the downward direction, use of conventional filters or moving average techniques would result in inaccurate smooth data. The expected smooth data can be deduced to the upper envelope curve of the noisy signal.

Thus, Envelope Function Technique is used to smooth the reading from linear pot. As per its definition, smooth curves containing the noisy signal are generated in both upper and lower parts. It is shown in Figure 7.9 that the upper envelope is selected to be the smooth signal of time history of the vertical displacement.

The smooth time history of displacement allows the derivation to velocity and acceleration to be achieved. After converting to work in SI units, the first order derivative of the displacement gives time history of velocity as well as the acceleration after applying the derivative to velocity ( $2^{nd}$  order derivation of displacement). The acceleration obtained from the derivative of displacement can be then used to confirm the accuracy of accelerometer. As the uncertainty analysis shows the reliability of the linear pot, using an infinitesimal time step ( $10,240\text{ Hz}$ ) of the data acquisition instrument, the deduction of accuracy of the acceleration derived from the displacement can be supposed.

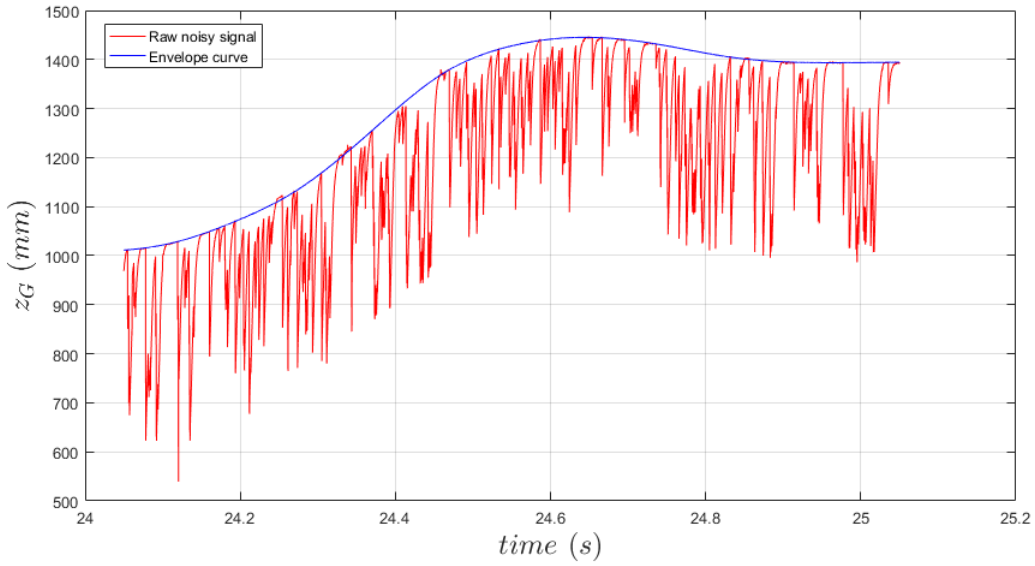


Figure 7.9: Sample of a displacement data with envelope curve zooming into the interval of impact.

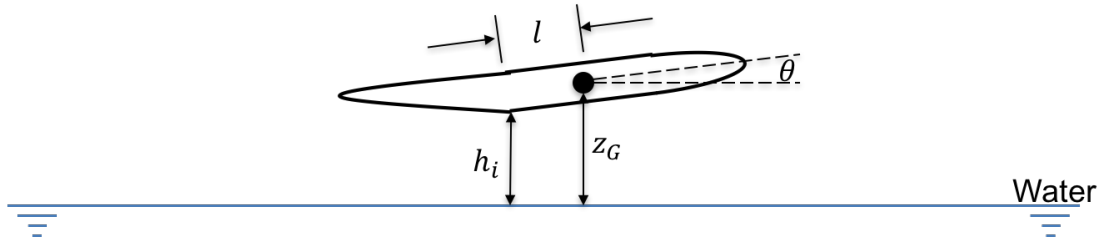


Figure 7.10: Definition of first impact location.

Moreover, following the geometry definition of the fuselage model. The smooth displacement time history allows the “instant of first impact” to be defined as shown in Figure 7.10.

The instant of impact is defined as an instant when the fuselage is firstly in contact with the water. In other words, it is the point where  $h_i = 0$ . Time histories of  $h_i$  can be obtained by the following relation:

$$h_i(t) = z_G(t) - l \cdot \sin \theta \quad (7.1)$$

Where  $l$  is the distance from CG to the location where the tail part begins.

Another instant of impact of interest is that so-called “instant of maximum impact load”. It is defined as the point where the acceleration peak is maximum during the small interval of impact. A sample of time histories of displacement, velocity and acceleration together with the indication of both instants of impact is shown in Figure 7.11:

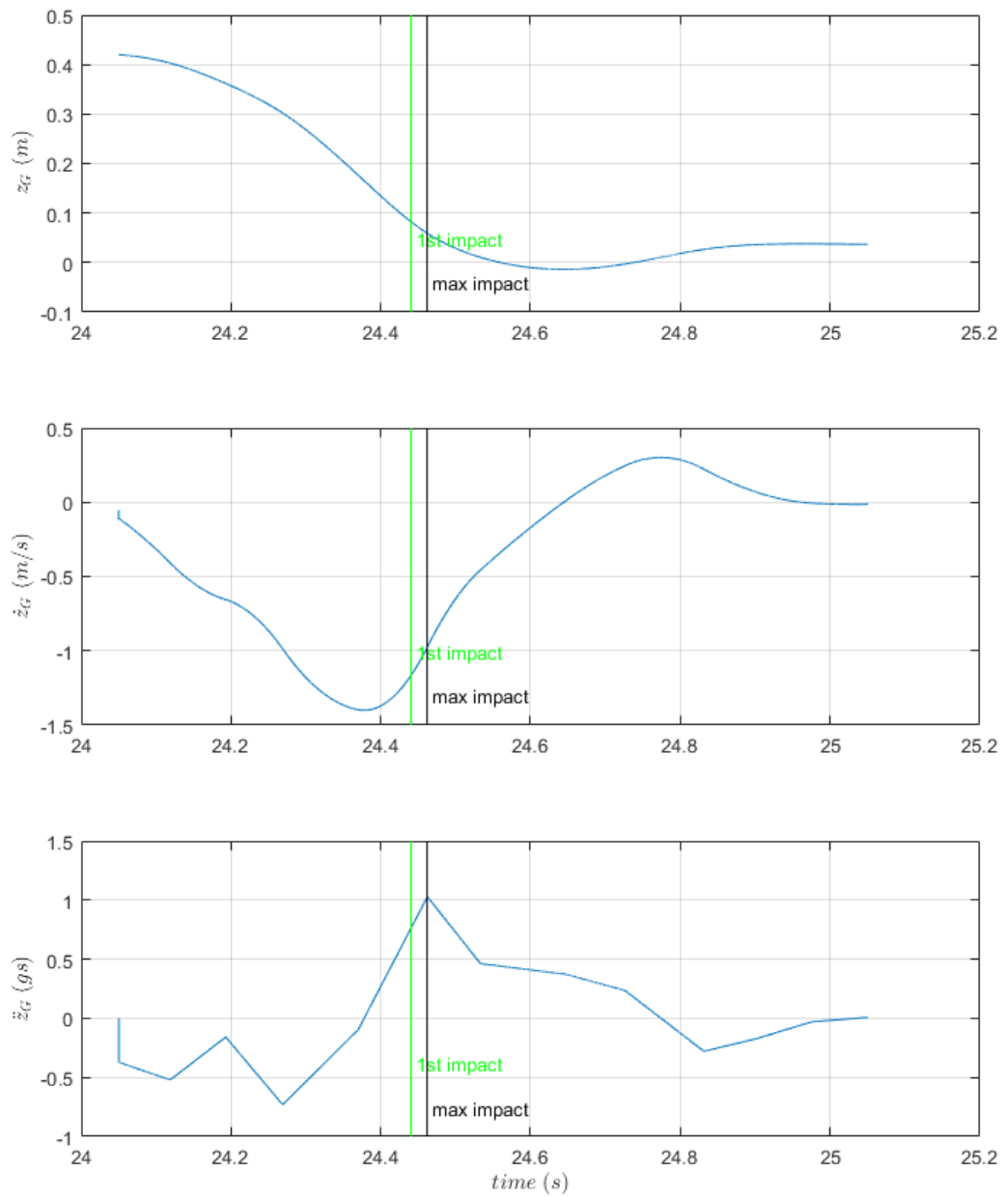


Figure 7.11: Sample of smooth displacement and velocity and acceleration derivation.

The time shifts between the instant of initial impact and maximum impact are shown in Table 7.5. The positive value represents the time lead of the maximum instant respected to the initial instant while the negative value represents the time lag.

Table 7.5: Time shift between instant of initial impact and maximum impact.

$\theta^\circ$	$U$ (m/s)	Initial Impact (s)	Maximum Impact (s)	Time Shift (s)
6	1	34.89824219	34.96992188	-0.071679687
	2	24.46191406	24.48173828	-0.019824219
	3	20.19130859	20.19296875	-0.001660156
	4	18.0734375	18.10234375	-0.02890625
7	1	34.43115234	34.56699219	-0.135839844
	2	23.04521484	23.08046875	-0.035253906
	3	18.91298828	18.9515625	-0.038574219
	4	17.46308594	17.56699219	-0.10390625
8	1	34.66220703	34.79892578	-0.13671875
	2	23.65136719	23.77695313	-0.125585937
	3	19.88076172	19.89296875	-0.012207031
	4	20.87158203	20.88095703	-0.009375
9	1	35.47919922	35.5984375	-0.119238281
	2	24.28916016	24.33994141	-0.05078125
	3	22.47373047	22.56894531	-0.095214844
	4	15.62236328	15.72597656	-0.103613281
10	1	35.19042969	35.20673828	-0.016308594
	2	22.89990234	22.90048828	-0.000585937
	3	19.70302734	19.71992188	-0.016894531
	4	16.87587891	16.88994141	-0.0140625

### 7.3.2 Vertical Acceleration

The raw signals achieved from the accelerometer also suffer disturbances of random amplitude. The difference from linear pot signals is that these signals are disturbed in both upward and downward directions.

Choosing the optimal filter is typically an interactive trial and error process. The goodness of a filter is best based on visual inspection of the results. Unlike previous cases, “Butterworth Low Pass Filter” is chosen to smooth the acceleration signals. The relevant controlling parameters in this operation are the order of filter,  $N_f$  and the cut-off frequency,  $f_c$ . In order to select the most adequate  $f_c$ , “Fast Fourier Analysis” is performed prior to smooth the signal. A sample of FFT together with the smooth signal is shown in Figure 7.12.

The resulting smooth signals of the accelerations obtained by using different  $f_c$  chosen from FFT are compared with the derivative accelerations from the displacements. The filtered signal with different  $f_c$  are also shown in Figure 7.12. The decision of  $f_c$  is

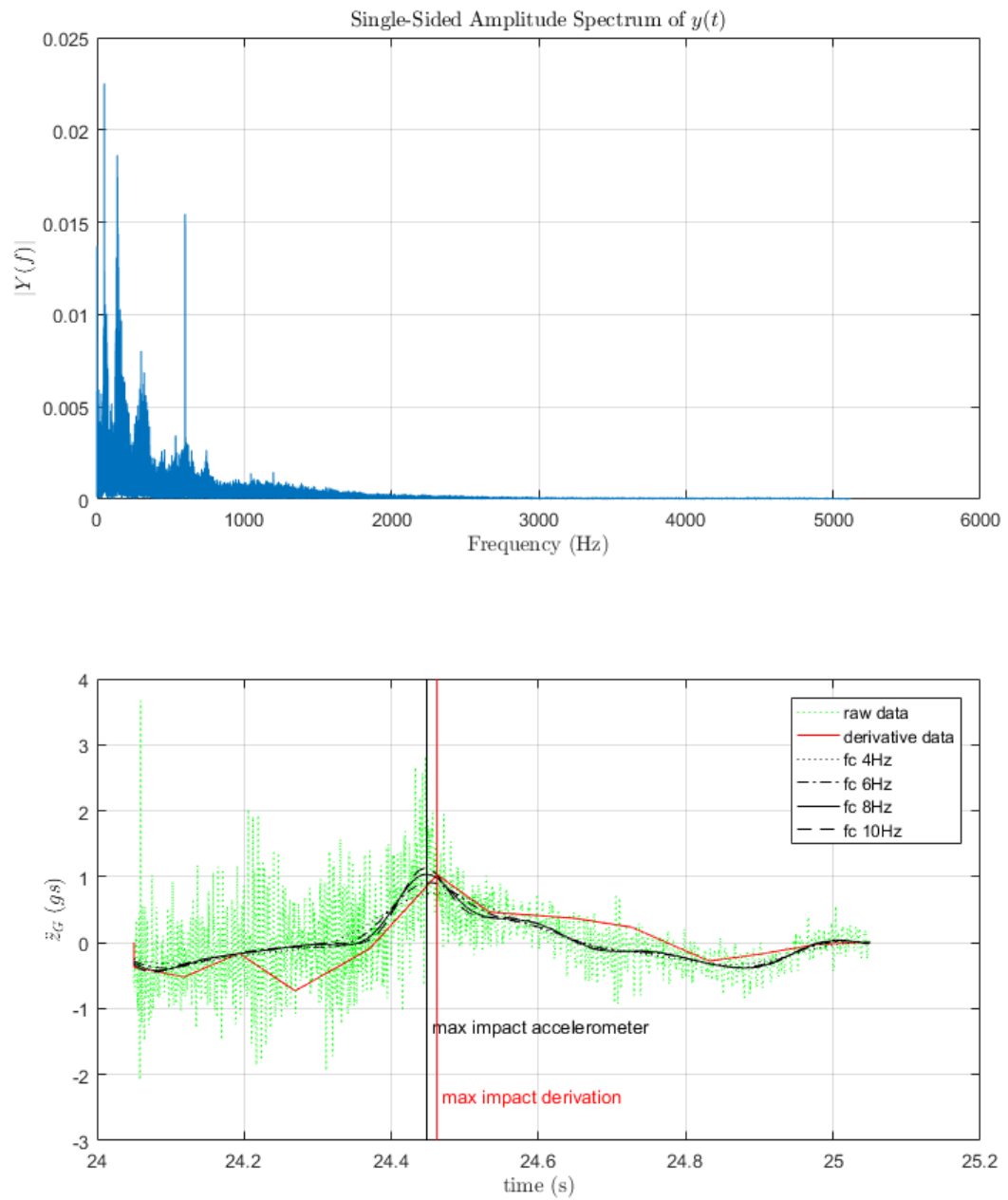


Figure 7.12: Sample of FFT analysis and smooth acceleration signals.



taken on the basis of those values that are capable of giving the closest peak values to those of derivative accelerations. Once the optimal  $f_c$  are used, Both sets of signals give very good agreement time histories with a small time shift of the instant of maximum impact. The maximum impact accelerations from both sources together with the instant of maximum impact and the time shifts are shown in Table 7.6.

Table 7.6: Maximum impact accelerations and time shift between reading and derivative data.

$\theta^\circ$	$U$ (m/s)	Maximum derived $\ddot{z}_G$ (g)	Maximum <i>smooth</i> $\ddot{z}_G$ (g)	% error to the derive value	Time Shift (s)
6	1	0.6975	0.7388	5.921146953	0.101953125
	2	1.0280	1.0360	0.778210117	0.013964844
	3	1.0390	1.0420	0.288739172	0.041992188
	4	0.9151	0.9151	0.000000000	0.000488281
7	1	0.6789	0.6694	1.399322433	0.175000000
	2	0.8761	0.8031	8.332382148	0.061523438
	3	1.0670	1.0590	0.749765698	0.05859375
	4	0.7090	0.7213	1.734837800	0.138085937
8	1	0.7226	0.7171	0.761140327	0.158984375
	2	0.6915	0.7118	2.935647144	0.151953125
	3	0.8053	0.8151	1.216937787	0.028027344
	4	0.9214	0.9165	0.531799436	0.019042969
9	1	0.8463	0.8608	1.713340423	0.131445313
	2	0.8930	0.8783	1.646136618	0.058984375
	3	0.7587	0.8407	10.80796099	0.100000000
	4	0.7617	0.7267	4.594984902	0.108007813
10	1	1.0560	1.0680	1.136363636	-0.019042969
	2	0.7885	0.8376	6.227013316	0.003515625
	3	1.0410	1.0400	0.096061479	0.022949219
	4	1.1870	1.1940	0.589721988	0.011914063

The order of magnitude of the time shift is less than 0.15 s. Comparing to the overall interval of the impact that lasts 0.3 s, it can be considered small, leading to the good agreement between both sources of acceleration data.

### 7.3.3 Vertical Impact Force

Unlike the vertical acceleration, there are no analytical or other reference sources to compare with the vertical and horizontal impact forces read from the loadcell. Selection of cut-off frequencies is carried out by visual approximation. A sample of FFT analysis and smooth signals filtered by different  $f_c$  is shown in Figure 7.13, together with the accelerations from both sources.

The location of impact force in time history can be assumed to be the identical instance as the impact acceleration. Although apparently there are several peaks that are larger than the deduced peak of impact in time history, the most important point of interest

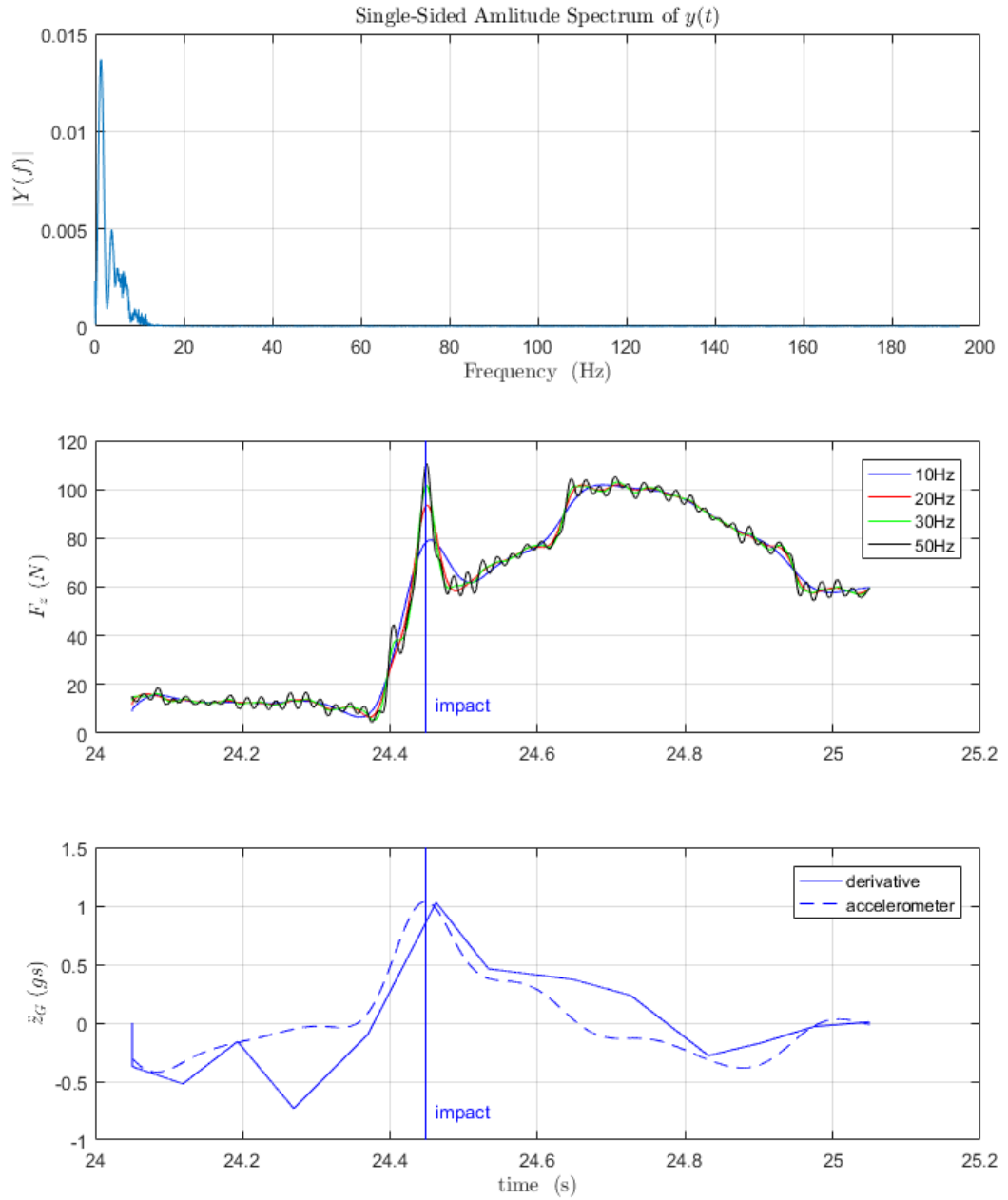


Figure 7.13: Sample of FFT analysis and smooth impact force signals.

in the present work is only the instant of impact and the other peaks might be neglected. For further in-depth consideration, time history of impact force obtained from the experiment will be compared with those from numerical simulations in the validation process.

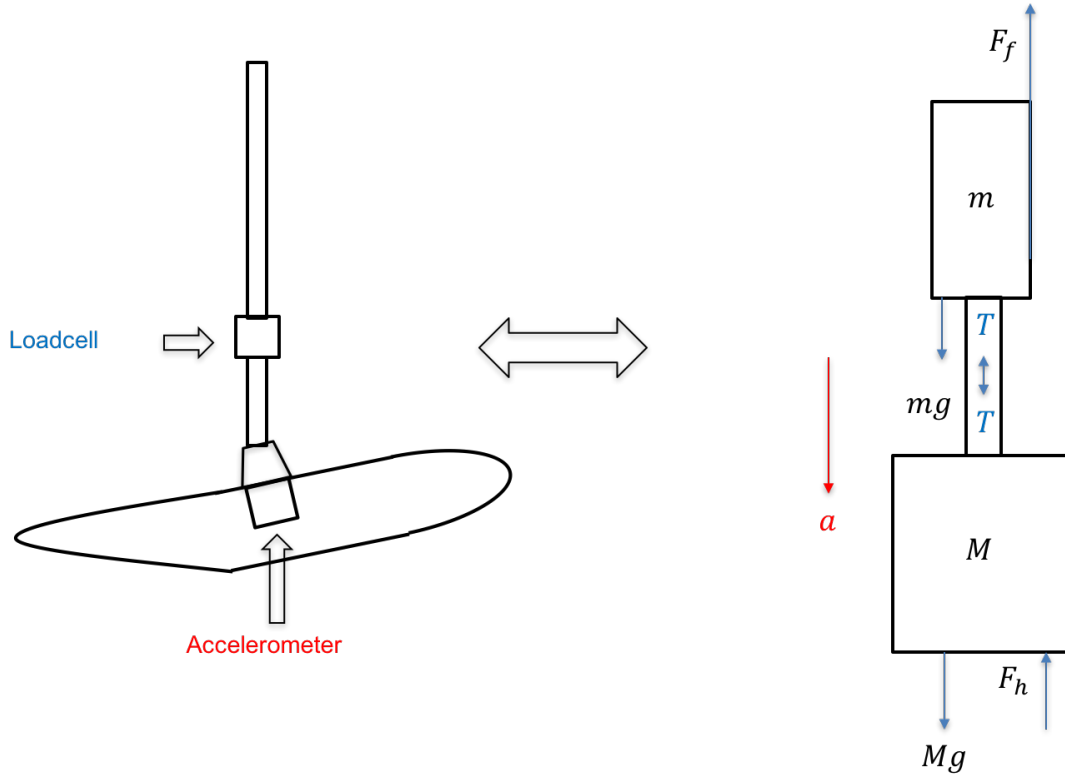


Figure 7.14: Free body diagram of the experimental rig system.

## 7.4 Validation

Following the aim of the actual experimental activities, the mathematical model developed in Chapter 6 will be validated using the results of the tests as validation reference.

### 7.4.1 Hydrodynamic Impact Force Extraction

Unlike the preliminary simulations, the actual situation of the experiments does not comply the real ditching event. When launching the model with the rig, there is friction between the rail and the carriages, including the opposite force generated by the restoring system of the linear pot. All of these additional forces cannot be neglected as their magnitude is significant, resulting in smaller vertical acceleration comparing to the gravity. While the real ditching event commits only the gravitational acceleration when approaching to land into the water.

Relying on the fact of additional forces mentioned earlier, the signal reading from the loadcell does not directly represent the hydrodynamic impact force. The free body diagram of the system is shown in Figure 7.14.

The hydrodynamic impact force can be obtained by using the following relations:

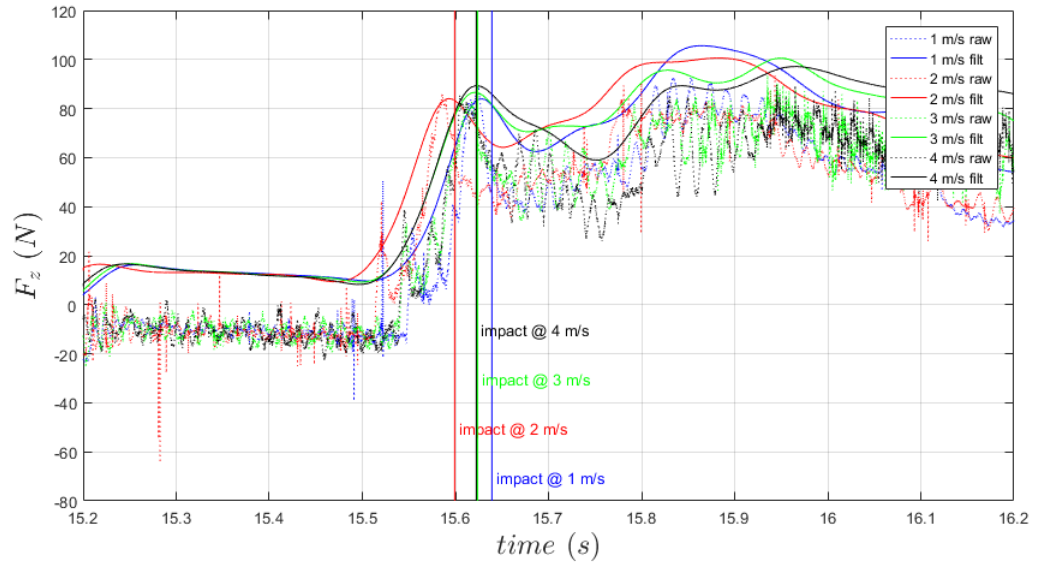


Figure 7.15: Sample of time histories of ditching event with variation of landing speed.

$$mg - T - F_f = ma \quad (7.2)$$

$$Mg + T - F_h = Ma \quad (7.3)$$

Where  $m$  and  $M$  are respectively the mass of sliding post (B) and the model's mass.  $T$  is the reading from loadcell.  $F_h$  and  $F_f$  are hydrodynamic impact force and the sum of frictions (linear pot restoring plus the friction between the rail and the carriages) respectively and finally  $a$  is the acceleration of the whole system. A sample of time history of the impact force is shown in Figure 7.15.

The variation of the impact forces in cases of committing the ideal gravitational acceleration is shown in Figures 7.16 - 7.17.

Note that, although the ideal preliminary numerical simulations (with gravitational acceleration) show that the impact force is directly proportional to the landing speed, in other words, increasing landing speed increases the impact force, the experimental results do not show the same manner. The maximum landing speed gives a drop in magnitude of the impact force. This occurrence is considered due to the fact that, as mentioned previously about the launching technique, the launching trigger activates at a very close instant when the carriage drastically decelerates to stop before reaching the end of the tank. This leads to a consideration that the landing speed caught in this interval is smaller than the desired speed due to the deceleration of the carriage.

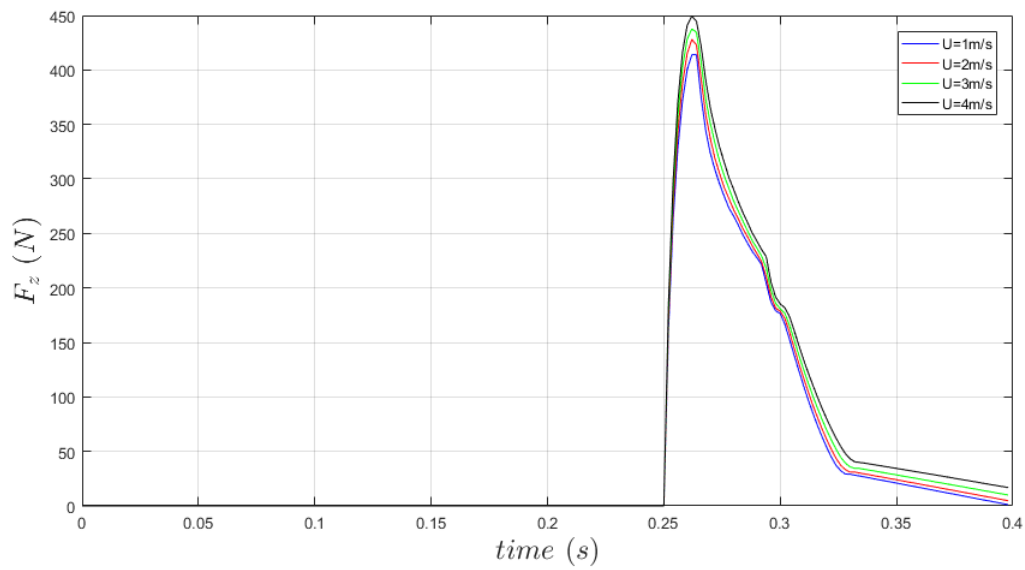


Figure 7.16: Sample of time histories of impact force resulting from simulations with ideal gravitational acceleration.

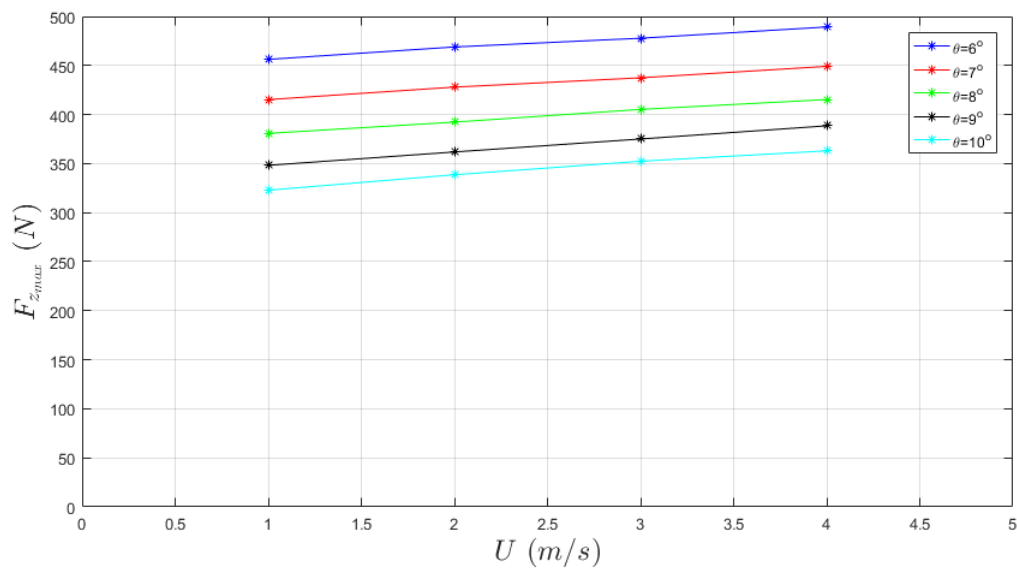


Figure 7.17: Variation of impact forces in term of landing speed from simulations with ideal gravitational acceleration.

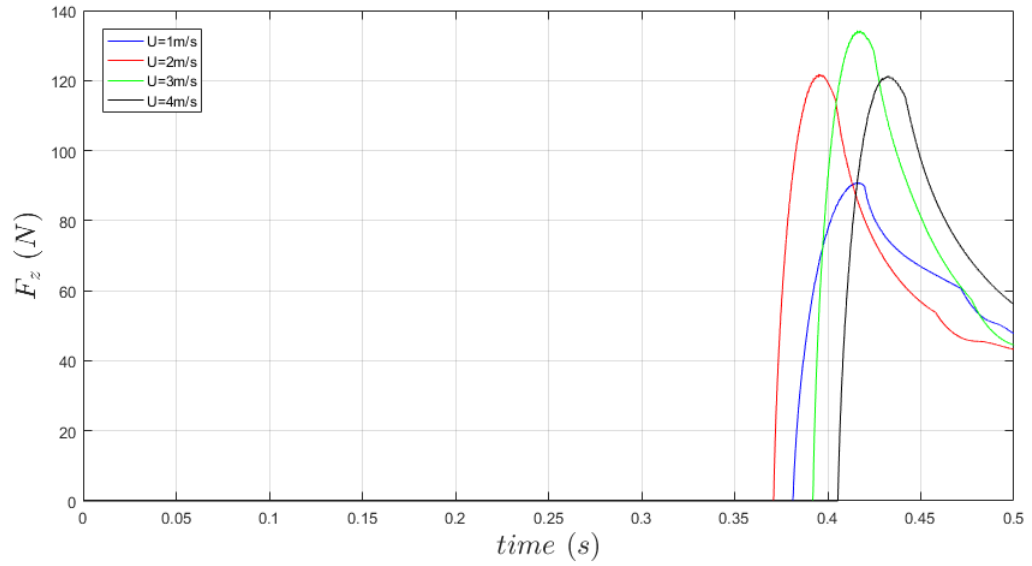


Figure 7.18: Sample of experiment's simulations.

#### 7.4.2 Simulations for Experimental Tests

As mentioned earlier, in order to carry out the accurate validation, a series of simulations by the mathematical model is set based on the dynamic conditions obtained from the experimental tests. Time histories of displacement, velocity and acceleration corresponding to each particular case are set as predefined motion conditions to run within the interval of impact. As it can be seen in Figure 7.18, due to the inappropriate event of early launching mentioned previously, most of the maximum speed landing cases present a slight drop of impact forces as happened in the experiments.

Moreover, flow separation location assumed in Chapter 6 is included in the mathematical model, allowing the appropriate selection of the best suitable time histories between both. Nevertheless, flow separation location is still only an assumption, the selection of its level is on the basis of that, at the lowest speed, the flow is fully attached to the fuselage, and begins to separate when increasing the landing speed.

#### 7.4.3 Comparison

The first notification to account for when comparing and validating these activities is that, the variation of magnitude of the impact forces is very slight. As the range of landing speeds is not wide enough to produce that notable variation. Each value differs from one to each other only in order of less than 5 N, as it can be seen also in the preliminary numerical simulations. When also considering the uncertainty of instruments, it results in a difficult issue to expect exactly the identical behaviours as it occurs in the simulations. Therefore, the scope of the actual validation is defined as

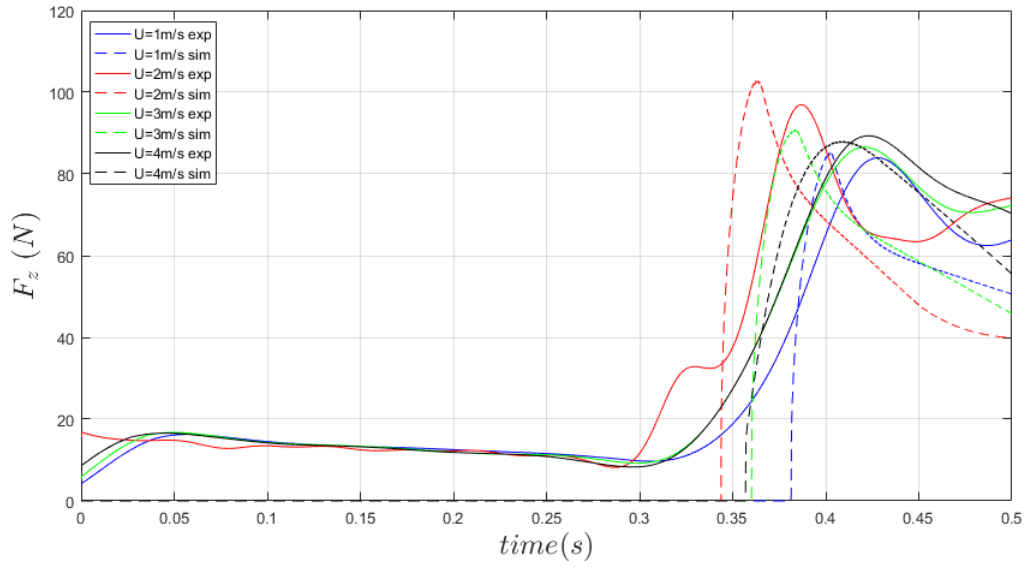


Figure 7.19: Sample of time histories resulting from both methodologies of a fixed trim varying landing speed .

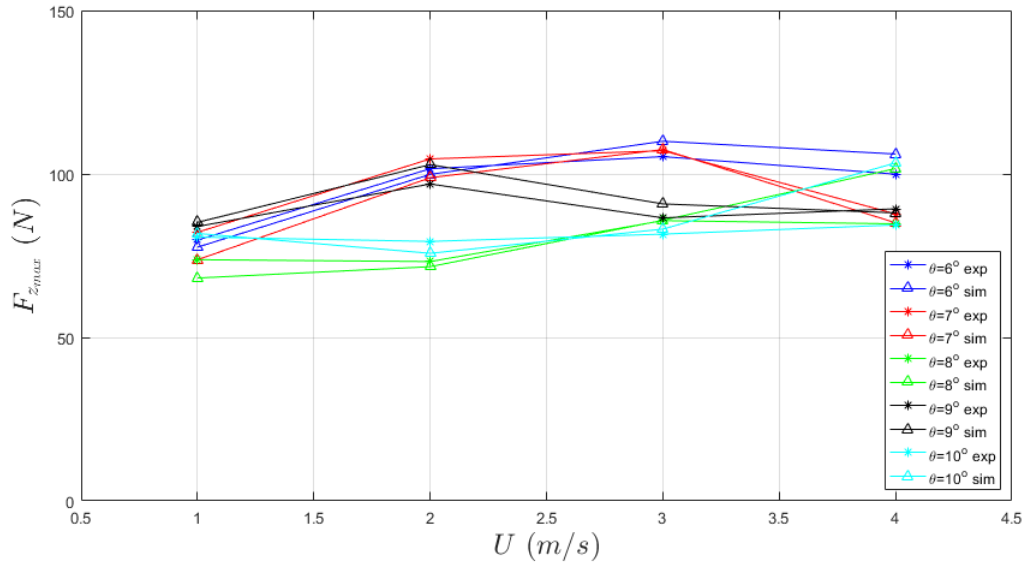


Figure 7.20: Impact forces in term of landing speed of experiments vs simulations.

the confirmation of solely the mathematical model excluding those of the real ditching event.

Figure 7.19 shows a sample of the resulting time history from both methodologies. The maximum impact forces are compared in Table 7.7.

Some observations can be seen from Figures 7.15 - 7.16 as follows;

Table 7.7: Data comparison of simulations vs experiments.

$\theta^\circ$	$U$ (m/s)	$F_{z_{max}}$ (Exp.) (N)	$F_{z_{max}}$ (Sim.) (N)	Relative Error	MAPE (%)
6	1	79.78	77.6045	0.027268742	3.759863702
	2	101.6	99.8739	0.016989158	
	3	105.3	109.9966	0.044601979	
	4	99.94	106.0898	0.061534668	
7	1	82.15	73.74535	0.102308593	4.788259665
	2	104.6	98.85137	0.054958199	
	3	107.1	107.4602	0.003363251	
	4	87.77	85.05788	0.030900344	
8	1	73.77	68.16977	0.075914768	7.453741267
	2	73.2	71.62452	0.021522921	
	3	85.72	85.83265	0.001314145	
	4	84.74	101.637	0.199397816	
9	1	83.93	85.19099	0.015024314	3.4788368
	2	96.93	102.8546	0.061122546	
	3	86.57	90.8259	0.049161392	
	4	89.33	88.09321	0.01384522	
10	1	80.69	81.80091	0.013767654	7.57789219
	2	79.36	75.72427	0.04581319	
	3	81.59	83.12531	0.018817394	
	4	84.4	103.3662	0.22471745	

- The impact force corresponding to the maximum landing speed of each fixed trim slightly drops from the previous one.
- Variation of the impact forces in term of trim angle presents an uncertain trend, complying the prediction only when running with 3 m/s of landing speed.

These unexpected trend of variation are the effect of uncertain accelerations due to the external friction of the system committed in each launching run, including the accumulated deviation from the original calibration of the system. Moreover, the obvious cause of the slight drop of impact force at maximum speed is due to the difficulty of achieving launching instant precision when running at that speed, as mentioned in Section 7.4.1. However, in most cases, although the variation of impact forces in term of landing speeds does not show the same trend as predicted in Figures 7.16 - 7.17, both methodologies show fairly good agreement with a small unavoidable uncertainty due to that slight variation of their magnitude. The errors and the deviation between the resulting data from both methodologies are clearly under the uncertainty of instruments analysed previously. Table 7.7 shows the errors committed between both by mean of mean absolute percentage error.

The assumption to be further fulfilled is that, running at higher speed range would show a more obvious variation of impact forces. The variation of impact forces is directly



proportional to the variation of accelerations. It can be deduced that, actually, the range of this validity is confirmed only under the low landing speed. Providing that the present mathematical model is capable of predicting accurately the impact force at this range, it is believed that extrapolating the full scale or increasing the landing speed would give the expected behaviours.

The validation process of the present mathematical model has been carried out successfully under limitations mentioned throughout the chapter. It can be deduced to be capable of assessing ditching impact loads effectively. To fulfil the survivability of the aircraft after impact, further implementations of the model and more complex corresponding experiments are recommended.

## Chapter 8

# Conclusion and Further Work

The aims and objectives of the present research involve fundamentally in the development of a mathematical model with the capability of simulating high-speed planing dynamics. The works done so far during the project have fulfilled that requirement, investigating the application of the model to include transverse motions and simulating aircraft ditching.

The project aims to develop, implement and optimize a mathematical model following the principle of potential flow based strip theory originally developed by [Zarnick \(1978, 1979\)](#). Several researchers have implemented Zarnick's model by adding and modifying some coefficient in order to react to more realistic physical phenomena. Nevertheless, none of these related works mentioned in detail how to optimally use this kind of model. The fundamental contributions of the project are verification and optimization of the mathematical model of high-speed planing dynamics, providing the understanding of influence of the relevant controlling parameters, including the extension application to transverse asymmetrical plane motions and aircraft ditching load prediction.

The whole contributions mentioned above lead to the deduction of application of the simplified sectional added mass expression of an expanding flat plate. It has been used as the fundamental contribution to various applications along the whole process of the project. Moreover, it has been proven to be widely applicable in different geometries, implying the simplification of use with sufficient accuracy. Details of the contributions are explained further along with their application.

### 8.1 Conclusion

The overview of work process, their results and conclusions of the whole project is summarized as follows.

- Development of the Mathematical Model:
  - The system of equations of motions has been developed from the 2<sup>nd</sup> law of Newton using the wedge water entry principle to evaluate sectional forces. The system is initially developed to be capable of evaluating the longitudinal plane motions. Consequently, the added mass coefficient used here is only heave added mass.
  - The implementation of the model is based on [Zarnick \(1978\)](#)'s mathematical model. However, some notable modification has been done on the term of partial differential of sectional added mass along the ship length,  $\partial m_a / \partial x'$ . Due to the different flow characteristic zone along the ship length, sectional added mass distribution,  $m_a$  is a sharp discontinuous function implying the discontinuity of its partial differential. Zarnick avoided the discontinuity of this term by using integration by part substitution, however, this technique eliminates the possibility of showing the pressure distribution along the ship length. It has been modified here using the continuous integration method.
  - It has been found that by varying (increasing) number of strip sections,  $N_s$ , the term  $\partial m_a / \partial x'$ , did not fluctuate that sharply, but the largest fluctuation in term of  $N_s$  is instead the time derivative term,  $\dot{m}_a$ . This term varies sharply in discontinuous points and is of large magnitude. Furthermore, when being multiplied by relative velocity perpendicular to the keel,  $V$ , the product is of extremely magnitude and leads to significant different values in terms of  $N_s$ .
- Verification of the Mathematical Model:
  - The verification process consists of the analysis of accuracy of time histories. The proposed "Hypothesis of Accuracy of Time Histories" stated that when varying (increasing or decreasing) the relevant controlling parameters, time histories should converge to a uniform form that is considered as the most accurate resulting series. Moreover, the real time histories of these simulations do not exist in reality. The "accuracy" of time histories is then defined as the RMSE of different time series evaluated by using different controlling parameters (number of sections,  $N_s$  and time step sizes,  $\Delta t$ ), comparing to those using the highest resolution. Smaller RMSE implies a higher accuracy of the series. In other words, the time series get converged when their corresponding RMSE get smaller comparing to the superior data (when simulating with the finest pair of controlling parameter in this case). The first step of verification is performed by analysing the influence of  $N_s$  and  $\Delta t$  separately.
  - At a stopped time step, the controlling parameter of the resulting forces and accelerations is  $N_s$ . This parameter influences directly to the terms associated to  $m_a$ , especially  $\dot{m}_a$ . The peak value of  $\dot{m}_a$  distribution along the ship length cannot be accurately picked if the resolution of  $N_s$  is not high enough.

Then, when the simulation time is released, the controlling parameter in this dynamical process is  $\Delta t$ .

- Various time marching numerical solvers have been analysed varying  $\Delta t$ . The optimal solvers considering the computational time and the accuracy are those from Runge-Kutta family methods confirming the original assumption of [Zarnick \(1978\)](#). Also, when considering the point of view of time marching step, the solvers can be classified into two categories. The convergence verification varying  $\Delta t$  mentioned previously is evaluated using that so called “Fixed-Step Solver”. This means  $\Delta t$  is always constant during the whole time history. While the original time marching solver used by [Zarnick \(1978\)](#) is “Variable-Steps Solver”. In comparison with the fixed-step solver, it is found that when using the initial  $\Delta t < 0.01$  s, there is no iteration performed under 1% of error stopping criteria. The use of fixed-step solver is then deduced due to the less complication in calculation routine providing better convergence behaviour.
- The mathematical model is then verified in a series of time history simulations varying together both  $N_s$  and  $\Delta t$ . For both regular and irregular wave simulations, once the optimal parameters for accuracy are defined, it is necessary to consider as well the optimal computational time. The pairs of RMSE together with computational time ratio,  $T_{cs}$  corresponding to each pair of  $N_s$  and  $\Delta t$  are analysed by mean of Pareto Efficiency. This consideration is essential due to the fact that in some cases of simulations, varying controlling parameters results in altering small fluctuation of accuracy but magnifying computational time or vice versa.
- The cases of moderate and large deadrise angles ( $\beta = 20^\circ$  and  $\beta = 30^\circ$ ) can be simulated properly with the model using small  $N_s$  and large  $\Delta t$  and give accurately the resulting time histories. Moreover, it is applicable for almost the whole range of wave frequencies and amplitudes, implying also the short computational times. Although using  $\Delta t < 0.002$  s is preferable for better accuracy, the consideration of whether it is worth or not magnifying computational times to gain non-significant difference of accuracy needs to be accounted for.
- In case of small deadrise angle hull form ( $\beta = 10^\circ$ ), more dedicated selection of the relevant controlling parameters is necessary to account for, due to the sensitivity of distribution of  $m_a$  and its derivations. Above all, when it is travelling in the waves with small frequency and large amplitude (large wave slope), increasing  $N_s$  and decreasing  $\Delta t$  are inevitable, leading to the consequence of longer computational time. Nevertheless, once  $\Delta t$  applied is smaller than approximately 0.002 s,  $N_s$  disengages its influence in convergence of time histories, due to the fact that the peak values of accelerations can be achieved appropriately and leads to the accurate motions for the next time step.

- In order to comply with the whole range of applicability, some more aspects of planing hull geometry are considered and analysed. Practically, the modern planing craft have evolved their geometry, resulting in non-constant deadrise angle hull form. The verification of optimal parameters also has been done simulating a variable deadrise planing hull. The overall convergence behaviours do not differ from the cases of constant deadrise, as long as the minimum, or the main body deadrise is identical to the range of that constant deadrise.
- Scale effects also have been investigated. Two scaled up models of those constant deadrise hulls have been simulated in the scaled up wave conditions. The resolution of controlling parameters is set in the identical manner of variation, in order to deduce the dimensional effect of those parameters. The overall convergence shows the same behaviours as the original models, including the better behaviours of the case of small deadrise angle that converges better at  $\Delta t < 0.002$  s. this could lead to the validity of the mathematical model to a rich variety of scale and geometry.
- Validation of the Mathematical Model:
  - The present mathematical model is validated against [Fridsma \(1969, 1971\)](#)'s experiments and [Zarnick \(1978, 1979\)](#)'s simulations for performances in regular and irregular waves.
  - The attitude in calm water simulated by the present model gives a good agreement to the references except at low speed, due to the fact that there is no inclusion of wave resistance component in the model, which is a predominant component in that speed range.
- Extension to Transverse Asymmetrical Motions:
  - The first extension to the present mathematical model is the capability of simulating transverse plane motions. The model implementation follows the basis of [Ruscelli \(2009\)](#)'s work providing more sources of validation. The first source is a series of fixed heel planing hull experiments carried out by [Li \(2014\)](#). The other is an extensive series of experiments performed by [Rosén and Garne \(2006\)](#).
  - The comparison to the first source shows a fairly good agreement in term of the trend of parameters, although the magnitude presents uniformly constant differences. This leads to the deduction of a lack of an additional factor terms in the equations of motions that can be proposed as an implemented future work.
  - The comparison to the second source shows an overall good agreement, except the responses in the zone of resonant frequency that the simulations present

a larger magnitude. This happens due to the lack of appropriate damping component in the equations of motions, as it is predominant in this frequency area.

- Application to Aircraft Ditching:
  - In conjugation with the aircraft ditching, this application is proposed considering the fact that the original research approaching planing dynamics was seaplane landing load prediction done by [von Karman \(1929\)](#) and [Wagner \(1931\)](#). In this application, the present mathematical model is basically modified to gain the capability of evaluating pressure acting on semi-circular shape rather than the original wedge shape.
  - The sectional added mass term in the equations of motions is modified following the assumption of an expanding flat plate as in the case of a wedge shape. The most challenging part of this implementation is finding an appropriate expression of sectional added mass coefficient. This approach has been fulfilled by the classic Lewis Conformal Mapping, that by merging with the expression of sectional added mass, the expression in form of deadrise dependent has been found.
  - Unlike the wedge shape geometry, the semi-circular shape experiences a uniform change of deadrise angle as increasing the submergence, leading to the consideration of modification of the other deadrise dependent terms in the equations of motions.
  - The first approach verification that is the confirmation of validity of sectional added mass expression shows good agreement results compared with the previous references. Consequently, by combining with the other modification of components, the adequate equations of motions for semi-circular shape object is set.
  - The cross-validation is carried out compared with other two techniques provided by Stirling Dynamics Ltd. ([Bonanni et al., 2015](#); [Vandewaeter et al., 2015](#)). A series of ditching simulations in different conditions is performed, covering the overall possibility of occurrences in reality. The three methodologies present fairly good agreement with results under the following considerations:
    - \* The motions of aircraft prior and after impact are under the steady state with constant velocities in both vertical and horizontal directions.
    - \* The aircraft is always under towed condition implying the constant horizontal landing speed after impact.
  - As the real ditching event does not behave under the conditions mentioned above, the validity of those methodologies can be confirmed under limitation of the instant of impact and a short interval post impact. The impact loads

and the initial post impact motions are believed to be valid when evaluating with those methodologies.

- To enable the complete applicability, the mathematical model has also implemented the capability of unsteady state simulations with a simple assumption of available deceleration components. Unlike the real ditching events, the simulation keeps a significant higher horizontal velocity at the end of identical time interval, while in the real ditching event, the post impact horizontal deceleration is extremely high that stops the aircraft in very short distance once the hull has hit the water.
- Fundamental cause of this occurrence is the lack of an appropriate model of horizontal added mass. The original mathematical model ignores this component, as when the planing craft is operating, the wetted surface area is small enough to not involving with the water added mass in the horizontal direction. On the other hand, as the body of the fuselage is no longer propelled once being in contact with the water, it commits a larger sinkage, leading to the increment of wetted surface area, and consequently, the horizontal added mass component cannot be neglected. Modelling the horizontal added mass within the strip theory is complicated, some simplification should be suggested as a further possible implementation of the present project.
- Another significant phenomenon observed from the simulations is that, the pressure distribution at the tail sections is in the opposite direction of that in the cylindrical sections. In other words, the tail part suffers suction loads when being in contact with the water. This phenomenon can be explained mathematically by the last term of the sectional force expression (Equation 3.10). Due to its space derivative property, when a geometry form diminishes its size, it becomes predominant and causes the negative value for the whole expression. Moreover, this term has a pronounced effect leading to a very high negative magnitude in which initially, the results significantly differ from the those achieved from CFD simulations.
- However, a fact from this occurrence is discovered, the aircraft fuselage has no transom stern, horizontal flow direction does not separate obviously as it happens around the transom of planing hull. The location of horizontal flow separation around the tail part of the fuselage is difficult to define, although the vertical flow can be simply supposed to separate beyond the maximum beam when the circular form reaches the half submergence. Therefore, a set of assumptions of flow separation locations is proposed varying from no horizontal separation gradually to the maximum separation at the beginning point of the tail. A certain level of flow separation enables the results to get a better fit to the results from other two methodologies. Nevertheless, the flow separation locations present speed dependent property, more in-depth analysis in this phenomenon is proposed as a further implement work to the

present project, which could also fulfil the capability when developing into the fully unsteady state simulations.

- Ditching Experiment and Validation:
  - A series of experimental tests has been carried out, in order to strengthen the validity of simulation tools. It was planned initially to be capable of covering the validity of the whole range of landing speeds recommended by the relevant authorities, however, due to the limitation of available resources and facilities, it was only able to perform solely in the low range of landing speeds.
  - Several challenges have been presented during the experimental planning. First of all, regarding the previous works, the ditching tests were done with the full-scale geometry or at least large model scaling. This required a gigantic system and facilities and consequently, a large amount of resource and budget. Another fact is that, it has been complicated to carry out the whole range of desired results, i.e., motions, accelerations of the impact and pressure distribution altogether. As by employing the hanging and free fall ditching technique, only motions and accelerations can be achieved but pressure distributions. In the opposite way, using guided launching technique allows the pressure distribution and the impact force to be read, but as it is towed, the real motion behaviours are restricted.
  - Regarding the technique used in the experimental tests, as the validity of numerical technique is still limited to present only impact force, accelerations and motions in a small interval post impact, a guided launching technique is chosen. It allows impact forces to be achieved and compared with those obtained from the numerical simulations. The assumption of comparison is based upon the belief that, providing that the comparison in low-speed range gives good agreement results, the numerical should be valid to simulate also in the higher speed range.
  - Prior to the experimental events, the expected behaviours have been simulated through the numerical simulations. The results can be interpreted into a trend line of impact force in term of landing speed. This trend line then also is capable of giving an approximation of expected result stated earlier for the high-speed range.
  - The motions during each run are recorded and used again as input data to re-simulate the real experimental behaviours using the numerical technique. By doing so, the overall result comparisons show good agreement leading to the deduction of the full validity of the numerical technique and a partial one when considering the higher speed range.



## 8.2 Future Work

The principal targets of the project have been successfully reached, overcoming the huge amount of task to carry out under the limited time. All of the works presented have been developed to certain conditions that are widely opened for various possible further implementations such as:

- Regarding the transverse motion prediction, the mathematical model still has a missing correction factor to be included, in order to be capable of predicting more accurately calm water behaviour when navigating with transverse instability situation. On the other hand, in lateral and oblique wave simulations, although the capability of the model in high frequency area is effective, damping component as predominant term in natural frequency area needs to be included in order to fulfil the whole range of applicability. Analysis approaching the damping component of planing roll motion is strongly recommended, commencing from possibility of using conventional roll damping until achieving the most appropriate for this particular case.
- Regarding the aircraft ditching prediction, its validity is under the limitation of applicability only the short interval during impact, due to the lack of an appropriate horizontal acceleration component to modelled accurately the full motions after impact. Analysis approaching horizontal added mass of the fuselage under water is proposed as first priority in order to modelled correctly its behaviour once in contact with the water. On the other hand, it is also necessary to investigate appropriate flow separation models in order to be able to simulate more accurately the pressure distribution of the tail part of fuselage. As its influence reflects back directly to the fuselage damage due to post impact loads and motion behaviours.
- Regarding the ditching experiments, once the facility of higher landing speed is available, the numerical tool validity can be completely strengthened using the results covered any range of landing speeds.

## Appendix A

# Detailed Development of Equations of Motions

Detailed of the fully developed equations of motions of the longitudinal plane motions, as well as the extension to the transverse plane motions are explained here.

### A.1 System of Equations of Motions

The system of equations of motions is derived from the 2<sup>nd</sup> Law of Newton and after reducing to two degrees of freedom (heave and pitch) implying the towed condition with constant forward speed ( $\ddot{x}_G = 0$  and  $\dot{x}_G = \text{constant}$ ), it is expressed in the following form:

$$\begin{aligned} M \cdot \ddot{z}_G(t) &= \sum F_z(\ddot{x}_G(t), \dot{x}_G(t), \bar{x}_G(t), t) \\ I_{yy} \cdot \ddot{\theta}(t) &= \sum M_y(\ddot{x}_G(t), \dot{x}_G(t), \bar{x}_G(t), t) \end{aligned} \tag{A.1}$$

Where:

- $M$  : is ship's mass in  $kg$
- $I_{yy}$  : is ship's moment of inertia around axis  $y'$
- $\ddot{z}_G$  : is ship's acceleration in  $z$  direction
- $\sum F_z$  : is sum of forces in  $z$  direction
- $\sum M_y$  : is sum of moments around  $y'$  direction

- $\ddot{\vec{x}} = (\ddot{x}_G, \ddot{z}_G, \ddot{\theta})$  : Acceleration vector
- $\dot{\vec{x}} = (\dot{x}_G, \dot{z}_G, \dot{\theta})$  : Velocity vector
- $\vec{x} = (x_G, z_G, \theta)$  : Displacement vector
- $t$  : time

This is a system of two fully nonlinear equations which is a function of accelerations, velocities, displacement and time. The right hand side of the equations are the sum of forces and moments acting on the ship's hull, it consist of the following components:

$$\begin{aligned} \sum F_z &= -(F_{hyd} + F_{cfd}) \cdot \cos \theta - F_b + D \cdot \sin \theta + W \\ \sum M_y &= M_{hyd} + M_{cfd} + M_b - D \cdot x_d \end{aligned} \quad (A.2)$$

Substituting Equation A.2 into Equation A.1 we have:

$$\begin{aligned} M \cdot \ddot{z}_G &= -(F_{hyd} + F_{cfd}) \cdot \cos \theta - F_b + D \cdot \sin \theta + W \\ I_{yy} \cdot \ddot{\theta} &= M_{hyd} + M_{cfd} + M_b - D \cdot x_d \end{aligned} \quad (A.3)$$

Where each component is the integration along the ship length of individual sectional forces:

- $F_{hyd} = \int_L f_{hyd} dx'$ : Hydrodynamic Lift Force
- $F_{cfd} = \int_L f_{cfd} dx'$ : Cross Flow Drag
- $F_b = \int_L f_b dx'$ : Buoyancy Force
- $D$ : Drag Force
- $W$  : Ship Weight
- $M_{hyd} = \int_L f_{hyd} x' dx'$  : Hydrodynamic Lift Moment
- $M_{cfd} = \int_L f_{cfd} x' dx'$  : Cross Flow Drag Moment
- $M_b = \int_L f_b x' dx'$  : Buoyancy Moment
- $x_d$ : Drag Arm

## A.2 Sectional Forces

The forces acting on an individual section along the ship length are explained as follows:

### A.2.1 Sectional Hydrodynamic Lift Forces

The sectional hydrodynamic lift forces are associated to the rate of change of fluid momentum. They are determined according to the theory of a calm water penetrating wedge of [Wagner \(1931\)](#). The 2D penetrating wedge is replaced by a flat lamina by the assumption that the fluid accelerations are much larger than gravitational acceleration. According to [Wagner \(1931\)](#), the force associated to the rate of change of fluid momentum of the oncoming fluid in terms of the added mass of the particular cross section is:

$$\begin{aligned} f_{hyd} &= \frac{D}{Dt} (m_a \cdot V) \\ &= m_a \cdot \dot{V} + \dot{m}_a \cdot V - U \cdot \frac{\partial}{\partial x'} (m_a \cdot V) \end{aligned} \quad (\text{A.4})$$

From Equation [A.4](#),  $U$  is velocity of the ship parallel to keel normal to  $V$ . Both velocity components  $U$  and  $V$  can be expressed in terms of earth-fixed coordinate system components as follows:

$$\begin{aligned} U &= U(x') \\ &= \dot{x}_G \cdot \cos \theta - (\dot{z}_G - w_w(x')) \sin \theta \\ V &= V(x') \\ &= \dot{x}_G \cdot \sin \theta + (\dot{z}_G - w_w(x')) \cos \theta - \dot{\theta} \cdot x' \\ \dot{V} &= \dot{V}(x') \\ &= \ddot{x}_G \cdot \sin \theta + (\ddot{z}_G - \dot{w}_w(x')) \cos \theta + \dot{\theta}(\dot{x}_G \cos \theta - (\dot{z}_G - w_w(x')) \sin \theta) - \ddot{\theta} \cdot x' \end{aligned} \quad (\text{A.5})$$

Where  $w_w(x')$  and  $\dot{w}_w(x')$  are wave orbital vertical velocity and acceleration respectively, which is functions of only ship length coordinate in each time step.

According to [Wagner \(1931\)](#), the added mass for a penetrating wedge can be approximated by the high frequency solution. Note that in the case, the added mass used in this mathematical model is only heave added mass which can be elaborated to obtain other motion's coefficients.

$$m_a = C_m \cdot \frac{\pi}{2} \cdot \rho \cdot b^2 \quad (\text{A.6})$$

Where:

- $m_a$  is sectional added mass.
- $C_m$  is sectional added mass coefficient.
- $\rho$  is water density.
- $b$  is half beam of individual section.

And consequently, time derivative of the added mass is expressed as:

$$\dot{m}_a = \frac{\partial m_a}{\partial t} = C_m \cdot \pi \cdot \rho \cdot b \cdot \frac{db}{dt} \quad (\text{A.7})$$

The half beam  $b$  is related to the section submergence  $h$  by  $b = h / \tan \beta$ . As mentioned previously, the water pile-up phenomenon influences significantly to the alteration of half beam, the expression of this factor found by [Payne \(1981\)](#) is shown as follows:

$$C_{pu} = \frac{\pi}{2} - \beta \left( 1 - \frac{2}{\pi} \right) \quad (\text{A.8})$$

And then the corrected half beam including pile-up phenomena becomes  $b = C_{pu} h / \tan \beta$ . Thus, the expression of sectional added mass and its time derivative can be expressed as a function of section submergence as follows:

$$\begin{aligned} m_a &= C_m \cdot \frac{\pi}{2} \cdot \rho \cdot \left( \frac{C_{pu} h}{\tan \beta} \right)^2 \\ \dot{m}_a &= C_m \cdot \pi \cdot \rho \cdot h \cdot \left( \frac{C_{pu}}{\tan \beta} \right)^2 \frac{dh}{dt} \end{aligned} \quad (\text{A.9})$$

This implies that the sectional added mass and its time derivative are functions of deadrise angle,  $\beta$ , and section submergence,  $h$ . Both can be expressed as a function of body-fixed coordinate:

$$\begin{aligned}
\beta &= \beta(x') \\
h &= h(x') \\
&= z'_k + \left( \frac{z_G - x' \sin \theta}{\cos \theta} \right) - \frac{r}{\cos \theta} \\
\dot{h} &= \dot{h}(x') \\
&= \frac{dh(x')}{dt} = \left( \frac{(\dot{z}_G - x' \cos \theta \dot{\theta}) + (z_G - x' \sin \theta) \sin \theta \dot{\theta}}{\cos^2 \theta} \right) - \left( \frac{\dot{r} \cos \theta + r \sin \theta \dot{\theta}}{\cos^2 \theta} \right)
\end{aligned} \tag{A.10}$$

Where:

- $z'_k$ : Coordinate of keel in ship-fixed coordinate system.
- $r(x')$  and  $\dot{r}(x')$ : Wave elevation and its time derivative at **Each Time Step**.

The expression of wave elevation, its time derivative, wave orbital vertical velocity and acceleration are functions of time and space. As the present calculation is in each time step, the functions are reduced to be only space dependent in earth-fixed coordinate System ( $x$ ) as follows:

$$\begin{aligned}
r &= r_0 \cos(kx + \omega t) \\
\dot{r} &= -r_0 \sin(kx + \omega t) \frac{d}{dt}(kx + \omega t) \\
&= -r_0 \sin(kx + \omega t) (k\dot{x} + \omega) \\
w_w &= r_0 \omega \sin(kx + \omega t) \\
\dot{w}_w &= r_0 \omega \cos(kx + \omega t) (k\dot{x} + \omega)
\end{aligned} \tag{A.11}$$

Then, converting to be functions of space in body-fixed coordinate system ( $x'$ ):

$$\begin{aligned}
r(x') &= r_0 \cos(k(x_G + x' \cos \theta - (z_G - x' \sin \theta) \tan \theta) + \omega t) \\
\dot{r}(x') &= \frac{d}{dt} r(x') \\
w_w(x') &= -r_0 \omega \sin(k(x_G + x' \cos \theta - (z_G - x' \sin \theta) \tan \theta) + \omega t) \\
\dot{w}_w(x') &= \frac{d}{dt} w_w(x')
\end{aligned} \tag{A.12}$$

Substituting Equation A.12 and Equation A.10 into Equation A.9, the sectional added mass  $m_a$  and its time derivative  $\dot{m}_a$  will be a function of only body-fixed coordinate  $x'$

at each time step as the rest of variables in Equation A.10 are fixed and updated later when the time is released to progress.

$$\begin{aligned} m_a(x') &= C_m \cdot \frac{\pi}{2} \cdot \rho \cdot \left( \frac{C_{pu}(x')h(x')}{\tan \beta(x')} \right)^2 \\ \dot{m}_a(x') &= C_m \cdot \pi \cdot \rho \cdot h(x') \cdot \left( \frac{C_{pu}(x')}{\tan \beta(x')} \right)^2 \frac{dh(x')}{dt} \end{aligned} \quad (\text{A.13})$$

Finally, by substituting Equation A.13 and Equation A.5 into Equation A.4 the expression of sectional hydrodynamic lift force in function of  $x'$  is obtained:

$$\begin{aligned} f_{hyd}(x') &= \frac{D}{Dt} (m_a(x') \cdot V(x')) \\ &= m_a(x') \cdot \dot{V}(x') + \dot{m}_a(x') \cdot V(x') - U(x') \cdot \frac{\partial}{\partial x'} (m_a(x') \cdot V(x')) \end{aligned} \quad (\text{A.14})$$

### A.2.2 Sectional Cross Flow Drag Force and Moment

The additional lift term due the cross-flow drag on the surface of a water penetrating wedge is expressed as:

$$f_{cfd} = C_{D,c} \cdot \cos \beta \cdot \rho \cdot b \cdot V^2 \quad (\text{A.15})$$

It is as well a function of  $x'$  by substituting Equation A.5 and Equation A.10 into A.15:

$$f_{cfd}(x') = C_{D,c} \cdot \cos \beta(x') \cdot \rho \cdot \left( \frac{C_{pu}(x')h(x')}{\tan \beta(x')} \right) \cdot V(x')^2 \quad (\text{A.16})$$

Where  $C_{D,c}$  is the cross flow drag coefficient which Zarnick (1978) used the value of 1.0 while Keuning (1994) used 1.33.

### A.2.3 Sectional Buoyancy Force

In this case, the buoyancy force on a segment is assumed to act perpendicularly to the keel and equal to the equivalent static buoyancy of section multiplied by a correction factor  $a_{bf}$ :

$$f_b = a_{bf} \cdot \rho \cdot g \cdot A_{sub}(x') \quad (\text{A.17})$$

Where  $A_{sub}(x')$  is section submerged area. It is considered as the 2D sectional area under still water level. This implies that the case where the chine is already wet or fully submerged, the total submerged area is still accounted in order to meet the requirement of use of buoyancy correction factor  $a_{bf}$ . In other words,  $a_{bf}$  is already established to correct the flow separation phenomenon, therefore, the submerged area needs to be expressed as it is without flow separation.

### A.3 Total Forces and Moments

#### A.3.1 Total Hydrodynamic Forces and Moments

The total hydromechanic forces and moments are the integration along the ship length of sectional forces. Due to the presence of flow separation at transom, a correction factor called “**Near Transom Correction Factor:  $C_{tr}$** ” presented by [Garne \(2005\)](#) is applied, in order to correct the pressure distribution at transom zone in which the pressure is reduced to atmospheric. The expression of near transom correction factor is written as:

$$C_{tr} = \tanh \left( \frac{2.5}{0.34 \cdot B_m \cdot C_v} \cdot (x' - x'_{tr}) \right) \quad (\text{A.18})$$

Where:

- $B_m$ : Full breadth of the main section.
- $C_v = \frac{V_s}{\sqrt{g \cdot B_m}}$ : Froude number over breadth.
- $x'_{tr}$ : Body-fixed coordinate of transom stern.

The total forces and moments are evaluated as follows:



$$\begin{aligned}
F_{hyd} &= \int_L C_{tr} \cdot f_{hyd} dx' \\
M_{hyd} &= \int_L C_{tr} \cdot f_{hyd} x' dx' \\
F_{cfd} &= \int_L C_{tr} \cdot f_{cfd} dx' \\
M_{cfd} &= \int_L C_{tr} \cdot f_{cfd} x' dx' \\
F_b &= \int_L C_{tr} \cdot f_b dx' \\
M_b &= \int_L C_{tr} \cdot f_b x' dx'
\end{aligned} \tag{A.19}$$

### A.3.2 Drag Force and Moment

Drag force or frictional resistance is determined by:

$$D = \frac{1}{2} \cdot \rho \cdot U^2 \cdot S_w \cdot C_F \tag{A.20}$$

Where:

- $\rho$ : Water density.
- $U$ : Velocity component parallel to keel.
- $S_w = \int_L s_w(x') dx'$ : Wetted surface area.
- $s_w(x')$ : Sectional wetted curve.
- $C_F$ : Drag coefficient.

The frictional resistance is strongly dependent of three fully nonlinear parameters,  $U$ ,  $S_w$  and  $C_F$ . Wetted surface area is obtained by integrating sectional wetted curve along the ship length, taking into account the three different zone of flow phenomena and water pile-up.

The friction coefficient is determined using the ITTC formula:

$$C_F = \frac{0.075}{(\log R_n - 2)^2} \tag{A.21}$$

And finally, the Reynolds number is:

$$R_n = \frac{U \cdot L_k}{\nu} \quad (\text{A.22})$$

Where  $\nu$  is kinematic viscosity of fluid domain and  $L_k$  is keel wetted length. The keel wetted length can be determined as a function of section submergence  $h$  whereas in a particular section,  $h \geq 0$  means the keel at this local is wet. Otherwise, if  $h < 0$ , the keel is dry.

## A.4 The Global System and Matrix Form

Substituting Equation A.19 and Equation A.20 into Equation A.3 resulting in:

$$\begin{aligned} M \cdot \ddot{z}_G &= - \left( \int_L C_{tr} \cdot f_{hyd} dx' + \int_L C_{tr} \cdot f_{cfd} dx' \right) \cdot \cos \theta - \int_L C_{tr} \cdot f_b dx' + D \cdot \sin \theta + W \\ I_{yy} \cdot \ddot{\theta} &= \int_L C_{tr} \cdot f_{hyd} x' dx' + \int_L C_{tr} \cdot f_{cfd} x' dx' + \int_L C_{tr} \cdot f_b x' dx' - D \cdot x_d \end{aligned} \quad (\text{A.23})$$

Then, the system can be elaborated into the following form:

**Heave Equation:**

$$\begin{aligned}
M\ddot{z}_G = & -\left(\ddot{x}_G \sin \theta \int_L C_{tr} m_a dx' \right. \\
& + \dot{x}_G \cos \theta \dot{\theta} \int_L C_{tr} m_a dx' \\
& + \ddot{z}_G \cos \theta \int_L C_{tr} m_a dx' \\
& - \dot{z}_G \sin \theta \dot{\theta} \int_L C_{tr} m_a dx' \\
& - \cos \theta \int_L C_{tr} m_a \dot{w}_w dx' \\
& + \sin \theta \dot{\theta} \int_L C_{tr} m_a w_w dx' \\
& - \ddot{\theta} \int_L C_{tr} m_a x' dx' \\
& + \int_L C_{tr} \dot{m}_a \cdot V dx' \\
& - \int_L C_{tr} UV \frac{\partial m_a}{\partial x'} dx' \\
& + \cos \theta \int_L C_{tr} U m_a \frac{\partial w_w}{\partial x'} dx' \\
& + \dot{\theta} \int_L C_{tr} U m_a dx' \\
& + \int_L C_{tr} \cdot C_{D,c} \cdot \cos \beta \cdot \rho \cdot b \cdot V^2 dx' \Big) \cos \theta \\
& - \int_L C_{tr} \cdot a_{bf} \rho g A_{sub} dx' \\
& + D \sin \theta \\
& + W
\end{aligned} \tag{A.24}$$

**Pitch Equation:**

$$\begin{aligned}
I_{yy}\ddot{\theta} = & \ddot{x}_G \sin \theta \int_L C_{tr} m_a x' dx' \\
& + \dot{x}_G \cos \theta \dot{\theta} \int_L C_{tr} m_a x' dx' \\
& + \ddot{z}_G \cos \theta \int_L C_{tr} m_a x' dx' \\
& - \dot{z}_G \sin \theta \dot{\theta} \int_L C_{tr} m_a x' dx' \\
& - \cos \theta \int_L C_{tr} m_a \dot{w}_w x' dx' \\
& + \sin \theta \dot{\theta} \int_L C_{tr} m_a w_w x' dx' \\
& - \ddot{\theta} \int_L C_{tr} m_a x'^2 dx' \\
& + \int_L C_{tr} \dot{m}_a \cdot V x' dx' \\
& - \int_L C_{tr} UV \frac{\partial m_a}{\partial x'} x' dx' \\
& + \cos \theta \int_L C_{tr} U m_a \frac{\partial w_w}{\partial x'} x' dx' \\
& + \dot{\theta} \int_L C_{tr} U m_a x' dx' \\
& + \int_L C_{tr} \cdot C_{D,c} \cdot \cos \beta \cdot \rho \cdot b \cdot V^2 x' dx' \\
& - \int_L C_{tr} \cdot a_{bf} \rho g A_{sub} dx' \\
& - Dx_d
\end{aligned} \tag{A.25}$$

The integral terms in Equation A.24 and Equation A.25 will be assigned to the following coefficients:

$$\begin{aligned}
C_A &= \int_L C_{tr} m_a dx' & C_B &= \int_L C_{tr} m_a \dot{w}_w dx' \\
C_C &= \int_L C_{tr} m_a w_w dx' & C_D &= \int_L C_{tr} m_a x' dx' \\
C_E &= \int_L C_{tr} \dot{m}_a V dx' & C_F &= \int_L C_{tr} UV \frac{\partial m_a}{\partial x'} dx' \\
C_G &= \int_L C_{tr} U m_a \frac{\partial w_w}{\partial x'} dx' & C_H &= \int_L C_{tr} U m_a dx' \\
C_K &= \int_L C_{tr} m_a \dot{w}_w x' dx' & C_M &= \int_L C_{tr} m_a w_w x' dx' \\
C_N &= \int_L C_{tr} m_a x'^2 dx' & C_O &= \int_L C_{tr} \dot{m}_a \cdot V x' dx' \\
C_P &= \int_L C_{tr} UV \frac{\partial m_a}{\partial x'} x' dx' & C_Q &= \int_L C_{tr} U m_a \frac{\partial w_w}{\partial x'} x' dx' \\
C_R &= \int_L C_{tr} U m_a x' dx'
\end{aligned}$$

By eliminating the terms associated to  $\ddot{x}_G = 0$  and using the coefficients defined above, Equation A.24 and Equation A.25 can be rewritten into the following form:

$$M\ddot{z}_G = -\left(C_A \cos \theta \dot{x}_G \dot{\theta} + C_A \cos \theta \ddot{z}_G - C_A \sin \theta \dot{z}_G \dot{\theta} - C_B \cos \theta + C_C \sin \theta \ddot{\theta} - C_D \ddot{\theta} \right. \quad (\text{A.26})$$

$$\left. + C_E - C_F + C_G \cos \theta + C_H \dot{\theta} - F_{cfd} \right) \cos \theta - F_b + D \sin \theta + W \quad (\text{A.27})$$

$$I_{yy} \ddot{\theta} = C_D \cos \theta \dot{x}_G \dot{\theta} + C_D \cos \theta \ddot{z}_G - C_D \sin \theta \dot{z}_G \dot{\theta} - C_K \cos \theta + C_M \sin \theta \ddot{\theta} - C_N \ddot{\theta} \quad (\text{A.28})$$

$$+ C_O - C_P + C_Q \cos \theta + C_R \dot{\theta} + M_{cfd} + M_b - Dx_d \quad (\text{A.29})$$

Then, the terms associated to the accelerations are moved to the left hand side of the system:

$$\begin{aligned}
M\ddot{z}_G + C_A \cos^2 \theta \ddot{z}_G - C_D \cos \theta \ddot{\theta} &= -\left(C_A \cos \theta \dot{x}_G \dot{\theta} - C_A \sin \theta \dot{z}_G \dot{\theta} - C_B \cos \theta + C_C \sin \theta \ddot{\theta} \right. \\
&\quad \left. + C_E - C_F + C_G \cos \theta + C_H \dot{\theta} - F_{cfd} \right) \cos \theta - F_b + D \sin \theta + W \\
I_{yy} \ddot{\theta} - C_D \cos \theta \ddot{z}_G + C_N \ddot{\theta} &= C_D \cos \theta \dot{x}_G \dot{\theta} - C_D \sin \theta \dot{z}_G \dot{\theta} - C_K \cos \theta + C_M \sin \theta \ddot{\theta} \\
&\quad + C_O - C_P + C_Q \cos \theta + C_R \dot{\theta} + M_{cfd} + M_b - Dx_d
\end{aligned} \quad (\text{A.30})$$

The equations A.30 can be re-ordered to the following matrix form:

$$A \cdot \ddot{\vec{x}} = B \quad (\text{A.31})$$

Where:

$$A = \begin{pmatrix} M + C_A \cos^2 \theta & -C_D \cos \theta \\ -C_D \cos \theta & I_{yy} + C_N \end{pmatrix} \quad (\text{A.32})$$

$$\ddot{\vec{x}} = \begin{pmatrix} \ddot{z}_G \\ \ddot{\theta} \end{pmatrix} \quad (\text{A.33})$$

$$B = \begin{pmatrix} F'_z + D \sin \theta + W \\ F'_\theta - D x_d \end{pmatrix} \quad (\text{A.34})$$

In which  $F'_z$  and  $F'_\theta$  are the total hydromechanic forces and moments minus the terms associated to the motion accelerations.

To solve the system, it will be re-arranged in the following form:

$$\ddot{\vec{x}} = A^{-1} \cdot B \quad (\text{A.35})$$

Now the accelerations corresponding to each time step are obtained. The next step is to evaluate the time marching procedure to get the time history of displacements and velocities.

## A.5 Modification to Application in Asymmetric Conditions

The present mathematical model is modified here to be capable of dealing with asymmetric water entry problem. Each component is developed as follows:

### A.5.1 Hydrodynamic Lift Force:

The Hydrodynamic lift force will be evaluated separately in two equivalent port and starboard side sections and following the fundamental the formulation of rate of change of fluid momentum:

$$f_{h_{P,S}} = \frac{1}{2} \left( \frac{D}{Dt} (m_{a_{P,S}} V_{P,S}) \right) = \frac{1}{2} \left( m_{a_{P,S}} \dot{V}_{P,S} + \dot{m}_{a_{P,S}} V_{P,S} - U \frac{\partial}{\partial x} (m_{a_{P,S}} V_{P,S}) \right) \quad (\text{A.36})$$

The expression for the sectional added mass adopted in the present formulation is described in the following form:

$$m_{a_P} = C_m \rho \frac{\pi}{2} \left( \frac{C_{pu} h_P}{\tan(\beta - \phi)} \right)^2 \quad (\text{A.37})$$

$$m_{a_S} = C_m \rho \frac{\pi}{2} \left( \frac{C_{pu} h_S}{\tan(\beta + \phi)} \right)^2 \quad (\text{A.38})$$

The expression of time derivative of sectional added mass appears to be more complicated due to the appearance of roll angle and its dynamic properties which are time dependent :

$$\dot{m}_{a_P} = C_m \rho \pi \left( \frac{h_P C_{pu}}{\tan(\beta - \phi)} \right) \frac{d}{dt} \left( \frac{h_P C_{pu}}{\tan(\beta - \phi)} \right) \quad (\text{A.39})$$

$$\dot{m}_{a_S} = C_m \rho \pi \left( \frac{h_S C_{pu}}{\tan(\beta + \phi)} \right) \frac{d}{dt} \left( \frac{h_S C_{pu}}{\tan(\beta + \phi)} \right) \quad (\text{A.40})$$

The time derivative in the last part of the expression of time derivative of sectional added mass can be developed as follows:

$$\frac{d}{dt} \left( \frac{h_P C_{pu}}{\tan(\beta - \phi)} \right) = \frac{(\dot{h}_P C_{pu} + h_P \dot{C}_{pu}) \tan(\beta - \phi) + h_P C_{pu} [(\tan^2(\beta - \phi)) \dot{\phi}]}{\tan^2(\beta - \phi)} \quad (\text{A.41})$$

$$\frac{d}{dt} \left( \frac{h_S C_{pu}}{\tan(\beta + \phi)} \right) = \frac{(\dot{h}_P C_{pu} + h_P \dot{C}_{pu}) \tan(\beta + \phi) - h_P C_{pu} [(\tan^2(\beta + \phi)) \dot{\phi}]}{\tan^2(\beta + \phi)} \quad (\text{A.42})$$

Figures A.1 - A.2 show that the effective deadrise angle corresponding to port and starboard side are  $(\beta - \phi)$  and  $(\beta + \phi)$  respectively. The pile-up correction factor  $C_{pu}$  in this case will be assumed to be that corresponding to the side of larger effective deadrise angle:

$$C_{pu} = \frac{\pi}{2} - (\beta + |\phi|) \left( 1 - \frac{2}{\pi} \right) \quad (\text{A.43})$$

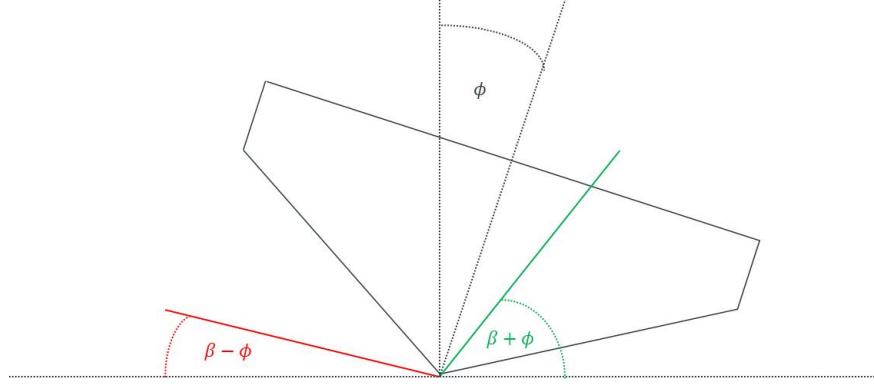


Figure A.1: Asymmetric Geometrical Equivalent I

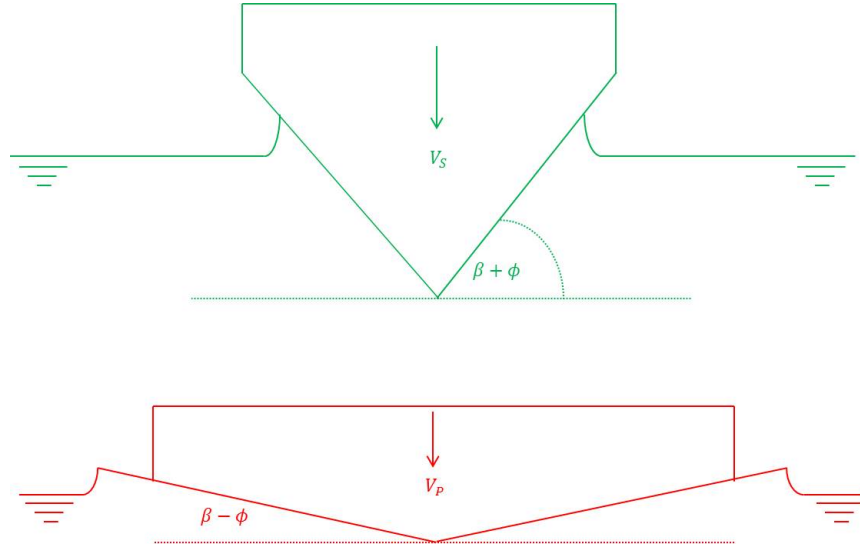


Figure A.2: Asymmetric Geometrical Equivalent II

And its time derivative:

$$\dot{C}_{pu} = \left( \frac{2}{\pi} - 1 \right) \cdot \dot{\phi} \quad (\text{A.44})$$

The section submergence as well needs to account for the different effective deadrise angle:

$$h_P = z'_k \cos \phi + \left( \frac{z_G - x' \sin \theta}{\cos \theta} \right) - \frac{r_P}{\cos \theta} \quad (\text{A.45})$$

$$h_S = z'_k \cos \phi + \left( \frac{z_G - x' \sin \theta}{\cos \theta} \right) - \frac{r_S}{\cos \theta} \quad (\text{A.46})$$

Consequently, their time derivatives are expressed as:



$$\dot{h}_P = -\sin \phi \dot{\phi} + \left( \frac{(\dot{z}_G - x' \cos \theta \dot{\theta}) + (z_G - x' \sin \theta) \sin \theta \dot{\theta}}{\cos^2 \theta} \right) - \left( \frac{\dot{r}_P \cos \theta + r_P \sin \theta \dot{\theta}}{\cos^2 \theta} \right) \quad (\text{A.47})$$

$$\dot{h}_S = -\sin \phi \dot{\phi} + \left( \frac{(\dot{z}_G - x' \cos \theta \dot{\theta}) + (z_G - x' \sin \theta) \sin \theta \dot{\theta}}{\cos^2 \theta} \right) - \left( \frac{\dot{r}_S \cos \theta + r_S \sin \theta \dot{\theta}}{\cos^2 \theta} \right) \quad (\text{A.48})$$

The relative sectional velocities parallel or normal to the keel are defined based on the similar analogy of the case of coupled heave and pitch motions taken into account the effect of roll motion in especially the normal velocity  $V$ . Each equivalent port and starboard side sections with corresponding effective deadrise angle is actually affected by roll velocity  $\dot{\phi}$  and are expressed as follows:

$$U = \dot{x}_G \cdot \cos \theta - (\dot{z}_G - w_w) \sin \theta \quad (\text{A.49})$$

$$V_P = \dot{x}_G \cdot \sin \theta + (\dot{z}_G - w_{w_S}) \cos \theta - \dot{\theta} \cdot x' - \dot{\phi} \cdot y'_P \quad (\text{A.50})$$

$$V_S = \dot{x}_G \cdot \sin \theta + (\dot{z}_G - w_{w_P}) \cos \theta - \dot{\theta} \cdot x' - \dot{\phi} \cdot y'_S \quad (\text{A.51})$$

$$\dot{V}_P = \ddot{x}_G \cdot \sin \theta + (\ddot{z}_G - \dot{w}_{w_P}) \cos \theta + \dot{\theta}(\dot{x}_G \cos \theta - (\dot{z}_G - w_{w_P}) \sin \theta) - \ddot{\theta} \cdot x' - \ddot{\phi} y'_P \quad (\text{A.52})$$

$$\dot{V}_S = \ddot{x}_G \cdot \sin \theta + (\ddot{z}_G - \dot{w}_{w_S}) \cos \theta + \dot{\theta}(\dot{x}_G \cos \theta - (\dot{z}_G - w_{w_S}) \sin \theta) - \ddot{\theta} \cdot x' - \ddot{\phi} y'_S \quad (\text{A.53})$$

The roll lever arms  $y'_P$  and  $y'_S$  are defined in the case hydrodynamic lift force as centre of pressure corresponding to each equivalent side section following the theory of wedge shape water entry of [Wagner \(1931\)](#).

$$y'_P = \frac{\frac{\pi}{(\beta-\phi)} \left( 1 - \sqrt{1 - y'^2_{0P}} \right) + \frac{1}{2} \ln (1 - y'^2_{0P}) + \frac{1}{2} y'^2_{0P}}{\frac{\pi}{(\beta-\phi)} \arcsin y'_{0P} + \frac{1}{2} \ln \left( \frac{1-y'_{0P}}{1+y'_{0P}} \right) + y'_{0P}} \quad (\text{A.54})$$

$$y'_S = \frac{\frac{\pi}{(\beta+\phi)} \left( 1 - \sqrt{1 - y'^2_{0S}} \right) + \frac{1}{2} \ln (1 - y'^2_{0S}) + \frac{1}{2} y'^2_{0S}}{\frac{\pi}{(\beta+\phi)} \arcsin y'_{0S} + \frac{1}{2} \ln \left( \frac{1-y'_{0S}}{1+y'_{0S}} \right) + y'_{0S}} \quad (\text{A.55})$$

Where  $y'_{0P,S}$  are the abscissa where the pressure distribution is equal to zero and expressed as:

$$y'_{0P} = \sqrt{1 - \left( \frac{\sqrt{\pi^2 - 4(\beta - \phi)^2} - \pi}{2(\beta - \phi)} \right)^2} \quad (\text{A.56})$$

$$y'_{0S} = \sqrt{1 - \left( \frac{\sqrt{\pi^2 - 4(\beta + \phi)^2} - \pi}{2(\beta + \phi)} \right)^2} \quad (\text{A.57})$$

This definition of roll arms is valid only in hydrodynamic forces, the roll arm of hydrostatic force will be explained in the further section.

### A.5.2 Cross-Flow Drag:

The expression of sectional cross flow drag adopted to equivalent port and starboard side are expressed as:

$$f_{cfdP} = \frac{1}{2} C_{D,c} \cos(\beta - \phi) \rho \left( \frac{C_{pu} h_P}{\tan(\beta - \phi)} \right) V_P^2 \quad (\text{A.58})$$

$$f_{cfdS} = \frac{1}{2} C_{D,c} \cos(\beta + \phi) \rho \left( \frac{C_{pu} h_S}{\tan(\beta + \phi)} \right) V_S^2 \quad (\text{A.59})$$

### A.5.3 Buoyancy:

As it can be seen in Figure A.3, physical submerged geometry of a particular section with instantaneous heel angle is a composition of various sub-geometry. Generally it can be divided into two equivalent port and starboard sides, nevertheless, in this case, the geometry can be evaluated only in half section form. The geometry of sections can be grouped into two main ranges of flow characteristic. In the dry chine range, the submerged geometry is a simple triangle while in the wetted chine range, it is composed of a triangle and a trapezoid. The expressions are as follows:

$$\left. \begin{aligned} A_P &= h_P^2 \cot(\beta - \phi) \\ A_S &= h_S^2 \cot(\beta + \phi) \end{aligned} \right\} \quad \text{if } 0 < h_{P,S} < a \quad (\text{A.60})$$

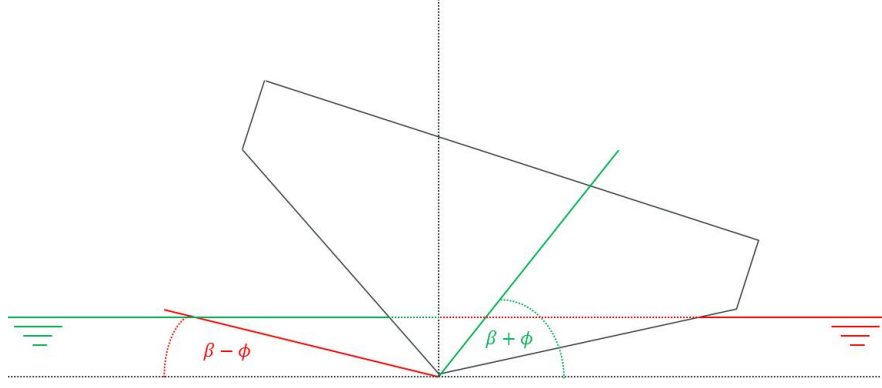


Figure A.3: Asymmetric Geometrical of Buoyancy

$$\left. \begin{aligned} A_P &= \frac{1}{2} a_P^2 \cot(\beta - \phi) + \frac{1}{2} (h_P - a_P) [2a_P \cot(\beta - \phi) + (h_P - a_P) \tan \phi] \\ A_S &= \frac{1}{2} a_S^2 \cot(\beta + \phi) + \frac{1}{2} (h_S - a_S) [2a_S \cot(\beta + \phi) - (h_S - a_S) \tan \phi] \end{aligned} \right\} \text{ if } h_{P,S} \geq a$$

(A.61)

The roll moment of buoyancy is evaluated with different arm defined previously for hydrostatic forces which is the centre of pressure acting on each section. In this cases, the centre of application of buoyancy force corresponding to each equivalent port and starboard side sections is defined as the centre of mass of the submerged geometry respect to the centre of roll motion (actually is the CG). In case of a simple triangle, it can be assumed as  $1/3$  of the triangle base. The expression of centre of geometry of a trapezoid can be found in literature as  $y' = (a^2 + ab + b^2) / 3(a + b)$

#### A.5.4 Total Forces and Moments:

After obtaining sectional forces corresponding to each equivalent port and starboard side, by integrating along the ship length, the total forces and moments of each side are obtained. Finally, by summing both side, the total forces and moments acting on the hull are obtained. They are explained in the following expressions:

$$F_h = \sum_{i=P,S} \int_L f_{h_i} dx' = \sum_{i=P,S} \frac{1}{2} \int_L m_{a_i} \dot{V}_i + \dot{m}_{a_i} V_i - U \frac{\partial}{\partial x'} (m_{a_i} V_i) dx' \quad (\text{A.62})$$

$$F_{cfd} = \sum_{i=P,S} \int_L f_{cfd_i} dx' = \sum_{i=P,S} \frac{1}{2} \int_L C_{D,C} \cos \beta \rho b_i V_i^2 dx' \quad (\text{A.63})$$

$$F_b = \sum_{i=P,S} \int_L f_{b_i} dx' = \sum_{i=P,S} \frac{1}{2} \int_L a_{bf} \rho g A_i dx' \quad (\text{A.64})$$

$$M_{h_{y'}} = \sum_{i=P,S} \int_L f_{h_i} x' dx' = \sum_{i=P,S} \frac{1}{2} \left[ \int_L m_{a_i} \dot{V}_i + \dot{m}_{a_i} V_i - U \frac{\partial}{\partial x'} (m_{a_i} V_i) \right] x' dx' \quad (\text{A.65})$$

$$M_{cfd_{y'}} = \sum_{i=P,S} \int_L f_{cfd_i} x' dx' = \sum_{i=P,S} \frac{1}{2} \int_L C_{D,C} \cos \beta \rho b_i V_i^2 x' dx' \quad (\text{A.66})$$

$$M_{b_{y'}} = \sum_{i=P,S} \int_L f_{b_i} x' dx' = \sum_{i=P,S} \frac{1}{2} \int_L a_{bf} \rho g A_i x' dx' \quad (\text{A.67})$$

$$M_{h_{x'}} = \sum_{i=P,S} \int_L f_{h_i} y'_i dx' = \sum_{i=P,S} \frac{1}{2} \left[ \int_L m_{a_i} \dot{V}_i + \dot{m}_{a_i} V_i - U \frac{\partial}{\partial x'} (m_{a_i} V_i) \right] y'_i dx' \quad (\text{A.68})$$

$$M_{cfd_{x'}} = \sum_{i=P,S} \int_L f_{cfd_i} y'_i dx' = \sum_{i=P,S} \frac{1}{2} \int_L C_{D,C} \cos \beta \rho b_i V_i^2 y'_i dx' \quad (\text{A.69})$$

$$M_{b_{x'}} = \sum_{i=P,S} \int_L f_{b_i} y'_i dx' = \sum_{i=P,S} \frac{1}{2} \int_L a_{bf} \rho g A_i y'_i dx' \quad (\text{A.70})$$

Substituting and developing all terms of the expression of the total forces and moments in the global equations of motions and following the same methodology as in the case of coupled heave and pitch motions and taken into account the influence of *Near Transom Correction Facetor*  $C_{tr}$ , the system can be translated to the matrix form with the pre-defined coefficients:

**Heave Equation:**

$$\begin{aligned}
M\ddot{z}_G = & - \left( \ddot{x}_G \sin \theta \sum_{i=P,S} \frac{1}{2} \int_L C_{tr} m_{a_i} dx' \right. \\
& + \dot{x}_G \cos \theta \dot{\theta} \sum_{i=P,S} \frac{1}{2} \int_L C_{tr} m_{a_i} dx' \\
& + \ddot{z}_G \cos \theta \sum_{i=P,S} \frac{1}{2} \int_L C_{tr} m_{a_i} dx' \\
& - \dot{z}_G \sin \theta \dot{\theta} \sum_{i=P,S} \frac{1}{2} \int_L C_{tr} m_{a_i} dx' \\
& - \cos \theta \sum_{i=P,S} \frac{1}{2} \int_L C_{tr} m_{a_i} \dot{w}_{w_i} dx' \\
& + \sin \theta \dot{\theta} \sum_{i=P,S} \frac{1}{2} \int_L C_{tr} m_{a_i} w_{w_i} dx' \\
& - \ddot{\theta} \sum_{i=P,S} \frac{1}{2} \int_L C_{tr} m_{a_i} x' dx' \\
& - \ddot{\phi} \sum_{i=P,S} \frac{1}{2} \int_L C_{tr} m_{a_i} y'_i dx' \\
& + \sum_{i=P,S} \frac{1}{2} \int_L C_{tr} \dot{m}_{a_i} V_i dx' \\
& - \sum_{i=P,S} \frac{1}{2} \int_L C_{tr} U_i V_i \frac{\partial m_{a_i}}{\partial x'} dx' \\
& + \cos \theta \sum_{i=P,S} \frac{1}{2} \int_L C_{tr} U_i m_{a_i} \frac{\partial w_{w_i}}{\partial x'} dx' \\
& + \dot{\theta} \sum_{i=P,S} \frac{1}{2} \int_L C_{tr} U_i m_{a_i} dx' \\
& + \dot{\phi} \sum_{i=P,S} \frac{1}{2} \int_L C_{tr} U_i m_{a_i} \frac{\partial y'_i}{\partial x'} dx' \\
& + \sum_{i=P,S} \frac{1}{2} \int_L C_{tr} C_{D,c} \cos \beta \rho b_i V_i^2 dx' \Big) \cos \theta \\
& - \sum_{i=P,S} \frac{1}{2} \int_L C_{tr} a_{bf} \rho g A_{sub_i} dx' \\
& + D \sin \theta \\
& + W
\end{aligned} \tag{A.71}$$

**Roll Equation:**

$$\begin{aligned}
I_{xx}\ddot{\phi} = & \ddot{x}_G \sin \theta \sum_{i=P,S} \frac{1}{2} \int_L C_{tr} m_{a_i} y'_i dx' \\
& + \dot{x}_G \cos \theta \dot{\theta} \sum_{i=P,S} \frac{1}{2} \int_L C_{tr} m_{a_i} y'_i dx' \\
& + \ddot{z}_G \cos \theta \sum_{i=P,S} \frac{1}{2} \int_L C_{tr} m_{a_i} y'_i dx' \\
& - \dot{z}_G \sin \theta \dot{\theta} \sum_{i=P,S} \frac{1}{2} \int_L C_{tr} m_{a_i} y'_i dx' \\
& - \cos \theta \sum_{i=P,S} \frac{1}{2} \int_L C_{tr} m_{a_i} \dot{w}_{w_i} y'_i dx' \\
& + \sin \theta \dot{\theta} \sum_{i=P,S} \frac{1}{2} \int_L C_{tr} m_{a_i} w_{w_i} y'_i dx' \\
& - \ddot{\theta} \sum_{i=P,S} \frac{1}{2} \int_L C_{tr} m_{a_i} x' y'_i dx' \\
& - \ddot{\phi} \sum_{i=P,S} \frac{1}{2} \int_L C_{tr} m_{a_i} y_i'^2 dx' \\
& + \sum_{i=P,S} \frac{1}{2} \int_L C_{tr} \dot{m}_{a_i} V_i y'_i dx' \\
& - \sum_{i=P,S} \frac{1}{2} \int_L C_{tr} U_i V_i \frac{\partial m_{a_i}}{\partial x'} y'_i dx' \\
& + \cos \theta \sum_{i=P,S} \frac{1}{2} \int_L C_{tr} U_i m_{a_i} \frac{\partial w_{w_i}}{\partial x'} y'_i dx' \\
& + \dot{\theta} \sum_{i=P,S} \frac{1}{2} \int_L C_{tr} U_i m_{a_i} y'_i dx' \\
& + \dot{\phi} \sum_{i=P,S} \frac{1}{2} \int_L C_{tr} U_i m_{a_i} \frac{\partial y'_i}{\partial x'} y'_i dx' \\
& + \sum_{i=P,S} \frac{1}{2} \int_L C_{tr} C_{D,c} \cos \beta \rho b_i V_i^2 y'_i dx' \\
& + \sum_{i=P,S} \frac{1}{2} \int_L C_{tr} a_{bf} \rho g A_{sub_i} y'_i dx'
\end{aligned} \tag{A.72}$$

**Pitch Equation:**

$$\begin{aligned}
I_{yy}\ddot{\theta} = & \ddot{x}_G \sin \theta \sum_{i=P,S} \frac{1}{2} \int_L C_{tr} m_{a_i} x' dx' \\
& + \dot{x}_G \cos \theta \dot{\theta} \sum_{i=P,S} \frac{1}{2} \int_L C_{tr} m_{a_i} x' dx' \\
& + \ddot{z}_G \cos \theta \sum_{i=P,S} \frac{1}{2} \int_L C_{tr} m_{a_i} x' dx' \\
& - \dot{z}_G \sin \theta \dot{\theta} \sum_{i=P,S} \frac{1}{2} \int_L C_{tr} m_{a_i} x' dx' \\
& - \cos \theta \sum_{i=P,S} \frac{1}{2} \int_L C_{tr} m_{a_i} \dot{w}_{w_i} x' dx' \\
& + \sin \theta \dot{\theta} \sum_{i=P,S} \frac{1}{2} \int_L C_{tr} m_{a_i} w_{w_i} x' dx' \\
& - \ddot{\theta} \sum_{i=P,S} \frac{1}{2} \int_L C_{tr} m_{a_i} x'^2 dx' \\
& - \ddot{\phi} \sum_{i=P,S} \frac{1}{2} \int_L C_{tr} m_{a_i} x' y'_i dx' \\
& + \sum_{i=P,S} \frac{1}{2} \int_L C_{tr} \dot{m}_{a_i} V_i x' dx' \\
& - \sum_{i=P,S} \frac{1}{2} \int_L C_{tr} U_i V_i \frac{\partial m_{a_i}}{\partial x'} x' dx' \\
& + \cos \theta \sum_{i=P,S} \frac{1}{2} \int_L C_{tr} U_i m_{a_i} \frac{\partial w_{w_i}}{\partial x'} x' dx' \\
& + \dot{\theta} \sum_{i=P,S} \frac{1}{2} \int_L C_{tr} U_i m_{a_i} x' dx' \\
& + \dot{\phi} \sum_{i=P,S} \frac{1}{2} \int_L C_{tr} U_i m_{a_i} \frac{\partial y'_i}{\partial x'} x' dx' \\
& + \sum_{i=P,S} \frac{1}{2} \int_L C_{tr} C_{D,c} \cos \beta \rho b_i V_i^2 x' dx' \\
& + \sum_{i=P,S} \frac{1}{2} \int_L C_{tr} a_{bf} \rho g A_{sub_i} x' dx'
\end{aligned} \tag{A.73}$$

Similar to the case of coupled heave and pitch motions, the integral terms will be assigned to the following coefficients:

$$\begin{aligned}
C_A &= \sum_{i=P,S} \frac{1}{2} \int_L C_{tr} m_{a_i} dx' & C_B &= \sum_{i=P,S} \frac{1}{2} \int_L C_{tr} m_{a_i} \dot{w}_{w_i} dx' \\
C_C &= \sum_{i=P,S} \frac{1}{2} \int_L C_{tr} m_{a_i} w_{w_i} dx' & C_{D1} &= \sum_{i=P,S} \frac{1}{2} \int_L C_{tr} m_{a_i} x' dx' \\
C_{D2} &= \sum_{i=P,S} \frac{1}{2} \int_L C_{tr} m_{a_i} y'_i dx' & C_E &= \sum_{i=P,S} \frac{1}{2} \int_L C_{tr} \dot{m}_{a_i} V_i dx' \\
C_F &= \sum_{i=P,S} \frac{1}{2} \int_L C_{tr} U_i V_i \frac{\partial m_{a_i}}{\partial x'} dx' & C_G &= \sum_{i=P,S} \frac{1}{2} \int_L C_{tr} U_i m_{a_i} \frac{\partial w_{w_i}}{\partial x'} dx' \\
C_{H1} &= \sum_{i=P,S} \frac{1}{2} \int_L C_{tr} U_i m_{a_i} dx' & C_{H2} &= \sum_{i=P,S} \frac{1}{2} \int_L C_{tr} U_i m_{a_i} \frac{\partial y'_i}{\partial x'} dx' \\
C_K &= \sum_{i=P,S} \frac{1}{2} \int_L C_{tr} m_{a_i} \dot{w}_{w_i} x' dx' & C_M &= \sum_{i=P,S} \frac{1}{2} \int_L C_{tr} m_{a_i} w_{w_i} x' dx' \\
C_{N1} &= \sum_{i=P,S} \frac{1}{2} \int_L C_{tr} m_{a_i} x'^2 dx' & C_{N2} &= \sum_{i=P,S} \frac{1}{2} \int_L C_{tr} m_{a_i} x' y'_i dx' \\
C_{O1} &= \sum_{i=P,S} \frac{1}{2} \int_L C_{tr} \dot{m}_{a_i} V_i x' dx' & C_{O2} &= \sum_{i=P,S} \frac{1}{2} \int_L C_{tr} \dot{m}_{a_i} V_i y'_i dx' \\
C_P &= \sum_{i=P,S} \frac{1}{2} \int_L C_{tr} U_i V_i \frac{\partial m_{a_i}}{\partial x'} x' dx' & C_Q &= \sum_{i=P,S} \frac{1}{2} \int_L C_{tr} U_i m_{a_i} \frac{\partial w_{w_i}}{\partial x'} x' dx' \\
C_{R1} &= \sum_{i=P,S} \frac{1}{2} \int_L C_{tr} U_i m_{a_i} x' dx' & C_{R2} &= \sum_{i=P,S} \frac{1}{2} \int_L C_{tr} U_i m_{a_i} \frac{\partial y'_i}{\partial x'} x' dx' \\
C_S &= \sum_{i=P,S} \frac{1}{2} \int_L C_{tr} m_{a_i} \dot{w}_{w_i} y'_i dx' & C_T &= \sum_{i=P,S} \frac{1}{2} \int_L C_{tr} m_{a_i} w_{w_i} y'_i dx' \\
C_U &= \sum_{i=P,S} \frac{1}{2} \int_L C_{tr} m_{a_i} y_i'^2 dx' & C_V &= \sum_{i=P,S} \frac{1}{2} \int_L C_{tr} U_i V_i \frac{\partial m_{a_i}}{\partial x'} y'_i dx' \\
C_W &= \sum_{i=P,S} \frac{1}{2} \int_L C_{tr} U_i m_{a_i} \frac{\partial w_{w_i}}{\partial x'} y'_i dx' & C_{X1} &= \sum_{i=P,S} \frac{1}{2} \int_L C_{tr} U_i m_{a_i} y'_i dx' \\
C_{X2} &= \sum_{i=P,S} \frac{1}{2} \int_L C_{tr} U_i m_{a_i} \frac{\partial y'_i}{\partial x'} y'_i dx'
\end{aligned}$$





## Appendix B

# Detailed Evaluation of Terms in Equations of Motions and Choices of Numerical Methods

The components of the terms in the system of equations of motions are evaluated in details in this section. The evaluation is performed in an instantaneous time step (frozen time) with the following input and output variables:

- Input Variables:
  - Time:  $t$
  - Displacements:  $\bar{x} = (x_G, z_G, \theta)$
  - Velocities:  $\dot{\bar{x}} = (\dot{x}_G, \dot{z}_G, \dot{\theta})$
- Output Variables:
  - Accelerations:  $\ddot{\bar{x}} = (0, \ddot{z}_G, \ddot{\theta})$

The input variables are known from the integration from the previous time step to the actual time step or in case of the first time step, they are initial conditions. The accelerations are the desired output at each time step in order to evaluate velocities and displacement respectively in the next time step.

### B.1 Evaluation of Wave Functions

The wave related functions are expressed follows:

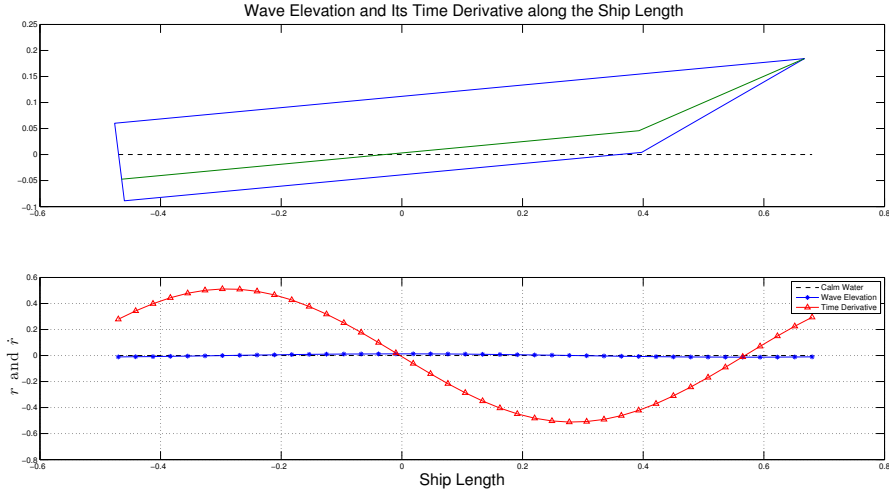


Figure B.1: Wave elevation and its time derivative.

### B.1.1 Wave Elevation and Its Time Derivative: $r$ and $\dot{r}$

The wave elevation and its time derivative are the most fundamental parameters that form a part of the other terms and parameters. The regular head wave elevation and its time derivative are expressed as follows:

$$\begin{aligned} r &= r_0 \cos(kx + \omega t) \\ \dot{r} &= -r_0(k\dot{x} + \omega) \sin(kx + \omega t) \end{aligned} \quad (\text{B.1})$$

Generally, the wave elevation is a function of time and space, but due to the use in case of frozen time step, it turns into a function of only space. The space of interest is only the intersection between the sea and the ship hull. Therefore, Equation B.1 can be expressed as a function in body-fixed coordinate as follow:

$$\begin{aligned} r(x') &= r_0 \cos(k(x_G + x' \cos \theta - (z_G - x' \sin \theta) \tan \theta) + \omega t) \\ \dot{r}(x') &= \frac{d}{dt} r(x') \end{aligned} \quad (\text{B.2})$$

As the displacements  $(x_G, z_G, \theta)$  and velocities  $(\dot{x}_G, \dot{z}_G, \dot{\theta})$  in earth-fixed coordinate are pre-determined and fixed at each time step, those functions are only space dependent ( $f(x')$ ).

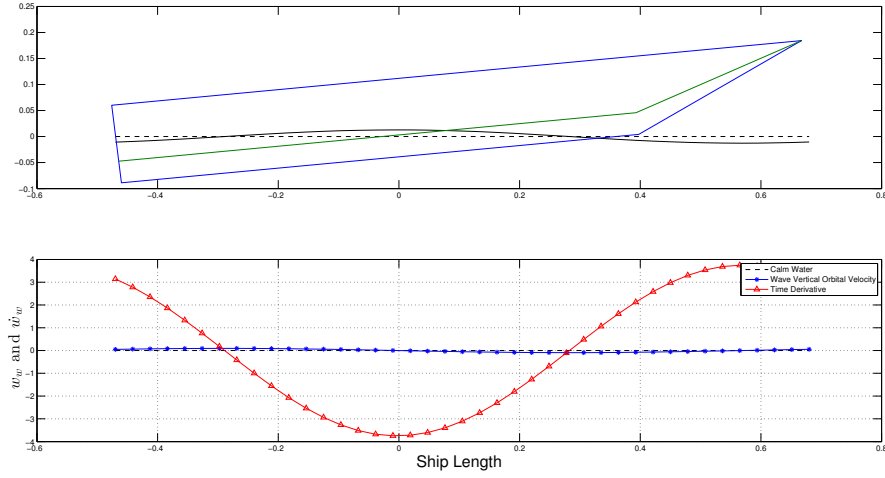


Figure B.2: Wave orbital vertical velocity and its time derivative.

### B.1.2 Wave Vertical Orbital Velocity and Its Time Derivative: $w_w$ and $\dot{w}_w$

Following the same principle as the wave elevation, the expression of wave vertical orbital velocity and its time derivative are:

$$\begin{aligned} w_w(x') &= -r_0\omega \sin(k(x_G + x' \cos \theta - (z_G - x' \sin \theta) \tan \theta) + \omega t) \\ \dot{w}_w(x') &= \frac{d}{dt} w_w(x') \end{aligned} \quad (\text{B.3})$$

Which are as well only space dependent.

### B.1.3 Space Partial Derivative of Wave Vertical Orbital Velocity: $\frac{\partial w_w}{\partial x'}$

According to A.30, the coefficients  $C_G$  and  $C_Q$  consist of a partial derivative with respect to  $x'$  of the component  $w_w$ . This component can be evaluate both analytically or numerically.

The analytical partial derivative is expressed as:

$$\frac{\partial w_w}{\partial x'} = -r_0k \cos(k(x_G + x' \cos \theta - \tan \theta (z_G - x' \sin \theta)) + \omega t) (\cos \theta + \sin \theta \tan \theta) \quad (\text{B.4})$$

Several numerical differentiation methods are available. The most appropriate method should be one that gives the closest solution to the analytical solution. Choices of numerical differentiation methods are as follows:

- A Simple Symmetric Method:

- Expression:  $f'(x') = \frac{f(x'+h) - f(x'-h)}{2h}$
- Error:  $O(h^2)$

- A Four Points Method (fourth-order approximation):

- Expression:  $f'(x') = \frac{f(x'-2h) - 8f(x'-h) + 8f(x'+h) - f(x'+2h)}{12h}$
- Error:  $O(h^4)$

- Richardson's Extrapolation (sixth-order approximation):

- Expression:  

$$f'(x') = \frac{16 \left( \frac{f(x'-2h) - 8f(x'-h) + 8f(x'+h) - f(x'+2h)}{12h} \right) - \left( \frac{f(x'-4h) - 8f(x'-2h) + 8f(x'+2h) - f(x'+4h)}{24h} \right)}{15}$$
- Error:  $O(h^6)$

The Fridsma (1969)'s prismatic hull model of  $20^\circ$  deadrise angle is chosen to perform a numerical verification by varying number of hull sections as the controlling parameter. According to the results comparison, the four points numerical differentiation gives the closet solution to the analytical ones. This can lead to the conclusion that this method is the most appropriate numerical method. In case of regular wave, the analytical expression of space derivative is simple to obtain and use, nevertheless, if the case of irregular wave is presented, use of numerical differentiation is indeed necessary, as the analytical expression is mostly impossible to evaluate.

## B.2 Evaluation of Section Submergence and Its time Derivative: $h$ and $\dot{h}$

Section submergence is another fundamental parameter after the wave expressions. It depends on the actual displacement (position) related to the water level. The section submergence and its time derivative at each time step varies along the ship length, and are continuous functions and expressed as:

$$\begin{aligned} h &= z'_k + \left( \frac{z_G - x' \sin \theta}{\cos \theta} \right) - \frac{r}{\cos \theta} \\ \dot{h} &= \frac{dh}{dt} = \left( \frac{(\dot{z}_G - x' \cos \theta \dot{\theta}) + (z_G - x' \sin \theta) \sin \theta \dot{\theta}}{\cos^2 \theta} \right) - \left( \frac{\dot{r} \cos \theta + r \sin \theta \dot{\theta}}{\cos^2 \theta} \right) \end{aligned} \quad (B.5)$$

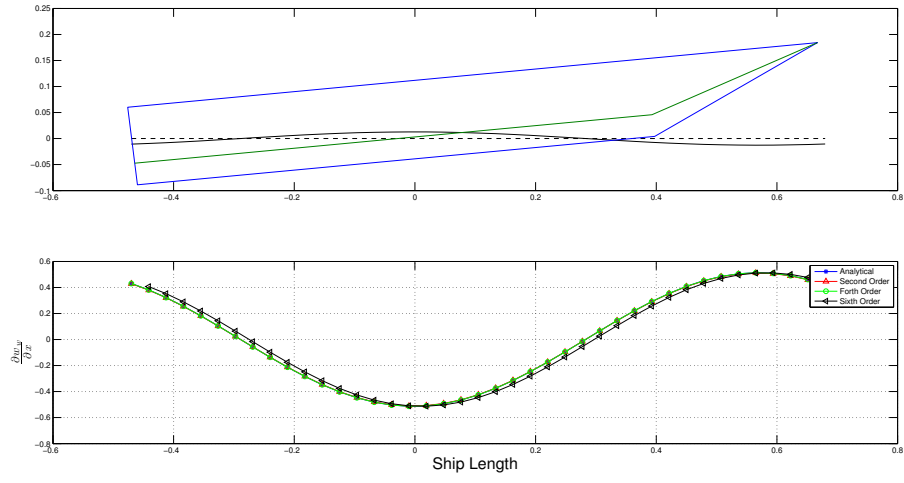


Figure B.3: Partial derivative of wave vertical orbital velocity along the ship length.

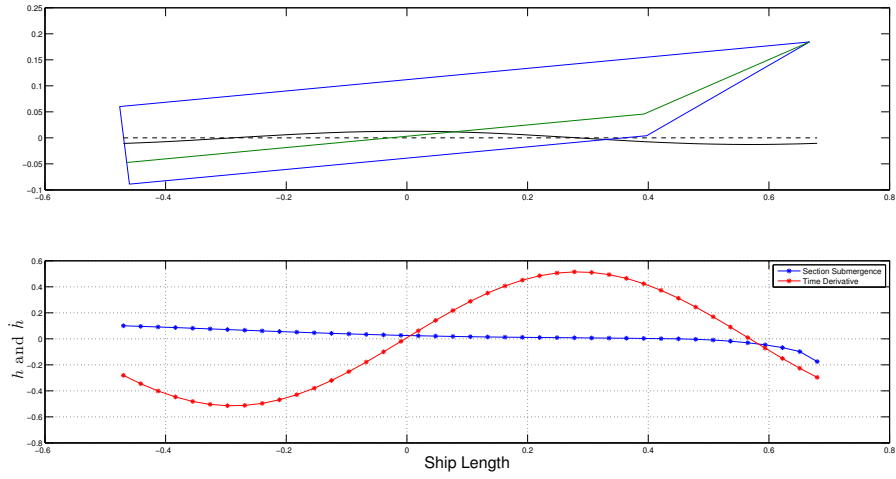


Figure B.4: Section submergence and its time derivative.

The section submergence and its time derivative form a part of other common parameters which are half breadth dependent ( $b = h/\tan\beta$ ) in the coefficients  $C_A$  to  $C_R$  defined in the Appendix A, i.e., sectional added mass  $m_a$ , sectional cross-flow drag  $f_{cf}$  and sectional buoyancy  $f_b$ .

According to Figure B.4, the section submergence is evaluated continuously along the ship length, its value is positive when a particular sectional keel is wetted while it is negative when it is out of water.

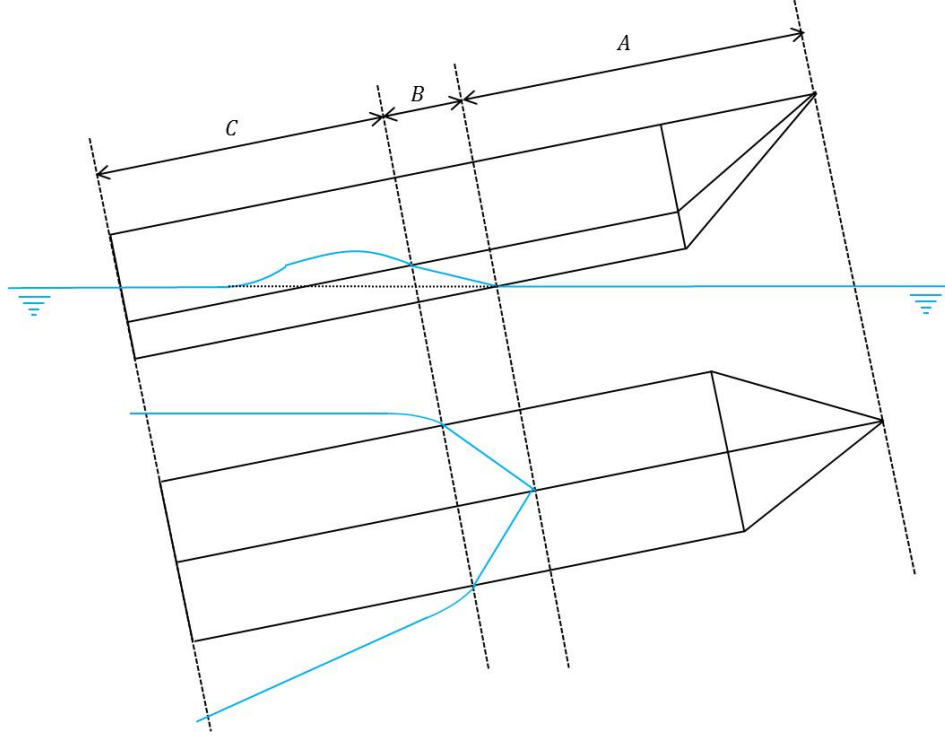


Figure B.5: Flow-hull characteristic zones (longitudinal).

### B.3 Evaluation of Sectional Added Mass and Its Time Derivative

The expression of sectional added mass and its time derivative for a wedge shape of high frequency solution are:

$$\begin{aligned} m_a &= C_m \cdot \frac{\pi}{2} \cdot \rho \cdot \left( \frac{C_{pu} h}{\tan \beta} \right)^2 \\ \dot{m}_a &= C_m \cdot \pi \cdot \rho \cdot h \cdot \left( \frac{C_{pu}}{\tan \beta} \right)^2 \frac{dh}{dt} \end{aligned} \tag{B.6}$$

Which are functions of body-fixed coordinate at each time step. The integral evaluation along the ship length to obtain the total added mass appears not to be constantly evaluable considering the physical characteristic of each particular sectional flow along the ship length. There are several conditions of the use of  $C_{pu}$  due to different flow-hull characteristics. As can be seen in the Figures B.5 and B.6: the ship is divided into three zones along the ship length:

- Zone A is the zone of dry keel. The integral from the point where the keel intersects with the still water line to bow peak of the ship is equal to zero, as the ship sections

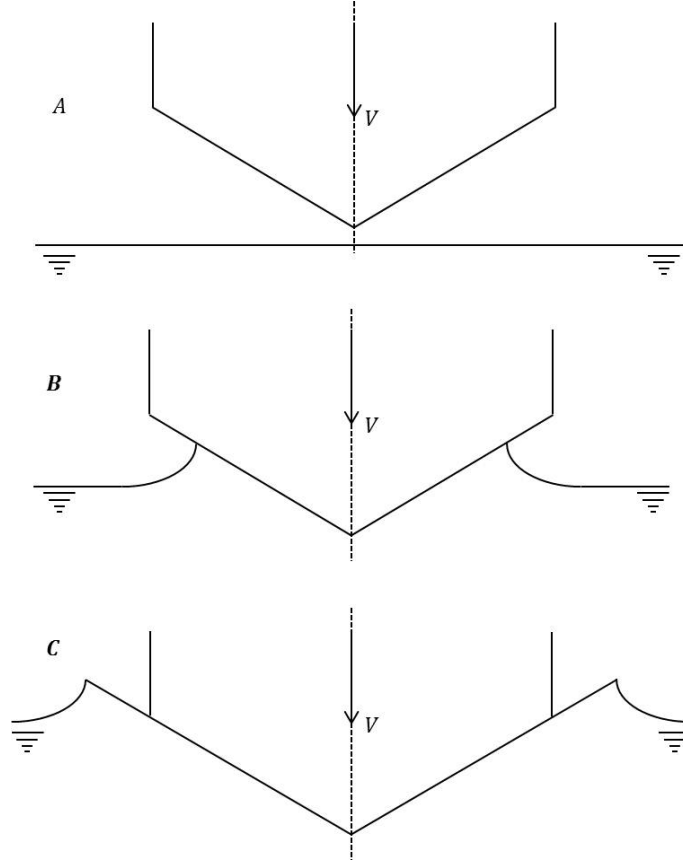


Figure B.6: Flow-hull characteristic zones (transverse).

are out off the water. Consequently, the value of section submergence accounting with the effect of the pile-up correction factor,  $h \cdot C_{pu}$ , is negative,  $h \cdot C_{pu} < 0$ .

- Zone B is the zone of wetted keel but dry chine. This zone accounts the sections from the intersection point of chines and water line to the limitation of zone A. The first section at the first wetted keel point begins to penetrate into the water taking into account the influence of the  $C_{pu}$  factor. The section is considered to be wetted up to the water pile-up. The sectional added mass accounted with  $C_{pu}$  changes its value along the ship length as well as its time derivative. Nevertheless, at a certain point before the wetted chines point, the water pile-up reaches the chines and makes them stand the flow phenomena like in wetted chines zone (Zone C). In this case, the value of  $h \cdot C_{pu}$  varies between zero and vertical distance from keel to chine  $a$ , in which  $a = b \cdot \tan \beta$  where  $0 < h \cdot C_{pu} < a$ .
- Zone C is the zone of wetted chine. The sectional added mass does not change its value along the ship length (in case of prismatic hull with constant deadrise angle) neither its time derivative, in other words, the sectional added mass reaches its maximum value when the water level reaches the chine. In this zone, the value of  $h \cdot C_{pu}$  is greater than  $a$ ,  $h \cdot C_{pu} > a$ . Thus, the value of  $m_a$  remains its maximum value at the chine position,  $m_a = C_m \pi / 2 \rho b_{max}^2$  and consequently  $\dot{m}_a = 0$ .



According to the zoning criteria mentioned previously, the expression of sectional added mass is obviously discontinuous functions:

$$m_a = \begin{cases} C_m \cdot \frac{\pi}{2} \cdot \rho \cdot \left( \frac{a}{\tan \beta} \right)^2 & \text{if } h \cdot C_{pu} > a \\ C_m \cdot \frac{\pi}{2} \cdot \rho \cdot \left( \frac{C_{pu} h}{\tan \beta} \right)^2 & \text{if } 0 < h \cdot C_{pu} < a \\ 0 & \text{if } h \cdot C_{pu} < 0 \end{cases} \quad (\text{B.7})$$

As well as its time derivative:

$$\dot{m}_a = \begin{cases} 0 & \text{if } h \cdot C_{pu} > a \\ C_m \cdot \pi \cdot \rho \cdot h \cdot \left( \frac{C_{pu}}{\tan \beta} \right)^2 \frac{dh}{dt} & \text{if } 0 < h \cdot C_{pu} < a \\ 0 & \text{if } h \cdot C_{pu} < 0 \end{cases} \quad (\text{B.8})$$

### B.3.1 Availability of Sectional Added Mass Coefficients $C_m$

2D added heave mass coefficient for a wedge water entry is an essential part for a prismatic planing boat.

**Added mass coefficient suggested by Faltinsen (2000):** According to Faltinsen (2000) it can be considered as deadrise ( $\beta$ ) dependent and varies between 0.6 to 1.0 as follows:

$$m_a = \rho d^2 K \quad (\text{B.9})$$

$$= \frac{\rho d^2}{\tan \beta} \left( \frac{\pi}{\sin \beta} \frac{\Gamma(1.5 - \beta/\pi)}{\Gamma^2(1 - \beta/\pi) \Gamma(0.5 + \beta/\pi)} - 1 \right) \quad (\text{B.10})$$

**Added mass coefficient used by Zarnick (1978):** Zarnick used the maximum value (identical to the suggestion of Wagner):

$$C_m = 1$$

**Added mass coefficient suggested by Payne (1994):** Payne suggested the dependency of deadrise angle of added mass coefficient as:

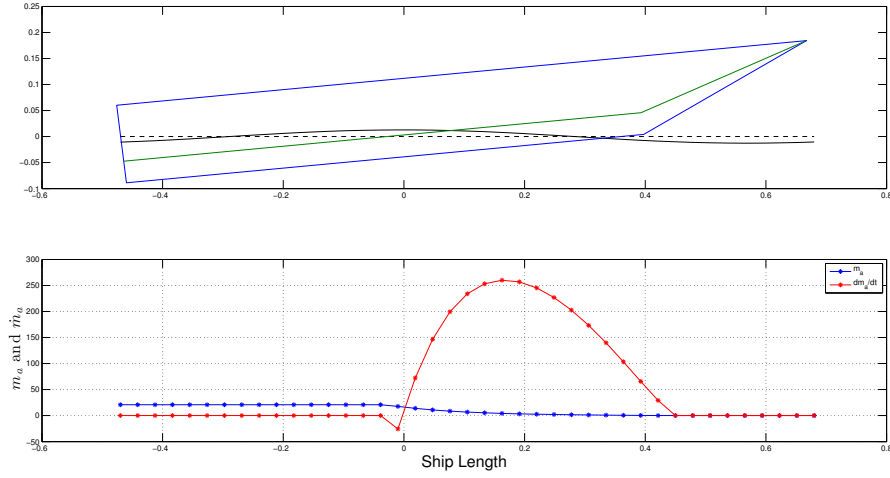


Figure B.7: Sectional added mass and its time Derivative.

$$C_m = \left(1 - \frac{\beta}{2\pi}\right)^2$$

**Added mass coefficient suggested by Vorus (1996):** Vorus suggested in the similar manner that the added mass coefficient is deadrise angle dependent expressed by:

$$C_m = \frac{\pi^2}{4} \left(1 - \frac{\beta}{90} \cdot 0.4 \cdot (1 - KAR)\right)$$

Where  $KAR$  is an added mass correction factor. Using  $KAR = 1.0$  is equivalent to using the added mass coefficient of Wagner, while using  $KAR = 0.0$  roughly matches the added mass coefficient curve of Vorus.

#### B.4 Evaluation of Space Partial Derivative of Sectional Added Mass: $\frac{\partial m_a}{\partial x'}$

Due to the discontinuous property along the ship length of  $m_a$ , the points of discontinuous are not differentiable. Therefore, their partial derivatives respect to  $x'$  need to be re-considered in evaluation. If the partial derivative is performed continuously along the ship length, it will violate the mathematical property at the discontinuous points. Consequently, the expression of partial derivative needs to be discontinuous as well.

Zarnick (1978) avoided this problem by using the property of the integration by parts and substitute in the coefficients  $C_F$  and  $C_P$  by:

$$\int_L m_a \frac{\partial UV}{\partial x'} dx' = - \int_L UV \frac{\partial m_a}{\partial x'} dx' + UV m_a|_{bow}^{stern} \quad (B.11)$$

So

$$C_F = \int_L UV \frac{\partial m_a}{\partial x'} dx' = -UV m_a|_{stern} - \int_L m_a \frac{\partial UV}{\partial x'} dx' \quad (B.12)$$

$$C_P = \int_L UV \frac{\partial m_a}{\partial x'} x' dx' = -UV m_a x'|_{stern} - \int_L m_a \frac{\partial UV}{\partial x'} x' dx' \quad (B.13)$$

However, by using this technique, the representation of pressure distribution along the ship length will not be possible to perform, due to the first term in the right hand side of the substitution by integration by parts.

According to the expression of  $m_a$ , the discontinuous points are those boundary points between the three zones along the ship length defined in the previous section. In case of prismatic hull, it is expressed as:

$$\frac{\partial m_a}{\partial x'} = \begin{cases} 0 & \text{if } h \cdot C_{pu} > a \\ \frac{\partial m_a}{\partial x'} & \text{if } 0 < h \cdot C_{pu} < a \\ 0 & \text{if } h \cdot C_{pu} < 0 \end{cases} \quad (B.14)$$

The term  $\frac{\partial m_a}{\partial x'}$  can be evaluated both analytically and numerically. As in the case of  $\frac{\partial w_w}{\partial x'}$ , the analytical expression is easy to apply if the ship profile is given principally in function of  $x'$ . Otherwise, more mathematical treatment is necessary. While numerical expression is more global to perform taking into account the error corresponding to each method.

The distribution of  $\frac{\partial m_a}{\partial x'}$  along the ship length by different methods of evaluation are represented in Figure B.8:

Nevertheless, the continuous partial derivative is also perform in order to compare with the discontinuous case. If the results are not significantly different, the continuous one might be the better choice for the numerical model, as it is simpler to perform and evaluate.

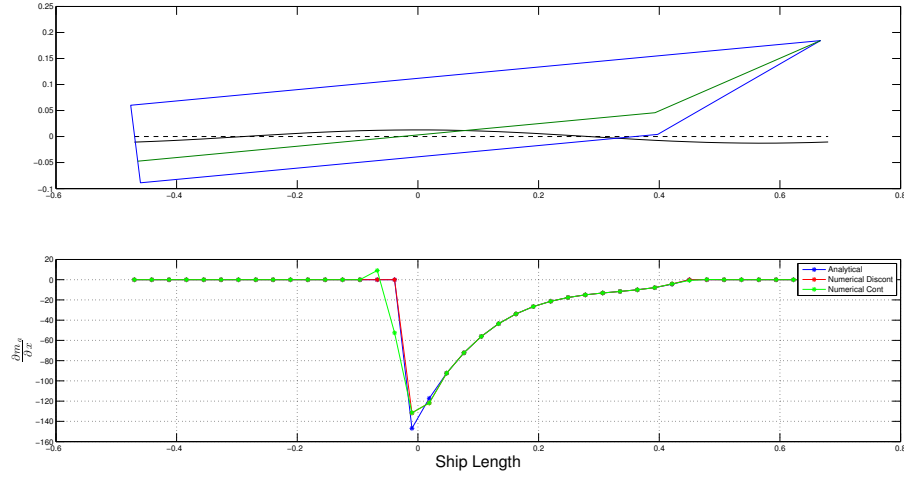


Figure B.8: Partial derivative of sectional added mass along the ship length.

## B.5 Evaluation of Sectional Cross-Flow Drag

The expression of sectional cross-flow drag is:

$$f_{cfd} = C_{D,c} \cdot \cos \beta \cdot \rho \cdot b \cdot V^2 \quad (\text{B.15})$$

Which is half breadth  $b$  dependent as well as the sectional added mass. By substituting the relation between the half breadth,  $b$  and the section submergence,  $h$ , it allows Equation B.15 to be evaluated in function of ship length.

$$f_{cfd} = \begin{cases} C_{D,c} \cdot \cos \beta \cdot \rho \cdot a \cdot \cot \beta \cdot V^2 & \text{if } h \cdot C_{pu} > a \\ C_{D,c} \cdot \cos \beta \cdot \rho \cdot h \cdot C_{pu} \cdot \cot \beta \cdot V^2 & \text{if } 0 < h \cdot C_{pu} < a \\ 0 & \text{if } h \cdot C_{pu} < 0 \end{cases} \quad (\text{B.16})$$

Which is a discontinuous function as  $m_a$ . Nevertheless, although this parameter is discontinuous, it does not need any special treatment as the partial derivative along the ship length is not presented.

### B.5.1 Evaluation of Sectional Buoyancy

The sectional buoyancy depends directly on the submerge area of a particular section. Along the ship length, each particular section is a function of section submergence

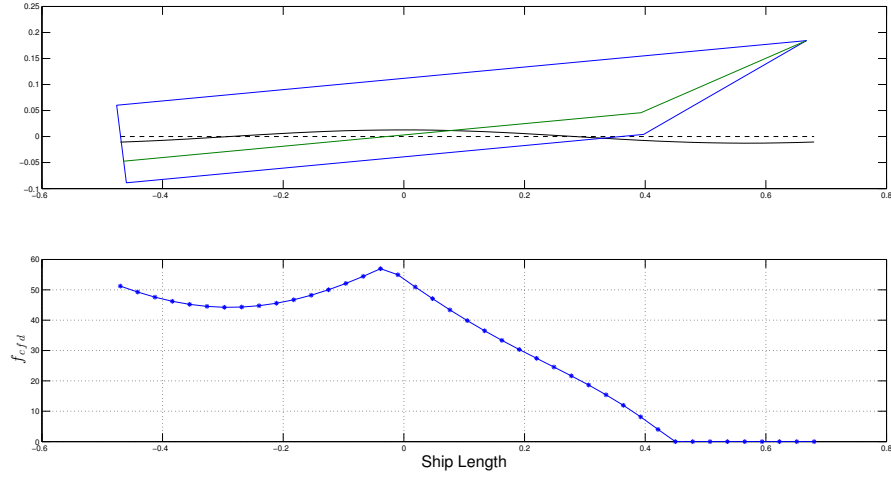


Figure B.9: Sectional cross-flow drag.

*h.* It depends again on different three zones defined previously as in case of sectional added mass  $m_a$ . Nevertheless, due to the small influence, the section submergence to be applied in the case of section submerged area does not account the presence of  $C_{pu}$  and is expressed as:

$$A_{sub} = \begin{cases} a \cdot (2 \cdot h - a) \cdot \cot \beta & \text{if } h \cdot C_{pu} > a \\ h^2 \cdot \cot \beta & \text{if } 0 < h \cdot C_{pu} < a \\ 0 & \text{if } h \cdot C_{pu} < 0 \end{cases} \quad (\text{B.17})$$

Then it will be used in:

$$f_b = a_{bf} \cdot \rho \cdot g \cdot A_{sub} \quad (\text{B.18})$$

As well as the case of sectional cross-flow drag, the sectional buoyancy has no dealt with the partial derivative along the ship length, the discontinuous property along the ship length does not cause special consideration for the calculation.

## B.6 Evaluation of Drag

The drag component is different from the previous forces component. It is not fundamentally calculated as sectional component. The drag force is approximate directly in the global form. Nevertheless, due to the fact that it is wetted surface dependent, the

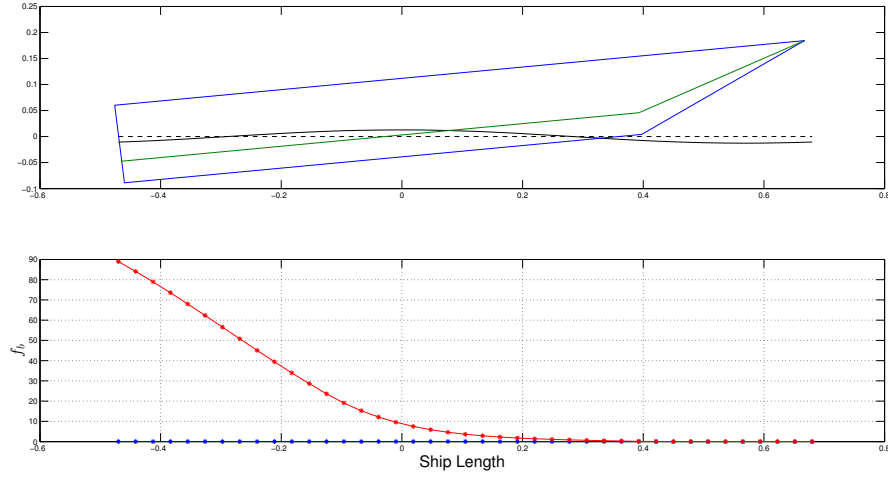


Figure B.10: Sectional buoyancy

wetted surface is evaluated as the integration of particular sectional wetted curves along the ship length. The expression of sectional wetted curves is:

$$s_w = \begin{cases} 2 \cdot a \cdot \csc \beta & \text{if } h \cdot C_{pu} > a \\ 2 \cdot h \cdot C_{pu} \cdot \csc \beta & \text{if } 0 < h \cdot C_{pu} < a \\ 0 & \text{if } h \cdot C_{pu} < 0 \end{cases} \quad (\text{B.19})$$

Which is a discontinuous function in the same condition as  $m_a$ . Normally, the drag force has a direction opposite to the forward speed and parallel to keel. Its horizontal component is neglected due to the presence of towed condition. The vertical component is taken into account although it is small. The expression of the drag force is:

$$D = \frac{1}{2} \cdot \rho \cdot U^2 \cdot S_w \cdot C_F \quad (\text{B.20})$$

## B.7 Evaluation of Coefficients $C_A$ to $C_R$ and Total Forces and Moments

The total forces and moments are obtained integrating those sectional functions along the ship length in term of  $x'$ . The integration was evaluated in term of the coefficients defined in the Appendix A and then composes to form the global equations of motions of instantaneous time step. The integration can be performed both analytically and numerically. The analytical cases could give the exact solution but due to the complication

of mathematical property of some parameters, the analytical expression will no longer valid for arbitrary cases but only the prismatic case. The numerical evaluation could give more appropriate solutions by accounting for the errors committed corresponding to different methods. There are several numerical integration methods available such as:

- Trapezoidal Integration:

- Expression:  $I = \frac{h}{2} \left( f(x'_0) + f(x'_n) + 2 \sum_{i=1}^{n-1} f(x'_i) \right)$
- Error:  $O(h^3)$

- Simpson's Integration:

- Expression:  $I = \frac{h}{3} \left( f(x'_0) + f(x'_n) + 4 \sum_{i=1,3,5}^{n-1} f(x'_i) + 2 \sum_{i=2,4,6}^{n-2} f(x'_i) \right)$
- Errors:  $O(h^4)$

The comparison of analytical and numerical solutions is shown in Table B.1, which can be seen that the Simpson's Integration gives the closest solution to the analytical solution.

After performing the total forces and moments evaluation and substituting into Equation A.30 the system converts into a system of two 1<sup>st</sup> order linear equations with two unknowns. This can be easily solved by Guassian elimination matrix and finally, the desired output which is the accelerations of the present time step is found.

## B.8 Time Marching Integration Methods

Choices of time marching integration methods are explained in details in this section.

### B.8.1 Basic Algorithms of Equations of Motions

Consider a single object with mass  $m$  moving in one dimension. With its time-dependent position denoted  $x(t)$ , the differential equation governing its dynamics is:

$$\ddot{x} = \frac{1}{m} F[x(t), \dot{x}(t), t] \quad (\text{B.21})$$

Where  $F$  is the total force acting on the object, and  $\dot{x}$  and  $\ddot{x}$  are the first and second time derivatives of  $x$ . It has been indicated that the force may depend on  $x$ ,  $\dot{x}$  and  $t$ .

Table B.1: Comparison of integration methods along the ship length.

Coefficients	Simpson	Trapezoidal	Analytical
$C_A$	11.53801262	11.53312835	11.5427949
$C_B$	-12.92408755	-12.89000995	-12.94564161
$C_C$	0.567961145	0.56720465	0.567991875
$C_D$	-2.105567827	-2.106710485	-2.10581859
$C_E$	53.73086514	53.44297983	52.0561311
$C_F$	-84.39223648	-84.41618899	-90.13331325
$C_G$	-10.56500424	-10.53715701	-10.58262188
$C_H$	68.88491511	68.85569907	68.91344447
$C_K$	-1.456265447	-1.469394439	-1.456927748
$C_M$	-0.188101539	-0.187881134	-0.188085681
$C_N$	0.752334375	0.75367225	0.752229585
$C_O$	10.81124117	10.79685258	10.73272458
$C_P$	-7.560243931	-7.588972089	-7.28325424
$C_Q$	-1.19148573	-1.20221381	-1.192026565
$C_R$	-12.57989966	-12.58669176	-12.58139374
$F_h$	140.468402	140.1982752	144.5386581
$M_h$	18.63471784	18.65144429	18.27933231
$F_b$	22.37731006	22.38869691	22.32098327
$M_b$	-6.49510415	-6.506566624	-6.491825361
$F_{cfd}$	34.91151905	34.90156658	34.86348142
$M_{cfd}$	-3.318506691	-3.328063492	-3.342781137

These dependencies typically come from a position dependent static potential, a velocity dependent damping (friction), and a time-dependent driving force, but there are other natural possibilities as well, e.g., a position dependent friction.

To study the system numerically, it is convenient to rewrite the 2<sup>nd</sup> order differential equation above as two coupled 1<sup>st</sup> order equations. Giving the velocity its standard symbol  $v(t)$ , ones can be written:

$$\dot{x}(t) = v(t) \quad (\text{B.22})$$

$$\dot{v}(t) = \frac{1}{m} F[x(t), v(t), t] \quad (\text{B.23})$$

To integrate this set of equations, the time axis is discretize as  $t = t_0, t_1, \dots, t_n$  with a constant time step  $t_{n+1} - t_n = \Delta t$ . The initial values  $x_0 = x(t_0)$  and  $v_0 = v(t_0)$  are used to start the integration process. In this case those initial values are static stability conditions.



### B.8.2 Euler Algorithm

The simplest way to advance the time from  $t_n$  and  $t_{n+1}$  is to use the 1<sup>st</sup> order approximation:

$$v_{n+1} = v_n + \Delta t \cdot a_n \quad (\text{B.24})$$

$$x_{n+1} = x_n + \Delta t \cdot v_n \quad (\text{B.25})$$

Where  $a_n = F(x_n, v_n, t_n)/m$  is the acceleration. Clearly, the error made in each time step of this algorithm is  $O(\Delta t^2)$ . The method, which is called “*Euler’s Forward Method*” is in general not very useful in practice. For example, in system with no damping or driving force, the energy should be conserved. However, with the Euler method, the energy typically diverges with time, whereas in most higher-order methods the energy errors are bounded. This method is later modified by several researchers and consequently, the accuracy has increased.

### B.8.3 Modified Euler Method or Simple Predictor-Corrector Method

The predictor-corrector method consists in two steps of integration. In the first step, one method is used to predict a solution and then uses other method to correct the first method and iterate the correction until the desired convergence is found. The most simple one uses Euler method in predictor step and use the modified Euler method in corrector step:

$$v_{n+1}^p = v_n + \Delta t \cdot a_n \quad \text{Prediction} \quad (\text{B.26})$$

$$v_{n+1}^c = v_n + \frac{1}{2} \cdot \Delta t \cdot [a_n + a(v_{n+1}^p, t_{n+1})] \quad \text{Correction} \quad (\text{B.27})$$

$$v_{n+1}^p = v_{n+1}^c \quad \text{if } v_{n+1}^p - v_{n+1}^c > |\epsilon| \quad (\text{B.28})$$

$$v_{n+1} = v_{n+1}^c \quad \text{if } v_{n+1}^p - v_{n+1}^c < |\epsilon| \quad (\text{B.29})$$

As well as the integration of  $v$  to obtain  $x$ :

$$x_{n+1}^p = x_n + \Delta t \cdot v_n \quad \text{Prediction} \quad (\text{B.30})$$

$$x_{n+1}^c = x_n + \frac{1}{2} \cdot \Delta t \cdot [v_n + v_{n+1}^p] \quad \text{Correction} \quad (\text{B.31})$$

$$x_{n+1}^p = x_{n+1}^c \quad \text{if } x_{n+1}^p - x_{n+1}^c > |\epsilon| \quad (\text{B.32})$$

$$x_{n+1} = x_{n+1}^c \quad \text{if } x_{n+1}^p - x_{n+1}^c < |\epsilon| \quad (\text{B.33})$$

The correction step keeps repeating until the convergence of the last prediction with the actual correction is of desired value. This method is simple and yield modest accuracy but if the extreme accuracy is required, a more sophisticated method should selected.

#### B.8.4 Runge-Kutta Method

The Runge-Kutta (RK) method can be considered as the most classic of all high-order schemes. There is a whole range of methods of this type in different orders, but the RK name is most commonly associated with the 4<sup>th</sup> order variant (discretization error  $O(\Delta t^5)$ ). In case of equations of motions, Runge-Kutta method can be expressed as:

$$v_{n+1} = v_n + \frac{1}{6} \cdot (k_1 + 2k_2 + 2k_3 + k_4) \quad (\text{B.34})$$

$$x_{n+1} = x_n + \frac{1}{6} \cdot (l_1 + 2l_2 + 2l_3 + l_4) \quad (\text{B.35})$$

$$k_1 = \Delta t \cdot a(x_n, v_n, t_n) \quad (\text{B.36})$$

$$l_1 = \Delta t \cdot v_n \quad (\text{B.37})$$

$$k_2 = \Delta t \cdot a\left(x_n + \frac{1}{2}l_1, v_n + \frac{1}{2}k_1, t_{n+\frac{1}{2}}\right) \quad (\text{B.38})$$

$$l_2 = \Delta t \cdot \left(v_n + \frac{1}{2}k_1\right) \quad (\text{B.39})$$

$$k_3 = \Delta t \cdot a\left(x_n + \frac{1}{2}l_2, v_n + \frac{1}{2}k_2, t_{n+\frac{1}{2}}\right) \quad (\text{B.40})$$

$$l_3 = \Delta t \cdot \left(v_n + \frac{1}{2}k_2\right) \quad (\text{B.41})$$

$$k_4 = \Delta t \cdot a(x_n + l_3, v_n + k_3, t_{n+1}) \quad (\text{B.42})$$

$$l_4 = \Delta t \cdot (v_n + k_3) \quad (\text{B.43})$$

The Runge-Kutta method appears to be the most appropriate method of assessing time marching integration due to its property of capable of self-starting, in the other word, this method can start the calculation with the input data of the actual time step. Unlike the predictor-corrector method and multi-step method which need information of various previous time steps. Although the formulation is quite complex, time consumption in calculation is acceptable. The actual Runge-Kutta method is of 4<sup>th</sup> order, it has been modified by several researchers to some higher orders.

#### B.8.5 Runge-Kutta-Merson Method

This method is a modification by Merson of the Runge-Kutta method and it is of 5<sup>th</sup> order with corresponding error of  $O(\Delta t^6)$ . The expression of this method is as follows:

$$v_{n+1} = v_n + \frac{1}{6} \cdot (k_1 + 4k_4 + k_5) \quad (\text{B.44})$$

$$x_{n+1} = x_n + \frac{1}{6} \cdot (l_1 + 4l_4 + l_5) \quad (\text{B.45})$$

$$k_1 = \Delta t \cdot a(x_n, v_n, t_n) \quad (\text{B.46})$$

$$l_1 = \Delta t \cdot v_n \quad (\text{B.47})$$

$$k_2 = \Delta t \cdot a\left(x_n + \frac{1}{3}l_1, v_n + \frac{1}{3}k_1, t_{n+\frac{1}{3}}\right) \quad (\text{B.48})$$

$$l_2 = \Delta t \cdot \left(v_n + \frac{1}{3}k_1\right) \quad (\text{B.49})$$

$$k_3 = \Delta t \cdot a\left(x_n + \frac{1}{6}l_1 + \frac{1}{6}l_2, v_n + \frac{1}{6}k_1 + \frac{1}{6}k_2, t_{n+\frac{1}{3}}\right) \quad (\text{B.50})$$

$$l_3 = \Delta t \cdot \left(v_n + \frac{1}{6}k_1 + \frac{1}{6}k_2\right) \quad (\text{B.51})$$

$$k_4 = \Delta t \cdot a\left(x_n + \frac{1}{8}l_1 + \frac{3}{8}l_3, v_n + \frac{1}{8}k_1 + \frac{3}{8}k_3, t_{n+\frac{1}{2}}\right) \quad (\text{B.52})$$

$$l_4 = \Delta t \cdot \left(v_n + \frac{1}{8}k_1 + \frac{3}{8}k_3\right) \quad (\text{B.53})$$

$$k_5 = \Delta t \cdot a\left(x_n + \frac{1}{2}l_1 - \frac{3}{2}l_3 + 2l_4, v_n + \frac{1}{2}k_1 - \frac{3}{2}k_3 + 2k_4, t_{n+1}\right) \quad (\text{B.54})$$

$$l_5 = \Delta t \cdot \left(v_n + \frac{1}{2}k_1 - \frac{3}{2}k_3 + 2k_4\right) \quad (\text{B.55})$$

This modification has been widely used by [Zarnick \(1978\)](#), [Keuning \(1994\)](#) and [Akers \(1999\)](#) as it is more accurate than the ordinary Runge-Kutta with a slight alteration in formulation which results in insignificant different time consumption.

### B.8.6 Runge-Kutta-Fehlberg

The method is a modification of Runge-Kutta of the 6<sup>th</sup> order with corresponding error of  $O(\Delta t^7)$ .

$$v_{n+1}^{iv} = v_n + \left( \frac{25}{216} k_1 + \frac{1408}{2565} k_3 + \frac{2197}{4104} k_4 - \frac{1}{5} k_5 \right) \quad (\text{B.56})$$

$$v_{n+1}^v = v_n + \left( \frac{16}{135} k_1 + \frac{6656}{12825} k_3 + \frac{28561}{56430} k_4 - \frac{9}{50} k_5 + \frac{2}{55} k_6 \right) \quad (\text{B.57})$$

$$x_{n+1}^{iv} = x_n + \left( \frac{25}{216} l_1 + \frac{1408}{2565} l_3 + \frac{2197}{4104} l_4 - \frac{1}{5} l_5 \right) \quad (\text{B.58})$$

$$x_{n+1}^v = x_n + \left( \frac{16}{135} l_1 + \frac{6656}{12825} l_3 + \frac{28561}{56430} l_4 - \frac{9}{50} l_5 + \frac{2}{55} l_6 \right) \quad (\text{B.59})$$

$$k_1 = \Delta t \cdot a(x_n, v_n, t_n) \quad (\text{B.60})$$

$$l_1 = \Delta t \cdot v_n \quad (\text{B.61})$$

$$k_2 = \Delta t \cdot a \left( x_n + \frac{1}{4} l_1, v_n + \frac{1}{4} k_1, t_{n+\frac{1}{4}} \right) \quad (\text{B.62})$$

$$l_2 = \Delta t \left( v_n + \frac{1}{4} k_1 \right) \quad (\text{B.63})$$

$$k_3 = \Delta t \cdot a \left( x_n + \frac{3}{32} l_1 + \frac{9}{32} l_2, v_n + \frac{3}{32} k_1 + \frac{9}{32} k_2, t_{n+\frac{3}{8}} \right) \quad (\text{B.64})$$

$$l_3 = \Delta t \cdot \left( v_n + \frac{3}{32} k_1 + \frac{9}{32} k_2 \right) \quad (\text{B.65})$$

$$k_4 = \Delta t \cdot a \left( x_n + \frac{1932}{2197} l_1 - \frac{7200}{2197} l_2 + \frac{7296}{2197} l_3, v_n + \frac{1932}{2197} k_1 - \frac{7200}{2197} k_2 + \frac{7296}{2197} k_3, t_{n+\frac{12}{13}} \right) \quad (\text{B.66})$$

$$l_4 = \Delta t \cdot \left( v_n + \frac{1932}{2197} k_1 - \frac{7200}{2197} k_2 + \frac{7296}{2197} k_3 \right) \quad (\text{B.67})$$

$$k_5 = \Delta t \cdot a \left( x_n + \frac{439}{216} l_1 - 8 l_2 + \frac{3680}{513} l_3 - \frac{845}{4104} l_4, v_n + \frac{439}{216} k_1 - 8 k_2 + \frac{3680}{513} k_3 - \frac{845}{4104} k_4, t_{n+1} \right) \quad (\text{B.68})$$

$$l_5 = \Delta t \cdot \left( v_n + \frac{439}{216} k_1 - 8 k_2 + \frac{3680}{513} k_3 - \frac{845}{4104} k_4 \right) \quad (\text{B.69})$$

$$k_6 = \Delta t \cdot a \left( x_n - \frac{8}{27} l_1 + 2 l_2 - \frac{3544}{2565} l_3 + \frac{1859}{4104} l_4 - \frac{11}{40} l_5, v_n - \frac{8}{27} k_1 + 2 k_2 - \frac{3544}{2565} k_3 + \frac{1859}{4104} k_4 - \frac{11}{40} k_5, t_{n+\frac{1}{2}} \right) \quad (\text{B.70})$$

$$l_6 = \Delta t \cdot \left( v_n - \frac{8}{27} k_1 + 2 k_2 - \frac{3544}{2565} k_3 + \frac{1859}{4104} k_4 - \frac{11}{40} k_5 \right) \quad (\text{B.71})$$



## Appendix C

# Aircraft Ditching Load Prediction Tools Provided by Stirling Dynamics Ltd.

Following the aim and the objective of the collaborative work sponsored by NATEP, SDL and UoS developed numerical model and evaluated the load prediction together using different methodologies in order to carry out cross-validation. The mathematical model developed by UoS has been already mentioned in Chapter 6. Description of the other method developed by SDL and the high fidelity CFD setting are explained in the following section.

### C.1 SDL Ditching Loads Calculation Methodology

The methodology developed by SDL for calculating ditching loads is based in a linear combination of three types of loads:

- Added Mass Loads: Due to the vertical component of the aircraft velocity and acceleration.
- Steady Hydrodynamic Loads: Due to the forward component of the aircraft velocity.
- Hydrostatic Loads: Due to the submerged volume.

The following sections detail the calculation of each of the three types of loads. The SDL methodology has also been implemented within the dynamic response simulation tool SD-GLOSS.

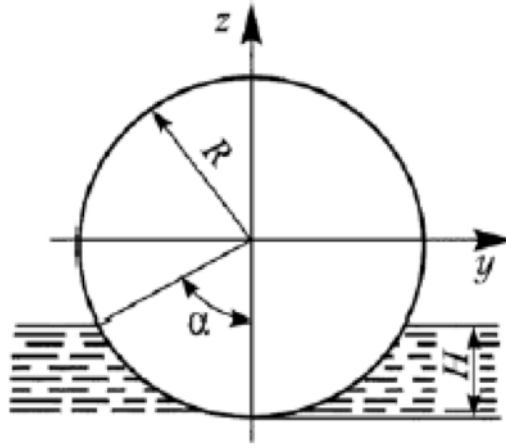


Figure C.1: Added mass term evaluated by formulation of [Korobkin \(2004\)](#).

### C.1.1 Added Mass Loads

The added mass represents the mass of the fluid that is moved as a reaction to the motion of the aircraft body. The water impact loads represent the loads acting on the body due to the inertia of the added mass, and is therefore obtained by evaluating the intrinsic variation of the added mass momentum, independent of the presence of any flow. This section details the calculation of the added mass term. The derivation directly follows from the expressions presented by [Korobkin \(2004\)](#) for circular two-dimensional sections moving in the proximity of the water surface.

The added mass of a 2D circular section moving vertically over a water surface can be calculated as a function of the section depth. The following nomenclature is adopted:

- $R$  is the radius of the cylinder.
- $\alpha$  is the angle defined in Figure [C.1](#).
- $K = 1 - \alpha/\pi$ .
- $h = R(1 - \cos \alpha)$ .

The added mass per unit length is expressed as ([Korobkin, 2004](#)):

$$\lambda_{33} = \rho R^2 \left( \frac{\pi \sin^2 \alpha}{6k^2} (1 + 2k^2) - \alpha + \frac{1}{2} \sin 2\alpha \right) \quad (\text{C.1})$$

For a vertical motion, the reaction of force  $F_z$  can be expressed as a function of the time derivative of the vertical velocity  $w$  as:

$$F_z = \lambda_{33} \frac{\partial w}{\partial t} \quad (\text{C.2})$$

For the case where the body is on the surface, the coefficient  $\lambda_{33}$  is also dependent on time  $t$ , through the variable  $\alpha$  (and  $k$ ) and therefore, the chain rule is applied:

$$F_z = \frac{\partial (\lambda_{33} (\lambda(t)) w)}{\partial t} \quad (\text{C.3})$$

The reaction force  $F_z$  can be rewritten as:

$$F_z = \frac{\partial \lambda_{33}}{\partial \alpha} \cdot \frac{\partial \alpha}{\partial h} \cdot \frac{\partial h}{\partial t} \cdot w + \lambda_{33} \frac{\partial w}{\partial t} \quad (\text{C.4})$$

Where  $\partial h / \partial t = w$ , therefore, this expression can be further simplified as:

$$F_z = \frac{\partial \lambda_{33}}{\partial \alpha} \cdot \frac{\partial \alpha}{\partial h} \cdot w^2 + \lambda_{33} \frac{\partial w}{\partial t} \quad (\text{C.5})$$

From this expression,  $F_z$  can be seen as a function of both the vertical velocity  $w$  and the vertical acceleration  $\partial w / \partial t$ .

### C.1.2 Steady Hydrodynamic Loads (Doublet Lattice Method)

The steady hydrodynamic loads acting on the airframe during the ditching phase are calculated by solving the inviscid incompressible flow around the airframe by a Doublet Lattice Method DLM technique (Bonanni et al., 2015). This approach accounts for an estimation of the water surface deformation during ditching Figure C.2. The doublets are distributed on a grid that approximates the water surface deformed by the aircraft motion. The surface is created by calculating the submerged portion of the aircraft and then interpolating the depths of each submerged triangle by a cubic surface spline defined on a selected portion of the water plane Figure C.2.

The actual DLM problem is then solved on a surface that comprises the interpolating surface and its mirrored copy with respect to the undisturbed water plane. This last step is needed to enforce symmetry to the potential flow generated by the doublets. Once the flow is made symmetric with respect to the water plane, the induced velocities at each point on the water plane are parallel to the undisturbed water plane itself (reflecting



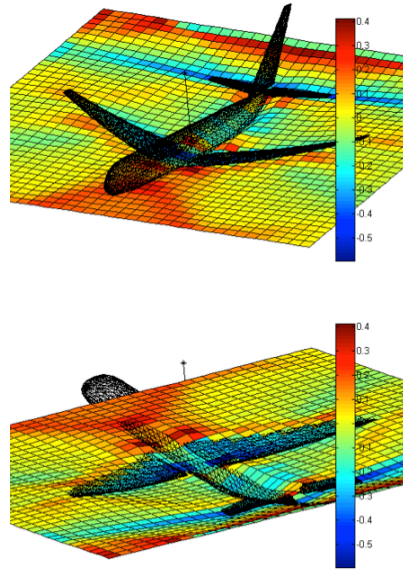


Figure C.2: Hydrodynamic loads are calculated from the pressure distribution of the Doublet Lattice Method ([Bonanni et al., 2015](#)).

therefore the steady horizontal motion of the aircraft through the water). This approach is deemed more accurate for the pressure distribution on the submerged part of the aircraft (where the interpolating spline well approximates the aircraft geometry) and less in the wake region where no information is available on the actual shape of the water wake.

### C.1.3 Hydrostatic Loads

The calculation of the hydrostatic loads is based on hydrostatic pressure integration over a discretized representation of the submerged portion of the airframe. The integration only accounts for the elements of the discretized surface whose midpoints are submerged below the water line, and whose external normal have a component pointing downwards with respect to the normal of the undisturbed water surface (this last condition identifies the elements that are assumed “dry” during ditching).

### C.1.4 SD-GLOSS Simulation Tool

As mentioned, the SDL methodology has been implemented within the Stirling Proprietary Software SD-GLOSS for dynamic ditching simulations. SD-GLOSS is a software tool for calculating the dynamic response of flexible aircraft structures and subsequent airframe loads due to landing, ground, manoeuvre and wheels-up landing. This section details the SD-GLOSS calculation methodology, relevant to the inclusion of the ditching simulation capability.

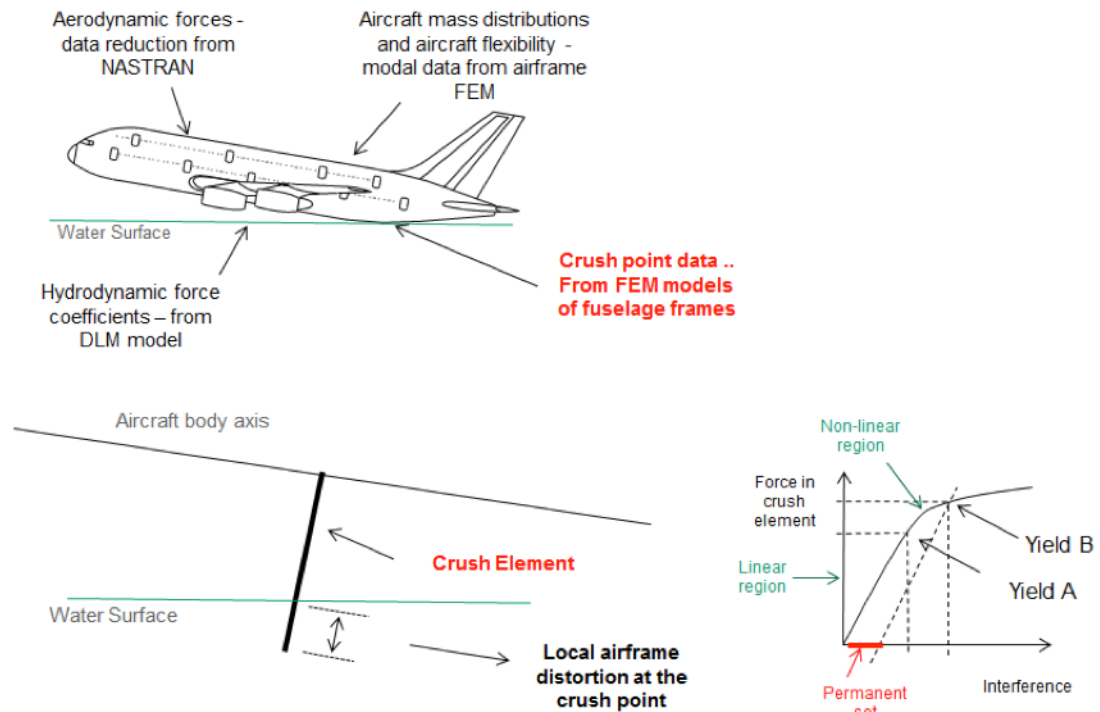


Figure C.3: SD - GLOSS methodology summary.

SD - GLOSS obtains the dynamic response of the aircraft during a manoeuvre by applying the general equations of unsteady motion for the rigid body response and the method of normal modes for the elastic motions. The modelling approach used in SD-GLOSS is illustrated in Figure C.3, and superimposes both global deformation of the structure (along the main fuselage axis) and local deformation of the fuselage cross-sections from the defined crush elements on the rigid body motion. The ditching loads act on this set of crush elements which are defined along the belly line of the fuselage. It is proposed that the computation of the impact forces and hydrostatic forces be computed at each time step and the hydrodynamic forces obtained from a set of force coefficients that are a function of aircraft state and derived from the DLM model. This method using force coefficients will then enable investigative studies and parametric analysis.

Thus the analytical framework developed for the calculation of the dynamic response of the aircraft during ditching is based on the following assumptions:

- Fully flexible aircraft with flexibility described by normal mode methods (stick model).
- 6-DOF rigid body response with the rigid body response carrying the flexibility description.
- Airframe outer shape carrying crush points that deform linearly and non-linearly as a function of the applied force.

- Aerodynamic forces as a function of incidence and elevator angle.
- Symmetric initial balance equating gravitational and aerodynamic forces/moments established with the closest airframe crush point set just above the water surface.
- Current implementation is limited to a smooth water surface and a symmetric aircraft response.

## C.2 CFD Model

A computational Fluid Dynamics tool has been used to validate the developed loads prediction methodologies described in the previous sections.

### C.2.1 Aircraft Fuselage Geometry

The fuselage model used for the present analysis has been designed to be a simplified but representative shape of a typical civil aircraft. It features:

- A circular cross-section of constant diameter.
- Steam lined nose section.
- Tapered tail section.

The full geometry is created by sweeping the circular cross section along the top and bottom curve. The top and bottom curve are not analytically defined and are represented in Figure C.4.

The surface of the fuselage is then discretized by triangular elements. The discretization features 25 cross sections in the main stream direction and 15 vertices for each circular section. Main fuselage dimensions are:

- $L_x = 23.33 \text{ m}$ .
- $L_y = L_z = 2.20 \text{ m}$ .

### C.2.2 CFD Physical Model

The computational Fluid Dynamic (CFD) model used for simulating the flow around the submerged part of the ditching aircraft is based on a URANS  $k - \epsilon$  turbulence model. The software used is the commercial package CD - Adapco StarCCM+. The two - phase flow (air + water) is modelled by an Eulerian Volume of Fluid (VOF) model.

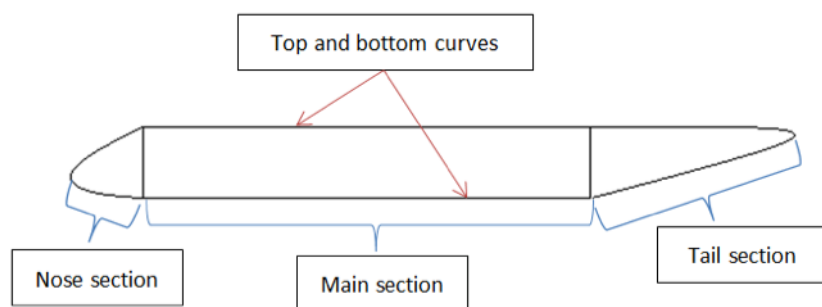


Figure C.4: A fuselage shape has been used for validation of the loads calculation methodologies.

### C.2.3 Computational Mesh

The CFD computational mesh features an unstructured Cartesian topology (trimmed mesh) and is designed with the aim of accurately calculating the loads acting on the airframe, with no specific requirement for maintaining a high fidelity in the downstream wake. This implies using a refinement region around the airframe and along the water surface. A refined water surface region is needed to keep a sharp separation between water and air phases. For all the cases where both a horizontal and a vertical component of the velocity are considered, a moving mesh is employed. The overall set-up can be summarized as follows:

- The moving mesh is attached to the airframe and moves with respect to the earth axes.
- The motion of the mesh can be set to follow a prescribed trajectory or be the result of the loads acting on the airframe (in the latter case a Dynamic Fluid Body Interaction (DFBI) problem is solved).
- The undisturbed water phase occupies a time invariant in earth axes.

The above definition of the CFD problem allows using one computational mesh without recurring to overset meshes (meshes with relative motion with respect to each other). This approach avoids the inaccuracies introduced by the interpolation of the CFD solution at the boundary of the overset meshes.

An example of the CFD mesh is depicted in Figure C.5. It must be noted that the mesh is designed to be aligned with the main flow direction at all times (with exception for the DFBI cases where the pitch angle of the fuselage varies in time as a result of the airframe motion).

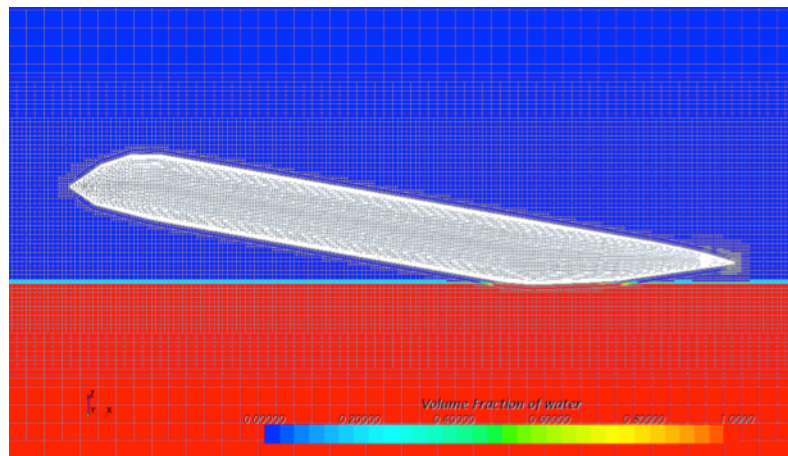


Figure C.5: Example of the Unstructured Cartesian CFD mesh employed for loads calculation.

## Appendix D

# Ditching Experimental Equipment and Instrumentation

The use of launching equipment or the launching rig needs to meet the conditions of the facility and the preliminary simulations. The horizontal landing speed can be achieved by the towing speed of the tank's carriage. While the vertical motions will be restricted by a guided rail form component. The whole equipment is shown schematically in Figure D.1. It consists of the following components:

**Main Rig: Component A:** It is made of aluminium alloy in order to lighten the weight as much as possible to match the strength of the aluminium frame of the carriage and its dimension. A steel rail is fixed at middle part laying down along the length of the rig. Two hanging fangs are installed in the back part of the hose. All of the parts are pre-calculated with FEM simulations following the maximum load predefined by numerical simulations in both horizontal and vertical directions.

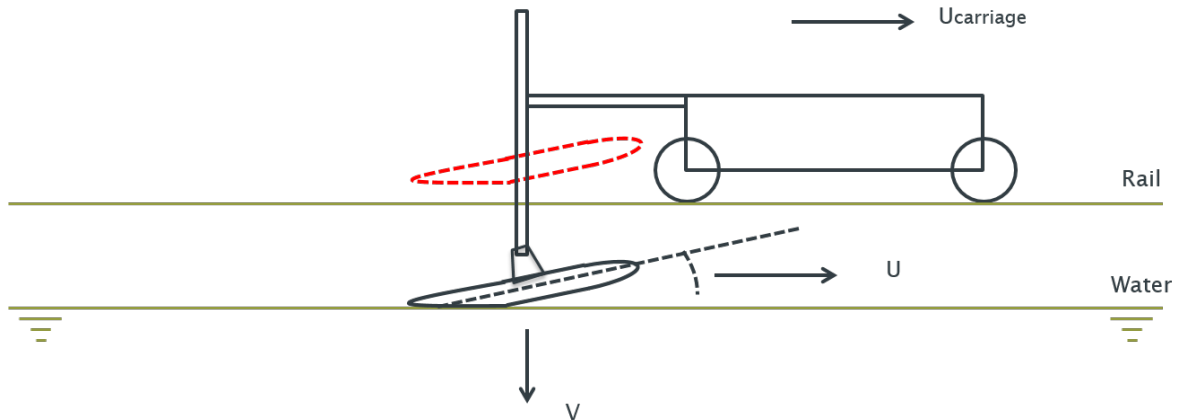


Figure D.1: Full launching equipment.

**Sliding Post: Component B:** This component is also made of aluminium alloyed and attached at the back part by two steel carriages provided by the same supplier as the steel rail in the rig. The carriages allow the post to slide smoothly along the rail and restrict the displacement of the post to be guided solely in the rail direction. Note the no matter how smooth could it slide, it experiences a significant amount of friction between the carriages and the rail. This leads the inclusion of this loss when considering the real vertical acceleration of the ditching event, as it does commit the pure gravitational acceleration as expected.

**Loadcell Case: Component C:** The case consists of two separate parts, the upper and the lower. The upper part has two bolt channels to attach to the sliding post allowing the yaw alignment to be adjustable. Two screws are tightened to the upper face of the loadcell, while the other two are attached with the lower also through the screws. Both parts are not physically in contact, allowing a small clearance to avoid the interruption of loadcell deflection, but is still useful as a physical emergency stop.

**Trim Fitting: Component D:** The upper part is attached to the loadcell case through four screws while the lower to the model also by four screws. The small lateral holes in both sides allow the adjustment of trim angle from  $1^\circ$  to  $10^\circ$  covering the landing attitudes planned as a controlling parameter.

### D.0.1 Sensors and Instruments

The parameters of interest as mention previously in the experimental planning are the total impact force and impact acceleration. To fulfil this aim, three sensors are available covering the requirement of the further data processing.

**NOVATECH F332 2 Axis Loadcell:** Provided by Novatech Instruments. It is customized and calibrated respectively in vertical and horizontal directions to  $\pm 700\text{ N}$  and  $\pm 300\text{ N}$  as pre-calculated when designing the rig.

**PCB PIEZOTRONICS 353B31 Single Axis Accelerometer:** It is characteristically dynamic accelerometer calibrated to give the reading in  $g$ s unit. Attaching to a static object will give 0 reading while the free falling gives 1  $g$ .

**Linear String Potentiometer PT5A:** The instrument consists of a roll of a string with restoring mechanism. The restoring needs to be accounted for as a component of friction of the rig, when analysing the exact hydrodynamic force. It is calibrated to give the reading in millimetre.

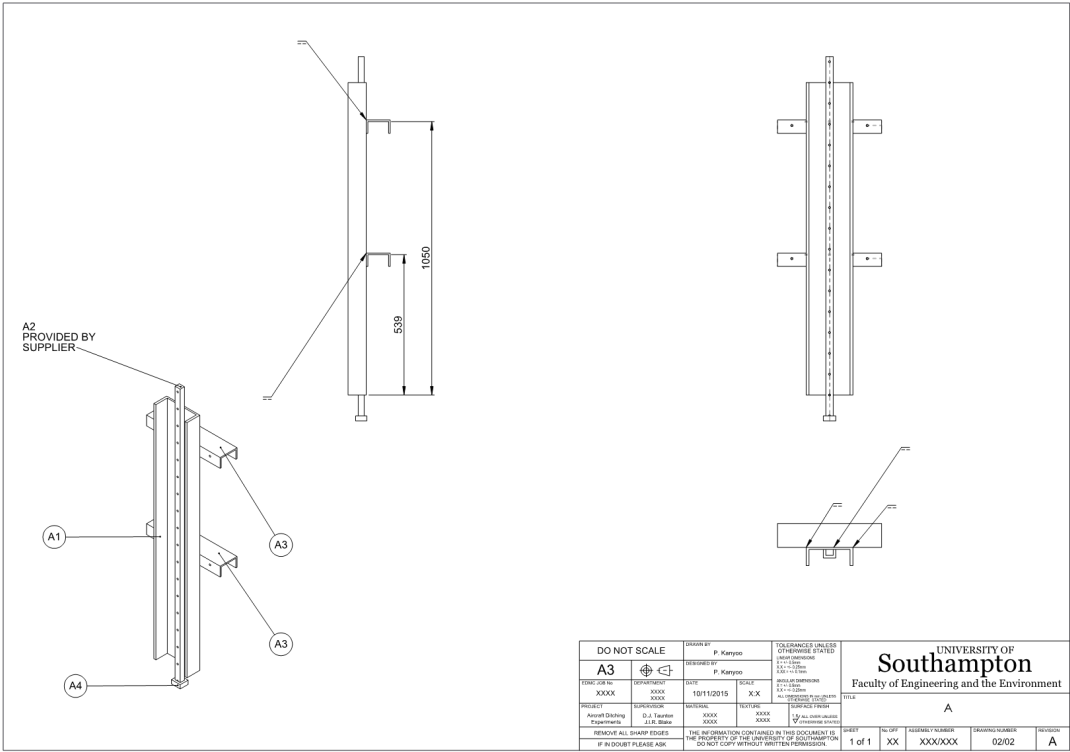


Figure D.2: Main rig.

**National Instruments CompactDAQ Controllers cDAQ-913x:** The logger comprises of several slots for various data acquisition socket. It contains its own operating system and acts as a computer. The access to the logger is done through a laptop using a remote computer application. The logger receives the signal data from the other instruments controlling the sample rate to be 10,240 Hz. This high frequency of sample rate does not allow the real-time graphic representation to be shown. The logger records the data of these three instruments in a spread sheet which can be further exported to filter and analyse in a mathematical modelling tool.



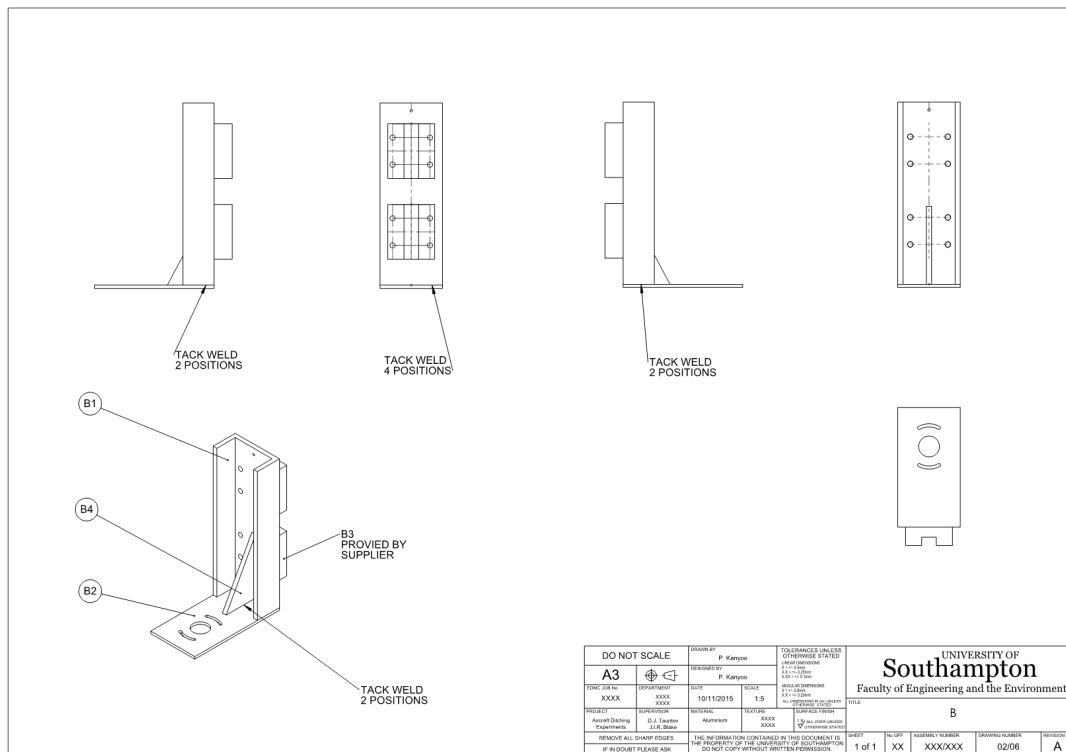


Figure D.3: Sliding post.

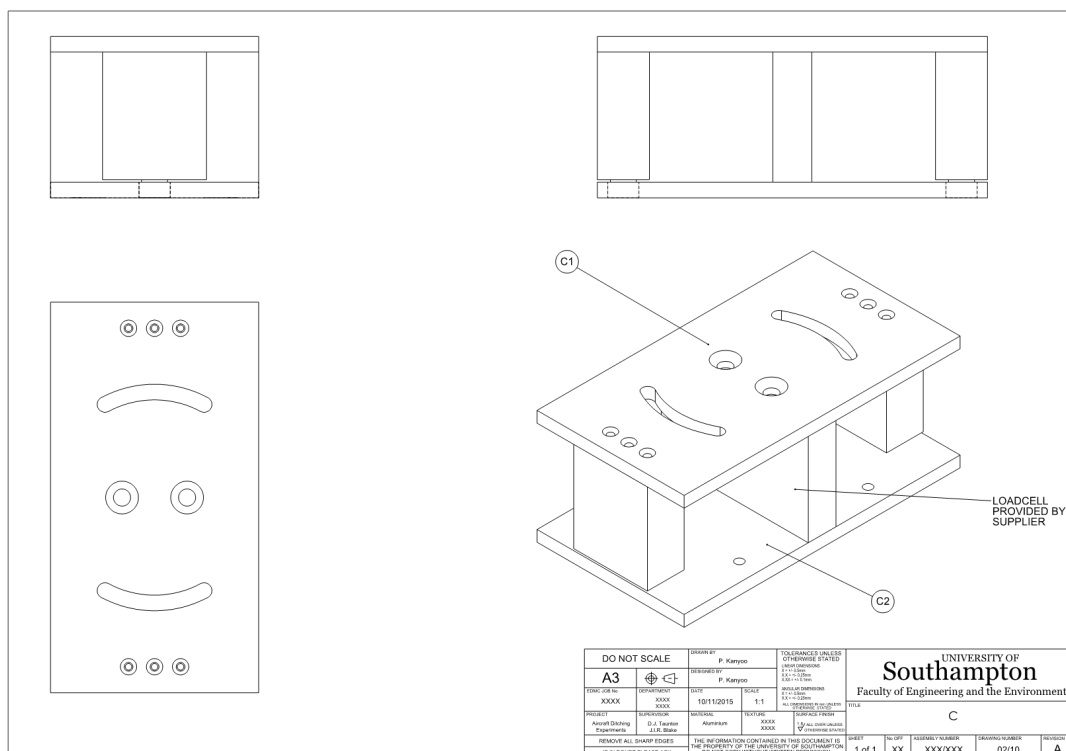


Figure D.4: Loadcell case.

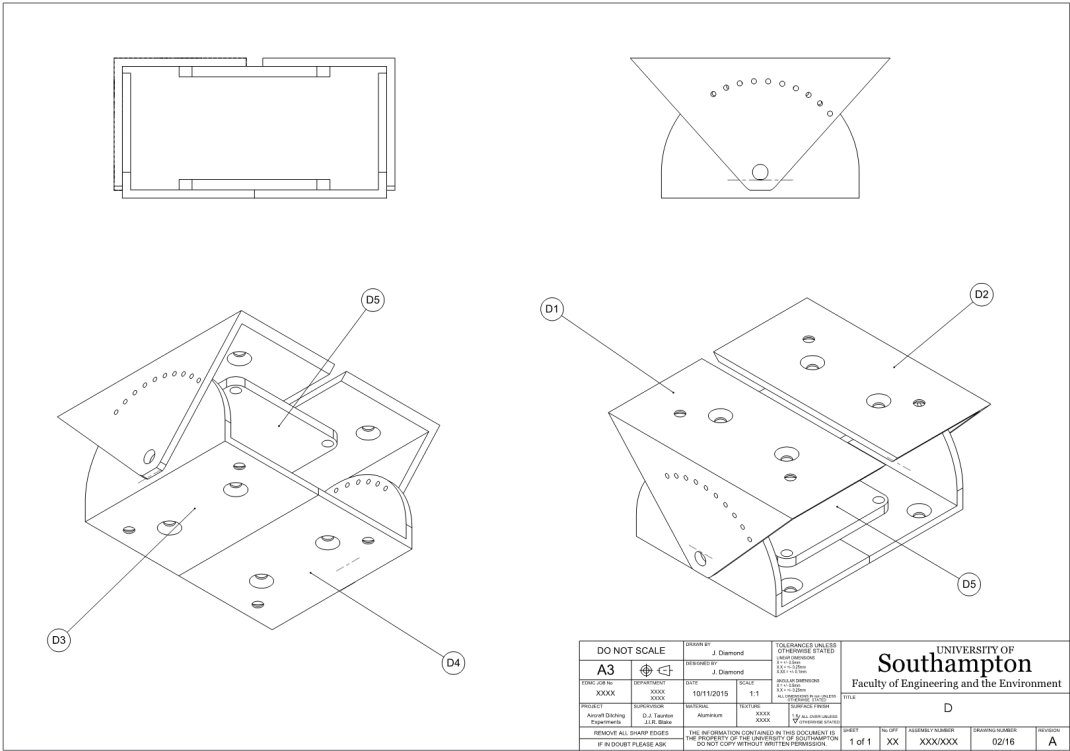


Figure D.5: Pitch fitting.



Figure D.6: NOVATECH F332 2 Axis Loadcell.



Figure D.7: Accelerometer.

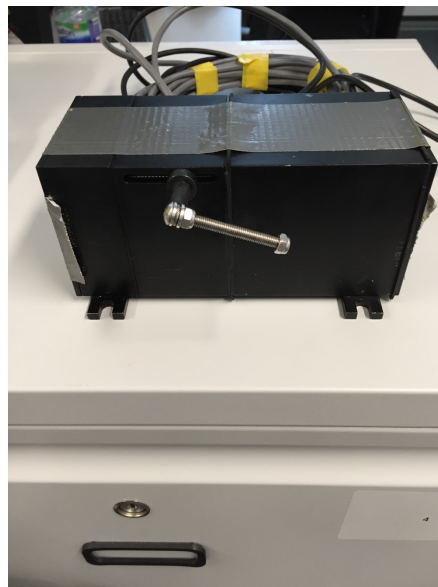


Figure D.8: Linear String Potentiometer PT5A.



Figure D.9: National Instruments CompactDAQ Controllers cDAQ-913x.

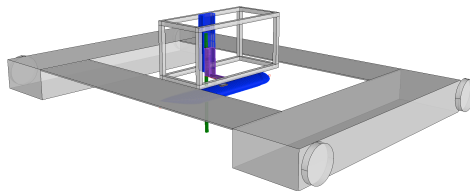


Figure D.10: Overview of the rig installed on the carriage (1).

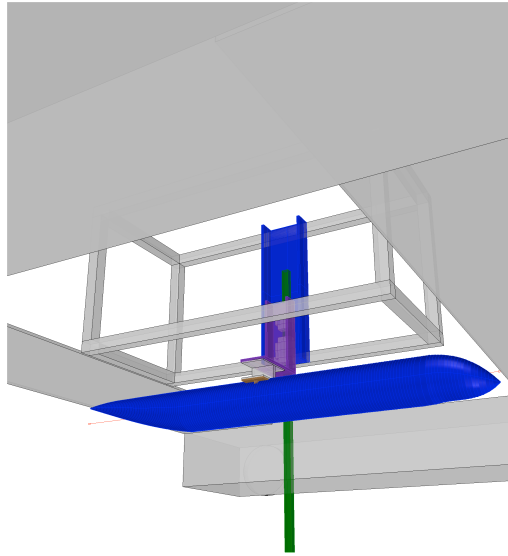


Figure D.11: Overview of the rig installed on the carriage (2).

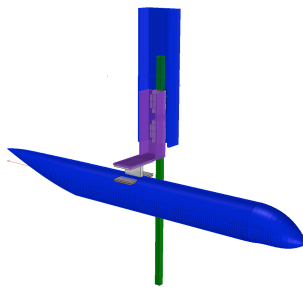


Figure D.12: Overview of the rig installed on the carriage (3).

# References

- AIAA (1998). Guide for the Verification and Validation of Computational Fluid Dynamics Simulations. Technical report, American Institute of Aeronautics and Astronautics, Reston, Virginia.
- Akers, R. H. (1999). Dynamic Analysis of Planing Hulls in the Vertical Plane. *New England Section, SNAME*.
- Algarín, R., Bula, A., and Tascón, O. (2011). CFD Modeling of 2D Impact with Symmetric Entry. *Ship Science & Technology*, 4(8):31–39.
- Algarín, R. and Tascón, O. (2011). Hydrodynamic Modeling of Planing Boats with Asymmetry and Steady Condition. *HSMV*, 2(May):1–9.
- Arai, M. and Matsunaga, K. (1989). A Numerical and Experimental Study of Bow Flare Slamming. *Journal of Society of Naval Architecture Japan*, 166.
- Armand, J. L. and Cointe, R. (1987). Hydrodynamic Impact Analysis of a Cylinder. In *5th International Offshore Mechanics and Arctic Engineering Symposium*, pages 609–634, Tokyo.
- Azcueta, R. (2003). Steady and Unsteady RANSE Simulations for Planing Crafts. In *FAST 2003 The 7th International Conference on Fast Sea Transportation*, pages 41–48, Abano Terme, Italy.
- Azcueta, R., Caponnetto, M., and Soeding, H. (2003). Planing Boats in Waves. *Numerical Towing Tank Symposium*, pages 3–15.
- Blake, J. I. R. (2000). *An Analysis of Planing Craft Dynamics in Calm Water and in Waves*. PhD Thesis, University of Southampton.
- Bonanni, A., Vandewaeter, L., Havill, C., Kanyoo, P., Taunton, D. J., Blake, J. I. R., Cropper, E., and Hancock, S. (2015). Aircraft Ditching Loads Simulation Tool. *Applied Mechanics and Materials*, 798:531–535.
- Bretschneider, C. L. (1952). Revised Wave Forecasting Relationships. In *2nd Conference on Coastal Engineering*, pages 1–5.

- Bretschneider, C. L. (1957). Revision in Wave Forecasting: Deep and Shallow Water. In *6th Conference on Coastal Engineering*, pages 30–67.
- Brown, P. W. and Klosinski, W. E. (1995). Experimental Determination of the Added Inertia and Damping of Planing Boats in Roll. Technical report, Davidson Laboratory, Stevens Institute of Technology, Hoboken, New Jersey.
- Campbell, I. M. C. and Weynberg, P. A. (1980). Measurement of Parameters Affecting Slamming. Technical report, Wolfson Unit for Marine Technology and Industrial Aerodynamics, University of Southampton, Southampton.
- Cartwright, D. E. and Longuet-Higgins, M. S. (1956). The Statistical Distribution of the Maxima of a Random Function. *Proceedings of the Royal Society A: Mathematical, Physical and Engineering Sciences*, 237(1209):212–232.
- Chiu, F.-c. and Fujino, M. (1989). Nonlinear Prediction of Vertical Motions and Wave Loads of High Speed Craft in Head Sea. *International Shipbuilding Progress*, 36(406):193–232.
- Climent, H., Benitez, L., Rosich, F., Rueda, F., and Pentecote, N. (2006). Aircraft Ditching Numerical Simulation. In *25th International Congress of the Aeronautical Sciences*, Hamburg.
- Deyzen, A. V. (2008). A Nonlinear Mathematical Model of Motions of a Planing Monohull in Head Seas. In *in Proceedings of the 6th International Conference on High Performance Marine Vehicles*, pages 187–200, Naples.
- Dommermuth, D., Sussman, M., Beck, R., O’Shea, T. T., Wyatt, D., Olson, K., and MacNeice, P. (2004). The Numerical Simulation of Ship Waves using Cartesian Grid Methods with Adaptive Mesh Refinement. In *25th Symposium on Naval Hydrodynamics*, St. John’s, Newfoundland and Labrador.
- Dommermuth, D. G., O’Shea, T. T., Wyatt, D. C., Ratcliffe, T., Weymouth, G. D., Hendrikson, K. L., Yue, D. K. P., Sussman, M., Adams, P., and Valenciano, M. (2007). An Application of Cartesian-Grid and Volume-of-Fluid Methods to Numerical Ship Hydrodynamics. In *9th International Conference on Numerical Ship Hydrodynamics*, Ann Arbor, Michigan.
- Dommermuth, D. G., O’Shea, T. T., Wyatt, D. C., Sussman, M., Weymouth, G. D., Yue, D. K. P., Adams, P., and Hand, R. (2006). The Numerical Simulation of Ship Waves using Cartesian-Grid and Volume-of-Fluid Methods. In *26th Symposium on Naval Hydrodynamics*, Rome.
- Ensign, W., Hodgdon, J. A., Prusaczyk, W. K., Ahlers, S., Shapiro, D., and Lipton, M. (2000). A Survey of Self-Reported Injuries among Special Boat Operators. Technical report, Naval Health Research Center, San Diego, CA.

- Fabula, A. (1957). Ellipse Fitting Approximation of Two-Dimensional Normal Symmetric Impact of Rigid Bodies on Water. In *5th Midwestern Conference on Fluid Mechanics*. University of Michigan Press.
- Faltinsen, O. M. (2000). *Hydrodynamics of High-Speed Marine Vehicles*. Cambridge University Press, The Edinburgh Building, Cambridge, CB2 2RU, United Kingdom.
- Faltinsen, O. M. and Sun, H. (2007). Hydrodynamic Forces on a Planing Hull in Forced Heave or Pitch Motions in Calm Water. In *22nd International Workshop on Water Waves and Floating Bodies*, pages 185–188, Plitvice.
- Faltinsen, O. M. and Sun, H. (2010). Numerical Study of Planing Vessels in Waves. *Journal of Hydrodynamics*, 22(5):468–475.
- Faltinsen, O. M. and Sun, H. (2011). Dynamic Behavior of Semi-Displacement and Planing Vessels in Calm Water and Waves. In *IX High Speed Marine Vehicles*, Naples.
- Fridsma, G. (1969). A Systematic Study of the Rough-Water Performance on Planing Boats (Part I: Regular Waves). Technical report, Davidson Laboratory, Stevens Institute of Technology, Hoboken, New Jersey.
- Fridsma, G. (1971). A Systematic Study of the Rough-Water Performance on Planing Boats (Part II: Irregular Waves). Technical report, Davidson Laboratory, Stevens Institute of Technology, Hoboken, New Jersey.
- Fu, T. C., Akers, R. H., O’Shea, T. T., Brucker, K., Dommermuth, D. G., and Lee, E. (2011). Measurements and Computational Predictions of A Deep-V Monohull Planing Hull. In *FAST 2011 11th International Conference on Fast Sea Transportation*, pages 404–412, Honolulu Hawaii.
- Fu, T. C., O’Shea, T. T., Judge, C. Q., Dommermuth, D., Brucker, K., and Wyatt, D. C. (2013). A Detailed Assessment of Numerical Flow Analysis (NFA) to Predict the Hydrodynamics of a Deep-V Planing Hull. In *International Shipbuilding Progress*, volume 60, pages 143–169.
- Garne, K. (2004a). Model Experiment Addressing the Impact Pressure Distribution on Planing Craft in Waves. *International Journal of Small Craft Technology*, 146.
- Garne, K. (2004b). *Modeling of Planing Craft in Waves*. PhD Thesis, Royal Institute of Technology KTH.
- Garne, K. (2005). Improved Time Domain Simulation of Planing Hulls in Waves by Correction of the Near-Transom Lift. *International Shipbuilding Progress*, 52(3):201–230.
- Garne, K. and Rosén, A. (2003). Time-Domain Simulations and Full-Scale Trials on Planing Craft in Waves. *International Shipbuilding Progress*, 50(3):177–208.



- Ghadimi, P., Dashtimanesh, A., and Djeddi, S. R. (2012). Study of water entry of circular cylinder by using analytical and numerical solutions. *Journal of the Brazilian Society of Mechanical Sciences and Engineering*, 34(3):225–232.
- Greenhow, M. (1988). Water-Entry and -Exit of a Horizontal Circular Cylinder. *Journal of Applied Ocean Research*, 10:191–198.
- Hasselmann, K., Barnett, T. P., Bouws, E., Carlson, H., Cartwright, D. E., Enke, K., Ewing, J. A., Gienapp, H., Hasselmann, D. E., Kruseman, P., Meerburg, A., Muller, P., Olbers, D. J., Richter, K., Sell, W., and Walden, H. (1973). Measurements of Wind-Wave Growth and Swell Decay during the Joint North Sea Wave Project (JONSWAP). Technical report, Deutsches Hydrographisches Institut, Hamburg.
- Howison, S. D., Ockendon, J. R., and Wilson, S. K. (1991). Incompressible Water-Entry Problems at Small Deadrise Angles. *Journal of Fluid Mechanics*, 222:215–230.
- Hua, J., Wu, J.-L., and Wang, W.-H. (2000). Effect of Asymmetric Hydrodynamic Impact on the Dynamic Response of a Plate Structure. *Journal of Marine Science and Technology*, 8(2):71–77.
- Iafrati, A. and Calcagni, D. (2013). Numerical and Experimental Studies of Plate Ditching. In *28th International Workshop on Water Waves and Floating Bodies*, Marseille.
- Iafrati, A., Siemann, M. H., and Benítez Montañés, L. (2014). Experimental Study of High Speed Plate Ditching. In *29th International Workshop on Water Waves and Floating Bodies*, Osaka.
- Ikeda, Y. and Katayama, T. (2000). Stability of High Speed Craft. In Vassalos, D., Hamamoto, M., Papanikolaou, A., and Molyneux, D., editors, *Contemporary Ideas on Ship Stability*, pages 401–409, Oxford. Elsevier Ltd.
- Journée, J. and Massie, W. W. (2001). *Offshore Hydromechanics*. Delft, first edition.
- Kanyoo, P., Taunton, D. J., and Blake, J. I. R. (2014). Preliminary Modifications to High Speed Planing Craft Simulation for Prescribed Trajectory of Wingless Prismatic and Tubular Form into Water. Technical report, University of Southampton, Southampton, UK.
- Kanyoo, P., Taunton, D. J., and Blake, J. I. R. (2015). Development and Optimization of Mathematical Model of High Speed Planing Dynamics. In *FAST 2015*, Wansington, D.C.
- Keuning, J. A. (1994). *The Nonlinear Behaviour of Fast Monohulls in Head Waves*. PhD Thesis, Delft University of Technology.
- Korobkin, A. (2004). Analytical Models of Water Impact. *European Journal of Applied Mathematics*, 15:821–838.

- Korvin-Kroukovsky, B. V. and Jacobs, W. R. (1957). Pitching and Heaving Motions of a Ship in Regular Waves. Technical report, Davidson Laboratory, Stevens Institute of Technology, Hoboken, New Jersey.
- Lewis, E. V. (1988). *Principles of Naval Architecture*. SNAME, 2nd edition.
- Lewis, S. G., Hudson, D. A., and Turncock, S. R. (2007). Simulation of a free falling wedge into water using 2D CFD with applications in the prediction of high speed craft motions. In *10th Numerical Towing Tank Symposium*, Hamburg.
- Lewis, S. G., Hudson, D. A., Turnock, S. R., and Taunton, D. J. (2010). Impact of a Free-Falling Wedge with Water: Synchronized Visualization, Pressure and Acceleration Measurements. *Fluid Dynamics Research*, 42(3).
- Li, A. (2014). Off-Design Operation of High Speed Craft and its Impact on Safety Issues. Technical report, University of Southampton, Southampton, UK.
- Lloyds, A. R. J. M. (1998). *Seakeeping: Ship Behaviour in Rough Weather*. RPM Reprographic, 26 Spithead Avenue, Gosport, Hampshire, United Kingdom.
- Logvinovich, G. V. (1969). *Hydrodynamics of Flows with Free Boundaries*. Naukova Dumka Publishing House, Kiev, Ukraine.
- Martin, M. (1976a). Theoretical Determination of Porpoising Instability of High-Speed Planing Boats. Technical report, David W. Taylor Naval Ship Research and Development Center, Bethesda MD.
- Martin, M. (1976b). Theoretical prediction of motions of high-speed planing boats in waves. Technical report, David W. Taylor Naval Ship Research and Development Center, Bethesda MD.
- McBride, E. E. and Fisher, L. J. (1953). Experimental Investigation of the Effect of Rear-Fuselage Shape on Ditching Behavior. Technical report, National Advisory Committee for Aeronautics, Langley Field, Virginia.
- Mei, X., Liu, Y., and Yue, D. K. P. (1999). On the Water Impact of General Two-Dimensional Sections. *Applied Ocean Research*, 21:1–15.
- Ochi, M. K. and Hubble, E. N. (1976). Six Parameter Wave Spectra. In *5th Coastal Engineering Conference*, pages 301–328, Honolulu Hawaii. ASCE.
- Oliver, J. M. (2002). *Water Entry and Related Problems*. PhD Thesis, University of Oxford.
- Payne, P. R. (1981). The Vertical Impact of a Wedge on a Fluid. *Ocean Engineering*, 8(4):421–436.
- Payne, P. R. (1992). A Unification in the Added Mass Theory of Planing. *Ocean Engineering*, 19(1):39–55.

- Payne, P. R. (1994). Recent Developments in “Added-Mass” Planing Theory. *Ocean Engineering*, 21(3):257–309.
- Pierson, J. D. and Leshnover (1950). A Study of the Flow, Pressure and Loads Pertaining to Prismatic Vee-Planing Surfaces. Technical report, Davidson Laboratory, Stevens Institute of Technology, Hoboken, New Jersey.
- Pierson, W. J. J. and Moskowitz, L. (1964). A Proposed Spectral Form for Fully Developed Wind Seas Based on the Similitude Theory of S.A. Kitaigorodskii. *J. Geophys. Res.*, 69(24):5181–5190.
- Rosén, A. and Garne, K. (2006). Pressure Investigation on a High-Speed Craft in Waves. Technical report, Royal Institute of Technology KTH, Stockholm.
- Ruscelli, D. (2009). *Dynamics of High Speed Craft*. PhD Thesis, Università degli Studi di Genova.
- Salvesen, N., Tuck, E. O., and Faltinsen, O. M. (1970). Ship Motions and Sea Loads. *Trans. SNAME*, 78:250–287.
- Savitsky, D. (1964). Hydrodynamic Design of Planing Hulls. *Marine Technology*, 1(1):71–95.
- Savitsky, D. (1968). On the Seakeeping of Planing Monohulls. *Marine Technology*, 5(2):164–174.
- Savitsky, D. and Brown, P. W. (1976). Procedures for Hydrodynamic Evaluation of Planing Hulls in Smooth and Rough Water.pdf. *Marine Technology*, 14(4):381–400.
- Sebastiani, L., Bruzzone, D., Gualeni, P., Rambaldi, G., Ruscelli, D., and Viviani, M. (2008). A practical method for the prediction of planing craft motions in regular and irregular waves. In *27th International Conference on Offshore Mechanics and Arctic Engineering*, volume 4, pages 687–696, Estoril.
- Seif, M. S., Mousaviraad, S. M., and Sadathosseini, S. H. (2004). The effect of asymmetric water entry on the hydrodynamic impact. *IJE Transactions A: Basic*, 17(2):205–212.
- Siemann, M. H., Kohlgruber, D., Benítez Montañés, L., and Iafrati, A. (2012). Numerical Simulation and Experimental Validation of Guided Ditching Tests. In *WCCM XI ECCM V ECFD VI*.
- Smiley, R. F. (1951). A Semiempirical Procedure for Computing the Water Pressure Distribution on Flat and V-Bottom Prismatic Surfaces During Impact or Planing. Technical report, Langley Aeronautical Laboratory, Washington DC.

- Smith, A. G., Warren, C. H. E., and Wright, D. F. (1952). Investigations of the Behaviour of Aircraft When Making a Forced Landing on Water (Ditching). Technical report, Aeronautical Research Council Reports and Memoranda, Ministry of Supply, London.
- St Denis, M. (1980). On the Statistical Description of Seaways of Moderate Severity. In *Ship Technol. Res. Symp.*, pages 21–49. SNAME.
- Streckwall, H., Lindenau, O., and Bensch, L. (2007). Aircraft Ditching: A Free Surface/Free Motion Problem. *Archives of Civil and Mechanical Engineering*, 7(3):177–190.
- Su, Y., Chen, Q., Shen, H., and Lu, W. (2012). Numerical Simulation of a Planing Vessel at High Speed. *Journal of Marine Science and Application*, 11(2):178–183.
- Sun, H. and Faltinsen, O. M. (2006). Water Impact of Horizontal Circular Cylinder and Cylindrical Shells. *Journal of Applied Ocean Research*, 28:299–311.
- Taunton, D. J., Hudson, D. A., and Sheno, R. A. (2011a). Characteristics of a Series of High Speed Hard Chine Planing Hulls-Part I: Performance in Calm Water. *International Journal of Small Craft Technology*, 152:55–75.
- Taunton, D. J., Hudson, D. A., and Sheno, R. A. (2011b). Characteristics of a Series of High Speed Hard Chine Planing Hulls-Part II: Performance in Waves. *International Journal of Small Craft Technology*, 153:1–22.
- Toxopeus, S. L., Keuning, J. A., and Hooft, J. P. (1997). Dynamic Stability of Planing Ships. In *International Symposium on The Safety of High Speed Craft*, London.
- Toyama, Y. (1993). Two-Dimension Water Impact of Unsymmetrical Bodies. *Journal of Society of Naval Architecture Japan*, 173:285–291.
- Vandewaeter, L., Bonanni, A., Havill, C., Kanyoo, P., Taunton, D. J., Blake, J. I. R., Cropper, E., and Hancock, S. (2015). Dynamic Simulation of Aircraft Ditching: Development and Verification of a Software Tool. In *5th EASN Association International Workshop on Aerostructures*, Manchester, UK.
- von Karman, T. (1929). The Impact on Seaplane Floats during Landing. Technical report, National Advisory Committee for Aeronautics, Washington DC.
- Vorus, W. S. (1996). A Flat Cylinder Theory for Vessel Impact and Steady Planing Resistance. *Journal of Ship Research*, 40:89–106.
- Wagner, H. (1931). Landing of seaplanes. Technical report, National Advisory Committee for Aeronautics, Washington DC.
- Wagner, H. (1932). The Phenomena of Impact and Planing on Water. Technical report, National Advisory Committee for Aeronautics, Washington DC.

- Xu, G. D., Duan, W. Y., and Wu, G. X. (2008). Numerical simulation of oblique water entry of an asymmetrical wedge. *Ocean Engineering*, 35(16):1597–1603.
- Xu, L. (1998). *A Theory for Asymmetric Vessel Impact and Steady Planing*. PhD Thesis, University of Michigan.
- Zarnick, E. E. (1978). A Nonlinear Mathematical Model of Motions of a Planing Boat in Regular Waves. Technical report, David W. Taylor Naval Ship Research and Development Center, Bethesda MD.
- Zarnick, E. E. (1979). A Nonlinear Mathematical Model of Motions of a Planing Boat in Irregular Waves. Technical report, David W. Taylor Naval Ship Research and Development Center, Bethesda MD.
- Zhao, R., Faltinsen, O. M., and Aarsnes, J. V. (1996). Water Entry of Arbitrary Two Dimensional Section with and without Flow Separation. In *21st Symposium on Naval Hydrodynamics*.
- Zhu, X., Faltinsen, O. M., and Hu, C. (2006). Water Entry and Exit of a Horizontal Circular Cylinder. *Journal of Offshore Mechanics and Arctic Engineering*, 129(4):253–264.